

Imperial College London
Department of Physics

Stories from different worlds in the universe of complex systems

**A journey through microstructural dynamics and emergent
behaviours in the human heart and financial markets**

Alberto Ciacci

Supervised by Professor Kim Christensen

Submitted in part fulfilment of the requirements for the degree of
Doctor of Philosophy in Physics of Imperial College London, April 2022

Statement of Originality

I herewith certify that to the best of my knowledge, the material of this dissertation is my own work. This dissertation has not been submitted for any degree other than the PhD in Physics of Imperial College London.

The majority of the results presented in this dissertation have already been published in scientific articles I have co-authored. Sections using statements and figures from these manuscripts include a short preamble note which acknowledges the origins of the contents. Details on permissions and contributions to published works I have co-authored are provided in the appendices.

Finally, I herewith certify that all material in this dissertation, such as figures and statements, which is not my own work has been properly referenced and acknowledged. Details on origins, copyrights and permissions for figures that have been extracted from others' works are reported in the appendices.

Alberto Ciacci, March 2022

Copyright Declaration

The copyright of this thesis rests with the author. Unless otherwise indicated, its contents are licensed under a Creative Commons Attribution-Non Commercial 4.0 International Licence (CC BY-NC).

Under this licence, you may copy and redistribute the material in any medium or format. You may also create and distribute modified versions of the work. This is on the condition that: you credit the author and do not use it, or any derivative works, for a commercial purpose.

When reusing or sharing this work, ensure you make the licence terms clear to others by naming the licence and linking to the licence text. Where a work has been adapted, you should indicate that the work has been changed and describe those changes.

Please seek permission from the copyright holder for uses of this work that are not included in this licence or permitted under UK Copyright Law.

This thesis includes external images that are distributed under different Creative Commons licences. Some of these images have been modified to different extents. The re-distribution of these modified images is governed by the licenses of the associated original images, i.e., some

of them must be re-distributed while others cannot be re-distributed. The appendix contains a dedicated section in which you can find details about sources, licenses and amendments for each external image.

This thesis also includes materials, such as text and images, from published articles. To reuse these materials, you must obtain the required permissions from their publishers and authors. The appendix contains a dedicated section in which you can find details about permissions and attributions for each published article included in this thesis.

Publications

The contents of this dissertation are based on the following articles I have co-authored during my doctoral studies:

1. Alberto Ciacci, Max Falkenberg, Kishan A Manani, Tim S Evans, Nicholas S Peters, Kim Christensen
Understanding the transition from paroxysmal to persistent atrial fibrillation
Physical Review Research, **2**, 023311 (2020).
2. Max Falkenberg, Alberto Ciacci, Gwyneth Matthews, Jack Way, Balvinder Handa, Li Xinyang, Nicholas S Peters, Fu Siong Ng, Kim Christensen.
Increased gap-junction coupling terminates myocardial fibrillation by optimizing phase singularity meander-an insilico study
In submission (2022).
3. Max Falkenberg, Andrew J Ford, Anthony C Li, Robert Lawrence, Alberto Ciacci, Nicholas S Peters, Kim Christensen
Unified mechanism of local drivers in a percolation model of atrial fibrillation
Physical Review E, **100**, 062406 (2019).
4. Alberto Ciacci, Takumi Sueshige, Hideki Takayasu, Kim Christensen, Misako Takayasu
The microscopic relationships between triangular arbitrage and cross-currency correlations in a simple agent based model of foreign exchange markets
PLoS one, **15**, 6 (2020).

5. Luca Mertens, Alberto Ciacci, Fabrizio Lillo, Giulia Livieri
Liquidity fluctuations and the latent dynamics of price impact
Quantitative Finance, 1-21 (2021).

In addition to the works mentioned in the above list, I have co-authored additional articles which will not be presented in this dissertation:

6. Max Falkenberg, David Hickey, Louie Terrill, Alberto Ciacci, Nicholas S Peters, Kim Christensen
Identifying Potential Re-Entrant Circuit Locations From Atrial Fibre Maps
Computing in Cardiology (CinC), 1-4 (2019).
7. Max Falkenberg, James Coleman, Sam Dobson, David Hickey, Louie Terrill, Alberto Ciacci, Belvin Thomas, Nicholas S Peters, Arunashis Sau, Fu Siong Ng, Jichao Zhao, Kim Christensen
Identifying locations susceptible to micro-anatomical reentry using a spatial network representation of atrial fibre maps
bioRxiv (2021).

Abstract

A physical system is said to be *complex* if it exhibits unpredictable structures, patterns or regularities emerging from microstructural dynamics involving a large number of components. The study of complex systems, known as *complexity science*, is maturing into an independent and multidisciplinary area of research seeking to understand microscopic interactions and macroscopic emergence across a broad spectrum systems, such as the human brain and the economy, by combining specific modelling techniques, data analytics, statistics and computer simulations. In this dissertation we examine two different complex systems, the human heart and financial markets, and present various research projects addressing specific problems in these areas.

Cardiac fibrillation is a diffuse pathology in which the periodic planar electrical conduction across the cardiac tissue is disrupted and replaced by fast and disorganised electrical waves. In spite of a century-long history of research, numerous debates and disputes on the mechanisms of cardiac fibrillation are still unresolved while the outcomes of clinical treatments remain far from satisfactory. In this dissertation we use cellular automata and mean-field models to qualitatively replicate the onset and maintenance of cardiac fibrillation from the interactions among neighboring cells and the underlying topology of the cardiac tissue. We use these models to study the transition from paroxysmal to persistent atrial fibrillation, the mechanisms through which the gap-junction enhancer drug Rotigaptide terminates cardiac fibrillation and how focal and circuital drivers of fibrillation may co-exist as projections of transmural electrical activities.

Financial markets are hubs in which heterogeneous participants, such as humans and algorithms, adopt different strategic behaviors to exchange financial assets. In recent decades the widespread adoption of algorithmic trading, the electronification of financial transactions, the increased competition among trading venues and the use of sophisticated financial instruments drove the transformation of financial markets into a global and interconnected complex system. In this thesis we introduce agent-based and state-space models to describe specific microstructural dynamics in the stock and foreign exchange markets. We use these models to replicate the emergence of cross-currency correlations from the interactions between heterogeneous participants in the currency market and to disentangle the relationships between price fluctuations, market liquidity and demand/supply imbalances in the stock market.

Acknowledgements

There aren't enough good words to express my gratitude to **Prof. Kim Christensen** for his academic and human guidance throughout this journey.

I thank my colleague **Dr. Max Falkenberg** for our collaborations during these years. His passion, dedication and deep understanding of our research have been truly inspiring.

I extend my gratitude to the Complexity and Networks research group at Imperial College London, and in particular to **Prof. Henrik Jeldtoft Jensen** and **Dr. Tim Evans**. I thank this interdisciplinary team for introducing me to a broad range of interesting topics, connecting me with motivated researchers and supporting my international academic collaborations.

I thank **my family** for their fantastic support during the high and lows of this experience.

I thank my friend **Dr. Julius Bonart** for introducing me to academic research.

I am grateful to **Prof. Misako Takayasu**, **Prof. Hideki Takayasu** and **Dr. Takumi Sueshige** for our research collaboration at Tokyo Institute of Technology.

I thank **Prof. Fabrizio Lillo**, **Dr. Luca Philippe Mertens** and **Dr. Giulia Livieri** for our research collaboration at Scuola Normale Superiore.

Contents

Declaration	1
Abstract	4
Acknowledgements	5
1 Introduction	22
1.1 Complex systems and complexity science	22
1.2 Academic research presented in this thesis	23
1.3 Organization of this thesis	28
2 Background theory	31
2.1 Physical systems and the philosophy of scientific modelling	31
2.1.1 Model development	31
2.1.2 Simulation	33
2.1.3 Calibration	35
2.1.4 Validation	36
2.2 Complex systems	38
2.2.1 Universal features of complex systems	39

2.2.2	Complexity	41
2.2.3	Emergence	42
2.2.4	Self-organization	45
2.2.5	Modelling complex systems	47
2.3	Summary of the chapter	61
3	Cardiac fibrillation as an emergent phenomenon	64
3.1	The human heart	66
3.1.1	Structural and functional aspects	66
3.1.2	Microstructural aspects	68
3.2	Cardiac conduction system and electrophysiology of cardiomyocytes	70
3.2.1	Anatomy	70
3.2.2	Action potential	72
3.2.3	Assessing the electrical activity of the heart	74
3.3	Atrial fibrillation	76
3.3.1	Introduction	76
3.3.2	Arrhythmogenesis	78
3.3.3	Mechanisms of atrial fibrillation	82
3.3.4	Treatments of atrial fibrillation	85
3.3.5	Cardiac remodelling and atrial fibrillation	87
3.4	Modelling atrial fibrillation	89
3.4.1	Overview of common approaches to the modelling of atrial fibrillation	89
3.4.2	The Christensen-Manani-Peters model	91

3.5	The transition from paroxysmal to persistent atrial fibrillation	104
3.5.1	Context	104
3.5.2	Introduction	105
3.5.3	A mean-field representation of the Christensen-Manani-Peters model . .	107
3.5.4	The role of complex critical structures	116
3.5.5	Discussion and outlook	124
3.6	Increased gap-junction coupling terminates myocardial fibrillation by optimising phase singularity meander - an insilico study	128
3.6.1	Context	129
3.6.2	Introduction	129
3.6.3	Model	131
3.6.4	Results	135
3.6.5	Discussion	143
3.6.6	Limitations	147
3.6.7	Conclusion	149
3.7	Unified mechanism of local drivers in a percolation model of atrial fibrillation .	150
3.7.1	Context	150
3.7.2	Introduction	151
3.7.3	Model definition	152
3.7.4	The spatial distribution of re-entrant circuits	152
3.7.5	The relationship between ablation success rate and fibre coupling	157
3.7.6	Discussion and outlook	160
3.8	Summary of the chapter	162

4	Emergent correlations and price formation in financial markets	165
4.1	Introduction	165
4.2	Scopes and organization of financial markets	168
4.2.1	Introduction	168
4.2.2	Quote driven markets	170
4.2.3	Order driven markets	171
4.3	Introduction to Market Microstructure	175
4.3.1	Overview	175
4.3.2	Market liquidity	176
4.3.3	Price impact of trades	177
4.4	Models of financial markets	180
4.4.1	Introduction	180
4.4.2	The Kyle Model	181
4.4.3	The Dealer Model	183
4.4.4	The Cont-Kukanov-Stoikov Model	184
4.5	The emergence of cross-currency correlations in a simple agent based model of foreign exchange markets	188
4.5.1	Context	188
4.5.2	The foreign exchange market	189
4.5.3	Introduction	192
4.5.4	The Arbitrager Model	192
4.5.5	Cross-correlation diagrams in the Arbitrager Model	197

4.5.6	The microscopic origins of cross-currency correlations in the Arbitrager Model	199
4.5.7	Summary and outlook	207
4.6	Liquidity Fluctuations and the Latent Dynamics of Price Impact	210
4.6.1	Context	211
4.6.2	Introduction	211
4.6.3	Literature review	213
4.6.4	The Cont-Kukanov-Stoikov Model on different time scales	215
4.6.5	A dynamical market impact model	219
4.6.6	Empirical results	221
4.6.7	Concluding remarks	231
4.7	Summary of the chapter	234
5	Conclusion	236
5.1	Summary and achievements of this thesis	236
5.2	Future work	239
	Bibliography	240
	Appendices	284
A	External images: attributions and permissions	285
B	Published work: contributions and permissions	292
B.1	Understanding the transition from paroxysmal to persistent atrial fibrillation .	292

B.2	Increased gap-junction coupling terminates myocardial fibrillation by optimising phase singularity meander-an insilico study	293
B.3	Unified mechanism of local drivers in a percolation model of atrial fibrillation	294
B.4	The microscopic relationships between triangular arbitrage and cross-currency correlations in a simple agent based model of foreign exchange markets	295
B.5	Liquidity Fluctuations and the Latent Dynamics of Price Impact	296
C	Data description and access	299
C.1	Introduction	299
C.1.1	The Electronic Broking Services market dataset	301
C.1.2	LOBSTER dataset	303
D	Supplementary materials for sections 3.4.2 and 3.5	307
D.1	Activation maps for critical structures appearing in Fig. 3.14	308
D.2	Activation maps for critical structures appearing in Figs. 3.23-3.24	318
D.3	Activation patterns in the CMP Model	320
D.4	Correspondence between the number of simple re-entrant circuits and overall coupling	322
E	Supplementary materials for section 3.6 ***	325
E.1	Parameters calibration	325
F	Supplementary materials for section 3.7	329
F.1	Details on model definition and calibration of the model	329
F.1.1	Heart muscle structure	329
F.1.2	Heart muscle physiology	330

F.1.3	Dimensionless parameters of the model	330
F.2	The spatial distribution of re-entrant circuits	331
F.3	Details on ablation experiments	334
G	Supplementary materials for section 4.5	337
G.1	Initialization and dynamic control of the Arbitrager Model	337
G.1.1	Introduction	337
G.1.2	Initial state of the LOB	338
G.1.3	Relationships between simulation time and real time	340
G.1.4	Parameters involved in the calculation of the current price trend	342
G.1.5	Trend-following strength parameter	342
G.2	An extended version of the Arbitrager Model	343
G.2.1	Motivations	343
G.2.2	The arbitrager	344
G.2.3	Market makers	345
G.2.4	An additional price-entangling mechanism	346
G.2.5	Cross-correlation diagrams and discussion	348
H	Supplementary materials for section 4.6	350
H.1	Data processing	351
H.2	Technical details on the estimation procedure	352
H.3	Econometric and modeling issues	353
H.3.1	Exogeneity of the OFI	353
H.3.2	Is Kalman the right filter?	354

H.3.3	Statistical issues in the two-step estimation procedure	355
H.4	Diagnostic testing for Kalman filter	356
H.5	The performance of the model for small tick stocks	356

List of Tables

3.1	Time in AF in the cMF model for different combinations of p/p_0 and N	116
4.1	Parameters governing the dynamics of the Arbitrager Model.	197
4.2	Transition rates between two configurations.	205
4.3	Summary of estimates of the model in Eq. (4.24).	223
4.4	Estimates of the parameter ρ after the first stage.	224
4.5	Performances comparison.	229
4.6	Estimates of the parameters c and λ in Eq. (4.30).	232
4.7	Estimates of the parameters α and γ in Eq. (4.31).	233
C.1	EBS dataset structure.	301
C.2	Tick sizes adopted in the EBS market.	302
C.3	Descriptive statistics for the investigated NASDAQ prices time series	304
C.4	Sample statistics for the investigated NASDAQ limit order books	305
G.1	Initial center of mass and market making spread in each market.	338
G.2	Approximate equivalences between real and model time.	342
H.1	Estimates of the VAR parameters.	355
H.2	Parameter estimates obtained from simulated data.	359

H.3	Descriptive statistics for the investigated small tick stocks.	360
H.4	Sample statistics for the orderbooks of the covered small tick stocks.	360
H.5	Estimates of the VAR parameters.	361
H.6	Estimates of the regression in Eq. (H.4).	362

List of Figures

2.1	Modelling a physical system.	33
2.2	Digital representation of a model and subsequent simulations.	34
2.3	Different systems and associated models.	40
2.4	Information required to describe the system as a function of the observation scale.	43
2.5	Flocking birds.	46
2.6	Common neighborhoods in CAMs.	49
2.7	Boundary conditions in CAMs.	51
2.8	ABMs basics.	53
2.9	Schematics of simple time-homogeneous Markov Chains.	57
2.10	Examples of different networks.	61
3.1	Schematics of the heart wall.	67
3.2	Anatomy and blood flow of the human heart.	69
3.3	The anatomy of a myocyte	70
3.4	Cardiac conduction system.	71
3.5	Cardiac action potential cycle.	73
3.6	ECG trace.	75

3.7	Schematics of after-depolarizations.	79
3.8	Schematics of the formation of an anatomical re-entry.	81
3.9	Classic theories of the mechanisms of AF.	83
3.10	Schematics of a rotor.	84
3.11	Healthy vs. fibrotic tissue.	88
3.12	Basic dynamics of the CMP model.	93
3.13	The formation of a re-entrant circuit in the CMP model.	95
3.14	Critical structures in the CMP model.	97
3.15	The classification of AF in the CMP model.	100
3.16	Relationship between the amount of coupling and the probability of inducing AF.	101
3.17	The spectrum of AF patterns in the CMP model.	102
3.18	The CMP model is condensed into a mean-field (MF) model of AF.	108
3.19	Relationship between the amount of coupling and the time in AF.	111
3.20	Relationship between the amount of coupling and the time in AF	113
3.21	Relationship between the amount of coupling and the time in AF.	115
3.22	Comparison of the main AF statistics in the cCMP, CMP and MF models.	118
3.23	The formation of a complex re-entrant circuit with asymmetric activation and deactivation rates.	121
3.24	The coupling of multiple re-entrant circuits such that the termination of one circuit immediately activates a secondary circuit.	122
3.25	Protracted AF episode.	124
3.26	The effect of varying the fraction of nodes that are susceptible to conduction block on the probability of inducing AF.	125

3.27	A schematic detailing the key rules of the discrete fibrillation model.	132
3.28	Node states sequence in the hexagonal lattice.	133
3.29	The probability of inducing fibrillation in the insilico model.	135
3.30	Spectrum of organisation in myocardial fibrillation with corresponding phase processed examples from the insilico model.	136
3.31	Phase processing statistics from the in the insilico model.	137
3.32	The probability of fibrillation being sustained for the full duration of the extended simulation presented alongside relevant statistics.	139
3.33	Survival curves for the probability of sustaining fibrillation over time.	141
3.34	The probability of sustaining fibrillation as a function of different factors.	143
3.35	Extending the CMP lattice to three dimensions.	153
3.36	Three-dimensional visualization of an AF driver located in the bulk of the atrial tissue.	154
3.37	Different projections of the same re-entrant circuit.	155
3.38	Emergence of AF at different fibrosis burdens.	156
3.39	Clinical vs. insilico activation maps from both the endo and epi perspectives.	158
3.40	Ablation success rates as a function of fibre coupling and depth.	159
4.1	Different approaches to the organization of financial interactions.	170
4.2	Schematics of a quote-driven market ecology.	172
4.3	Schematic of a LOB and related terminology.	173
4.4	Simple LOB dynamics.	174
4.5	Dealer Model basics.	184
4.6	Interactions in the Dealer Model.	185

4.7	Two ways of obtaining one unit of EUR.	190
4.8	Profitable misprices and associated triangular arbitrage strategies.	191
4.9	Schematic of the Arbitrager Model ecology.	193
4.10	Interactions in the Arbitrager Model.	195
4.11	Exploiting a triangular arbitrage opportunity in the Arbitrager Model.	196
4.12	Trading data vs. model based cross-correlation functions.	199
4.13	Correspondence between price trend signs and market states.	200
4.14	Statistical relationships between different FX markets.	202
4.15	Expected lifetime and appearance probability of the eight ecology configurations.	203
4.16	Complementary cumulative distribution function (CCDF) of the time required for the first triangular arbitrage opportunity to emerge.	204
4.17	Price trends and changes in market states.	206
4.18	Fraction of triangular arbitrage opportunities of the first and second type in each ecology configuration.	207
4.19	The sequence of transitions between configurations exhibits a clustered behavior.	208
4.20	The Cont-Kukanov-Stoikov on different time scales.	216
4.21	Statistical properties of the price impact coefficient estimates.	218
4.22	Price impact estimates average patterns through the trading day.	225
4.23	Price impact estimates average patterns on FOMC meeting days.	226
4.24	Out-of-sample Kalman filtering of market impact process.	227
4.25	Out-of-sample Kalman filtering of market impact.	228
4.26	Box-plot of the Pearson correlation between the compared models.	230
C.1	Mid price patterns	303

D.1	Activation and deactivation of the critical structure presented in Fig. 3.14 (a).	308
D.2	Activation and deactivation of the critical structure presented in Fig. 3.14 (b).	309
D.3	Successful activation of the critical structure presented in Fig. 3.14 (c).	310
D.4	Failed activation of the critical structure presented in Fig. 3.14 (c).	311
D.5	Successful activation of the critical structure presented in Fig. 3.14 (d).	312
D.6	Failed activation of the critical structure presented in Fig. 3.14 (d).	313
D.7	Successful activation of the critical structure presented in Fig. 3.14 (e).	314
D.8	Failed activation of the critical structure presented in Fig. 3.14 (e).	315
D.9	Successful activation of the critical structure presented in Fig. 3.14.	316
D.10	Failed activation of the critical structure presented in Fig. 3.14 (f).	317
D.11	Activation and deactivation of the complex critical structure presented in Fig. 3.23.	318
D.12	Sequence of activations of the coupled re-entrant circuits presented in Fig. 3.24.	319
D.13	Activation patterns in SR, paroxysmal AF and persistent AF.	320
D.14	An example of persistent AF in the CMP model.	321
D.15	Critical structures and time in AF.	322
D.16	The average number of tracked simple critical structures N as a function of the overall coupling value ν_{\perp} in the cCMP model.	323
E.1	APD restitution curves in in the model.	328
F.1	The distribution of re-entrant circuit depth z from the endocardium in the homogeneous model.	331
F.2	The distribution of re-entrant circuit depth z from the endocardium in the inhomogeneous model.	332
F.3	Risk of AF as a function of the topological features of the system.	333

F.4	Simulated ablation in a tissue with multiple drivers.	336
G.1	Inverse function sampling in the context of the Arbitrager Model.	339
G.2	Waiting times statistics in real trading data.	340
G.3	Waiting times statistics in the Arbitrager Model.	341
G.4	Trading data vs. model based cross-correlations functions.	344
G.5	Foreseeing a triangular arbitrage opportunity in the Arbitrager Model.	347
G.6	Trading data vs. model based cross-correlation functions.	348
H.1	Simulated and real intraday price impact pattern.	357
H.2	Some statistical properties of the standardized one-step ahead forecast errors. . .	358
H.3	Fitting the Cont-Kukanov-Stoikov model to a small tick stock.	361

Chapter 1

Introduction

1.1 Complex systems and complexity science

In physics, a *system* is defined as a subset of the universe [1]. Scientists are typically interested in describing how the state of a system changes following internal or external events [1]. Some of these systems host a large number of interacting components and their structures, patterns and dynamics cannot be satisfactorily described by assessing these components in isolation [2, 3]. For instance, a rapid collapse of stock prices cannot be understood by examining how a single market participant acted in the proximity of this event. Similarly, the dynamics of a pedestrians flow cannot be explained by assessing the behaviour of single individuals without considering how they mutually influence others' decisions. Scholars often describe these systems as *complex* and a dedicated discipline, known as *complexity science*, has gradually emerged in the last decades with the aim of developing theoretical and computational tools to understand how macroscopic, i.e., system-wide, structures emerge from microscopic interactions among the many parts of these systems.

A characteristic feature of complexity science is its interdisciplinary nature. In this context, similar theories and methodologies are often used to examine very different systems. For instance, network models have been employed to study competition between firms [4, 5, 6], the foreign exchange market [7, 8], scientific co-authorships [9, 10, 11] and urban traffic [12, 13] while mean-field models have been successfully used in astrophysics [14], disease spreading [15, 16], traffic flows [17, 18], epilepsy [19] and atrial fibrillation [20], among many others. In this setting, it is not surprising that complexity science scholars are interested in identifying universal traits

and features of complex systems rather than confining their research to a specific field of study [3]. As a result, a scientist devoted to complexity science is very likely to work on a broad spectrum of systems, e.g., earthquakes, brains, financial markets, and to collaborate with many researchers coming from different scientific backgrounds. The idea that physicists, mathematicians, economists, medics and many other figures can interact with each other, being inspired from and contribute to research areas beyond their original expertise is extremely fascinating if one considers the fact that modern scientific research is extremely specialized and fragmented.

1.2 Academic research presented in this thesis

The initial scope of my doctoral studies was to exclusively focus on the microstructural aspects of modern financial markets. At that time, I was eager to examine these physical systems from perspectives that stray from the well known mathematical theories of finance. My main criticism to these theories was the fact that they tend to focus on the mathematical modelling of asset price dynamics but completely overlook the microstructural interactions and constraints that lead to their formation. This motivated me to put financial interactions “under the microscope” [21] by turning my focus on an electronic record, known as *limit order book*, in which buy and sell orders from market participants are organized and prioritized according to a specific set of rules. Limit order book data offers a complete and timestamped record of buy and sell orders placement and cancellation as well as transactions that took place on a given market. From these granular records one can reconstruct, analyse and model the microstructural dynamics of a market and eventually gather important insights on how these events affect or even drive the behavior of the whole system. An increasing accessibility to “atomic” trading data has attracted the physics community into the analysis of financial markets, paving the way for unorthodox and intriguing perspectives and techniques that stray from the conventional approaches from the economics and finance communities. For instance, the full rationality assumption has been challenged by the view that the price formation process taking place in limit order books might be also driven by bounded rationality or even purely mechanistic dynamics. The Santa Fe Model [22, 23, 24] is a classic example of this new paradigm. Introduced in early 2000s by a research group directed by Doyne Farmer at the Santa Fe Institute, the model idealizes a limit order book in which buy and sell orders enter and leave the system according to a Poisson distribution, thus replacing rational agents with a *zero-intelligence* setup [21]. Unsurprisingly, these unrealistic simplifications do not allow the model to capture many stylized facts of real

limit order books. However, the model successfully replicates the distribution of the bid-ask spreads of several stocks covered in a recent analysis of Bouchaud *et al.* [21], thus reinforcing the hypothesis that some macroscopic properties of financial markets might have purely mechanistic origins.

In the early days of my pre-doctoral postgraduate program I started to consider the possibility of expanding my interests towards the microscopic dynamics of other systems. This vision was rather motivated by my profound conviction that a PhD program is one of the best opportunity to unleash personal curiosity and embracing new challenges, therefore, concentrating my effort on a single physical system was not clearly the best approach to make the best of this once in a lifetime opportunity. This prompted me to attend the class *Theory of Complex Systems* taught by Prof. Henrik Jeldtoft Jensen at Imperial College London in order to understand how scientists working in this area are able to explore a variety of physical systems within a single research framework. These lectures not only delivered a masterful introduction to this subject but also provided fascinating examples of how certain mathematical and computational tools can be used to examine multiple and apparently unrelated systems. This experience inevitably reinforced the idea of transitioning from a market microstructure centered research to a more general setup in which my work on financial markets can co-exists with the exploration of open problems in other physical systems. The catalyst came when Dr. Julius Bonart, my pre-doctoral supervisor, decided to take a different path outside the academic world. This inevitably ended our academic collaboration but, at the same time, it gave me a chance to turn my research ambitions into reality as I decided to join the *Centre for Complexity Science* at Imperial College London to commence my doctoral studies under the guidance of Prof. Kim Christensen. In this environment, the constant presence of a brilliant supervisor and talented colleagues set the ground for years of stimulating and productive academic collaborations.

One of the main focuses of the research group led by Prof. Kim Christensen is understanding how cardiac fibrillation, i.e., a diffuse disease in which the regular electrical conduction in the heart is temporarily or permanently disrupted, emerges from cell-to-cell and cell-to-structure. To do so, the group model and analyse these microscopic interactions through complexity science approaches, such as cellular automata, network theory and agent-based models. The first milestone of this long-term project was the Christensen-Manani-Peters model [25]. In this framework, the atrial tissue is conceived as a simple bi-dimensional lattice in which nodes represent cardiac cells connecting longitudinally and eventually transversally while electrical

charges are periodically released from the pacemaking region and propagate across the lattice. The model shows that accumulation of fibrosis, which is modelled as an increasingly anisotropic distribution of cell-to-cell connections, prompts the emergence of regions, known as *critical structures*, in which a disruption of a planar electrical wave, i.e., one or more nodes fail to excite thus blocking the conduction, might allow the stimulus proceeding in the adjacent fiber to leak back, initiating a circuital activity that drives fibrillation [25]. My research at Imperial College London conceived the original Christensen-Manani-Peters model as a baseline framework upon which I co-developed three novel models of cardiac fibrillation. First, I have studied how paroxysmal atrial fibrillation, i.e., short-lived episodes, becomes persistent, i.e., long-lasting episodes, in the Christensen-Manani-Peters model [20]. To do so, the original model is dissected by removing its spatial components, i.e., the regions between critical structures, and those critical structures whose activation/deactivation require multiple conduction blocks [20]. This led to a null model, i.e., *mean-field*, in which critical structures requiring single conduction blocks are condensed into particles activating and deactivating with fixed probability and an intermediate model in which the spatial components are re-introduced, i.e., a lattice based model like the original, while the placement of dysfunctional nodes is controlled to avoid the formation of critical structures that require multiple failures to activate and deactivate [20]. Both these two simplified models underestimate the average time that the system spends in fibrillation at a given level of fibrosis - a result that can be explained by the fact that the original model is the only one allowing for the presence of *complex critical structures* in which the probability of activation exceeds the probability of deactivation due to the topological features of the surrounding region [20]. Once activated, these structures host long lasting spatially stable rotational activities that are responsible for the transition from paroxysmal to persistent fibrillation [20].

Next, I introduce another model of myocardial fibrillation in which the tissue is represented by a bi-dimensional lattice where nodes may connect longitudinally and diagonally [26]. The scope of this model is to study how the gap-junction enhancer drug Rotigaptide terminates myocardial fibrillation, thus expanding on a recent clinical study [27] which highlighted how high dosages of this drug led to a transition from ventricular fibrillation to ventricular tachycardia which ultimately resulted in self-termination in a subset of experimental rat hearts. In this model, the continuous spectrum of fibrillation, i.e., the transition between multiple disorganized circuital drivers to organized drivers revolving around phase singularities, can be described by

the co-action of the accumulation of fibrosis and the degree of responsiveness of cardiac cells to incoming electrical stimuli [26]. A comprehensive analysis of the behavior of the model across this phase space reveals that in the region in which the probability of termination is maximised the fraction of excitable tissue, i.e., responsive to electrical stimuli, per phase singularity and the meander of the most stable phase singularities are also maximised [26]. As this region is characterized by increased connectivity between cells, i.e., the effect of Rotigaptide infusions, these in-silico evidences suggest that Rotigaptide terminates myocardial fibrillation by averting the spatial stabilization of phase singularities, thus causing these drivers to drift across the tissue and eventually collide with other drivers or tissue boundaries [26].

Finally, I present a tri-dimensional extension of the Christensen-Manani-Peters model in which the atrial bulk is modelled by a more realistic cubic topology where neighboring nodes may connect longitudinally and transversally, i.e., within the same bi-dimensional sheet, but also to nodes belonging to adjacent sheets [28]. The scope of this model is to dig further on recent clinical reports supporting an unifying theory of atrial fibrillation drivers in which transmural circuitual activities may project as rotational activities on the endocardium, i.e., the inner layer of the atrial tissue, and as focal points on the epicardium, i.e., the outer layer of the atrial tissue [29, 30, 31, 32, 33, 28]. The model reproduces the relationships between the accumulation of fibrosis and the emergence of atrial fibrillation, suggesting that paroxysmal episodes are driven by rotational activities near the endocardium whereas persistent episodes are driven by activities that are distributed across the entire lattice [28]. Furthermore, these drivers project as rotational activities when the lattice is observed from the endocardium and as focal point when the lattice is observed from the epicardium, thus confirming the clinical evidences presented in [29]. Simulations of ablation procedure, i.e., the leading clinical treatment of atrial fibrillation in which the area suspected of driving fibrillation is “burned”, show that success rates are related to the fibrotic burden [28]. In highly fibrotic tissues even iterated lesions fail to terminate fibrillation as drivers tend to distribute across the bulk. However, success rates rapidly increase when fibrosis becomes less severe as drivers are more likely to be concentrated near the endocardial surface [28].

My research on the microscopic dynamics of financial markets has developed in parallel with my work on cardiac fibrillation models mainly through two long-lasting collaborations with researchers based at Tokyo Institute of Technology and Scuola Normale Superiore. In the former experience I have worked at the Prof. Misako Takayasu laboratory on agent-based

modelling of financial interactions in orderbook-based markets. The goal of this project was to model the dynamic interactions between multiple foreign exchange markets to understand the microscopic origins of the cross-currency correlations observed in real-trading data [34]. Building on the Dealer Model of Yamada *et al.* [35], a market is conceived as a simple system in which an arbitrary number of agents continuously show a bid and an ask price for the traded assets, thus acting as stylized market makers [34]. Market makers update their prices according to a stochastic differential equation in which the drift is the “market trend”, i.e., a weighted average of the most recent price changes, and trade anytime a bid price matches or exceeds an ask price [34]. The ecology consists of three independent markets populated by market makers and a special trader, known as the *arbitrager*, who trades opportunistically by submitting buy and sell orders across the three venues to exploit any misprice that guarantee risk free profit [34]. In this setting, the arbitrager actions are the only channel through which the otherwise independent dynamics of the three markets are temporarily “synchronized” [34]. Simulations of this ecology shows that the interplay between arbitrage and trend-following strategies, i.e., the arbitrager causes price changes affecting the trend signals used by market makers, creates pronounced cross-correlations between price changes in different markets which are reminiscent of those observed in real trading data [34]. The model provides insights on how these interactions affect the ecology at a more macroscopic dimension. Imagining each market as a particle which can take two states, i.e., +1 if price is up-trending and -1 if the price is down-trending, the state of the ecology can be represented as a triplet of market states [34]. The presence of the arbitrager breaks the equal probabilities of observing one of the eight possible triplets, making certain triplets more likely to emerge and survive than others [34]. As a result, the probability of observing two markets in the same and opposite states is not $1/2$ anymore, hence price trajectories become correlated [34].

My collaboration with the research group headed by Prof. Fabrizio Lillo at Scuola Normale Superiore revolved around two projects on the price formation process in securities markets. In this thesis I present a model which describes price fluctuations as the product of the order flow imbalance, which quantifies demand/supply imbalances as the signed sum of the volumes of every order book event within a given time window [36], and the price impact coefficient, which quantifies the direction and magnitude of price changes induced by forthcoming orderbook events and it is effectively a dimension of the broader notion of market liquidity [37]. In this setting, the price impact coefficient is written as the product of an intraday pattern, a daily

level and a stochastic autoregressive component and is estimated via Kalman filter on trading data of multiple securities traded on NASDAQ [37]. This leads to a novel high-frequency state-space model in which price impact is conditionally estimated “on the fly” and price fluctuations are driven by the product of the latest price impact coefficient and the order flow imbalance generated by recent orderbook events [37]. The model suggests that at high frequency time-scales price impact becomes auto-regressive and more dependent on recent orderbook dynamics while the linear relationships between order flow imbalance and price fluctuations established by Cont *et al.* [36] weakens as the discrete nature of price increments becomes more and more relevant [37]. Interestingly, this work examines a complex system through approaches and methods that are rather closer to statistics, econometrics and data analytics, straying from the complexity science perspective which underlies this dissertation. Nonetheless, such analysis was a necessary step to elucidate the relationships between price dynamics, market liquidity and supply/demand imbalances in securities markets, setting the ground for the subsequent project in this collaboration which aims to introduce a model of the evolution of the orderbook as a system in which the intensities of different order types depend on the current state of the system and the recent order flow imbalance. As the project is on its final stages, I have decided together with the other authors to exclude this work from this dissertation.

1.3 Organization of this thesis

This thesis portrays the academic journey I have described in the previous paragraphs. I talk about the human heart and financial markets; two complex systems that have been the core of my research in the last five years. In line with the typical complexity science approaches, I often focus on the microscopic dynamics of these systems and on how these can be modelled to understand how global patterns and structures unfold from events taking place at much smaller scales. The primary goal of this dissertation is to present multiple research questions I faced during my doctoral studies, their motivations and how I tried to answer them in a series of scientific manuscripts I have co-authored with several colleagues across different laboratories. This thesis is organized in three major chapters. In the first chapter I build the background theory that is required to understand and assess the contributions of my work. I introduce the notion of *physical system* and subsequently discuss some general aspects of the development, implementation and assessment of models in scientific research. Then, I focus on *complex systems* and elaborate on the key concepts of *complexity*, *emergence* and *self-organization* before

presenting a detailed survey of the main modelling techniques that have been used to mimic and analyze the behavior of complex systems.

After a comprehensive introduction to the complex systems framework, the thesis enters into its core sections by presenting multiple applications of this discipline to practical problems in cardiology and financial markets. The second chapter is devoted to *myocardial fibrillation*; a diffuse and potentially fatal disease of the cardiac conduction system in which the planar propagation of electrical waves is disrupted and replaced by chaotic and intense activities which might either appear in the atria, i.e., upper chambers of the heart, or in the ventricula, i.e., lower chambers of the heart. My goal is to model this pathology as an emergent phenomena stemming from changes in the cell-to-cell interactions and to use these models to gather insights on specific clinically-relevant issues. The chapter starts from a description of the macrostructure, microstructure and pumping function of the human heart. Next I introduce the cardiac conduction system and examine how electrical stimuli periodically arise and propagate across the cardiac muscle to drive its blood pumping activity. At this point, I focus on atrial fibrillation by examining its onset, the ongoing controversial debates on its maintenance mechanisms, its burden on our society, the available treatments and its remodelling effects on the structure of the atrial tissue. This comprehensive discussion is followed by a short survey of the main modelling paradigms that have been employed in atrial fibrillation research. Special attention is given to the recent model of Christensen *et al.* [25] which has served as “baseline” for the models of atrial fibrillation I have co-developed within my research group. The rest of the chapter is devoted to detailed presentations, analyses and discussions of these novel models and their contributions to different open problems in fibrillation research, namely, i) the transition from paroxysmal to persistent atrial fibrillation, ii) the mechanisms through which the gap-junction enhancer drug Rotigaptide terminates myocardial fibrillation and iii) the ongoing debate on the driving mechanisms of atrial fibrillation.

The third chapter examines financial markets. In the last three years my research has sought to understand how certain empirical phenomena and processes of financial markets, such as price correlations and price formation, are rooted into microscopic and mesoscopic dynamics of these systems. The chapter begins by introducing some basic theoretical notions of financial markets before expanding on different approaches that exchanges across the globe have adopted to organize financial trades. Next, I offer a general overview of *Market Microstructure*, an interdisciplinary field which studies agent-to-agent and agent-to-market structure interactions arising

during the trading process and how these microscopic dynamics are involved in the origination of macroscopic emergence. At this point I present three models of financial markets that have influenced my research: the Kyle's model [38], the Dealer model [35] and the Cont-Kukanov-Stoikov model [36]. The rest of the chapter is devoted to the outcomes of my research. First, I introduce an agent-based model of the foreign exchange market to understand the mechanistic origins of the widely documented cross-currency correlations between foreign exchange rate pairs. Second, I present and examine various insights on the relationships between price dynamics, market liquidity and supply/demand imbalances emerged from a novel model-based approach to the high frequency estimation of the price impact of orderbook events. The thesis concludes with a general summary of the research I have conducted during my doctoral studies and an outline of the future directions that can be pursued from the results of my work.

Chapter 2

Background theory

2.1 Physical systems and the philosophy of scientific modelling

In physics, a system is defined as a subset of the universe [1]. Examples of systems are the ocean and its inhabitants, a sealed glass containing a certain gas, a hive, a financial market, among many others. Typically, scientists are interested in understanding how changes in certain conditions affect the evolution of a system [1]. However, setting up, performing and examining experiments *in situ*, i.e., by direct observations of the system dynamics, is often an arduous, if not impossible approach. For instance, clinicians aiming to understand how structural features of the human atrial muscle influence the emergence of arrhythmias cannot perform experiments *in vivo* without putting the life of the living sample in extreme danger. To overcome these limitations, researchers conceive models that aim to mimic the behaviors of real systems.

2.1.1 Model development

Models are *task-driven* in the sense that they are developed to address at least one specific question about the system of interest [39]. This approach forces the modelers to concentrate only on those features of the system, e.g., entities, relationships, that provide a non-negligible contribution towards the accomplishment of the driving task. As a result, the model captures a “simplified” picture of the system which does not include various components and relationships that are perceived as irrelevant for the task [39]. This reduction is followed by another

simplification, known as *abstraction*, in which the modelers split the features of the system that are captured by the model into a core and a peripheral group [39]. The former, being deemed as crucial for meeting the goals of the model, are modelled such that they can mirror in full details their “real world” counterparts. The latter, being deemed as relevant but non crucial for meeting the goals of the model, are modelled in less detail, i.e., abstracted [39].

The sequence of decisions that the modellers take during the simplification and abstraction phases use as a reference the system of interest as it is “perceived” by the modellers [39]. No human has a complete, direct access to reality, therefore, the pillars on which models of a certain phenomenon build reflect how scientists are currently perceiving the phenomenon itself [39]. The inevitable consequence of perception-based modelling is that theories and associated models may drastically change when scientific and technological advancements offer scientists new tools to re-examine a system. For instance, the perception of the universe and its mechanisms in various ancient civilizations favored the diffusion of geocentric models in which stars, planets and natural satellites orbit the Earth [40]. Several centuries later, i.e., 1600 AC circa, the advent of the telescope allowed Galileo to document various phenomena of the Solar System, such as the rotation of the Sun and the presence of sunspots on its surface, the cluster of natural satellites orbiting Jupiter and the phases of Venus [41, 42, 43, 44, 45, 46]. At the same time, Kepler was introducing the three laws of planetary motion [47, 48] which were mathematically formalized by Newton few decades later. These advancements prompted a dramatic shift in the perception of the universe, paving the way for a generalized reception of the heliocentric model and the simultaneous abandonment of geocentric theories.

Finally, the development of a model is affected by a broad range of constraints [39]. For instance, the process of gathering information and data about a component of a system might be hampered by the presence of physical constraints, e.g., the lack of adequate tools to observe an elusive particle, or ethical constraints, e.g., the harming of sentient beings [39]. The knowledge of the modelers also poses further constraints to the development of the model. Assuming that no human has a perfect, complete knowledge of a certain topic, models can always be improved as their quality cannot exceed the knowledge that modelers have used to conceive it [39].

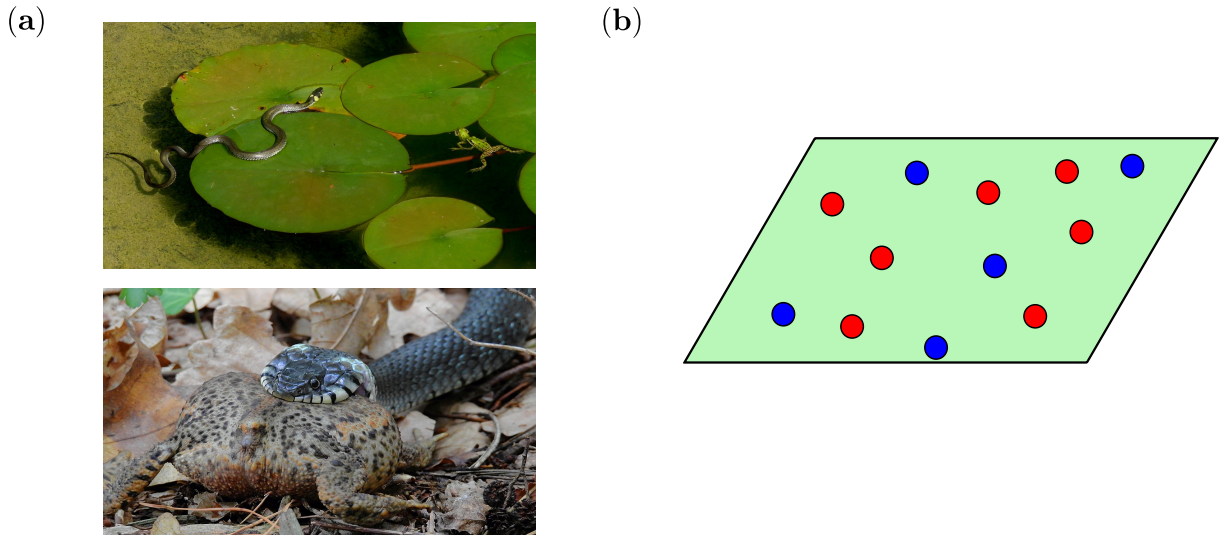


Figure 2.1: **Modelling a physical system.** (a) The system of interest is a forest populated by various animal species. (b) A scientist is interested in understanding how the antagonistic relationships between toads (preys) and snakes (predators) in the real world change with the dimensions of the hosting environment, i.e., the forest, and various features of the two competing species. To do so, she develops a model of a forest based on her perception of the real ecosystem portrayed in (a). As models are devised to fulfill a specific task, the scientist discards all the components of a real forest that she considers irrelevant for the scopes of the model. In this example, she neglects every animal specie other than toads and snakes and the interference of climate conditions. This simplification process leaves the scientist with very few components of the real system: toads, snakes and the forest ground. At this point, the remaining elements are significantly abstracted in order to obtain an extremely simple framework. The forest ground is idealized as an $L_x \times L_y$ parallelogram (green-colored area) without obstacles, e.g., trees. At time t_0 , the forest hosts $N_{\text{toads}}(t_0)$ toads (blue circles) and $N_{\text{snakes}}(t_0)$ snakes (red circles). The number of attacks occurring within a fixed time window obeys a Poisson distribution with rate λ . During an attack, a toad succumbs with probability p . New toads and snakes settle in the forest with rates ν_t and ν_s respectively. Finally, existing toads and snakes leave the forest with rates η_t and η_s respectively. See appendix A for details about attributions and permissions for the images appearing in panel (a).

2.1.2 Simulation

After developing a model, modellers translate it into a sequence of algorithms and equations. These elements are embedded into a program that can be executed by a computer. The scope

of this program is to simulate the dynamics of the model under a set of parameters specified by the user. In this process, the “digital” representation of the model evolves in discrete time, i.e., steps, see Fig. 2.2. A single simulation lasts until the number of time steps reaches a maximum set by the user or a predefined *exit condition* is met. Digital representations of models usually embed at least one source of randomness, therefore, two simulations performed under identical settings are very likely to generate different values of the same quantity of interest. To collect information on the range of values that this quantity can take, scientists instruct the machine to execute the same program several times. This allows to sample a large number of observations which can be finally summarized by common descriptive statistics, e.g., sample mean and variance.

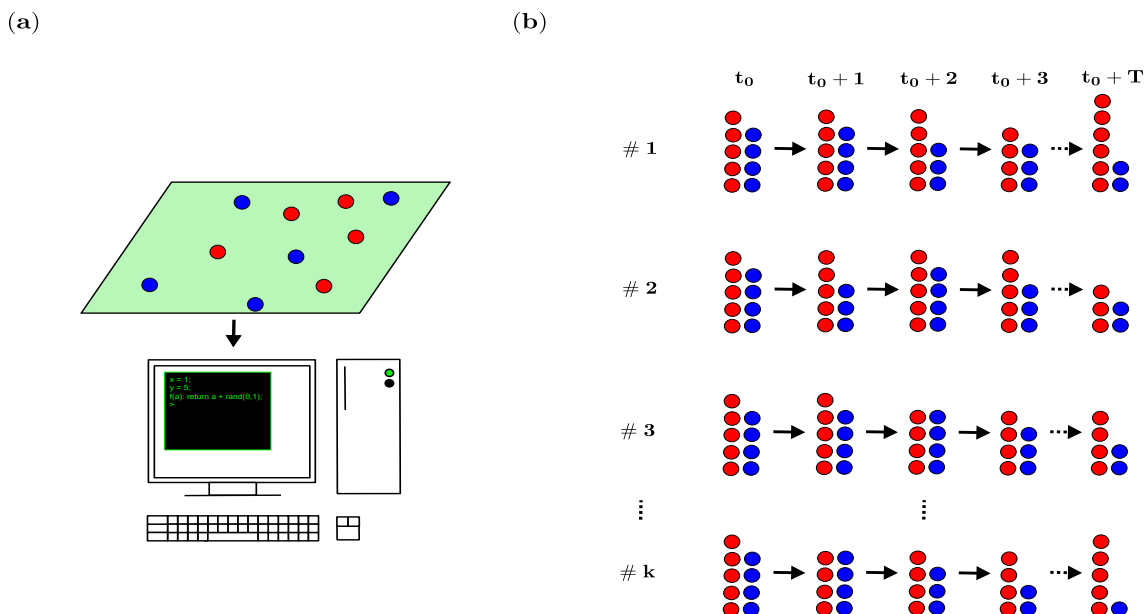


Figure 2.2: **Digital representation of a model and subsequent simulations.** (a) The simple model discussed in Fig. 2.1 is translated into a program (black window appearing on the screen) containing lines of executable code (green text). Modelers control a regular computer through which they manipulate the contents of the program or set the input parameters $(L_x, L_y, N_{\text{toads}}(t_0), N_{\text{snakes}}(t_0), \lambda, p, \nu_t, \nu_s, \eta_t, \eta_s)$. (b) The computer executes the same program k times. Simulations start at time t_0 from a common, predefined state of the model. Then, each experiment evolves independently for T consecutive time steps. Simple computers simulations are often run sequentially, i.e., one after the other. However, more powerful machines can drastically reduce the time required to complete the entire task by simultaneously executing multiple instances of the same program. Finally, modellers collect the quantities of interest from each simulation to form samples over which they compute summary statistics.

2.1.3 Calibration

Modellers must be able to identify the appropriate values of the input parameters before running simulations and collecting statistics [49]. To do so, they assess whether these values can be directly measured from the real system. For instance, the majority of the parameters governing the models of atrial fibrillation presented in [25, 28, 20] are fixed according to measurements collected by clinicians from real human atria. However, models belonging to other fields, e.g., watershed, rely on parameters that can hardly be measured from the system of interest [50]. In this scenario, modellers need to choose values of the input parameters such that the model adequately predicts behaviors and patterns revealed in data collected from the real system [50]. This procedure is known as *calibration* and the traditional approach to this task consists in examining how model predictions vary with different sets of input parameters until a satisfactory replication of real system data is reached [50]. However, this manual exercise becomes too onerous when the number of candidates parameter sets is large or the reference dataset includes many variables or very long time series [50]. To overcome these limitations, scientists have introduced automated calibration methods relying on an algorithmic driven search of the set of input parameters [50]. This paradigm relies on three phases. First, modellers identify a dataset containing meaningful empirical data on the phenomena of interest [50]. Second, modellers formalise an objective function quantifying the gap between model forecasts and the empirical observations contained in the target dataset, e.g., the sum of squared errors [50]. Third, the set of parameters that minimize the objective function is retrieved by implementing a mathematical optimization method [50]. Modern mathematical optimization builds on the groundbreaking works of Kantorovich [51], Dantzig [52, 53] and Von Neumann [54].

The first breed of optimization frameworks, such as the quasi-Newton method [55, 56, 57] and the Nelder-Mead simplex [58], usually rely on the sequential evaluation of different neighbouring points, i.e., the search moves from point to point according to a predefined rule, until a local minimum of the objective function is found.

The second breed of optimization frameworks date back to the early 80's when Kirkpatrick, Gelatt and Vecchi proposed the Simulated Annealing method [59] as a novel probabilistic approach to tackle the problem of minimizing an objective function f . In this context, the search of the optima proceeds as an inhomogeneous discrete-time Markov chain $\theta(t)$ “travelling” across different states, i.e., a state corresponds to a set of parameters for the objective function, belonging to a pre-determined state space \mathcal{P} [60]. Transition between neighboring states are

probabilistic and in the early phases of the search the Markov chain $\theta(t)$ might transit every now and then into states in which the objective function f increases with respect to the previous state [60]. These “counter-intuitive” transitions might be crucial for the Simulated Annealing to slip away from local minima [60]. Simulated Annealing converges in probability, i.e., $\lim_{t \rightarrow \infty} \mathbb{P}[\theta(t) \in p^*] = 1$, where $p^* \subset \mathcal{P}$ are the global minima of f , if certain conditions are satisfied [61, 60]. This result, overcoming one of the main pitfall of elder optimization techniques, became the quintessential feature of Simulated Annealing [62]. Simulated Annealing has inspired more recent methods, such as Ant Colony Optimization [63, 64, 65], Particle Swarn Optimization [66, 67, 68] and Tabu Search [69, 70, 71].

2.1.4 Validation

Depending on their goals and structures, models can provide predictions and theoretical insights on the system of interest. Considering that these outputs are even used to take important decisions in several spheres of our daily life, see [72] for examples, it is paramount to *validate* the model by assessing i) the accuracy of its quantitative forecasts and ii) its ability to capture mechanisms and behaviors of the specific aspects of the system it aims to describe. Surprisingly, there is no general consensus on an universal definition of *validity* and *validation* in the system modelling context [73, 74]. Recently, the United States Modelling and Simulation Coordination Office (MSCO) defined validation in the system modelling context as:

“the process of determining the degree to which a model and its associated data are an accurate representation of the real world from the perspective of the intended uses of the model” (MSCO 2010, from [74].)

In the MSCO framework, the question “*how well the model replicates the system of interest?*” must be addressed by taking into the account the objectives, i.e., “*the intended uses*”, of the model. This implies that a model conceived to describe a specific aspect x of a given system should not be validated outside its scope, e.g., by examining whether it can describe another aspect y of the same system.

Barlas [73] suggests that in the validation phase models should be classified in two groups:

1. Black-box models: data driven frameworks in which the goal is to produce quantitative features, e.g., statistics, forecasts, that are in strong agreement with quantities collected from the system of interest [73].
2. White-box models: theory driven frameworks in which the goal is not only the reproduction of quantitative features, but also the description of the mechanisms behind certain facets of the system of interest [73].

The former class of models reduces the validation phase to a mere statistical exercise [73]. For instance, a predictive model can be validated by measuring its accuracy in forecasting a label, e.g., 1 or 0, of previously unseen samples. In this case, the validation never probe whether the model effectively captures mechanisms, relationships and structures underlying the modelled system [73]. This pitfall is at the center of an important debate in the field of machine learning [72]. In the last decades machine learning applications have been breaking through a broad range of fields [75]. This rise has been fuelled by the increasing accessibility of large, granular datasets and powerful computing machines [75]. Most of the machine learning techniques are validated in a black-box fashion, raising concerns on the interpretability of their outcomes [76, 77].

“the interpretability of a model is the degree to which an observer can understand the cause of a decision.” (Biran and Cotton 2017, from [76, 78].)

Rudin [72] highlights the fact that the poor interpretability and accountability of many machine learning models have not hindered their increasing applications in pivotal decisions. Ignoring these limitations can lead to harsh repercussions for our society [72]. For instance, there are documented cases in which machine learning based decisions led to an erroneous denial of a parole right [79], wrong assessments of the quality of breathable air [80] and inefficient uses of costly resources in a broad range of industries [81]. Rudin argues that the solution to this issue does not lie in devising better methods to “explain” a black-box model, but in devising novel models that are intrinsically interpretable [72].

White-box models, introducing a theory on specific aspects of a given system, push the validation phase far beyond the mere statistical assessment of the discrepancies between real system data and model generated predictions [73]. For instance, a white-box model can be used to i)

examine how the modelled system reacts to changes and perturbations, ii) explain the internal origins of the dynamics of the system and iii) support decisions affecting the behavior of the system [73]. This implies that the inner structure of a theory driven model must mimic those features of the real system that are pertinent to the current task [73]:

“In short, it is often said that a system dynamics model must generate the right output behavior for the right reasons.” (Y.Barlas 1996, from [73].)

Nonetheless, validating the structure of a white-box model remains an uphill challenge due to technical and philosophical issues [73]. On a technical perspective, there is no widely accepted quantitative method to assess how “distant” the structure of a model is from the structure of the system it describes [73]. On a philosophical perspective, we need to recall that the structure of a white-box model bears a theory of specific facets of the mimicked system [73]. As theories build up on statements, the validation of the model structure faces the unsettled debate on how to prove the truthfulness of a statement [73].

2.2 Complex systems

In the last decades scientists have adopted a wide range of criteria to classify systems according to their features. An important dichotomy emerged from this exercise is the one between *simple* and *complex* systems. Both families are characterized by the presence of multiple constituents which play a non-negligible role in the behavior of the system as a whole. Simple systems build on a small number of components and their behavior can be completely predicted by examining each component alone. Examples of simple systems are a natural satellite orbiting a planet, a pendulum or an oscillator. On the other hand, complex systems usually host a large number of interacting components. These systems display a variety of behaviors and patterns that cannot be inferred by only looking at their parts in isolation [2, 3]. A typical example of a complex system is the human brain. This organ is made of two families of cells: neurons and neuroglia. The former release signals to distant, target cells while the latter perform a broad spectrum of other important tasks, such as metabolic and structural support [82]. The brain as a whole exhibit a variety of signals when the electrical activity propagating across this organ is assessed through an electroencephalogram (EEG). To understand how these non-trivial patterns unfold, the observer does not only need to know about the properties of the

brain components, e.g., dimensions and functions of a neuron, but also how these components interact, e.g., the mechanisms behind the transmission of signals between neurons.

2.2.1 Universal features of complex systems

The study of complex systems has gradually emerged as an interdisciplinary subject which builds on the progresses made in a wide range of disciplines, such as physics, economics and biology [3]. The scientific community has largely accepted the view that gaining further knowledge on physical systems that appear more and more entangled requires a gradual partition of science in different, specialized and mostly independent fields of study [3]. Complex systems stray from this belief as their most peculiar trait is the presence of universal features that transcend the discipline the system belongs to [3]. For instance, Cilliers [83] suggested ten characteristics that are ubiquitously observable across many different complex systems:

- These systems include a large number of components [2, 3, 83].
- These systems often communicate with the surrounding environment. This feature complicates the detection of their boundaries [83].
- These systems function when they are far from their equilibrium condition, i.e., the survival of the system depends on the stable presence of energy flows [83].
- These systems evolve in time and their past history has a significant influence on their current behavior [83].
- Components engage in specific interactions, such as physical contacts, commercial trades, exchanges of information and propagation of signals [83].
- Components are not aware of how the system behaves in its entirety as their actions build on the information they gather locally [83].
- Interactions are iterated in time, i.e., the system “stays alive” until its components continue to interact with each other [83].
- Interactions are *non-linear* in the sense that unpretentious events, e.g., a single contact between two agents, might trigger a *cascade effect* with systemic consequences [83].

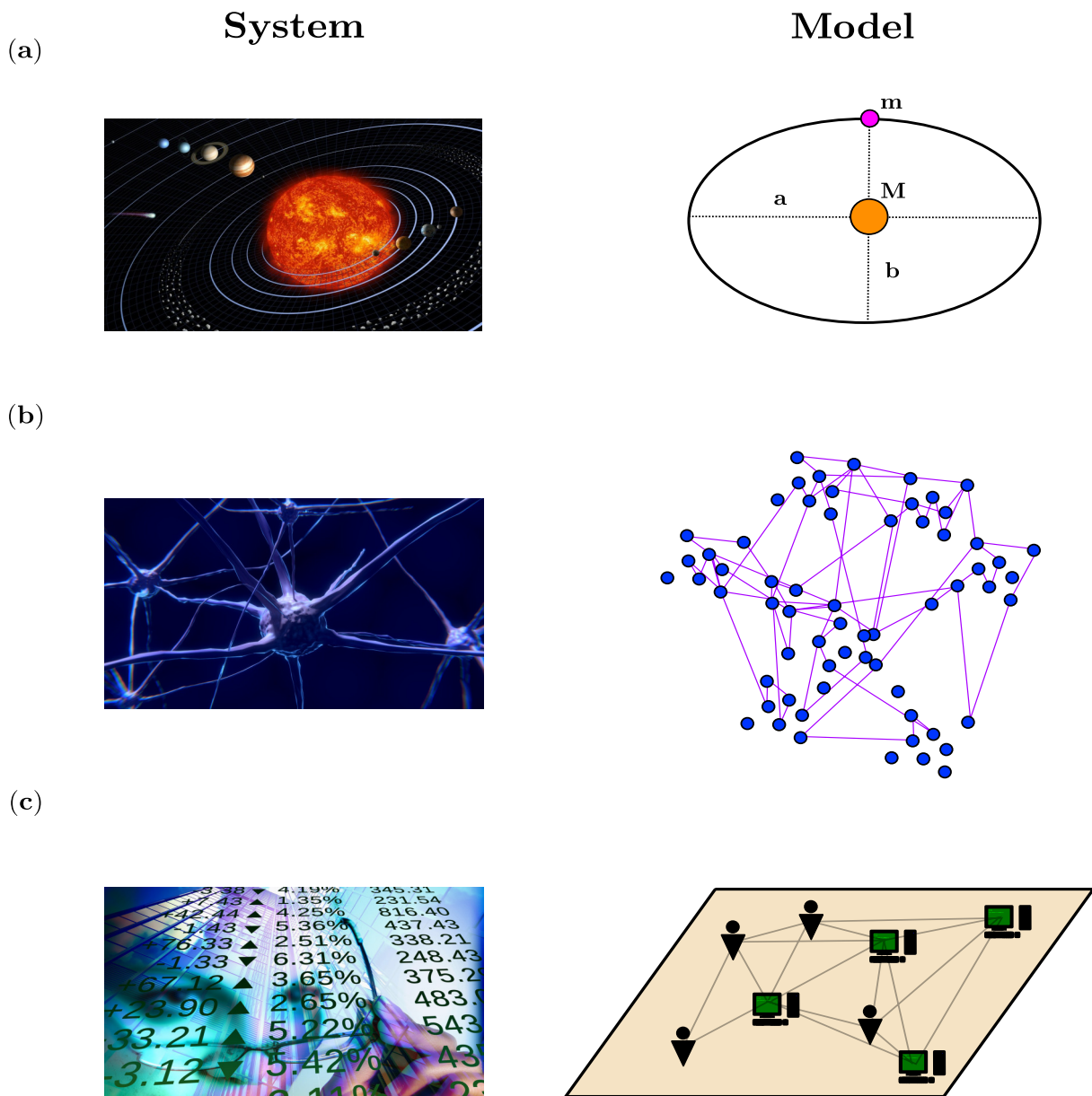


Figure 2.3: **Different systems and associated models.** (a) A planet orbiting around a star is a typical example of a simple system. In fact, its behavior can be fully predicted by a simple model of the laws of classical mechanics. (b) The microstructure of the human brain can be modelled as a network of interconnected nodes. In this setting, nodes mimic neurons while the distribution of connections is expected to capture the key properties of the connectivity structure of a real human brain. These tissues are a common example of a complex system as knowing the properties of its individual components is not enough to predict the spectrum of behaviors that the organ can exhibit as a whole. (c) A financial market can be modelled as an ecology in which different types of agents, e.g., human traders and computers, sequentially exchange units of a certain asset. Similarly to the human brain, a solid knowledge of the individual components of the systems, e.g., the trading strategy adopted by each agent, is not enough to predict the emergence of various macroscopic statistical regularities of financial markets. See appendix A for details about attributions and permissions for the images appearing in the left column of panels (a),(b) and (c).

- Interactions tend to be *short-ranged* as a certain component of the system is likely to gather information from close neighbouring components. Nonetheless, *long-ranged* interactions remain possible in those rarer scenarios in which distant contacts are not precluded by physical constraints [83].
- Interactions might include a *loop* as the consequences of a certain action can feed back onto themselves in a positive (negative) way, e.g., by boosting (undermining) the effects of the first action [83].

2.2.2 Complexity

The general features outlined by Cilliers [83] provide a plausible, qualitative description of what the term **complexity** means within the complex systems framework. However, building a more quantitative and formal description of the notion of complexity is a far more ambitious task and, so far, we have not been able to come up with an universally accepted definition of this concept [84]. As a result, complexity is often explained through i) practical examples, e.g., the interactions among billions of neurons in the human brain, ii) particular phenomena whose understanding requires a notable effort, e.g., percolation or turbulence, or iii) by comparing qualitative features of different systems [84]. In a recent effort, Bar-Yam described complexity as the amount of information that is necessary for the observer to describe the whole system [3]. To understand this concept more formally, we follow [3] by introducing a fictional system whose current state can be fully specified through a sequence of binary digits, e.g., 0100110101. The number of digits required to specify the present state is

$$I = \log_2(\Omega), \tag{2.1}$$

where Ω is the number of possible states of the system [3]. For instance, a string of n binary digits indicates that the system can take $\Omega = 2^n$ states. The most interesting aspect of the relationships introduced in Eq. (2.1) is that the amount of necessary information increases with the number of different states that the system can take.

The logic behind this trivial example turns out to be useful when we attempt to formalize the measurement of the complexity of a given system. Let ζ be the scale at which the system is examined, i.e., the level of details considered by the observer. In this definition, small values of ζ represent highly granular observations focused on the components of the system while

large values of ζ indicate that the observer opt for a more macroscopic perspective [3]. The amount of information $I(\zeta)$ required to specify the current state of the system is a monotonically decreasing function of the observation scale ζ , i.e., the higher the resolution of the observation the more pieces of information must be gathered [3]. This intuition stems from the fact that the information required to describe the system at a given scale is always embedded in the information required to describe the same system at a finer scale, i.e., $I(\zeta_i) \subset I(\zeta_j)$, $\zeta_j < \zeta_i$ [3]. The complexity of a certain system must be intimately related to the amount of information $I(\zeta)$ that we need to describe it, therefore, it can also be imagined as a monotonically decreasing function of the observation scale ζ [3]. Focusing on scales ζ that are marginally finer than the size of the system itself would allow the observer to examine the spatial movements and the dynamical changes of the system [3]. This level of granularity is acceptable when we examine systems like a planet orbiting around a star, see Fig. 2.2 (a). However, describing the behavior of other systems, such as the human brain or atrium, forces the observer to concentrate on much finer scales as the dynamics of the whole, being strictly dependent on the dynamics of its components, necessitate a thorough characterization of the components [3]. This implies that the complexity of a system is inversely proportional to the size of the components which must be described to characterize the whole system [3], therefore, systems like the human brain are far “more complex” than systems like planets revolving around stars.

2.2.3 Emergence

The concept of *emergence* plays a central role in the theory of complex systems. This notion appears in various disciplines, such as art, science and philosophy and can be associated to the idea that *the whole is not always the bare sum of the parts* - a view that can be traced back to the works of prominent philosophers in ancient societies:

“... *the totality is not, as it were, a mere heap, but the whole is something besides the parts ...*” (Aristotle, *Metaphysics*, Book H 1045a 8–10, from [85].)

In the second half of the 19th century various British philosophers inaugurated a new movement known as *Emergentism* [86]. This school of thought revolved around the belief that emergent entities stem from simpler entities and, in spite of this, they are different from and not reducible to them [86]. A seminal work of Emergentism is *A System of Logic, Ratiocinative and Inductive*, written by Mill in 1843 [86] :

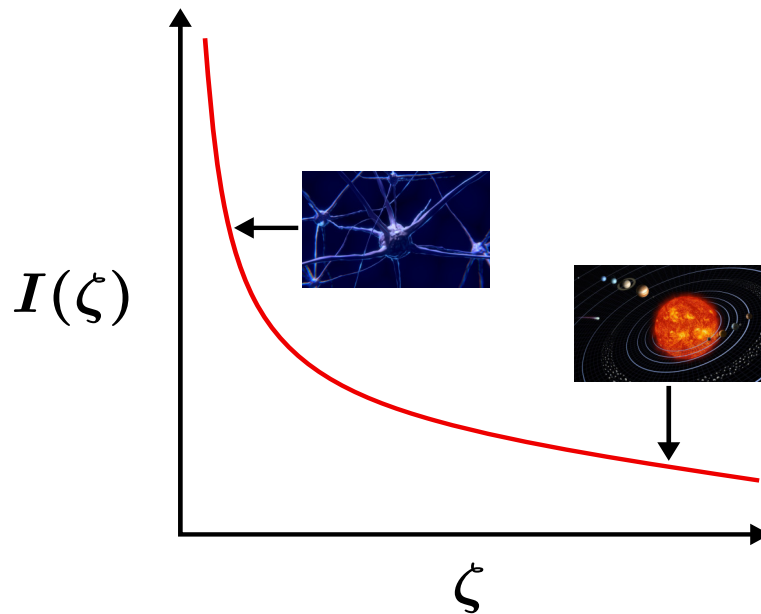


Figure 2.4: **Information required to describe the system as a function of the observation scale.** The amount of information $I(\zeta)$ that is needed to specify the current state of the system is a monotonically decreasing function (red line) of the observation scale ζ [3]. Building on this relationship, the complexity of a system is inversely proportional to the size of the components which must be described to characterize the whole system [3]. It follows that a system like the human brain, whose description requires a high amount of information $I(\zeta)$ due to the necessary characterization of the behavior of billions of microscopic components known as neurons, is far *more complex* than a planet orbiting around the Sun. See appendix A for details about attributions and permissions for the images appearing in this figure.

“All organised bodies are composed of parts, similar to those composing inorganic nature, and which have even themselves existed in an inorganic state; but the phenomena of life, which result from the juxtaposition of those parts in a certain manner, bear no analogy to any of the effects which would be produced by the action of the component substances considered as mere physical agents. To whatever degree we might imagine our knowledge of the properties of the several ingredients of a living body to be extended and perfected, it is certain that no mere summing up of the separate actions of those elements will ever amount to the action of the living body itself.” (J.S. Mill, A System of Logic, Bk.III, Ch.6, from [86].)

A fundamental idea emerging from Mill’s words is the dichotomic nature of causation - which can either be additive, i.e., *mechanical causation*, or emergent, i.e., *heteropathic causation* [87].

The latter is neither mechanical nor addictive and can be easily exemplified in the water originating from a reaction involving oxygen and hydrogen [87]. In fact, water properties are not “inherited” from its composing elements but arise as a consequence of their bonding [87]. In the next segment of the same chapter, Mill supports his reasoning with a practical example:

“The tongue, for instance, is, like all other parts of the animal frame, composed of gelatine, fibrine, and other products of the chemistry of the digestion; but from no knowledge of the properties of those substances could we ever predict that it could taste, unless gelatine or fibrine could themselves taste; for no elementary fact can be in the conclusion which was not in the premises.” (J.S. Mill, A System of Logic, Bk.III, Ch.6, from [88].)

Mill’s thinking reveals that important intuitions on complex systems and emergent phenomena as we know them today were already traceable in the 19th century. Nonetheless, he fell short of formulating an explicit definition of *emergence* or *emergent phenomena*. This milestone was achieved few decades later by Lewes:

“Although each effect is the resultant of its components, the product of its factors, we cannot always trace the steps of the process, so as to see in the product the mode of operation of each factor. In this latter case, I propose to call the effect an emergent. It arises out of the combined agencies, but in a form which does not display the agents in action.” (G.H.Lewes, 1875, vol.II, 412, from [87].)

The dichotomy between mechanical and heteropathic causation introduced by Mill and the notion of emergent proposed by Lewes were expanded in the work of various English philosophers of language in the very early decades of the 20th century [87]. This current, known as *Emergent Evolutionism* [89, 90, 91], included eminent thinkers and scientists of the likes of Morgan, Alexander, Broad and Sellars [87, 90, 91]. At that time, evolutionist theories faced the challenge of detecting continuity in the evolutionary processes taking place in both the inorganic and organic dimensions [91]. The notion of emergence was introduced to expand and rectify the extremely mechanistic perspective that Darwin’s work took on evolution [90]. In particular, various emergentist thinkers accepted the continuity of evolutionary dynamics in nature but

rebutted the idea that the characteristics of a certain event must mimic those of prior events that took place in the same evolutionary sequence [91].

“Evolution [...] is the name we give to the comprehensive plan of sequence in all natural events. However, the orderly sequence, historically viewed, appears to present, from time to time, something genuinely new. Under what I call emergent evolution stress is laid on this incoming of the new.” (C.L.Morgan, Emergent Evolution, 5, 1923, from [91].)

Emergent Evolutionism dissipated around 1940; followed by a new era in which the notion of emergence played a relevant role in biology, philosophy of science and early neuroscience [90]. In the last 40 years, the affirmation of complex systems as a standalone subject has significantly revived the scientific interest in the concept of emergence [90, 91]. The *neo-emergentist* landscape [90] still lack of an unified and universally accepted definition of emergence as this concept is applied in different ways across several disciplines [91]. Within the complex systems domain, a neo-emergentist definition of emergence was coined by Goldstein in 1999:

“Emergence, as in the title of this new journal, refers to the arising of novel and coherent structures, patterns, and properties during the process of self-organization in complex systems. ” (J. Goldstein, Emergence as a construct: History and issues, Emergence, vol.1, no.1, 1999 [92])

In this context, emergence is the formation previously unseen collective structures, patterns, and properties, i.e., involving the whole system, that cannot be anticipated even if the observer has a vast knowledge of the components of the system or the interactions between these components remain extremely simple [92, 93, 2]. These emergent phenomena are the large-scale consequences of local interactions between the components of the system during a process known as *self-organization* [92, 93, 2].

2.2.4 Self-organization

Emergent phenomena are the resultant of a chain of local events occurring at a more microscopic dimension [94]. The process that leads to an emergent, known as *self-organization*, is

spontaneous, i.e., the course of events can neither be controlled by the components of the system nor by external entities, and *collective*, i.e., it involves every component and region of the system [94]. The global extent of this phenomenon ensures that the emerging structures are inherently stable and resistant to external disturbances [94]. Self-organization can be traced in a plethora of systems. For instance, pedestrians proceeding in a congested walkway spontaneously organize into two parallel lanes in which they proceed in opposite directions, thus creating stable patterns in the flow of people moving through the walkway [93]. Birds organizing in flocks interchange feeding and scanning according to the predominant behavior of their neighbours [93, 95, 96]. This compromise, i.e., a “selfish” bird might find an optimal outcome in continuous feeding, in favor of a self-organized cooperative behavior ensures that the flock remains aware of potential predatory attacks [96]. Although self-organization begins with local



Figure 2.5: **Flocking birds.** Flocks are a typical example of self-organization in biological systems. See appendix A for details about attributions and permissions for the image appearing in this figure.

and isolated interactions, the highly interconnected topology of many complex systems ensures that events occurring in any region ripple through the system to affect distant and apparently extraneous regions [94]. The mutual influence between regions of a system, being based on non-trivial feedback effects, makes the resulting effects hardly foreseeable [94]. To better understand this process, recall that any component of the system has its own preferences towards outcomes that conform with its ultimate goals [94]. However, the diversity of the components across the system results in heterogeneous and often contrasting goals and preferences, such as in the typical biological scenario in which preys aim to escape predators while predators aim to eat preys [94]. In this setting, the full realization of an individual’s preferences is likely to be detrimental for all the other agents in the systems. For instance, if preys develop an uncommon

ability to escape attacks predators will not be able to feed themselves or if a company obtain a monopolistic position all the other competitors will be forced to leave the market [94]. As highlighted by Heylighen in [94], the “non zero-sum” nature of interactions can be exploited by the parts to attain an alternative outcome that is i) beneficial to every part and ii) superior to the outcome of not engaging in an interaction. This can be achieved by “accepting” a partial accomplishment of individual preferences in exchange of an attenuation of frictions between antagonistic goals [94]. To reach this *mutual adaptation*, every interacting part adopts a strategy, assesses its outcomes and eventually replaces it with a new one without being able to foresee the consequences of their actions on other components of the system [94]. In this “hit or miss” sequence, the involved fronts independently and concurrently adjust their actions to better conform to each other; gradually tailoring their behaviors until they reach an outcome that is beneficial to every parts [94].

When at least two components have compromised to attain a mutually favourable outcome, we have the first episode of local coordination [94]. At this point, other components of the system acting in the proximity of this region adjust their behaviors to gradually fit into this nascent subset of coordinated agents, thus triggering an expansive process that gradually involve every component of the system [94]. The pace at which a stable state expands across the system is dictated by the heterogeneity of its components: the higher the diversity, i.e., different objectives, the higher the effort that a component needs to pay to fit into the emerging organization [94].

2.2.5 Modelling complex systems

In this section, we review various approaches to complex systems modelling that are relevant to the problems presented in this dissertation. Developing models that successfully describe the emergence of macroscopic phenomena from local microscopic interactions remains a notable challenge. For instance, the interactions between a large number of heterogeneous components, a recurrent pivotal feature of complex systems, cannot be realistically modelled by a system of equations unless the modeller enforces major simplifying assumptions [93]. As a result, continuous models such as differential and recurrence equations usually neglect the spatial aspects of the system, e.g., the distance between components, and assume that agents engage in standardized long-ranged interactions [93]. This approach is known as *mean-field*. The advent of computer simulations has significantly eased this challenge by expanding the range

of modelling approaches available to scientists. Computer-based models evolve in discrete time, tend to build on less developed theories and their behavior is analyzed experimentally rather than analytically [93]. The pivotal advantage of these frameworks is their ability to capture the spatial features and the heterogeneity that characterize the microstructure of every complex system. This allows to explore features that play a primary role in the emergence of macroscopic patterns, such as the diversity of the system components, the mechanisms of their local interactions and the topology of the system of interest. Cellular automata, agent-based models and large networks are typical examples of computer-based models of complex systems.

Cellular automata models

Cellular Automata models (CAMs henceforth) are simple mathematical conceptualizations of a system of interest [97]. In a CAM the system evolves in discrete time, the space occupied by each component is discrete and any quantity spans between a finite range of predefined, discrete values [97]. A *cellular automaton* comprises a regular tiling of polygons, known as *sites* or *cells*, forming a lattice and a discrete variable which can be measured at each cell and at any time step [97]. Let us consider a simple cellular automaton composed by a 1d lattice of k square cells denoted by $x = 1, \dots, k$. Let $s \in \mathcal{S}$ be a discrete variable and \mathcal{S} a finite state space. At any time t , the state of the cellular automaton is specified by

$$S_t = \{s_t^{(1)}, \dots, s_t^{(k)}\}, \quad (2.2)$$

where $s_t^{(j)}$ is the value of the variable s on the j -th cell at time t . From Eq. (2.2) we can straightforwardly observe that the state of the cellular automaton S_t is completely determined by the values that s takes in each cell at time step t [97, 98]. In the 1d lattice presented in Eq. (2.2) the neighbour of the j -th cell is a triplet of contiguous cells defined by:

$$\text{NB}_j = \{x : |x - j| \leq 1\} = \{j - 1, j, j + 1\}. \quad (2.3)$$

These local structures play a pivotal role in the CAM theory as they determine how cells affect each other as the system evolves in time. In particular, the updates of the variable of interest s are influenced by the values that the same variable took in the neighborhood in the previous time step [97]. For instance, under the settings introduced in Eq. (2.3), the updated state $s_t^{(j)}$ is given by $g(s_{t-1}^{(j-1)}, s_{t-1}^{(j)}, s_{t-1}^{(j+1)})$, where $g : \mathcal{S}^{\text{Card}(\text{NB}_j)} \rightarrow \mathcal{S}$ is known as the *local rule* of the automaton [98, 99]. In a CAM, local rules are predetermined and updates are synchronous, that

is, the variable s is updated simultaneously across the lattice as soon as its value is determined by these rules [97, 98].

Let us now consider a 2d lattice of $k \times k$ square cells denoted by their coordinates (x, y) , $x = 1, \dots, k$, $y = 1, \dots, k$. The neighborhood of the cell (i, j) usually takes one of the following structures:

1. The Von Neumann neighborhood, a diamond shaped structure of adjacent cells centered on (i, j) , formally defined by:

$$\text{NB}_{(i,j)}^{\text{VN}} = \{(x, y) : |x - i| + |y - j| \leq d\}, \quad (2.4)$$

where $d = |x_1 - x_2| + |y_1 - y_2|$ is the Manhattan distance between two points (x_1, y_1) and (x_2, y_2) [100, 101, 102], see left panel of Fig. 2.6(b).

2. The Moore neighborhood, a square shaped structure of adjacent cells centered on (i, j) , formally defined by:

$$\text{NB}_{(i,j)}^{\text{M}} = \{(x, y) : |x - i| \leq c \text{ and } |y - j| \leq c\} \quad (2.5)$$

where $c = \max\{|x_1 - x_2|, |y_1 - y_2|\}$ is the Chebyshev distance between two points (x_1, y_1) and (x_2, y_2) [103, 101, 104], see right panel of Fig. 2.6(b).

(a)



(b)

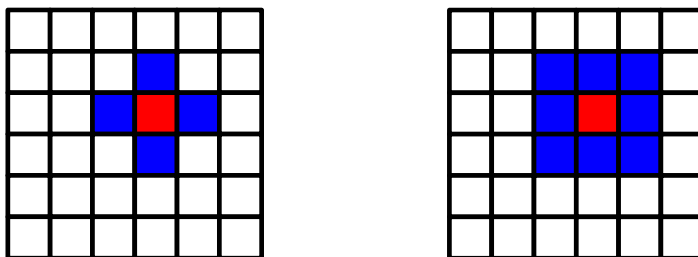


Figure 2.6: **Common neighborhoods in CAMs.** (a) In a 1d simple lattice of k square cells, the neighborhood of the red cell might include the cell itself and both its left and right neighbours (left panel), only its right neighbour (central panel) or only its left neighbour (right panel). (b) In a 2d lattice of $k \times k$ square cells, the neighborhood of the red cell is usually Von Neumann (left panel) or Moore (right panel).

The archetypal CAM, known as the Von Neumann automaton [100], is an infinite 2d lattice in which square cells can take 29 distinct states and neighborhoods obey to the Von Neumann scheme. Another seminal CAM is the Conway’s Game of Life [105], an automaton based on an infinite 2d lattice in which square cells can only take 2 states and neighborhoods follow the Moore scheme [98]. In spite of the fact that the vast majority of CAMs adopt squared shaped cells, the available literature offers interesting diversions from this dominant setup [99]. Examples include 2d lattices of hexagonal cells [106, 107, 108], triangular cells [109, 110, 111] and automata networks [112, 113, 114]. When a CAM is executed in a computer, the dimensions of the lattice must be finite. In this scenario, the adopted neighboring structure might not be directly applicable to boundary cells. For instance, in the 1d simple CAM presented in this section triplets of adjacent cells form overlapping neighborhoods, see Eq. (2.3). However, the leftmost and rightmost cells can only form a neighborhood with their right and left adjacent cells, respectively. This forces modellers to choose a *boundary scheme* in order to handle the missing neighbors of boundary cells [99]. The CAMs presented in this dissertation rely on the following boundary schemes:

- Open: the missing neighbors are included as fixed state cells lying one space unit beyond the edges of the lattice [99]. The most common variant is the null open boundary which consists in fixing the state of the missing neighbors to zero [99].
- Periodic: boundary cells neighbor each other [99]. If we were to enforce periodic boundary conditions in the 1d CAM presented in this section, the first cell would neighbor the k -th cell as they lie on the left and right edge of the lattice respectively:

$$\text{NB}_1 = \{k, 1, 2\}, \tag{2.6a}$$

$$\text{NB}_k = \{k - 1, k, 1\}. \tag{2.6b}$$

Additional schemes adopted in the available literature, e.g., adiabatic or reflexive boundary conditions, are surveyed in [99].

CAMs were initially conceived as frameworks for modelling the dynamics of biological and physical systems and gather theoretical insights on specific aspects of these systems [97, 98, 99]. These seminal applications came as no surprise as CAMs carry various properties of real physical systems, such as the local nature of interactions, homogeneity and parallelity [98]. More recently, these models became valuable tools in the solution of practical problems [99]. The

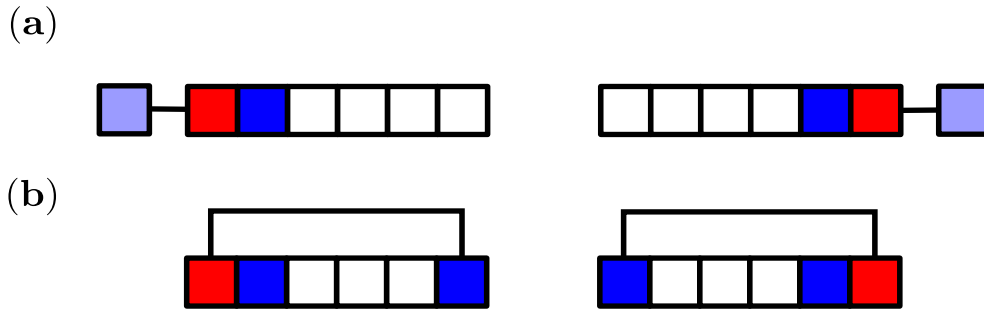


Figure 2.7: **Boundary conditions in CAMs.** Each column presents different boundary conditions for the left and right edges of the lattices, respectively. Boundary cells are highlighted in red while cells belonging to their neighborhoods are highlighted in blue. (a) Open boundary conditions: the faded blue cells beyond boundary cells maintain a fixed state, e.g., $s = 0$; completing the neighborhoods of the adjacent boundary cells. (b) Periodic boundary conditions: the left boundary cell neighbors the right boundary cell and vice-versa.

recent survey of Bhattacharjee *et al.* [99] highlights how CAMs have been applied in a broad range of fields, such as encryption and cryptography [115, 116, 117, 118], image processing [119, 120, 121], pattern recognition [122, 123, 124, 125] and medical sciences [126, 127, 128].

Agent based models

Agent based modelling is an emerging paradigm in complex systems simulation [2, 129]. An agent based model (ABM) idealizes the system of interest as a crowd of independent *living* entities known as *agents* [130]. Agents act within a common environment; a stylized representation of the real *habitat* at heart of the system of interest [131]. Similarly to CAMs, ABMs evolve in discrete time and at any time step each agent performs the following sequence of actions:

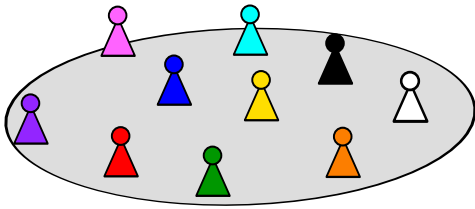
1. Assessment: the agent analyzes the current state of the system [130].
2. Decision: based on its assessment of the current situation, the agent decides its next action through pre-defined rules [130].

This decision making process is synchronous, i.e., each agent acts at the same time, and autonomous, i.e., agents examine and act independently from each other [130]. These decisions could prompt interactions between agents. For instance, in the ABM of financial markets proposed by Yamada *et al.* [35] several agents autonomously update their buy and sell prices

based on the current state of the market. These updates create a scenario in which an agent is willing to buy the traded asset at a price that is at least as high as the price at which another agent is ready to sell it; triggering a financial transaction between the two counterparts [35]. Depending on the scope of the model, the spatial positioning of the agents across the environment might be either relevant or irrelevant [131]. Furthermore, agents behaviors might be affected or constrained by the hosting environment [131]. For instance, in our recent ABM [34] the environment encompasses three foreign exchange markets and agents assigned to different markets cannot interact with each other. Another interesting aspect in the agent based paradigm is the level of rationality embedded in the rules that govern agents' decisions [131]. Loosely, agents are "rational" when the observer perceives that their actions are compatible with their ultimate objectives, e.g., maximizing their wealth [131]. Is "perfect" rationality always a desirable feature? This question has been at the center of a long lasting debate between different communities involved in modelling of financial systems [131, 132]. While economists have often explored specific issues under full rationality assumptions [38, 133, 134, 135], physicists employed agent based approaches to include agents with *bounded rationality* [136], e.g., the *Santa Fe Stock Market* [137].

ABMs exploit the capabilities of modern computers to simulate and analyze these interactions for a sufficiently extended time window [130]. The agent based paradigm takes a "bottom-up" perspective on the system of interest: the focusing is on modelling agents' diversity and interactions at a microstructural level while macroscopic patterns, behaviors and properties emerge as the idealized system evolves in time [130]. This striking ability to capture emergent phenomena makes ABMs a very natural and orthodox strategy to model complex systems [130]. More generally, ABMs are useful modelling tools when agents behaviors are either i) nonlinear, e.g., threshold based decisions, ii) non Markovian, e.g., learning agents or adaptive agents, or iii) cannot be aggregated, e.g., mean-field approaches, due to their significant heterogeneity [130]. As surveyed by Gilbert [131], these features have played an important role in the affirmation of the agent based paradigm in a wide spectrum of social sciences related fields, such as urban segregation studies [138, 139, 140, 141], formation and dynamics of opinions [142, 143], adoption of industrial innovations [144] and financial markets [35, 137, 145, 146].

(a)



(b)











Agent	Rule	Outcome
	$f(S_{t-1}, \theta_1)$	Action 1
	$f(S_{t-1}, \theta_2)$	Action 2
	$f(S_{t-1}, \theta_3)$	Action 1
	$f(S_{t-1}, \theta_4)$	Action 3
	$f(S_{t-1}, \theta_5)$	Action 2
	$f(S_{t-1}, \theta_6)$	Action 3
	$f(S_{t-1}, \theta_7)$	Action 1
	$f(S_{t-1}, \theta_8)$	Action 3
	$f(S_{t-1}, \theta_9)$	Action 2
	$f(S_{t-1}, \theta_{10})$	Action 1

Figure 2.8: **ABMs basics.** (a) An ABM consists in a multitude of different agents (colored pawns) acting within a common environment (grey circle) who i) autonomously examine the present state of the system, ii) use this information to decide their next action and iii) interact with each other. (b) At any time step t , each agent autonomously decide its next action according to a predefined rule f . Considering an extremely simple decision-making context, f takes into the account the current state of the system S_{t-1} , which is the same for every agent, and a set of parameters θ_j that is unique to each agent, e.g., the risk aversion profile of economic agents.

Mean field models

Mean field (MF henceforth) models are extremely simplified and coarse descriptions of a complex system [93]. It is often said that MF models rely on averages [93] as the diversity that can be found in different dimensions of mimicked system, such as:

- The distances between components,
- The features characterizing each component, e.g., their dimensions,
- The interactions that can be established between two or more components,

is neglected in favour of a more homogeneous setup in which average quantities, e.g., average dimensions, allow to “standardize” the components of the system, the spatial dimension of the system is ignored and the variety of local interactions is superseded by standardized long-ranged interactions [93].

MF models, providing an overly simplified representation of a complex system, do not aim for a comprehensive and faithful replication of the dynamics of interest. Instead, they provide important support in the early phases of the modelling process by offering insights on various behaviors of the system of interest.

Scientists have adopted MF approaches to investigate problems across a broad range of disciplines, such as astrophysics [14], chemistry [147, 148], disease spreading [15, 16], traffic flows [17, 18], physics [149, 150], epilepsy [19], opinion competition [151] and atrial fibrillation [20]. A seminal application of MF theory is the Kermack-McKendrick model of epidemics [15], which provides an extremely simplified framework to describe the diffusion of an infectious disease within an human group [93]. The model neglects the spatial features of the environment and the diversity of interactions to split the population in three communities [93]:

1. Carriers (C), people who contracted the disease and are able to spread it to healthy individuals.
2. Susceptible (S), healthy people who can contract the disease and turn into carriers.
3. Removed (R), people who either overcame the disease to achieve immunization, died of the disease or shield to avoid interactions.

The Kermack-McKendrick model describes the dynamics of these three groups through a system of differential equations:

$$\frac{dS}{dt} = -\alpha S(t)C(t), \quad (2.7a)$$

$$\frac{dC}{dt} = C(t) (\alpha S(t) - \beta), \quad (2.7b)$$

$$\frac{dR}{dt} = \beta C(t), \quad (2.7c)$$

where S is the number of susceptible individuals, C is the number of carriers, R is the number of removed individuals, α is the infection rate and β is the removal rate [93]. From Eq. (2.7) we can easily observe that the number of susceptible individuals cannot increase in time. This occurs because carriers who survive the disease are assumed to become permanently immune. The number of carriers $C(t)$ fluctuates upward and downward as a result of the antagonistic contributions of $\alpha S(t)$ and β . This reveals what is perhaps the most interesting feature of this simple epidemic model: when the initial number of susceptible individuals $S(t_0)$ is smaller than the threshold β/α , the system does not develop an epidemic as the number of carriers gradually decreases towards 0 [93]. This mimics real situations in which a disease cannot turn into an epidemic due to its low contagion rate, e.g., carriers are isolated before they can significantly spread the disease, or high mortality rate, e.g., carriers die before they can significantly spread the disease [93]. On the other hand, the epidemic develops if $S(t_0) > \beta/\alpha$: in this scenario, we observe a first phase in which the epidemic expands due to the increasing number of carriers followed by a second phase in which the epidemic starts to taper off as soon as $S(t) < \beta/\alpha$ [93].

Markov Chains

Let us consider a collection of random variables $X = \{X_t : t = 0, 1, 2, \dots\}$ representing the dynamics of a system of interest, i.e., the sequence of transitions from state to state, which take values on a finite set of states \mathcal{S} known as *state space* [152]. If the next state of the system X_{t+1} depends on the current state X_t but not on the past states X_{t-1}, \dots, X_0 , i.e.,

$$\mathbb{P}(X_{t+1} = j | X_t = i, X_{t-1} = a, \dots, X_0 = z) = \mathbb{P}(X_{t+1} = j | X_t = i) \quad j, i, a, z \in \mathcal{S} \quad (2.8)$$

the stochastic process is a Markov Chain [152]. The probability of transitioning from state i to state j , see Eq. (2.8), is often denoted by the more compact notation P_{ij} and serves as a single

entry of a transition probability matrix

$$\mathbf{P} = \begin{pmatrix} P_{11} & P_{12} & \cdots & P_{1n} \\ P_{21} & P_{22} & \cdots & P_{2n} \\ \vdots & \vdots & \ddots & \vdots \\ P_{n1} & P_{n2} & \cdots & P_{nn} \end{pmatrix}, \quad (2.9)$$

where n is the number of possible states, the columns of \mathbf{P} represent the departing states, the rows of \mathbf{P} represent the arrival states so summing over the rows satisfies the normalization constraint

$$\sum_{j=1}^n P_{ij} = 1 \quad i = 1, \dots, n. \quad (2.10)$$

The matrix presented in Eq. (2.9) contains the single step transition probabilities between every pair of possible states. This concept can be extended to an arbitrary number of steps k , i.e., the probability of transitioning from i to j in k steps, by making use of simple matrix algebra

$$\mathbf{P}^k = \mathbf{P} \times \mathbf{P} \cdots \times \mathbf{P}, \quad (2.11)$$

where the matrix multiplication is performed k times [152]. If the transition probabilities \mathbf{P} are time invariant the Markov Chain is *time-homogeneous*. Conversely, Markov Chains governed by time varying transition probabilities are known as *time-inhomogeneous*.

The state j is *reachable* from state i if $P_{ij} > 0$ [152]. When this holds in “both directions”, i.e., $P_{ij} > 0$ and $P_{ji} > 0$, the states i and j *communicate* [152]. When every state communicate, i.e., it is possible to “travel” from any state to any other state in $k \geq 1$ steps, the Markov Chain is *irreducible* [152]. Assuming that $X_0 = j$, i.e., the starting state, we say that the state j is *recurrent* (*transient*) if the probability of ever returning to the state j is $f_j = 1$ ($f_j < 1$) [152]. A state j is said to be *absorbing* if $P_{jj} = 1$, i.e., the process is “trapped” forever into j as soon as it reaches this state for the first time [152]. An important question in Markov Chain theory is how one should compute the “long run” [152] probability of observing the system in a certain state. Let us consider a finite Markov Chain X_t with state space $\mathcal{S} = \{1, 2, \dots, n\}$. Furthermore, the transition probability matrix \mathbf{P} and the initial states distribution $\nu_0 = (\mathbb{P}(X_0 = 1), \dots, \mathbb{P}(X_0 = n))^T$ are known. Then, we recursively update the

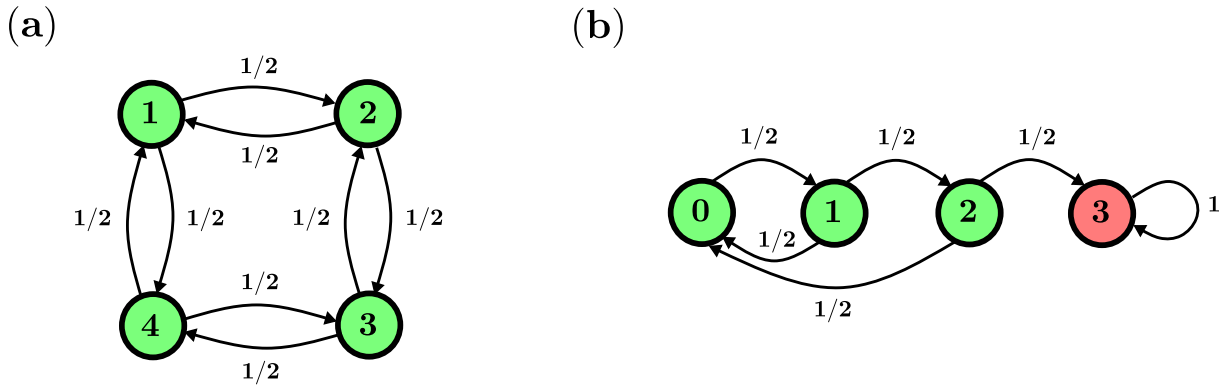


Figure 2.9: **Schematics of simple time-homogeneous Markov Chains.** Circles represent different states. The background color indicates whether the represented state is absorbing (red). Directed arrows mark possible transitions between a departing and an arrival state. Each arrow is paired with the corresponding transition probability. (a) The system can take four non absorbing states. At any time we expect the next state to be, with equal probability, either the left or right “neighbor” of the present state. (b) A Markov Chain is used to describe the dynamics a simple coin-based game in which the player flips a coin until she obtains three heads in a row, i.e., whenever the coin lands tail the count goes back to zero.

states distribution

$$\begin{aligned}
 \nu_1 &= \mathbf{P}\nu_0 \\
 \nu_2 &= \mathbf{P}^2\nu_0 \\
 &\vdots \\
 \nu_k &= \mathbf{P}^k\nu_0,
 \end{aligned}
 \tag{2.12}$$

by applying the total probability rule [152]. Finally, we let $k \rightarrow \infty$ to obtain

$$\lim_{k \rightarrow \infty} \mathbf{P}^k\nu_0 = \pi,
 \tag{2.13}$$

where π is a “long run” state distribution vector that does not depend on the initial distribution ν_0 [152]. If π satisfies the following conditions

$$\pi_j \geq 0 \text{ for } j = 1, \dots, n,
 \tag{2.14a}$$

$$\sum_{j=1}^n \pi_j = 1,
 \tag{2.14b}$$

$$\mathbf{P}\pi = \pi,
 \tag{2.14c}$$

then we say that π is a *stationary distribution* of the Markov Chain X_t [152].

Markov Chains can be extended to continuous time by relaxing the assumption that the stochas-

tic process X_t evolves, i.e., it moves from a state to another, in a discrete and equally spaced time grid [153]. By doing so, we obtain a process $\{X(t) : t \geq 0\}$, known as *continuous time Markov Chain* (CTMC henceforth), with the following features [153]:

- $X(t)$ takes values on a discrete states space \mathcal{S} .
- $X(t)$ retains the Markov property

$$\mathbb{P}(X(r + \tau) = j | X(r) = i, \{X(s) : 0 \leq s < r\}) = \mathbb{P}(X(r + \tau) = j | X(r) = i) = P_{ij}(\tau), \quad (2.15)$$

where $i, j \in \mathcal{S}$, $\tau \geq 0$, $r \geq 0$ and $\{X(s) : 0 \leq s < r\}$ is the entire dynamics of $X(t)$ up to time r .

- The time $X(t)$ spends on a given state i is a continuous and strictly positive random variable h_i known as *holding time* of state i . To preserve the memoryless property, the holding time must abide to an exponential distribution

$$\mathbb{P}(h_i \leq \tau) = 1 - e^{-\lambda_i \tau}, \quad (2.16)$$

where $\lambda_i > 0$ is the rate parameter of state i .

It is easy to observe that while the transition mechanism in CTMCs is analogous to the discrete case, the major difference between discrete and continuous Markov Chains lies in the time between two consequent transitions [153]. In particular, the former neglects these intervals by adopting a discrete and equally spaced time grid in which the process undergoes a transition in every time step while the latter relies on a more sophisticated approach in which the duration of intervals between transitions follows an exponential distribution.

To describe a CTMC, we need to study the “infinitesimal” behavior of the model. Let us start by observing that when the interval τ becomes very small Eq. (2.16) can be approximated as

$$\mathbb{P}(h_i \leq \tau) = \int_0^\tau \lambda_i e^{-\lambda_i t} dt = -e^{-\lambda_i x} \Big|_0^\tau = 1 - e^{-\lambda_i \tau} \approx \lambda_i \tau, \quad \lambda_i \tau \ll 1 \quad (2.17)$$

Then, we compute the following limit

$$\begin{aligned} \lim_{\tau \rightarrow 0^+} \frac{\mathbb{P}(X(\tau) \neq i | X(0) = i)}{\tau} &= \lim_{\tau \rightarrow 0^+} \frac{\mathbb{P}(N_i(\tau) = 1)}{\tau} \\ &= \lim_{\tau \rightarrow 0^+} \frac{\lambda_i \tau + o(\tau)}{\tau} \\ &= \lambda_i, \end{aligned} \quad (2.18)$$

where o is the “little o” notation and $N_i(t)$ is a Poisson counting process [153]. Note that in Eq. (2.18) we have obtained the instantaneous transition rate from state i , λ_i [153].

At this point we recall that when $X(t)$ departs state i it will travel to state j with probability P_{ij} , hence

$$\begin{aligned} \lim_{\tau \rightarrow 0^+} \frac{P_{ij}(\tau)}{\tau} &= \lim_{\tau \rightarrow 0^+} \frac{\mathbb{P}(X(\tau) \neq i | X(0) = i)}{\tau} P_{ij} \\ &= \lim_{\tau \rightarrow 0^+} \frac{\mathbb{P}(N_i(\tau) = 1)}{\tau} P_{ij} \\ &= \lim_{\tau \rightarrow 0^+} \frac{\lambda_i \tau + o(\tau)}{\tau} P_{ij} \\ &= \lambda_i P_{ij}, \end{aligned} \tag{2.19}$$

gives us the the instantaneous transition rate from state i to state j [153]. By applying the same reasoning, one finds that

$$\lim_{\tau \rightarrow 0^+} \frac{P_{ii}(\tau)}{\tau} = -\lambda_i. \tag{2.20}$$

Finally, the transition rates are collected into a matrix \mathcal{G} known as the *infinitesimal generator* of the Markov Chain

$$\mathcal{G} = \begin{pmatrix} -\lambda_1 & \lambda_2 P_{12} & \cdots & \lambda_n P_{1n} \\ \lambda_1 P_{21} & -\lambda_2 & \cdots & \lambda_n P_{2n} \\ \vdots & \vdots & \ddots & \vdots \\ \lambda_1 P_{n1} & \lambda_2 P_{n2} & \cdots & -\lambda_n \end{pmatrix}, \tag{2.21}$$

which allows us to describe the CTMC according to the instantaneous rates at which the process travels across states.

To sum up, Markov Chains are simple stochastic processes that “explore” a discrete state space. In the simplest setting, a Markov Chain evolves in discrete time. However, these processes can be also studied in continuous time by modelling the duration of the period between two consecutive transitions as an exponential random variable. Like MF models, Markov Chains are a *holistic* approach which tends to overlook dynamics occurring at microstructural dimensions in favor of a much simpler stochastic modelling of the macroscopic dynamics of the system of interest. This implies that the benefits of having a simple and computationally inexpensive framework are compensated by the difficulties of capturing more granular features of the system without adding further layers of complexity to the model. Markov Chains and similar models have been used to mimic a broad range of systems, such as opinion dynamics [154, 155], financial markets [156, 157, 158], neurons [159, 160], traffic flow [161, 162] and disease spreading [163].

Network models

The increasing availability of empirical data has revealed important insights on the topology of real systems [164]. In particular, several systems in our world are characterized by non-trivial sparse topologies where a small fraction of their components establish direct interactions while the remaining majority indirectly affect each other through chains of direct interactions [164, 165]. These topological features can be captured by *networks*, a powerful modelling paradigm in the field of complex systems [164]. A network is a collection of *vertices*, i.e., sites or nodes representing the components of the mimicked system, and *edges*, i.e., lines or links binding two vertices representing an existing relationship between components of the mimicked system [165]. In discrete mathematics, network analysis is known as *graph theory* and it is widely believed that the earliest proof in this field dates back to 1735 when Euler proposed a solution of the Königsberg bridge problem [165]. More recent, yet seminal applications of networks can be traced back to the early decades of the 20th century when sociologists identified this modelling paradigm as a powerful tool to examine human relationships [165]. In the last 30 years the ever growing accessibility to powerful computing machines and large, granular datasets has sparked a novel interest in large networks, e.g., millions of vertices, and their macroscopic statistical features [165].

Networks can be classified based on the properties of their vertices and edges [165]. The simplest network consists of N identical vertices and K identical edges [165]. More convoluted networks might comprise vertices of different size and class, e.g., social network models where individuals have different attributes, weighted edges, e.g., business network models where edge sizes represent the amount of goods exchanged between two firms, or directed edges, e.g., telecommunications network models where edge directions reflect the sender-receiver relationships between two terminals [165]. Networks in which single edges can connect three or more vertices are known as *hypergraphs* [165] whereas networks with time varying structure, e.g., edges appear and disappear in time, are often referred to as *dynamical networks*.

Network datasets might reveal important insights on the topology of the underlying network [166]. Scientists exploit the power of modern computers to process and analyze this data by employing concepts and tools that are typical of this field [166]. Centrality measures, such as degree centrality, eigencentrality or pagerank, are used to identify the most prominent vertices of a network [166]. Group analysis provides a toolkit of concepts, such as cliques and components, and techniques, such as hierarchical clustering, to detect and study communities, i.e.,

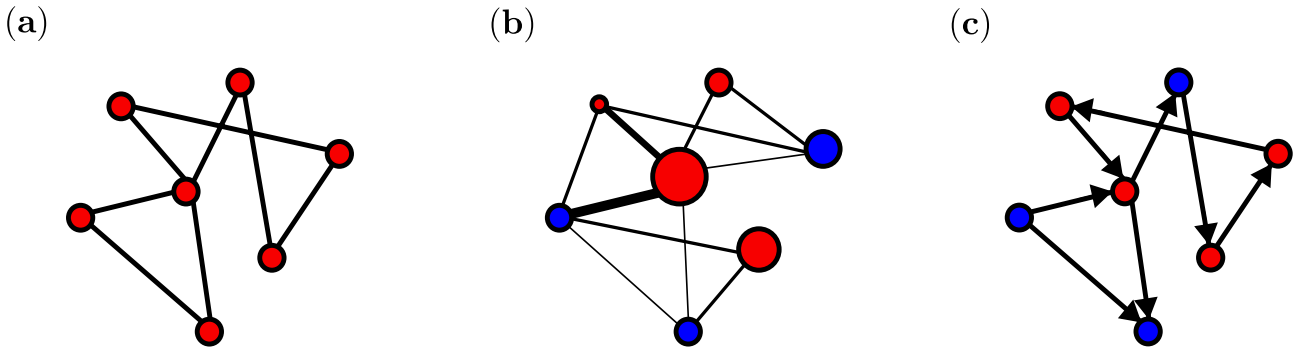


Figure 2.10: **Examples of different networks.** (a) An overly simplified network consisting of 7 identical vertices and 8 identical edges. (b) A network comprising 7 vertices of different size, i.e., circle diameter, and class, i.e., blue and red filling, and 11 weighted edges, i.e., line thickness. (c) A network comprising 7 vertices of same size and different class and 8 unweighted direct edges, i.e., arrows indicate the direction of the pairwise relationships.

group of vertices sharing a common tract, within a given network [166]. Similarity measures, such as cosine similarity and Pearson coefficients, provide a quantitative framework to assess the similarity between vertices [166].

As surveyed by Newman [165], our world encompasses many systems whose topology can be satisfactorily described by a network model, such as the digital economy [167], interactions and competition between firms [4, 5, 6], the foreign exchange market [7, 8], scientific co-authorships [9, 10, 11], archaeology [168, 169, 170] and urban traffic [12, 13, 171].

2.3 Summary of the chapter

In this chapter we have built the “backbone” of this dissertation by presenting the theoretical background required to understand and evaluate the research presented in the forthcoming chapters. We started from the simple definition of a physical system and argued that the behavior of any real system can be often studied through dedicated models. We have examined the key aspects of the model development process, the practical implementation of the model through computer-based simulations and the subsequent validation of the outcomes of these experiments. Then, we restricted our attention to complex systems, a family of physical systems characterized by the presence of a large number of constituents which engage in non-trivial interactions. Complex systems presents a broad spectrum of behaviors, structures and statistical features whose origins cannot be understood by the mere knowledge of their components [2, 3].

We have examined three core elements of complex systems theory: the notion of complexity, the emergence of system-wide structures and the microscopic process behind emergent phenomena known as self-organization. In particular, we have looked at the qualitative definition of complexity emerging from the work of Cilliers [83] and the recent effort of Bar-Yam [3] in formalizing this concept in quantitative terms. Then, we have explored the historical evolution of the notion of emergence by discussing how several elder philosophies neared or even elaborated on this concept way before its recent breakthrough in complex system theory. Finally, we have examined the mechanisms of self-organization in complex systems by following the work of Heylinghen [94]. The last segment of this chapter offered a detailed analysis of a broad spectrum of modelling techniques that can be applied to the study of complex systems. In particular, we have considered both *holistic*, i.e., mean-field and Markov Chains, and *reductionist*, i.e., cellular automata, agent-based models and networks, approaches and discussed examples, benefits and limitations.

This review paves the way to the core of this dissertation, i.e., the application of this background theory to the study of two real systems: the human heart and modern financial markets. In chapter 3, we examine atrial fibrillation, a diffused and life-threatening disease of the electrical conduction system of the heart. This condition turns the planar propagation of electrical impulses across the atrial tissue into a disorganized and rapid activity. In line with the “leit-motif” of this dissertation, we conceive atrial fibrillation as an emerging property of the heart triggered by non-trivial microscopic interactions between a large number of atrial cells and the topology of the hosting tissue. Within this paradigm, we tackle open questions in atrial fibrillation research by modelling the dynamics of this disease through cellular automata and mean-field models. These simple and computationally efficient models allow us to perform extended simulations of the electrical propagation over the atrial tissue and, ultimately, to provide relevant contributions to three specific areas of atrial fibrillation research: i) the progression from paroxysmal to persistent atrial fibrillation, ii) the mechanisms through which the gap junction enhancer drug Rotigaptide terminates atrial fibrillation and iii) the enduring dispute on the driving mechanisms of atrial fibrillation.

In chapter 4, we investigate financial markets. In this environment, a large number of heterogeneous agents, e.g., humans vs. computers, adopting different behaviors, e.g., trend-following vs. contrarian, exchange a broad spectrum of financial instruments, such as stocks, bonds and currencies. The iterated, non-trivial interactions occurring in the microscopic dimension of

these systems drive the evolution of the prices and determine many other macroscopic facts that can be observed in financial time series. In this thesis, we present two works which examined two distinct problems: i) the microscopic origins of the widely documented cross-correlations among currency price fluctuations and ii) the relationships between priced dynamics, market liquidity and supply/demand imbalances in modern electronic stock markets.

Chapter 3

Cardiac fibrillation as an emergent phenomenon

In this chapter we examine the emergence of cardiac fibrillation in the human heart. This pathology is a cardiac arrhythmia, i.e., a dysfunction in the electrical properties of the heart, which may affect the upper chambers, i.e., atrial fibrillation, and/or the lower chambers, i.e., ventricular fibrillation, of the cardiac muscle. In an atrial fibrillation episode the healthy planar propagation of electrical stimuli from the sinoatrial node is superseded by fast and disordered electrical waves meandering in the atria [172]. Scientists and clinicians have been investigating atrial fibrillation for more than a century without reaching a complete and unequivocal understanding of the mechanisms that govern its onset and maintenance [172, 173, 174, 175, 176, 33]. Therefore, it is not surprising that this area of research is theater of important controversies and that surgical treatments have so far delivered unsatisfactory outcomes [28].

My research group, headed by Prof. Kim Christensen, is part of the ElectroCardioMaths program at Imperial College London; a cross-faculty team whose purpose is to address open problems in the field of cardiac arrhythmias through research collaborations involving clinicians, physicists and biologists. We study the onset and maintenance of atrial fibrillation by developing simple, yet effective physical models in which we conceive this disease as an emergent phenomena involving the entire system of interest, i.e., the atrium. Atrial fibrillation emerges from non-trivial events occurring at a microstructural level where electrical impulses originating in specific regions of the heart propagate through fibers of connected cardiac cells. As individuals age, the microstructure of the atrium undergoes topological changes which, together

with alterations in the conduction properties of cardiac cells, plays a role in the emergence of arrhythmic conditions. These settings allow us to conceptualize the atrium as a complex system where the interplay between microscopic agents, i.e., cardiac cells, and the underlying topology, i.e., the connections between cells, give rise to unforeseeable emergent phenomena. The first milestone was achieved in 2015 when Prof. Kim Christensen, Dr. Kishan Manani and Prof. Nicholas S. Peters jointly developed a cellular automata model of atrial fibrillation [25]. In spite of its extreme simplicity, the model illustrates how decoupling of muscle fibers driven by fibrosis or other mechanisms might create the ideal settings for the emergence of atrial fibrillation. The Christensen-Manani-Peters model offered the ElectroCardioMaths group a new pathway for the investigation of atrial fibrillation through complexity science approaches. One of the main goal of my doctoral studies was to explore this avenue in order to investigate specific open questions through the development of novel modelling frameworks inspired by Christensen-Manani-Peters model. The results of this effort are presented in detail in the following sections.

This chapter is organized as follows. Section 3.1 presents the structural and functional aspects of the heart at both the macroscopic and microscopic dimensions. Section 3.2 introduces the anatomy of the electrical conduction system of the heart and important aspects of the electrophysiology of cardiac cells. Section 3.3 discusses an important family of diseases of the electrical conduction system of the heart known as arrhythmias. Particular emphasis is given to atrial fibrillation, the afore discussed arrhythmia which has been at the core of my research throughout my doctoral studies. Section 3.4 surveys the major modelling approaches in AF literature and provides a detailed presentation of the Christensen-Manani-Peters model. Section 3.5 presents a recent paper [20] in which we explore the transition from paroxysmal, i.e., intermittent and short episodes, to persistent, i.e., uninterrupted and long episodes, atrial fibrillation in the Christensen-Manani-Peters model. Section 3.6 is devoted to newly completed research project [26] in which we introduce another cellular automata model whose aim is to gather insights on how the gap-junction enhancer drug Rotigaptide may terminate fibrillation. Finally, section 3.7 discusses another article [28] in which we extend the original Christensen-Manani-Peters model to a tri-dimensional topology in order to reproduce and examine in an insilico framework recent clinical evidences [29] which could potentially reconcile some antagonistic theories on the mechanisms of AF maintenance [32].

Note

This chapter includes text and images that have been extracted, with any eventual alteration and extension, from articles I have co-authored [20], [26] and [28]. This material appears in the following subsections:

- 3.3.3 (from [28] and [20])
- 3.3.5 (from [20])
- 3.4.2 (from [20])
- 3.5 and related subsections. (from [20])
- 3.6 and related subsections. (from [26])
- 3.7 and related subsections. (from [28])

Details on copyrights, permissions and personal contributions to [20], [26] and [28] are reported in appendices B.1, B.2 and B.3, respectively.

3.1 The human heart

3.1.1 Structural and functional aspects

The human heart is a muscle residing in the protective thorax; behind the costal cartilages and the sternum; and enveloped in a bilayered membrane known as *pericardium* [177]. Its main purpose is to accumulate blood from various tissues across the body to pump it into the lungs and vice-versa [177].

The heart walls, see Fig. 3.1, include three layers:

- The outer layer, known as *epicardium* or *visceral pericardium*, corresponds to the innermost layer of the pericardium - the enveloping bilayered membrane surrounding the heart [177].
- The middle layer, known as *myocardium*, is made of contracting muscular tissues [177]. These tissues consist of cells, known as myocytes, which display a branching structure, bond through gap junctions and possess an unique nucleus [177].

- The inner layer, known as *endocardium*, consists of *endothelial* cells and covers the heart chambers and valves [177].

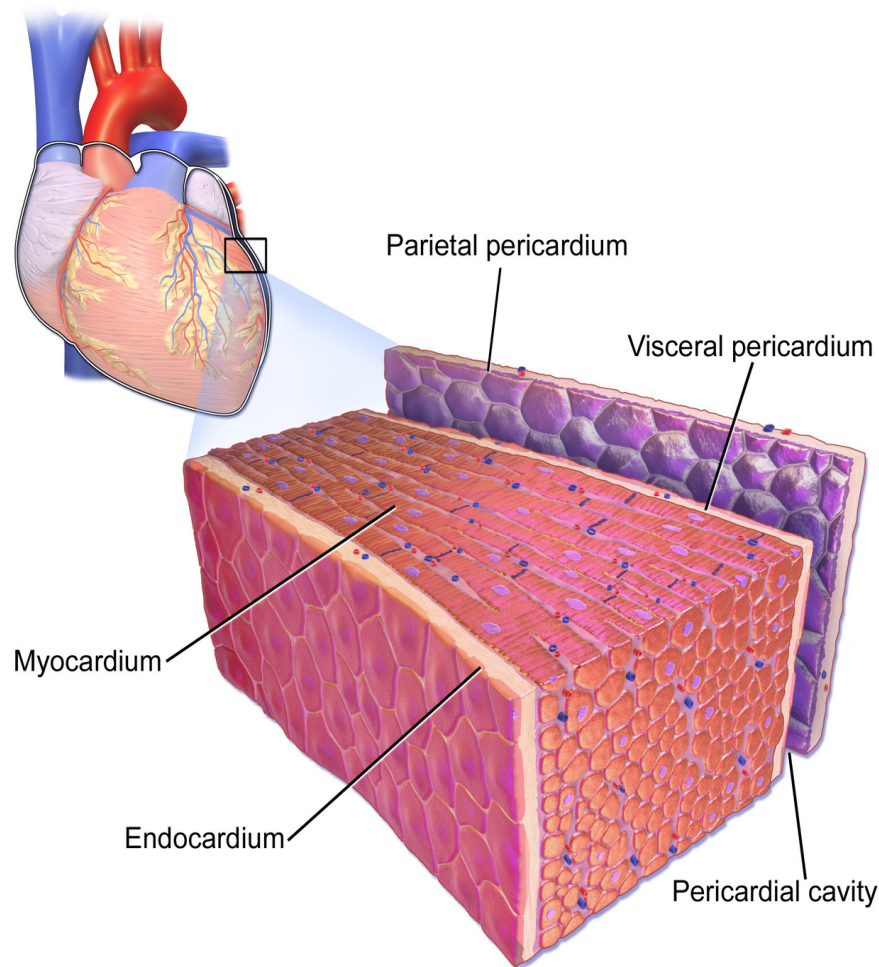


Figure 3.1: **Schematics of the heart wall.** The heart wall includes an outer layer known as epicardium or visceral pericardium, a middle layer known as myocardium and an inner layer known as endocardium. See appendix A for details about attributions and permissions.

The inner structure of the heart, see Fig. 3.2, presents four chambers [177]. The inferior chambers, known as *ventricles*, act as blood pumpers while the superior chambers, known as *atria*, function as blood collectors [177]. The right atrium gathers oxygen-poor blood from the superior and inferior venae cavae (SVC and IVC henceforth) which serve as channels for blood returning from upper and lower body tissues, respectively [177]. The oxygen-poor blood flows to the right ventricle where it is pumped to the lungs through the pulmonary trunk; an artery that branches before entering the lungs [177]. In the lungs blood increases its oxygen levels and expels carbon dioxide [177]. Oxygen-enriched blood travels back to the heart through the left and right pulmonary veins (PVs henceforth); two vessels which further branches before

approaching the left atrium [177]. Finally, oxygen-rich blood flows from the left atrium to the left ventricle where it exits the heart and enters the aortic artery; a key vessel through which oxygenated blood reaches tissues across the body [177].

This unidirectional flow is preserved by four valves: i-ii) the atrioventricular valves, known as *bicuspid* and *tricuspid*, which ensure that blood circulates from atria to ventricles and not vice-versa and iii-iv) the semilunar valves, known as *semilunar* and *pulmonary*, which ensure that blood leaves the ventricles to enter the great arteries and not vice-versa [177].

Interestingly, heart tissues receive only a small fraction of the required levels of nutrients and oxygen from the blood flow that enters and leaves this muscle during its primary pumping function [177]. An adequate supply is instead guaranteed by a specific vascular system whose sole goal is the provision of nourishment to heart tissues [177]. The afore discussed blood flow is governed by the interplay between contractions and relaxations of the myocardial tissue [178]. In particular, atrial contractions pump blood gathered in the atrial chambers into the ventricles while ventricular contractions pump blood from the cardiac bundle to the pulmonary artery or the aorta [178]. These myocardial contractions, known as *systoles* (associated with the systolic blood pressure), are triggered by a special apparatus of cardiac cells that is responsible for the periodic generation and ordered propagation of electrical stimuli across the myocardium [178], see section 3.2 for a detailed review. Contractions are followed by relaxations, known as *diastoles* (associated with the diastolic blood pressure), in which chambers are refilled with blood [178]. The full sequence of atrial and ventricular systole and diastole is known as *cardiac cycle*, i.e., the succession of events that make a single heart beat [178].

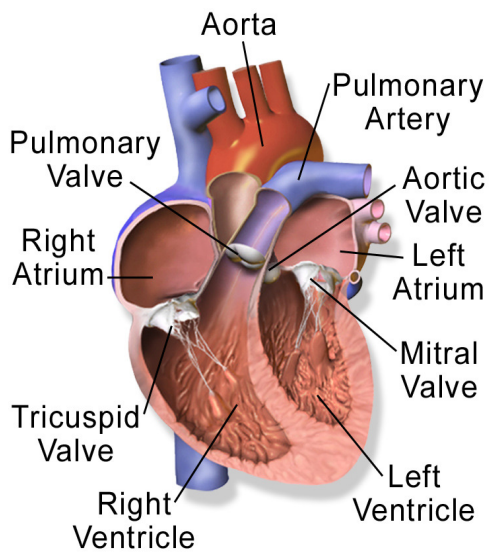
3.1.2 Microstructural aspects

Around three quarters of the myocardial tissue volume is inhabited by cells known as *cardiomyocytes*¹ [179, 180]. However, the total number of cardiomyocytes only make up approximately 30 - 40 % of the cells across the myocardium while the other 60 - 70% consists of multiple types of non-cardiomyocytes cells, primarily *fibroblasts* [179, 180].

Cardiomyocytes, whose primary tasks are electrical conduction and contraction, present a tubular shape with average diameter spanning between 10-20 μm and average length spanning between 50-100 μm [181], see Fig. 3.3. These cells are enveloped in a membrane, the *sarcolemma*, possess an unique nucleus and are filled with mitochondria which are responsible for the ade-

¹Note that in this dissertation we use the terms *cardiomyocyte*, *myocyte* and *cardiac cells* interchangeably.

(a)



(b)

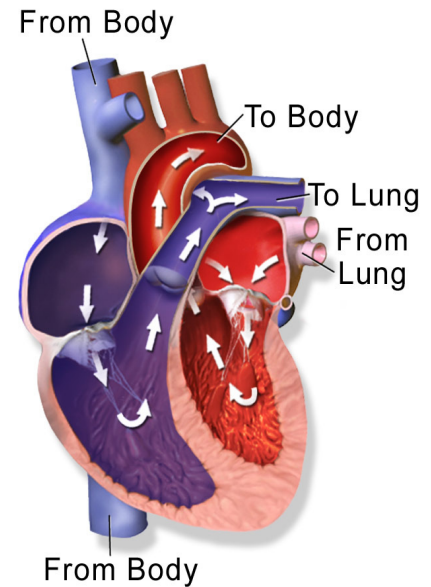


Figure 3.2: **Anatomy and blood flow of the human heart.** (a) Internal anatomy of the human heart. The image highlights the four chambers, the key vessels, i.e., arteries and veins, and the valves that preserve the unidirectional blood flow. (b) Blood flow in the human heart. The white arrows drive the blood flows across the various regions of the muscle. The color of the areas indicates whether the flowing blood is oxygen-poor (blue) or oxygen rich (red). See appendix A for details about attributions and permissions.

quate provision of ATP that these specialized cells need to perform their tasks [177, 182]. A myocyte is made of bundles of *myofibrilis*; long tubular structures composed of adjacent, non-overlapping units known as *sarcomeres* [183]. Sarcomeres are made of thick filaments of myosin proteins and thin filaments actin proteins, known as *myofilaments*, whose peculiar arrangement confers a striated look under the microscope [183].

The sarcolemma includes peculiar pathways, known as *ion channels*, through which ion currents enter and leave the myocyte [184]. The coordinated opening and closing of ion channels plays a key role in the propagation of electrical impulses across the heart. In particular, the inflow and outflow of ion currents through these pathways induce rapid variations in the membrane potential which are commonly known as action potential [184]. Action potential is transmitted to adjacent myocytes through gap junctions; dedicated channels through which flows of ionic currents transfer to neighboring cells [185]. Gap junctions are contained in the *intercalated*

discs; connective structures located in the edging regions of myocytes [186].

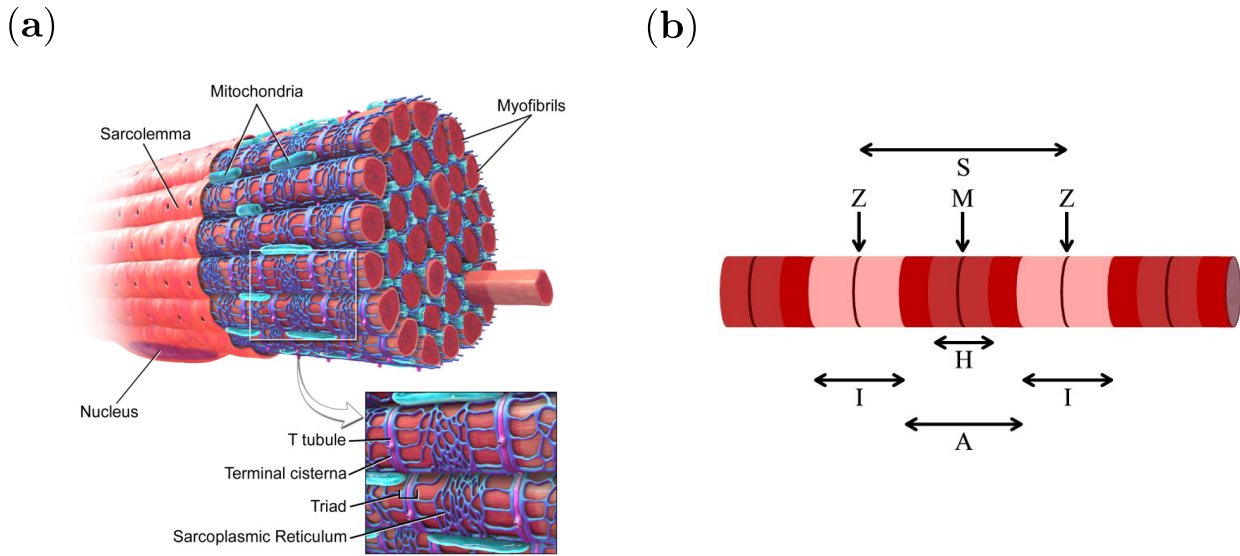


Figure 3.3: **The anatomy of a myocyte.** (a) Schematic close-up of a myocyte. We observe a single nucleus, the diffuse presence of mitochondria and the typical tubular structure resulting from adjacent bundles of myofibrils. (b) Schematic close-up of a section of a myofibrilis. We observe a sarcomere (S), its center (M), known as *m-line*, and its edges (Z), known as *z-lines*, a myosin-only filament (H), actin-only filaments (I) and a myosin region (A). See appendix A for details about attributions and permissions.

3.2 Cardiac conduction system and electrophysiology of cardiomyocytes

3.2.1 Anatomy

In the previous sections we have learnt that a healthy heart continuously pumps oxygen-poor blood towards the lungs and oxygen-rich blood towards several tissues across the body. To perform this pivotal function, the cardiac muscle sequentially contracts and relaxes. These myocardial contractions are triggered by the ordered, periodic propagation of electrical impulses which progressively excites the cardiomyocytes that form this layer of the heart wall. This section is devoted to the examination of these electrophysiological aspects.

The cardiac conduction system (CCS henceforth) is a network of specialized cells that are responsible for the creation and conduction of the electrical stimulus required by the heart

to perform its key pumping function [187], see Fig. 3.4. A well functioning CCS triggers approximately 72 heartbeats/minute, 100000 heartbeats/day, 38 millions heartbeats/year, 2.4 billions heartbeats throughout an average human lifespan [187]. The CCS includes five major elements:

1. The sinus-atrial node (SAN henceforth).
2. The atrio-ventricular node (AVN henceforth).
3. The His bundle.
4. The left and right branches.
5. The distal Purkinje fibres.

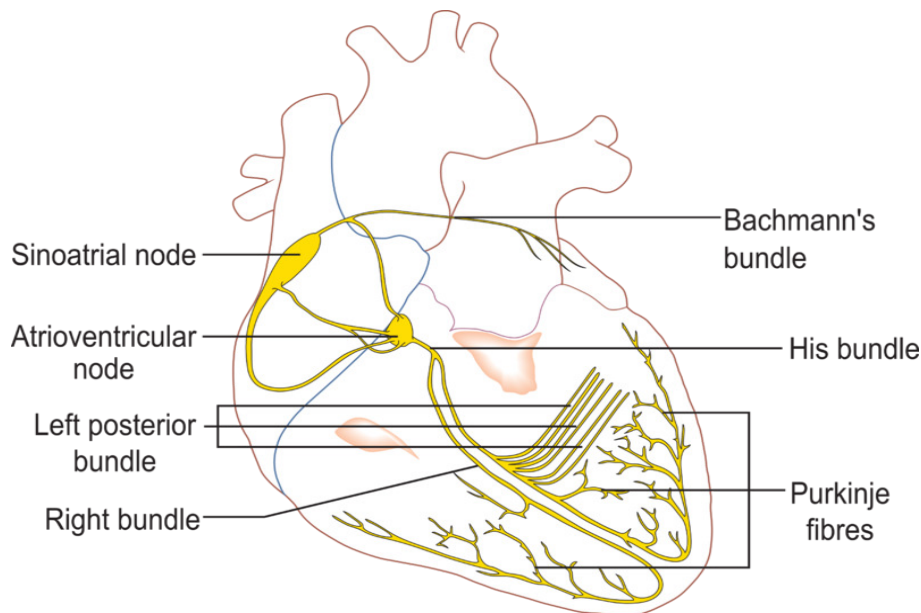


Figure 3.4: **Cardiac conduction system.** The yellow regions highlight the network of cardiac cells that are responsible for the conduction of electrical stimuli that are periodically released from the SAN. In a healthy heart, impulses orderly proceed from top-left, i.e., SAN, to bottom-right before branching left and right to reach the terminals of the Purkinje fibres. See appendix A for details about attributions and permissions.

Electrical impulses are released from the SAN which lie at the intersection between the right atrial chamber and the SVC [187]. The impulse then proceeds through the myocardium, triggering a rapid, sequential activation of myocytes which results in a simultaneous contraction of

both the right and left atrial chambers [187]. At this point, the electrical impulse approaches the AVN which serves as connector between the atrial and the ventricular sections of the CCS [187]. The AVN, slowing down the rapid progression of the impulse, gives enough time to the contracting upper chambers to pump the gathered blood into the ventricles [187]. Then, the electrical impulse regains pace and spread across the ventricular myocardium through the His bundle, the left and right branches and the distal Purkinje fibres [187]. These three elements of the CCS, forming the His-Purkinje system, are responsible for ventricular contraction, inter-ventricular coordination and intra-ventricular coordination [187].

3.2.2 Action potential

Taking a more microscopic perspective on the CCS, we now discuss how electrical impulses propagate from cell to cell. Adjacent myocytes require a *structural* connection which allow the electrical impulse to transfer from a cell to another. This role is played by the gap junctions described in section 3.1.2. Ionic currents originating in pacemaker regions, i.e., areas in which cells are capable of triggering electrical impulses without external stimuli, travel through gap junctions and activate other myocytes by altering their membrane potential.

The potential of a cellular membrane is the differential between its internal and external electric potential. Rapid and periodic changes in cells potential, known as *action potential* (AP henceforth), see Fig. 3.5, are triggered by consequent activations and deactivations of ionic currents across the cellular membrane [188, 189]. The AP of cardiac cells is mainly driven by Na^+ , Ca^{2+} and K^+ currents and follows a five stages cycle [188, 189]. The initiation of the AP cycle is preceded by the terminal phase of the previous one. In this scenario, known as *phase 4* of the AP cycle, the uneven distribution of ions, i.e., molecules or atoms with an electrical charge stemming from a non-zero difference between the number of electrons and protons, over the cell membrane ensures that resting myocytes preserve a stable negative potential [188]. The resting potential spans between -80mV and -90mV in atrial and ventricular cells, -50mV and -60mV in SAN cells, -60mV and -70mv in AVN cells, -90mV and -95mV in His-Purkinje cells [188].

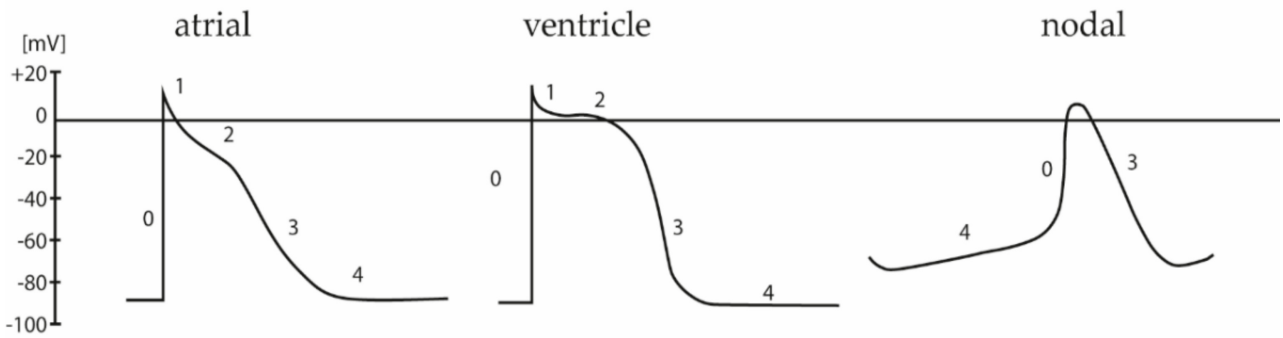


Figure 3.5: **Cardiac action potential cycle.** Simple schematics of the AP patterns in different types of cardiac cells. The diagrams show how the membrane potential (in mV, see y -axis) varies in response to an incoming electrical stimulus. Each segment of the patterns is associated to a number denoting the corresponding phase of the AP cycle. This figure includes images from Fig. 2(a) in [190], see appendix A for details about attributions and permissions.

When an electrical stimulus approaches a cardiomyocyte from a neighboring cell, i.e., through the gap junctions embedded in the intercalated discs, or is automatically initiated, e.g., in the SAN, we observe an increase in the membrane potential [188, 184]. If this membrane potential exceeds a threshold, the AP cycle is triggered [188]. When this occurs, a sudden and large increase in the membrane potential, i.e., an *up-stroke*, depolarizes the cell in what is known as *phase 0* of the AP cycle [188]. In atrial and ventricular cardiomyocytes and in the His-Purkinje fibers this abrupt depolarization is caused by the inflow of Na^+ current through Na^+ channels [188]. Conversely, the depolarization of SAN and AVN cells is primarily due the inflow of Ca^{2+} current through Ca^{2+} channels [188]. This up-stroke is followed by a swift and transitory decrease of the membrane potential towards 0mV [188, 184]. This early repolarization, known as *phase 1* of the AP cycle, is in part driven by a transitory outflow of K^+ current [188, 184]. Next, the decrease of the membrane attains a *plateau*. This segment, known as *phase 2*, is by far the longest phase of the AP cycle, i.e., its duration might be a multiple of 100ms, and is characterized by an overall decline of membrane conductance to the majority of the ions and a consequent equilibrium between polarizing and depolarizing ion currents [188, 184]. Finally, the membrane potential leaves this plateau and undergoes an abrupt and large decline. In this final segment, known as *phase 3* of the AP cycle, a weak inflow of positive charges is exceeded by an increasing outflow of K^+ ions [188]. This imbalance prompts a swift decrease of the membrane potential towards the typical values observed in phase 4, thus completing the repolarization of the cell [188]. Myocytes that have not fully repolarized, i.e., their membrane potential has not

returned to phase 4 levels yet, cannot excite in response of new stimuli coming from adjacent cells. This unresponsive time window is referred to as *refractory period*.

Cells located in different regions of the heart might exhibit different AP patterns and duration [189, 184]. This diversity stems from different expressions levels and/or features of Na^+ , Ca^{2+} and K^+ ionic channels and it is paramount for preserving the healthy, unidirectional diffusion of electrical impulses and the regular pacing of the heart [189].

3.2.3 Assessing the electrical activity of the heart

The electrical activity of the heart can be monitored and assessed through a diffused and non invasive test known as electrocardiogram (ECG henceforth). In this procedure multiple electrodes, i.e., wired sensors connected to a computer, are fixed to the patient’s chest and limbs in order to capture the cardiac electrical activity within a fixed time window [191]. An ECG system displays a “line” that tracks the dynamics of the voltage (y -axis) in time (x -axis) and provides clinicians with the option of including a reference grid in the background which is made of $j \times j$ squares, where j translates into 0.04s into the x -axis [192]. The baseline of an ECG trace is known as *isoelectric line* and represents resting membrane potential [192]. A regular ECG trace presents a sequence of deflections from the isoelectric line which captures the electrical activity in different segments of the impulse propagation across the cardiac muscle [192].

Fig. 3.6 shows the characteristic pattern of an ECG trace. The first deflection, known as *P wave*, traces the progressive depolarization of myocytes lying in the atrial chambers [192]. The inception of this wave is supposed to mark the depolarization of the SAN while the contraction of the atrial chambers is assumed to start at its summit [192]. The P wave is followed by the *QRS complex*, a sequence of “negative-positive-negative” deviations from the isoelectric line which traces the depolarization of myocytes lying in the ventricular chambers [192]. This sequence is followed by the *T wave*, the last deflection in the ECG trace which represents the repolarization of the ventricles [192]. The introductory article of Becker [192] reviews the basic procedures for the assessment of the ECG trace. Assuming that the trace is printed on the afore discussed reference grid, i.e., time vs. voltage, we say that the heart rate is *regular* if the distance between subsequent QRS complexes is constant [192]. When this occurs, the heart

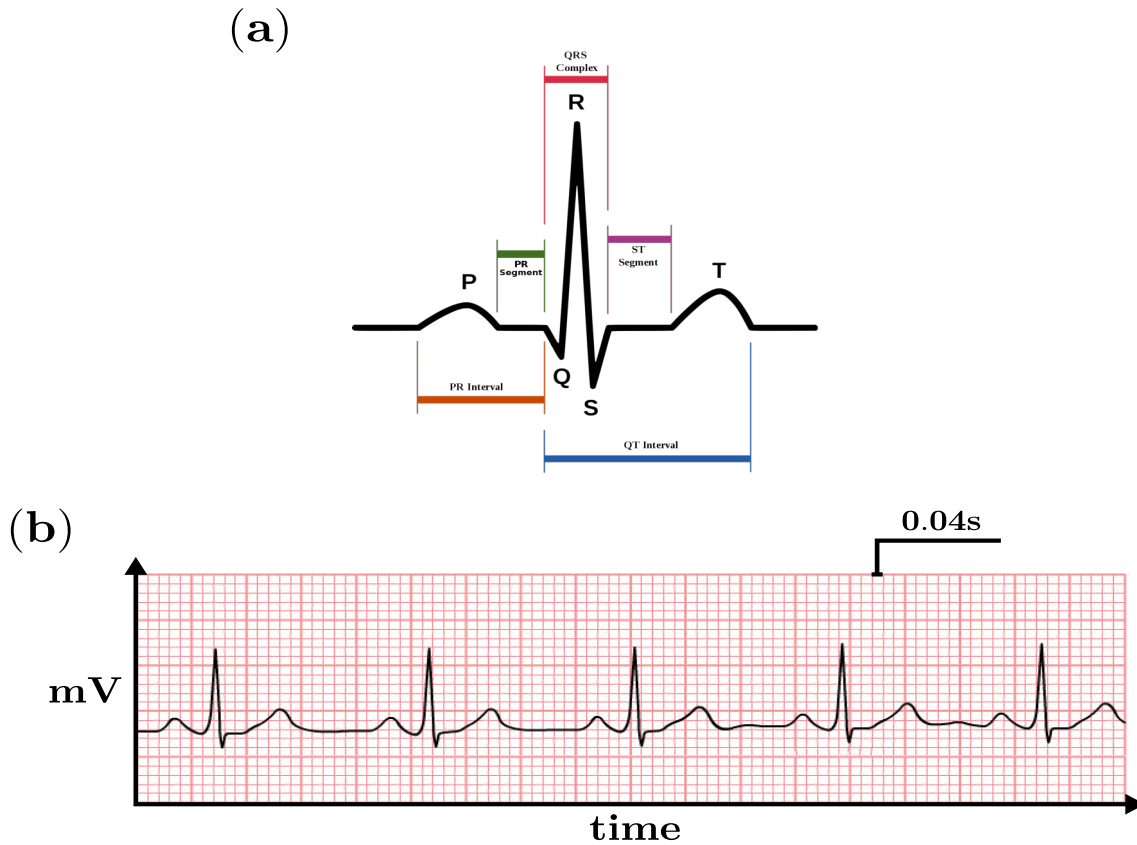


Figure 3.6: **ECG trace.** (a) Simple schematic of the ECG of a single pulse during SR. Deflections from the isoelectric line (black bold line) are denoted by the names of the corresponding waves, i.e., P, Q, R, S and T. Colored segments represent time intervals between different phases of the trace. (b) The ECG trace printed on a reference grid made of $j \times j$ squares, where j translates into 0.04s into the x -axis [192]. See appendix A for details about attributions and permissions for the images appearing in this figure.

rate, i.e., beats per minute, can be inferred by computing

$$\text{heart rate} = \frac{300}{n}, \tag{3.1}$$

where n is the number of large squares between subsequent QRS complexes and 300 is the number of adjacent large squares required to cover 60s in the x -axis [192].

The assessment of the regularity of the heart rate is usually the precursor of a broader analysis of the ECG trace [192]. Some examples of ECG patterns which might reveal anomalies in the CCS of the patient are:

- Heterogeneous or undetectable P waves might indicate that the pacing of the SAN has been overtaken by other regions [192].

- When the PR interval, see Fig. 3.6, exceeds its “usual” length, i.e., from 0.12s to 0.2s, the examiner might suspect a delay in the penetration of the electrical impulse into the ventricular chambers [192].
- When the QRS complex exceeds 0.1s the examiner might suspect *ventricular hypertrophy*, i.e., enlarged ventricular chambers, or that the ventricular region located below the AVN has become the initiator of ventricular depolarization [192].
- When the rate is irregular, the number of successive QRS complexes in 6s time windows might reveal “slower than normal” heart rate, i.e., *bradycardia*, if less than 6 QRS complexes are detected or “faster than normal” heart rate, i.e., *tachycardia*, if the count exceeds 10 [192].

The analysis of the ECG is a common pathway to the detection of ongoing pathologies. Anomalies in the electrical conduction of the heart undermine its correct functioning and might be life threatening for the patient. The following sections provide a detailed overview of one of the most common disease of the CCS, *atrial fibrillation*, introducing the reader to a broad spectrum of aspects of one of the core topic of this dissertation.

3.3 Atrial fibrillation

3.3.1 Introduction

The propagation of electrical impulses discussed in section 3.2.1 is known as *sinus rhythm* (SR henceforth); a term that is generally used to describe a heart in which depolarization periodically originates in the SAN and orderly propagates across the muscle. When this desirable heart rhythm is disrupted the heart is affected by a cardiac disorder known as *arrhythmia*. These anomalies in the heart rhythm might arise in the impulse generating region, i.e., SAN, or in impulse propagating regions, i.e., atria and ventricles [193]. Another common approach to arrhythmias classification is based on the effect that the underlying disease has on the pacing of the heart: variants in which the heart rate declines are known as *bradyarrhythmias* while variants in which the heart rate increases are known as *tachyarrhythmias* [193].

Atrial fibrillation (AF henceforth) is a diffuse cardiac arrhythmia in which the regular propagation of electrical signals from the SAN is disrupted and replaced by fast and disordered

waves of excitation meandering in the atria [172]. The incidence of AF correlates with patients' age; spanning between 0.5% in quinquagenarians and 10% in octogenarians [172]. Available data reveals of a steady increase of the AF incidence in the global population [194]. It is estimated that 2.4% of the British National Health Service (NHS henceforth) budget is devoted to this disease while Americans spend between 16-26 billions \$ every year in AF-related expenses [195, 196, 197, 198]. Existing literature reveal an increasing global incidence of AF [199, 200] which might be jointly driven by aging populations, lifestyle changes and other risk factors [197]. Data presented by Chugh *et al.* shows that estimated age-adjusted incidence of AF (per 100000 individuals a year) increased from 60.7 to 77.5 for men and 43.8 to 59.5 for women between 1990 and 2010 [197]. The number of adult individuals affected by AF in the United States is expected to at least double by 2050 [201, 197]. These dire statistics are accompanied by reports of rising hospitalization [202] and mortality [197] rates.

In healthy individuals the SAN, acting as pacemaker for the electrical impulse, retains a rate that varies between 60 beats per minute in complete rest and 180-200 beats per minute during extreme physical exercise [172]. Conversely, cardiac cells excite between 400 and 600 times per minute when the heart is affected by AF [172]. A person would have died shortly after the onset of AF if this high frequency activity were able to fully transfer to the ventricles [172]. However, the restricting carrying capacity of the AVN forms a "bottleneck" for the incoming, intense electrical stimulus, thus reducing the heart rate to an average of 150 pulses per minute [172].

The compromised atrial contraction induced by AF promotes a sluggish blood flow in the atria which in turn triggers the appearance of clots and thromboemboli [172]. The latter is prone to spread to other organs, e.g., kidneys and brains; increasing the risk of infarction [172]. Thus, it is not surprising that AF plays a primary act in the development of strokes [172]. In particular, AF alone is the first cause of ischaemic strokes in over 75s [203, 172].

AF can be classified as *paroxysmal* when single events self-terminate within a week or *persistent* when events do not self-terminate and survive for more than a week [204]. Eventually, AF becomes *permanent* when it is not possible to undertake any medical action to reinstate SR [204].

3.3.2 Arrhythmogenesis

The mechanisms underlying the onset and maintenance of arrhythmias are classified in two main families: anomalies in the origination of the electrical impulses, i.e., *abnormal automaticity* and *triggered activity*, or disruptions and alterations in the electrical conduction, i.e., *re-entry* [205].

Anomalies in the origination of electrical impulses

Cardiomyocytes that are capable of generating action potential without being stimulated by neighboring cells possess *automaticity* [205]. These periodic “self-excitations” are induced by diastolic depolarizations that are created during phase 4 of the AP cycle [205]. SAN cells exhibit automaticity and have the highest intrinsic firing rate, i.e., the number of excitations per minute [205]. As a result, SAN orchestrates the periodic release of electrical impulses when the heart is in SR while other pacemaking regions with lower firing rates are relegated to a marginal role [205]. Anomalies in automaticity play a primary role in arrhythmogenesis [205]. For instance, *enhanced automaticity* occurs when regions that are not normally capable of unsolicited depolarization, e.g., atrial and ventricular cardiomyocytes, develop this feature [206, 205]. Another anomaly occurs when pacemaker areas that are usually *overdriven* by the SAN, i.e., their generative activity is nullified by the higher frequency impulses originating from the SAN, cannot be reached by SAN-emitted impulses due to structural alterations of the cardiac tissue [205]. These alterations, which often arise after infarct or ischaemia episodes, fail to contain the propagation of electrical stimuli originating from these normally overdriven areas, thus, an healthy SR is disturbed by the presence of additional stimuli [205]. This phenomenon is known as *parasystole* [205].

After-depolarization (AD henceforth) is another anomaly in the origination of electrical impulses characterized by an additional depolarization occurring during or immediately after the regular AP cycle of a cardiomyocyte [205]. Early after-depolarization (EAD henceforth) delays or even halt the gradual repolarization that takes place during phases 2 and 3 of AP cycle [205], see Fig. 3.7 (a). Delayed after-depolarization (DAD henceforth) takes place in phase 4 of the AP cycle, i.e., when the myocyte exits the refractory period that followed a previous excitation [205], see Fig. 3.7 (b). Both EAD and DAD, creating positive changes in the membrane potential, might hit the threshold level that initiates the regular AP cycle, thus triggering an additional activity [205]. When this occurs, an *internally solicited* AP, i.e., the cell fires again without

being stimulated by neighboring cells, is initiated and the propagation of this additional AP results in a contraction of the cardiac muscle that is not induced by regular SR [205].

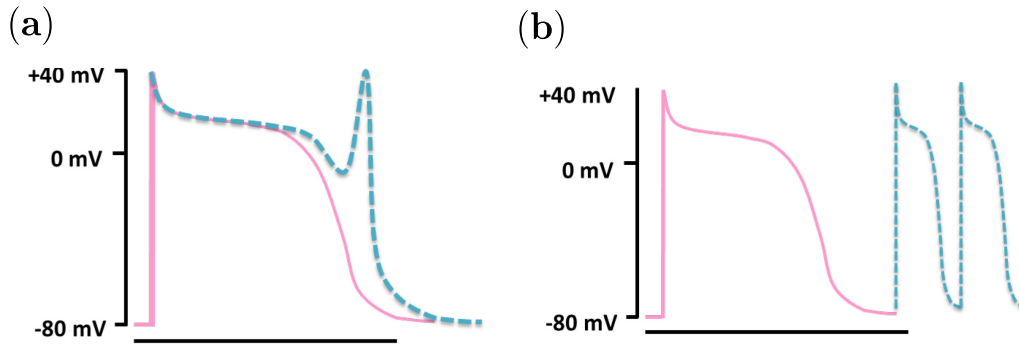


Figure 3.7: **Schematics of after-depolarizations.** The two panels show a stylized regular AP cycle (pink lines) and typical alterations of this pattern (blue lines). These alterations are triggered by a disorder known as *after-depolarization*, that is, the generation of additional positive shifts in the membrane potential right after the excitation of a cardiomyocyte. These variations might excite the cell again without any additional stimulation from the neighboring cells. After-depolarizations occurring in phases 2 and 3 of the AP cycle are known as *early after-depolarizations*, see panel (a), while after-depolarizations occurring in phase 4 of the AP cycle are known as *delayed after-depolarizations*, see panel (b). This figure includes images from Fig. 3(a)-(b) in [207], see appendix A for details about attributions and permissions.

Re-entry

Re-entry driven arrhythmias emerge when an active wavefront, i.e., an heading excited cell and a *tail* of refractory cells, travels around an anatomical or functional obstacle to periodically re-trigger the same region; forming a circuital activity known as *re-entry circuit* [205].

The concept of re-entry circuits developing around an anatomical obstacle, e.g., a scar, fibrosis or a peculiar component of the cardiac bundle such as the PV, was first proposed in [208] over 100 years ago, see Fig. 3.8. The authors observed the formation of circuital activity while performing experiments on different animal tissues but fell short from hypothesizing the arrhythmogenic properties of these motions [205]. Few years later, the works of Mines [209, 210] corroborated the findings of [208] and identified re-entry circuits as a plausible mechanism of arrhythmias [205]. These early works pinpointed the structural requirements for the formation and maintenance of re-entrant activities:

- The presence of an unidirectional block that forces the circuital motion of the wave of excitation to proceed in one direction [205].
- The spatially fixed pattern hosting the circuital motion must be long enough to ensure that cardiomyocytes complete their repolarization before they are reached by the next wavefront [205]. This condition is necessary to avoid a collision between the head and the tail of the wavefront, i.e., the excited cell heading the wave cannot trigger its refractory neighbor that is still repolarizing from the last excitation, that will immediately terminate the activity.

From these observations we can clearly observe that the maintenance of re-entry activities results from the interplay between pathway length, conduction velocity and refractory period [205]. Loosely, an anatomical re-entry can be sustained if

$$L_{\text{path}} \geq v \times \tau, \quad (3.2)$$

where L_{path} is the length of underlying, spatially fixed path, v is the conduction velocity and τ is the duration of the AP [205, 211]. The right hand side of Eq. (3.2) is often referred to as the cardiac wavelength $\lambda = v \times \tau$ [211].

When a re-entry is established, myocytes that form the hosting region are cyclically activated by a wave of excitation that permanently revolves within a spatially fixed pathways [172]. This event disrupts regular SR and promotes non-planar electrical conduction across the cardiac muscle. Arrhythmias can be either driven by a single, dominant re-entry circuit or by multiple coexisting circuits occupying different regions of the muscle [172]. The groundbreaking works of Mayer and Mines were accompanied by other seminal research, see [212], that advanced the hypothesis that the formation of circuital activities might occur without the necessary presence of anatomical obstacles [205]. In this case, a functional obstacle, such as a localized “patch” of refractory tissue, forces the wave of excitation into an iterated circuital progression around it. This assertion was later corroborated by empirical evidences gathered by Allesie *et al.* [213, 214] who artificially induced tachycardia, i.e., an important form of arrhythmia, in rabbit left atrium by releasing premature additional stimuli, i.e., immediately after the refractory period of the most recent beat, from the central region of the tissue [205]. These premature stimuli initiated circular motions that were preserved throughout the tachycardia episode; showing that re-entry circuits may emerge in the absence of anatomical obstacles

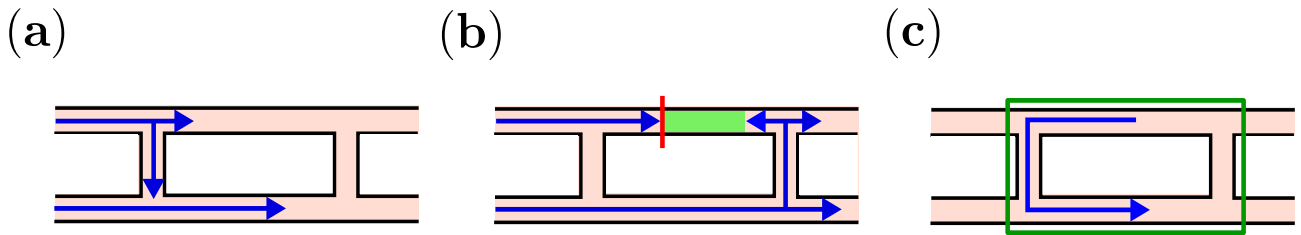


Figure 3.8: **Schematics of the formation of an anatomical re-entry.** (a) The electrical stimulus (blue arrows) propagates from left to right through two adjacent and sporadically connected fibers. (b) The electrical wave propagating in the upper fiber is terminated by a unidirectional conduction block (red line), e.g., a cardiomyocyte fails to excite, therefore the stimulus can only proceed in the branch that is not affected by the block. This event allows the stimulus to leak back in the obstructed fiber from below; opening a new pathway that was not accessible during regular conduction. If the length of this pathway (green highlighted segment) exceeds the cardiac wavelength, see Eq. (3.2), the head of the re-entering stimulus will not collide with cells that are still repolarizing from the last excitation that preceded the conduction block. This allows to establish a re-entry circuit that is anchored to the stylized triangular structure portrayed in panel (c).

and drive arrhythmias even in local regions of the cardiac muscle [213]. These observations culminated into a theory known as *leading circle*. In this framework, a unidirectional block triggers a circuitual motion of the electrical stimulus which in turn creates centripetal and centrifugal waves during its rotations [215]. Centripetal waves of excitation collide in a core central region, thus creating a refractory area which acts as a functional obstacle for the revolving wave [215]. At the same time, centrifugal waves propagate across the tissue and annihilate any other circuitual activity anchored to larger circles, i.e., waves emitted by smaller circles are faster [215]. Therefore, the term *leading* is used to highlight the fact that the smallest ongoing circle inevitably dominates all the other circles, thus establishing itself as the sole driver of the AF episode [215]. In line with the basic mechanisms of the anatomical re-entry, the leading circle theory assumes that the “dimension” of a circle must be larger than or equal to the cardiac wavelength, see Eq. (3.2), to avoid self-termination induced by wavefront-wavetail collisions [215].

3.3.3 Mechanisms of atrial fibrillation

Scientists and clinicians have been investigating AF for more than a century without reaching a complete and unequivocal understanding of the mechanisms that govern its onset and maintenance [172, 173, 174, 175, 176, 33]. In this context, it is not surprising that AF research has been theater of several debates and controversies. The most prominent argument is on whether AF is preserved by local, spatially fixed springs of fibrillatory impulses or whether AF preserves itself through the iterated collisions of electrical stimuli drifting across the atria [173, 175, 33]. The first predominant theory of AF was the *multiple wavelets hypothesis* introduced by Moe *et al.* in 1964 [216]. The authors developed an in-silico discrete model of the atria and simulated the propagation of electrical signals through the mimicked tissue. Computer-based simulations shown that waves of excitation survive and randomly meander across the model grid even after ceasing the artificial release of new stimuli [216]. These waves are “*turbulent*” as they progressively fragment into multiple irregular activities that the authors compared to real AF dynamics [216]. In line with empirical observations, the model shown that extending the refractory period of the in-silico cardiac cells gradually terminates the ongoing self-sustaining activity [216]. The cornerstone of this theory, i.e., AF can be maintained by self-sustaining meandering wavelets that are not anchored to any specific region, has found supporting evidences in more recent works [217, 218].

In the 90’s multiple works from Haissaguerre *et al.* [219, 220, 221] recognized that AF tends to be triggered by a focal source and that these sources are often located in the *myocardial sleeves* of the PV, a region that in spite of not being part of the cardiac bulk is reached by myocardial tissues of the left atrium [222]. These findings have been corroborated in various subsequent works, hence, the key role played by the PV in the onset of AF is to these days a widely accepted fact [222]. In spite of these important progresses in understanding the genesis of AF, the nature of the mechanisms governing the maintenance of this diffused arrhythmia remains one of the most controversial and debated topic in the entire field, see Fig. 3.9. There are two conflicting theories arguing on whether AF is driven and sustained by local (spatially fixed) sources of new fibrillatory waves, or whether AF is self-sustaining from the interaction and fragmentation of multiple meandering electrical wavelets in the atria [173, 175, 33]. Although this dispute is yet to be resolved, recent evidence appears to strengthen the case for local drivers as the primary mechanism of AF [223, 224, 225, 226, 227, 29, 30, 31, 174, 228, 229]. However, there is debate about the mechanistic origin of local drivers: Some studies have identified the drivers as

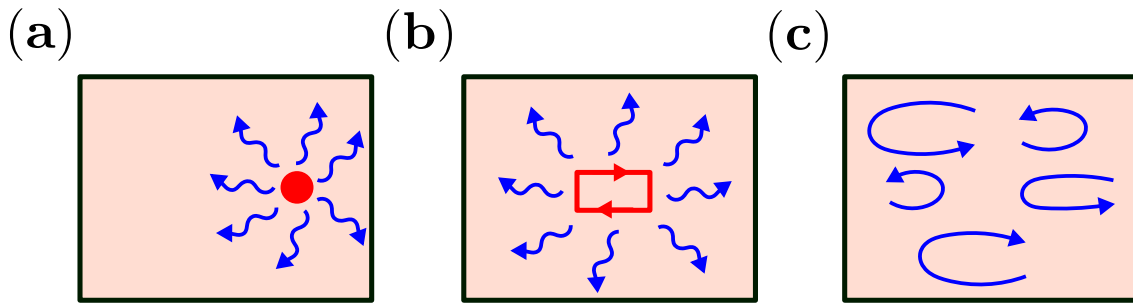


Figure 3.9: **Classic theories of the mechanisms of AF.** (a) AF (blue waves) is driven by an *ectopic focus* (red circle), i.e., a region of cardiomyocytes outside the SAN which exhibit automaticity. (b) AF is driven by a single spatially fixed re-entry circuit (red box). (c) AF is driven by multiple wavelets (blue waves) meandering across the atria.

rotors [225, 226], whereas others have identified the drivers as focal points [224]. The concepts of *rotor* and rotor-induced *spiral waves*, see Fig. 3.10, were introduced in [230, 231] and have been increasingly used since then to describe a driver of fibrillation whose spinning activity triggers curved vortices [232]. Although a rotor shares some commonalities with the *leading circle* of Alessie *et al.* [213, 214], i.e., lack of anatomical obstacles and the absence excitable cells between the front and the tail of the wave, there are multiple features that set this modern concept of AF driver apart from the classic definitions of anatomical and functional re-entry:

- The theory of rotors emphasizes the relationship between wavefront curvature and conduction velocity [232]. In particular, concave wavefronts progress faster than planar wavefronts, which are in turn faster than convex wavefronts [232].
- The core region of a rotor is an excitable tissue but the convex curvature of the wavefront in this area is so pronounced, i.e., it exceeds a critical threshold, to “block” the stimulus from entering it [232]. The absence of a refractory core region, which is indeed present in both anatomical and functional re-entry, allows rotors to wander, i.e., its position might change in time [232].
- The wavelength, i.e., the distance between wavefront and wavetail, changes with the distance from the rotor [232].

Another important contribution to the debate on the mechanisms of AF came from a recent work of Hansen *et al.* [29]. This article, which was later dubbed “*an intriguing study with*

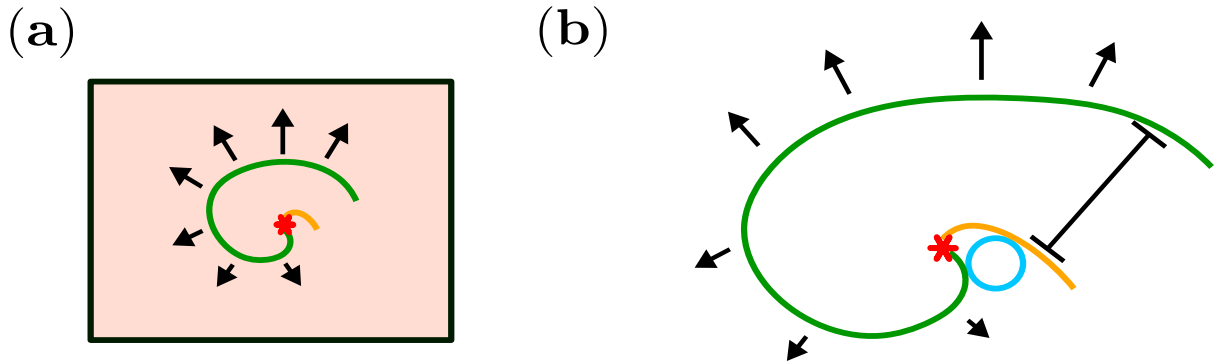


Figure 3.10: **Schematics of a rotor.** (a) Spiral waves around a rotor (red “*” symbol) driving AF in a fictional region of the atria (underlying background). (b) Anatomy of a rotor. We observe a wavefront (green line) of excited cardiomyocytes and a wavetail (orange line) of refractory cardiomyocytes [232]. The distance between wavefront and wavetail is known as *wavelength* (black segment) and the length of black arrows departing from the wavefront is proportional to the conduction velocity of the electrical stimulus [232]. The rotor is indicated by the black “*” symbol and is the “meeting point” of the wavefront and wavetail [232]. This point is known as *phase singularity* while the excitable, yet impenetrable tissue at the center of the rotor (cyan circle) is known as *core region* [232]. Note the relationships between the curvature of the wave and the conduction velocity: the closer we get to the rotor, the more curved becomes the wave, the lower the conduction velocity [232].

the potential to unify some of the previous discrepant observations” [32], has suggested that both focal and re-entrant drivers may be explained by the presence of small re-entrant circuits [29, 33]. Using high-resolution simultaneous optical mapping of the endocardium (inner heart wall) and epicardium (outer heart wall) in explanted, diseased human hearts, the study shows that stable transmural re-entrant circuits may project differently onto the endo and epicardium. Projections typically appear as rotational activity on the endocardium and focal (breakthrough) points on the epicardium. Hence, the apparently incompatible 2d projections onto the atrial walls are consistent with a single underlying mechanism of localised re-entrant circuits in the transmural region [29, 30, 31].

Questions concerning the underlying mechanism of AF are of particular importance because they inform potential treatment strategies. Historically, treatment for AF has focused on mitigating potential symptoms and lowering the risk of stroke through the use of rate control, and anti-arrhythmic drugs [233]. However, these treatments do not “cure” AF. Surgical ablation

strategies have been developed to destroy, or isolate, the regions of atrial muscle thought to be responsible for initiating and sustaining AF [33]. If local drivers are responsible for AF, ablating the focus of these drivers may terminate and prevent AF. If meandering wavelets underlie AF, ablation strategies which minimise the space wavelets can move into may be preferable. To these days, ablation still fails in a large subset of patients and AF re-occurs in many patients who were initially free of AF after surgery. In the next section we examine in details the current trends in the global incidence of AF and the spectrum of treatments that is available to clinicians.

3.3.4 Treatments of atrial fibrillation

In line with other arrhythmias, the standard treatment protocols for AF are the administration of specific drugs and surgical ablations [194]. However, the spectrum of available drugs has been stagnating for more than a decade and the overall outcome of this approach has been so far very poor [194, 234]. Common issues arising during the administration of AF-targeting drugs are diffuse low tolerance, side effects and even increased mortality [235]. In spite of these limitations, antiarrhythmic drugs usually remain the first option to treat both paroxysmal and persistent AF and surgical procedures are eventually made available to those patients that fail to respond to these treatments [235].

Ablations are surgical approaches in which clinicians annihilate the regions of the heart that are thought to be responsible for the ongoing AF. The Cox maze surgery [236] has been the predominant surgical approach until the advent of catheter ablation [237]. The Cox maze surgery is characterized by a trade off between high effectiveness and an extremely demanding procedure in which the patient undergoes an open heart operation [237]. This procedure has been subject to several improvements whose success rates, i.e., fraction of individuals which do not present evident AF symptoms on a given post-surgery window, approached 90% [238, 235]. However, associated risks, technical requirements and high invasiveness overshadowed the effectiveness of this procedure, paving the way for alternative surgical approaches [235]. In the last two decades catheter ablation rapidly rose from an experimental alternative to Cox maze surgery to become the standard surgical approach to AF [239]. This method relies on catheters, i.e., flexible and narrow tubes, reaching the cardiac muscle thanks to a carefully controlled progression through relevant blood vessels [240]. Catheters detect regions that are responsible for the ongoing arrhythmia by tracking the electrical activity of the heart [240]. Finally, surgeons

use the catheters feedback to detect and annihilate the driving regions by either freezing, i.e., cryoablation, heating, i.e., radiofrequency ablation, or lasering them [240]. These actions create scars which obstruct the propagation of electrical impulses through the targeted regions in the hope of halting the ongoing arrhythmic condition [240].

Recent data reveals that the administration of antiarrhythmic drugs exposes $\approx 17\%$ of the patients to significant long term side effect whereas only $\approx 8\%$ of the individuals who underwent catheter ablation suffer similar complications [241, 239]. A recent work of Rottner *et al.* [239], summarizing figures from previous analyses, reports that $\approx 80\%$ of pulmonary vein isolation operations, i.e., the most prominent catheter ablation strategy, on individuals affected by symptomatic paroxysmal AF are successful after 5 years with this number falling around 60% when the follow-up period is extended to 10 years. Furthermore, one quarter of patients affected by persistent AF regain SR after one catheter ablation operation while multiple interventions push the fraction of “cured” patients up to $\approx 68\%$ in a median follow-up window of 7 years [242, 239]. The recent CABANA trial, a study involving more than 2000 patients based in several institutes across the globe, has the declared goal of “*establishing the appropriate roles for medical and ablative intervention for atrial fibrillation (AF)*” [243]. Data from this large experiment does not provide enough statistical evidence to conclude that catheter ablation outperforms antiarrhythmic drugs in diminishing mortality and strokes occurrences, although the adoption of catheter ablations results in significant reductions in hospitalization rates and AF recurrence [244].

The numbers emerging from the afore discussed studies suggest that the current spectrum of AF treatments needs major improvements and additions to combat the ever increasing burden of this disease on our societies. Decent success rates in SR restoration from paroxysmal AF are offset by grim numbers in persistent AF and significant risk of side effects in both drug-based and surgery-based approaches. This picture is clearly entangled to the open controversies that have been at the core of AF research for many decades and, in particular, to the fact we have not reached yet an unequivocal consensus on the driving mechanisms of AF. Further understandings of the genesis and maintenance of AF, technological advancements and the identification of reliable markers for different variants of AF will provide tangible contributions to the effectiveness and safety of existing treatments, the establishment of novel approaches and the correct coupling of patient features and treatment type [245, 246].

3.3.5 Cardiac remodelling and atrial fibrillation

The progression of AF from paroxysmal to persistent is often associated with the idea that “AF begets AF” which was proposed by Wijffels *et al.* [247] in an article published in *Circulation* in 1995. The authors artificially induced an maintained AF in a dozen of goats, recording significant changes in the electrophysiological properties of the subjected hearts. In particular, artificial preservation of AF led to a pronounced reduction of the atrial effective refractory period (AERP henceforth), a weakened adaptation of the AERP to higher heart rates and boosted inducibility and stability [247]. Five out of twelve goats exhibited SR within four weeks from the end of the experiment while the afore discussed electrophysiological variations appeared to be reversible within seven days from the re-establishment of SR [247]. These seminal results provided important evidences in support of the idea that the atria undergo electrophysiological and structural changes which promote the progression of AF. Few years later, Franz *et al.* [248] found that both AF and *atrial flutter*, i.e., another atrial arrhythmia, are responsible for a significant electrical remodelling in the human atria. The authors performed *cardioversion*, i.e., clinical restoration of SR, in 20 chronically diseased human hearts (7 in AF and 13 in atrial flutter), recording a significant shortening of the AP cycle duration in the right atrial chamber even after a substantial time gap from the re-establishment of SR [248]. Another important work from Daoud *et al.* [249] examined the effects of AF on AERP in the human heart. The authors induced AF in 20 human hearts with no recorded structural issues, observing that even a relatively short AF episode, i.e., minutes, can temporarily reduce the AERP for up to ≈ 8 min after the re-establishment of SR [249]. They reported that the propensity to re-induce AF peaks around SR restoration and progressively decreases, together with the lifespan of re-induced AF episodes, as the AERP reverts back to its control values, and used these observations as a basis for an intriguing theory of AF self-maintenance [249]. More recently, Walters *et al.* [250] demonstrated that reversion of left atrium remodelling is associated with catheter ablation of paroxysmal AF, i.e., “early ablation”, while significant continuation of left atrium remodelling is associated with a developing, high-burden AF which is subject of medical management procedures, e.g., administration of anti-arrhythmic drugs. These observations support the idea that early ablation might be essential to prevent the development of “self-reinforcing” AF which might rapidly become persistent and hardly manageable [250].

The accumulation of fibrosis is an important structural development affecting the patient’s susceptibility to AF [251, 252, 253]. Cardiac fibrosis consists in the excessive accumulation

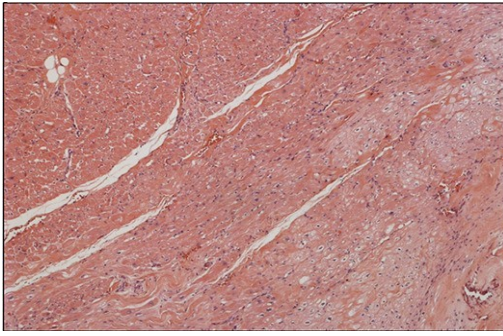
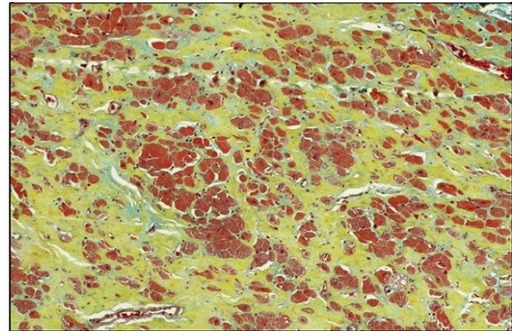
(a)**(b)**

Figure 3.11: **Healthy vs. fibrotic tissue.** Movat-stain, i.e., a contrast enhancing technique, highlighting different tissue types in human ventricle samples. The coloring allows us to detect muscle tissues (red), collagens (yellow) and glycoproteins and proteoglycans (green-blue spectrum) [263]. An healthy tissue is displayed in panel (a) while a fibrotic tissue is displayed in panel (b). Both images have been extracted from the graphical abstract of [263], see appendix A for details about attributions and permissions.

of extracellular matrix proteins, i.e., a network of fibres which serve as a “hosting structure” for cardiac cells, across the myocardium [254, 255], see Fig. 3.11(b). This proliferation can be triggered by different causes, such as acute myocardial infarction, aging, pressure overload induced by hypertension, alcohol consumption, diabetes and obesity [256, 257, 258, 259, 254]. The presence of fibrosis alters the topology of the myocardial tissue and influences the propagation of electrical stimuli by promoting anisotropy and creating both structural and functional obstacles [260, 261, 262]. Therefore, it is not surprising that recent studies [29, 31, 252] have identified the accumulation of fibrosis as a critical factor for the formation of re-entrant circuits that drive AF [29, 31, 252]. For instance, Hansen *et al.* [29] artificially induced AF in 8 *ex-vivo* right human atria and mapped the dynamics of the electrical signals through three high resolution cameras targeting different views, i.e., epicardium, endocardium and panoramic. Among their major findings, the authors observed that AF is driven by *transmural* re-entrant circuits, i.e., cyclical activity progressing through a “*3D micro-anatomic tracks*” [29], hosted by specific regions of the tissue characterized by high accumulation of fibrosis and pronounced differences in transmural fibers angles [29].

3.4 Modelling atrial fibrillation

3.4.1 Overview of common approaches to the modelling of atrial fibrillation

In the previous sections we have acknowledged that the AF landscape is still dominated by major debates, such as the one on the underlying mechanisms of this diffused arrhythmia. Furthermore, we have recognized that the ever increasing burden of AF is not effectively countered by the current spectrum of available treatments as success rates have been hindered by the lack of an unequivocal and comprehensive understanding of this disease. Although we are still far from what could be considered a desirable scenario, it is undeniable that the understanding of AF have been gradually improving for many decades [264]. In a recent survey [264], Trayanova identifies some key drivers of these progresses in the diffusion of multilevel electrophysiological experiments, i.e., from single animal cells to human cardiac tissues, and the ever growing body of models which idealize a broad range of AF-related phenomena. In particular, models of AF have been providing pivotal contributions and support to the formation of AF theories, integration of experimental results within an unified framework and, more recently, to the assessment of therapies and enhancement of patients' management [265, 264].

In this section we follow the aforementioned survey to introduce the major families of AF models that have gradually emerged in the last 70 years.

Models of cellular electrophysiology

These frameworks mimic the inward and outward flows of ionic currents through system of differential equations [264]. The foundations of this approach were set in 1952 by Hodgking and Huxley [266] in an article titled “*A quantitative description of membrane current and its application to conduction and excitation in nerve*”. In this work the authors modelled the electrophysiological properties of the squid giant axon by using differential equations, thus introducing a new modelling paradigm that have been later expanded and modified to examine other excitable tissues. Therefore, it is not surprising that a large fraction of more recent electrophysiological models of cardiac cells build on the Hodgking and Huxley framework [264]. In this group, Trayanova [264] identifies three influential models: i) Nygren *et al.* [267], ii) Courtemanche *et al.* [268] and iii) Grandi *et al.* [269]. These models have been later improved,

see [270, 271], and expanded to examine the “AF begets AF” theory [247], i.e., ongoing AF triggers electrophysiological changes that promote the progress of this disease towards a chronic state [264]. In recent years scientists have introduced electrophysiological models that are not reliant on the Hodgking and Huxley paradigm, see [272, 273], thus opening new pathways that might inspire novel models of AF [264].

Cellular automata models

The CA paradigm presented in section 2.2.5 has been also adopted to model AF. The seminal work of Moe *et al.* [216] introduced a CA model of the electrical propagation across a cardiac tissue. The observations that the authors made on the behaviour of the models set the foundations of the *multiple wavelets hypothesis*, see section 3.3.3. In recent years CA models of AF have recaptured the interest of researchers after decades of decreased popularity [264]. Important works belonging to this “new wave of CA models of AF” are Correa de Sa *et al.* [274], Alonso and Bar [275], Christensen *et al.* [25], Vigmond *et al.* [276] and Makowiec *et al.* [277]. The intrinsic simplicity of CA models of AF prevents any detailed replication the electrophysiological aspects of real cardiomyocytes, thus reducing the clinical relevance of this approach [264, 20]. This limitation is balanced by important benefits, such as computational efficiency and the possibility of performing large scale simulations and robust statistical analyses [264, 20].

Geometric and image-driven models

One recurrent feature of electrophysiological and CA models is the adoption of elementary bi-dimensional topologies to mimic the atrial tissue [264]. On the contrary, geometric models rely on more detailed representations of the atrium which typically comprise peculiar elements of this region, e.g., PV, or adopt more complex tri-dimensional topologies [264].

Trayanova [264] proposes two different classifications of geometric models of AF. The first one splits tri-dimensional models that overlook the role of the width of the wall surrounding the atrium [278, 279] from those that encompass this feature [280, 281]. The second one differentiates models adopting ideal topologies [282, 283, 28] e.g., a cube or a sphere, from those relying on topologies derived from imaging of human and animal hearts [284, 285, 286]. The diffusion of image-based models of the human heart began with early studies [280, 287, 288]

on the atrial geometry dataset² until MRI [290, 285] and computer tomography [291] became the most common channels for the acquisition of atrial images [264]. In recent years image-based models have been also used to study the relationships between persistent AF and fibrotic remodelling [264]. These pioneering frameworks [284, 285] rely on *late gadolinium enhancement* MRI techniques [292] which are capable to image atrial fibrosis [264]. Nonetheless, the scarcity of experimental records and limitations in the image acquisition process are still major hurdles for the establishment of this nascent approach [264].

Models of atrial fibrillation in this dissertation

In this thesis we exclusively focus on CA models of AF. We start from the Christensen *et al.* model of atrial fibrillation [25], a simple bi-dimensional automaton which allows to simulate the propagation of electrical stimuli across a generic tissue. The model is the result of a collaboration between physicists, i.e., Christensen and Manani, and clinicians, i.e., Peters, within the ElectroCardioMaths program at Imperial College London. The authors shown that the atrium can be effectively conceived as a complex systems where interactions between components, i.e., cardiomyocytes, and the topology of the underlying network, i.e., connections between cells, might conspire to undermine SR and establish spatially fixed rotational activities which drive AF. In this setting, AF is an emergent phenomena that cannot be predicted from the mere knowledge of the microstructural components of the model. Section 3.4.2 examines the Christensen *et al.* model [25] in details, thus offering the reader the opportunity to explore an important exponent of the recent revitalization of CA techniques in AF modelling and to contextualize the novelties proposed in this dissertation. This detailed introduction is followed by multiple sections in which we present three originals models of AF that I have co-developed during my doctoral studies at Imperial College London.

3.4.2 The Christensen-Manani-Peters model

Context

The Christensen-Manani-Peters (CMP henceforth) model of AF is a simple percolation based model that investigates how the formation of re-entrant circuits is dependent on the decoupling of neighbouring muscle fibres, through the action of fibrosis or otherwise [25]. In this CAM

²The atrial geometry dataset emerged from the “Visible Human project” [264], see [289] for details.

the atrium is mimicked by a squared lattice in which nodes representing myocytes connect longitudinally and vertically. Periodic planar impulses are released from pacemaker nodes lying on the left edge of the grid and spread by activating adjacent resting nodes. This simple transmission mechanism resembles the propagation of electrical impulses across the atrial tissue. The development of fibrosis can be mimicked by reducing the probability of generating vertical links between neighboring nodes. In particular, preserving a complete horizontal connectivity while decreasing the fraction of vertical connections makes the distribution of node-to-node connections anisotropic, thus capturing a distinctive feature of real cardiac fibrosis [260, 261, 262]. The model is not a fully realistic representation of the atria and it does not consider the precise evolution and propagation of action potentials across the atrial tissue. However, the model effectively demonstrates from basic principles how re-entrant circuits can form if fibrosis accumulates in sufficient quantities in a given local area.

Model definition

The atrial muscle consists of tubiform cells (myocytes) of length $\Delta x' \approx 100\mu\text{m}$ and diameter $\Delta y' = \Delta z' \approx 20\mu\text{m}$ [293, 294]. Myocytes are mainly connected longitudinally, composing discrete fibres that sporadically connect transversally. The CMP model condenses this branching network of anisotropic cells into an $L \times L$ square lattice of nodes [25]. A node represents a single (or multiple) atrial cell(s). Nodes are longitudinally connected to their neighbours with probability $\nu_{\parallel} = 1$ and transversally with probability $0 \leq \nu_{\perp} \leq 1$. This creates long arrangements of nodes, mimicking the protracted, interlaced fibres in the atrium. This simplified representation of the myocardial architecture captures the anisotropic distribution of gap junctions [293]. Furthermore, it reproduces the dynamics of electrical impulses which mainly propagate longitudinally (along single muscle fibres) rather than transversally (across multiple fibres) [295]. A cylindrical topology is obtained by applying open boundary conditions longitudinally and periodic boundary conditions transversally.

Nodes follow a well defined electrical cycle characterized by three different states: resting (a node that can be excited), excited or refractory (after exciting, the node cannot be excited for the next τ time steps). This course mimics the membrane potential of real myocardial cells. At a given time t , an excited node prompts the neighbouring resting nodes to become excited at time $t + 1$. An excited node at time t enters into a refractory state at time $t + 1$. The duration of the refractory period is τ time steps, see Fig. 3.12. In the CMP model, a fraction δ of nodes

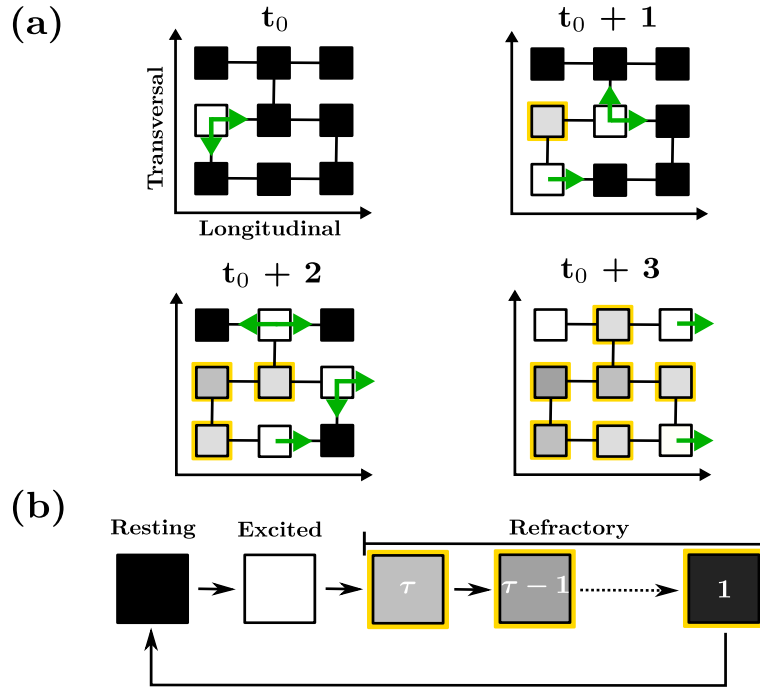


Figure 3.12: **Basic dynamics of the CMP model.** (a) Propagation of the wave of excitation across a small region of the CMP lattice. Nodes are connected longitudinally with probability $\nu_{\parallel} = 1$ and transversally with probability $0 \leq \nu_{\perp} \leq 1$. Excited nodes (white squares) continue the propagation of the wavefront by activating their neighbouring resting nodes (black squares) before entering into a refractory state (grey scale squares with yellow borders) for the next τ time steps. Depending on the architecture of the region, the excitation can proceed forward, backward and across fibres. (b) The full progression of a node through the three states of the electrical cycle: resting (black), excited (white) and refractory (grey scale with yellow borders). This figure has been extracted from [20], see appendix B.1 for details about attributions and permissions.

are susceptible to conduction block. These nodes are identified at the beginning of a simulation and are fixed in space. The probability that nodes that are susceptible to conduction block fail to excite is arbitrarily set to $\epsilon = 0.05$; the effect of varying this parameter is discussed in section 3.4.2. This probability of failure refers to the probability that a node susceptible to conduction block will not excite when prompted to do so by a neighbouring active node. This leaves us with a very simple framework in which the fraction of transversal connections, ν_{\perp} , and the fraction of nodes that are susceptible to conduction block, δ , serve as control parameters. For simplicity, we set $\delta = 0.01$ and examine how the behavior of the system varies with ν_{\perp} . The effect of changing δ is demonstrated in subsection 3.5.4 and has been investigated in [296].

The pacemaker (SAN) is placed on the left side of the 2D sheet and nodes lying on this edge regularly excite every T time steps. The excitation propagates as a planar wavefront, mimicking the coordinated contraction of the real atrial muscle. The parameters of the CMP model reflect clinical observations of real human atrial tissues [297, 298, 29, 299, 293, 294]. Clinical measurements are translated into model parameters, followed by a coarse-graining procedure leading to a square lattice of size $L = 200$ nodes, pacemaker period of $T = 220$ time steps, and refractory period of a node of $\tau = 50$ time steps. A single timestep in the model corresponds to approximately 3ms such that $T = 660$ ms and $\tau = 150$ ms. This refractory period is relatively short and corresponds to what may be seen clinically during burst pacing. The dynamics of the model are maintained under changes of τ , but the transition from SR to AF takes place at a different point in the coupling phase space. The longer (shorter) the refractory period, τ , the smaller (larger) the coupling value, ν_{\perp} , needs to be to induce AF [296].

The CMP model reveals that re-entrant circuits may emerge due to a combination of the electrical signal propagating on the branching structure of a heart muscle network, the three-state dynamics of nodes, and the occurrence of nodes susceptible to unidirectional conduction block. These latter nodes may fail to excite in response to an excited neighbour with small probability ϵ , stopping the regular propagation of the wavefront [25]. The wave of excitation proceeds forwards in the adjacent fibre until it reaches a transversal connection, leaking back through the fibre in which conduction has been previously blocked. For re-entrant circuits to emerge, the segment between the re-entry point and the node that has previously failed to excite must be long enough to prevent the backward propagating wave from being stopped by unresponsive refractory nodes. This happens when the probability of transverse connections decreases, for example, due to fibrosis. In the CMP model the formation of re-entrant circuits triggers AF. These activities survive until the circuitual motion of the wavefront is annihilated by a subsequent conduction block occurring within the path of the circuit (i.e., self-termination) or by other waves spreading from the neighbouring regions, see Fig. 3.13.

Note, in the CMP model nodes are coupled with probability ν_{\perp} across the whole tissue. However, in the real atrium only a small patch of fibrosis may be necessary to decouple fibres and induce a re-entrant circuit. Such small patches of fibrosis may be too small to see using current MRI technologies [300], inhibiting effective treatment.

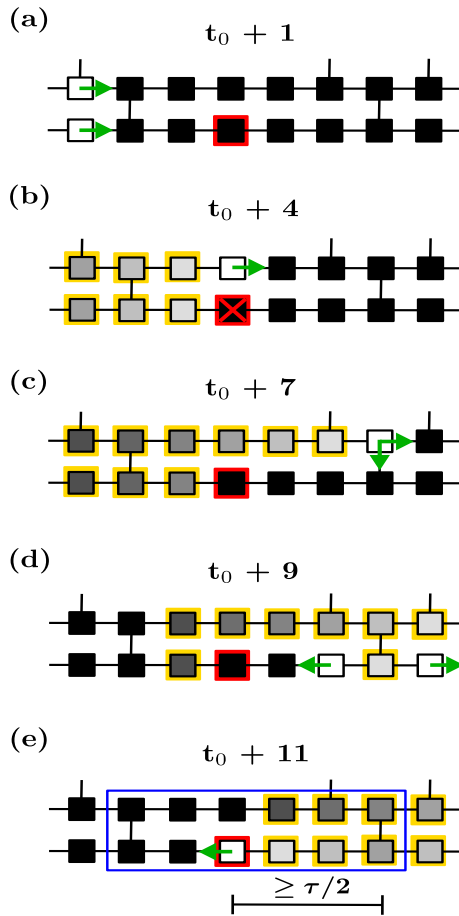


Figure 3.13: **The formation of a re-entrant circuit in the CMP model.** The node that is susceptible to conduction block is marked by a red square. (a) An incoming planar wavefront (green arrows) reaches the susceptible node. (b) The node fails to excite (red cross), blocking the progression of the wavefront in the lower fibre. The wavefront advances in the upper fibre, reaching the node with a transversal connection to the lower fibre. (c) At this point, the wavefront spreads both longitudinally and transversally, initiating a retrograde propagation through the lower fibre. (d) If the path denoted by the black segment includes at least $\tau/2$ nodes, the re-entering wavefront will not encounter refractory nodes while propagating backward in the lower fibre. This establishes a structural (i.e., spatially stable) re-entrant circuit in the region surrounded by the blue rectangular box. When the conduction blocking node fails to fire again, the re-entrant circuit is terminated. This figure has been extracted from [20], see appendix B.1 for details about attributions and permissions.

Theoretical CMP model results

The CMP model allows us to analytically compute the risk of developing AF with respect to the fraction of transversal connections ν_{\perp} , as shown in [25]. The risk is defined as the likelihood that the $L \times L$ grid has at least one region that can host a simple re-entrant circuit. The probability of having at least one transversal link on a given node is

$$p_{\nu_{\perp}} = 1 - (1 - \nu_{\perp})^2. \quad (3.3)$$

Let ℓ be the distance (in number of nodes) between a node that is susceptible to conduction block and the first node to the right which has at least one transversal connection. By making use of Eq. (3.3), we find that the probability of ℓ being equal to k nodes is

$$\mathbb{P}(\ell = k) = (1 - p_{\nu_{\perp}})^k p_{\nu_{\perp}}. \quad (3.4)$$

A given region cannot sustain a re-entrant circuit if ℓ is strictly smaller than $\tau/2$, see Fig. 3.13. The likelihood of this event can be calculated by summing over the probabilities of ℓ from 0 to $\tau/2 - 1$,

$$\mathbb{P}(\ell < \tau/2) = \sum_{j=0}^{\tau/2-1} (1 - p_{\nu_{\perp}})^j p_{\nu_{\perp}} = 1 - (1 - \nu_{\perp})^{\tau}. \quad (3.5)$$

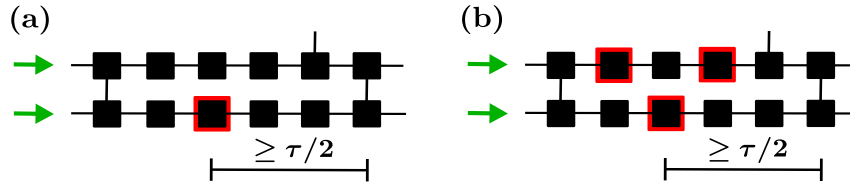
Because the average number of nodes that are susceptible to conduction block is δL^2 , the risk, R , of having at least one region that can host a re-entrant circuit is the complementary of the probability that the segments departing from these nodes are shorter than $\tau/2$,

$$R = 1 - (\mathbb{P}(\ell < \tau/2))^{\delta L^2} = 1 - [1 - (1 - \nu_{\perp})^{\tau}]^{\delta L^2}. \quad (3.6)$$

These equations have been derived in [25]. Eq. (3.6) provides a simple analytical tool to estimate the risk of developing AF in the CMP model. The result indicates that the risk of AF increases as the tissue becomes more decoupled/fibrotic, in agreement with the current clinical understanding [301]. Likewise, the theory predicts that the risk of fibrillation increases as the size of the atrial tissue increases, in agreement with clinical practice where left atrial volume is used as a predictor of the risk of developing AF [302].

This theoretical result builds on the assumption that re-entrant circuits form from the failure of a single conduction blocking node. However, this assumption does not account for all instances in which AF is triggered in the model. For instance, the probability of triggering a re-entrant circuit varies across the lattice depending on the architecture of the hosting region, see Fig. 3.14. Notably, some re-entrant circuits may only activate if two nodes susceptible to conduction block fail successively (i.e., in a single activation cycle).

Simple Structures



Complex Structures

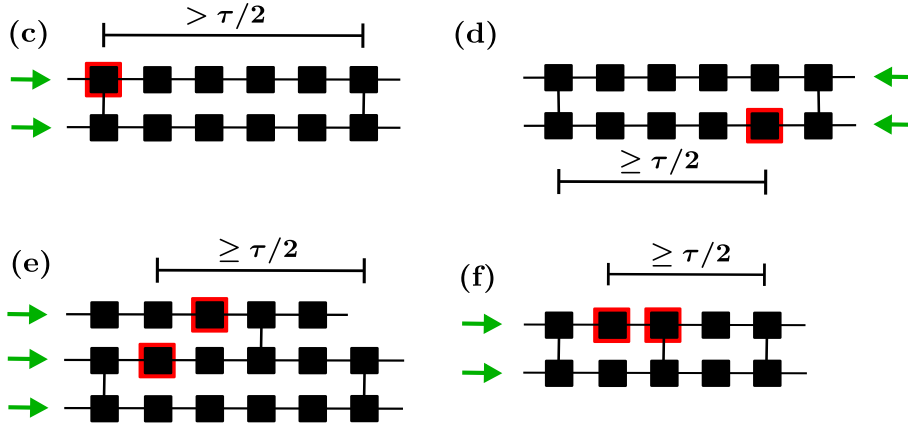


Figure 3.14: **Critical structures in the CMP model.** The black segment on top of each structure represents the minimum distance (in number of nodes) between the relevant conduction blocking node (red squared border) and the first regular node to the right which has at least one transversal connection for the structure to sustain a re-entrant circuit. The wavefront direction is indicated by the green arrows. (a)-(b) Simple critical structures are triggered by a single block of the incoming planar wavefront originating from sinus rhythm. These structures might include multiple nodes that are susceptible to conduction block, increasing the probability of self-termination. (c)-(f) The activation of complex critical structures requires a sequence of conduction blocks of the planar wave front or waves of excitation not originating from sinus rhythm. The probability of triggering these regions is much smaller than in (a)-(b). (c) The presence of at least one transversal connection departing from the conduction blocking node makes the activation more difficult as this node must fail to excite twice before prompting a re-entrant circuit. (d) This structure cannot be triggered from sinus rhythm but it can be triggered by a single block of a wave of excitation originating from elsewhere. (e)-(f) The activation of these structures requires multiple blocks of the planar wavefront to occur in different nodes. Examples of the evolution of each structure are shown in appendix D.1. This figure has been extracted from [20], see appendix B.1 for details about attributions and permissions.

These details indicate that the CMP theory represents an ideal case for AF driven by simple re-entrant circuits only. The theory assumes that if a simple circuit exists, the tissue spends 100% of the time in AF. Therefore, the theory curve sets a limit on the maximum time the model can spend in AF due to simple circuits only.

Model behavior

Local regions that are capable of hosting re-entrant circuits are called critical structures, see Fig. 3.13. A critical structure is active (inactive) when it hosts (does not host) a re-entrant circuit. In the CMP model, critical structures are classified according to the complexity of their activation and deactivation mechanisms. Structures which can activate and terminate from the failure of a single conduction blocking node from sinus rhythm are referred to as simple. This includes cases where a critical structure contains multiple conduction blocking nodes, but only one must fail to allow for the formation of a re-entrant circuit. All other configurations in which the planar wavefront from sinus rhythm requires multiple conduction blocks to fail to form a re-entrant circuit are referred to as complex. The latter class includes critical structures that are only triggered by waves of excitation not originating from sinus rhythm (proceeding from right to left on the lattice), see Fig. 3.14(d).

For large values of ν_{\perp} , the model is in SR indefinitely. The high number of transversal connections excludes the presence of regions that are critical for AF initiation and preservation as there are no sections of length $\geq \tau/2$ without a transverse connection. When ν_{\perp} decreases, for example due to increasing fibrosis [303], we observe a more pronounced branching structure of the lattice which favours the spontaneous emergence of structures that can host re-entrant circuits. This increases the risk of developing AF.

When ν_{\perp} is sufficiently small, increasing δ extends the time the system spends in AF. This occurs because a larger fraction of nodes are susceptible to conduction block and this increases the number of regions that can host a re-entrant circuit. However, the sensitivity of the system to the fraction of conduction blocking nodes, δ , rapidly vanishes as ν_{\perp} increases, suggesting that weak branching prevents the formation of critical structures independent of the fraction of nodes that are susceptible to conduction block [296]. The probability that a conduction blocking node fails to excite, ϵ , does not significantly influence the relationships between ν_{\perp} and the fraction of time the system spends in AF [296]. This implies that ϵ is mainly used to set the time scale of the model. More precisely, for simple re-entrant circuits, we note that ϵ

does not appear in the derivation of the risk of AF in Eq. (3.6). This is because ϵ effects both the probability that a simple re-entrant circuit activates and deactivates. If ϵ is reduced, it will, on average, take longer for a simple re-entrant circuit to activate. However, once active, that re-entrant circuit will take longer to de-activate than the equivalent circuit with a larger value of ϵ . That means that ϵ determines the duration of paroxysmal AF episodes and the time between paroxysmal AF episodes, but has a minimal effect on the overall risk of AF in the CMP model. Likewise, ϵ has no effect on the period of any simple re-entrant circuits formed. However, if circuits exist with an asymmetry between the probability of activation and deactivation, ϵ may play a role in the duration of individual fibrillatory events.

The length of the refractory period, τ , sets the minimum distance between the conduction blocking node and the first regular node to the right which has at least one transversal connection for the structure to sustain a re-entrant circuit, see Fig. 3.13 and Fig. 3.14. Given a fixed value of δ , lowering τ increases the number of regions that can host re-entrant circuits, increasing the time the system spends in AF.

In the CMP model, the system is defined to have entered AF if the number of active nodes per time step $a(t)$ exceeds $1.1 \times L$ (220) nodes for T consecutive time steps,

$$p_{\text{CMP}}^{\text{AF}}(t) = \begin{cases} 1 & \text{if } \min([a(t-T), \dots, a(t)]) \geq 220 \\ 0 & \text{otherwise} \end{cases} \quad (3.7)$$

where t can take integer values in the range $t = T, \dots, S$ and S is the duration of the experiment (in time steps)³. This is a working definition of AF in the CMP model which has been derived by inspection in previous work [25, 304, 296] and is not a unique choice. We have previously tested that this definition of AF correlates well with what would be expected from a clinical definition of AF [304]. This is shown in Fig. 3.15 where we plot (a) the number of active nodes in the model over time, (b) the corresponding simulated electrograms, and (c) the classification of whether the model is in AF or not according to our working definition of AF in the CMP model. The figure shows that the number of active nodes during SR follows a regular pattern with only small scale noise around the average number of active nodes. This average falls below the practical definition of AF where we require more than 220 active nodes. The corresponding electrograms are regular and consistent with SR pacing. When a re-entrant circuit forms, the number of active nodes rapidly exceeds the threshold, and rapid, irregular activity is observed in the electrograms. The activation frequency observed is significantly higher than expected in

³Note, it is coincidental in this case that $T = 220 = 1.1L$

SR. This state is classified as being in AF according to our working definition. For more details see [304]. We use Eq. (3.7) to study how the probability of inducing AF varies with the amount

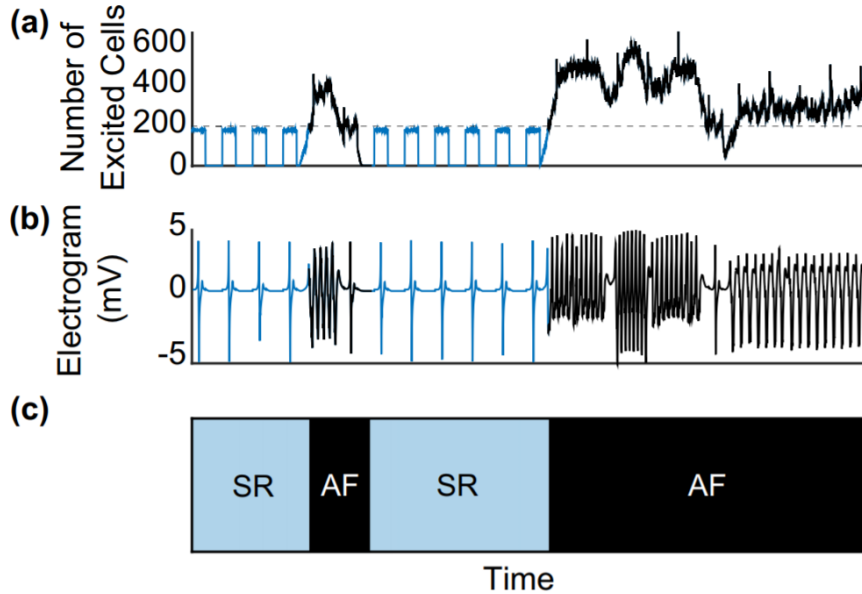


Figure 3.15: **The classification of AF in the CMP model.** (a) The number of active nodes over time. The dashed line indicates the AF threshold of 220 active nodes. (b) Simulated electrograms derived from the CMP simulations. (c) The classification of whether the model is in SR or AF over time. Blue lines indicate the model is in sinus rhythm, black lines indicate the model is in AF. This figure has been extracted from [20] (which was in turn used with permission from [304]), see appendices A and B.1 for details about attributions and permissions.

of coupling ν_{\perp} and compare this statistic with its theoretical estimations, see Eq. (3.6).

The definition used here is not unique and is not robust against changes in the pacing frequency T . The definition is designed to measure whether nodes in the model are activated more frequently than would be expected in sinus rhythm. This is based on the principle that if nodes are being activated at a rate higher than the pacing rate, then there must be a source of fibrillatory wavefronts other than the SAN. A superior method would be to measure the average activation frequency of nodes relative to the pacing frequency explicitly, rather than the number of active nodes, since this would be more robust against changes in T . However, to be consistent with previous work we use the existing definition. We stress that for fixed T , the two methods give almost identical results. Both methods compare well with a clinical definition of AF where AF is diagnosed from ECG or electrogram recordings, see Fig. 3.15. We do not generate electrograms as standard in the CMP model since this significantly increases the computational burden of

the simulations.

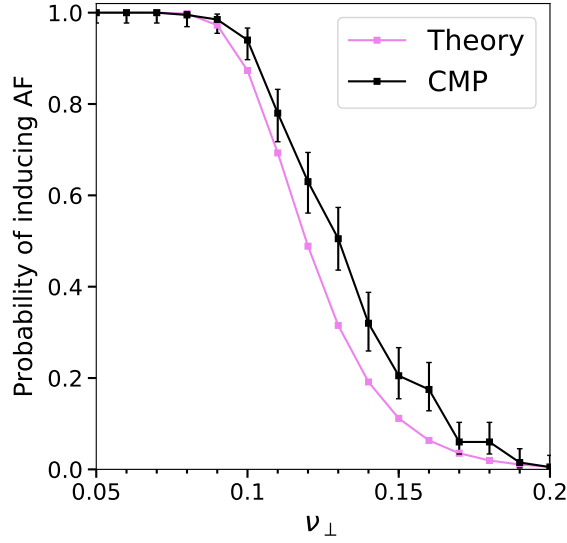


Figure 3.16: **Relationship between the amount of coupling and the probability of inducing AF.** Phase diagram of the probability of inducing AF as a function of the fraction of transversal connections ν_{\perp} . The violet line represents the theoretical risk curve, see Eq. (3.6). For each value of ν_{\perp} , we perform 200 simulations of the CMP model and compute the average probability of inducing AF (black square), see Eq. (3.7). The duration of each simulation is $S = 10^6$ time steps. For both the model and the theory, we observe that the system never (always) develops AF for $\nu_{\perp} \gtrsim 0.2$ ($\nu_{\perp} \lesssim 0.1$). Within this interval, the probability of developing AF rapidly increases as ν_{\perp} is lowered. For any value of ν_{\perp} between 0.1 and 0.2, the probability of inducing AF in the CMP model (black) is always higher than in the CMP theory (violet). This figure has been extracted from [20], see appendix B.1 for details about attributions and permissions.

The probability of inducing AF in simulations of the CMP model is systematically higher than in the CMP theory, see Fig. 3.16. These findings are somewhat surprising since the CMP theory assumes the most favourable conditions for the emergence of AF from simple re-entrant circuits only. We assert that this excess could be explained by the fact that re-entrant circuits in the CMP model might have multiple mechanistic origins that are not accounted for in the CMP theory. Furthermore, the CMP theory assumes that re-entrant circuits are triggered by single unidirectional conduction blocks, that is, AF is exclusively driven by simple critical structures, see Fig. 3.14.

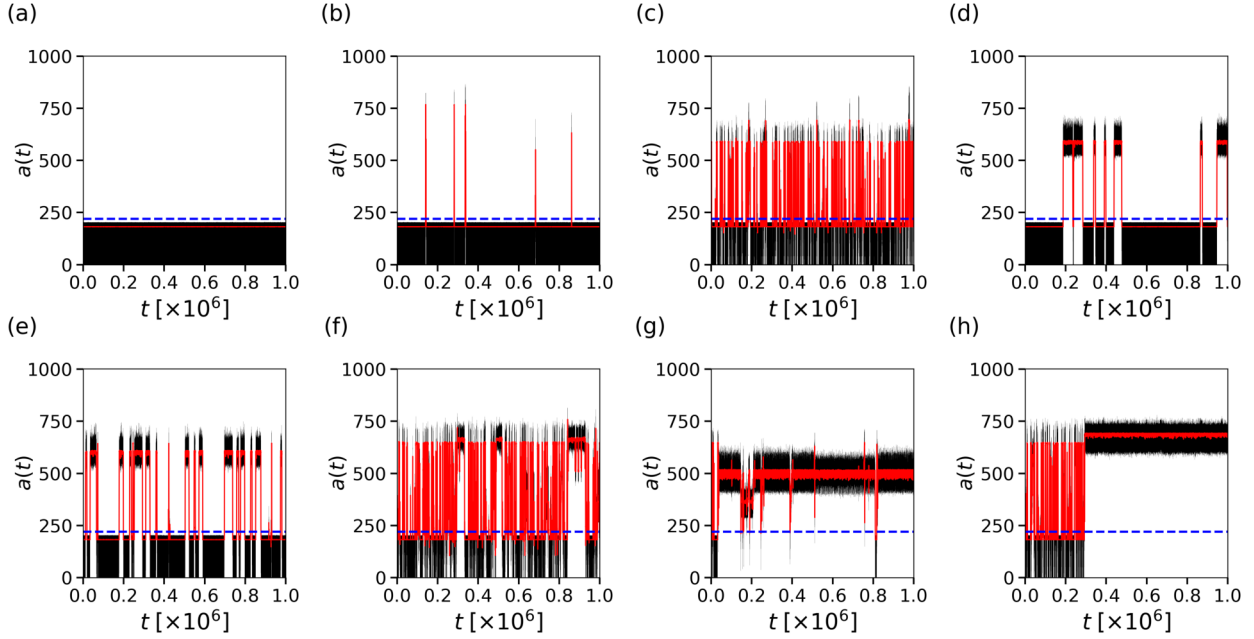


Figure 3.17: **The spectrum of AF patterns in the CMP model.** The number of excited nodes per time step $a(t)$ (black thin line) and its moving average $\langle a(t) \rangle$ calculated over $T = 220$ successive time steps (red solid line) in eight different simulations of the CMP model. All simulations are generated with identical model parameters. The coupling value is set at $\nu_{\perp} = 0.11$. The system is in AF when the number of excited nodes per time step exceed 220 (blue dashed line) for at least T time steps. The figure demonstrates the broad spectrum of AF persistence that naturally emerges in the CMP model, from (a) sinus rhythm, through (b)-(g) various forms of paroxysmal AF, to (h) fully persistent AF. The figures exhibit a range of different event times, and asymmetries between the period of time in and out of AF. Subfigures (b), (e) and (h) are dominated by short, intermediate, and long AF events respectively. Subfigures (f) and (g) exhibit an interplay between short and intermediate, and intermediate and long event times respectively. These figures demonstrate that complex behaviour can emerge at the model macrostructure from specific details at the model microstructure, independent of the parameters of the model. This figure has been extracted from [20], see appendix B.1 for details about attributions and permissions.

To better understand the discrepancy between theory and experiment, we look at the trace of the number of active nodes in the model. AF is paroxysmal when this statistic exhibits large fluctuations which prevent it from stabilizing above the AF threshold, i.e., the number of active nodes frequently falls below 220 nodes with only short periods of high frequency activity. AF is persistent when the number of active nodes consistently exceeds the AF threshold for extended periods of time. If AF in the model has a unique mechanistic origin, we would expect tissues at the same level of coupling to exhibit statistically similar behaviors in the number of the active nodes over time. However, we find that this is not the case – there is significant heterogeneity among systems characterized by the same parameters, e.g., the amount of uncoupling, or the fraction of conduction blocking nodes.

In Fig. 3.17 all tissues are generated using the same parameters, with $\nu_{\perp} = 0.11$. Tissue (a) remains in SR indefinitely. Tissue (b) remains mostly in SR, with rare fibrillatory events on the order of 10^3 time steps in the model. In real time, these events are on the order of 1s. It is plausible that clinically, such short events may be interpreted as an ectopic beat rather than AF. From tissue (c), through to tissue (g), we observe a spectrum of AF persistence. This includes short frequent events in (c), rare intermediate events in (d), frequent intermediate events in (e), a combination of short and intermediate events in (f), and long events with brief interruptions in (g). Only in (h) do we see a permanent transition from short paroxysmal AF, to persistent AF. The event shown in (h) is on the order of 30 minutes when converting to real time. Repeating those simulations where persistent AF appears to last until the end of the simulation, these simulations are extended to 10^9 time steps without the simulation reverting to SR. In real time, these events are on the order of 1 month. For practical reasons, we have not investigated events on timescales longer than 10^9 time steps. Note, that for visual clarity, the example chosen in Fig. 3.17(h) is driven by a single dominant driver which may be defined as AT rather than AF. However, in most cases, persistent activity is maintained for long time periods with the presence of multiple competing drivers, see appendix D.3 for an example.

3.5 The transition from paroxysmal to persistent atrial fibrillation

Personal contributions

This section presents the paper “*Understanding the transition from paroxysmal to persistent atrial fibrillation*” [20], published in Physical Review Research in June 2020. As primary co-author, I played a primary role in every major aspect of this project:

- Understanding the relevant literature.
- Development of the underlying theory.
- Development of the computational infrastructure required to analyse the behavior of the models.
- Management of computer-based simulations and data collection.
- Analysis and interpretation of computer-based simulations.
- Presentation of experimental results.
- Writing of the manuscript.

Note that an initial version of the mean-field model was introduced by Kishan Manani in [296] while its continuous extension was derived by Tim Evans.

3.5.1 Context

This section presents the paper “*Understanding the transition from paroxysmal to persistent atrial fibrillation*” [20], published in Physical Review Research in June 2020. The main goal of this research, which I have led as main author, is to perform an in-silico study of the mechanisms that allow AF to progress from an intermittent and short-lived condition, i.e., simple re-entrant circuits arising and dying sequentially, to a persistent condition in which the system remains in the fibrillatory state for extremely protracted time windows. By doing so, we address an important shortfall of related works [25, 304] that revealed, but failed to explain, a significant variability in the patterns of AF in samples with comparable microstructural properties, e.g.,

the same fibrosis burden in Fig. 3.17. Starting from a mean-field model where we describe AF as a simple birth-death process, we add layers of complexity to the model and show that persistent AF arises from re-entrant circuits which exhibit an asymmetry in their probability of activation relative to deactivation. As a result, different simulations generated at identical model parameters can exhibit fibrillatory episodes spanning several orders of magnitude from a few seconds to months. These findings demonstrate that diverse, complex fibrillatory dynamics can emerge from very simple dynamics in models of AF.

3.5.2 Introduction

The variability in the persistence of AF in the CMP model has been studied previously in [304]. The authors focused on the relationship between the amount of uncoupling in the lattice (i.e., ν_{\perp}) and the features of the developed AF in 32 independent experiments. In agreement with clinical observations [305, 306], they report high degrees of heterogeneity in the progression to persistent AF and in the amount of uncoupling required for AF to emerge. Similarly to Fig. 3.17, they observe very different AF patterns across systems characterized by the same amount of uncoupling, asserting that the emergence of re-entrant circuits is subject to the local distribution of transversal connections, not the global amount of coupling, i.e., ν_{\perp} . However, the authors do not satisfactorily explain how and why different AF patterns emerge from the microstructure of the CMP model.

The findings presented in Fig. 3.16 and Fig. 3.17 provide two important pieces of evidence against the assumption that AF is exclusively driven by simple re-entrant circuits. First, they show that the probability of inducing AF is systematically higher in the CMP model than in the CMP theory, see Fig. 3.16. Second, they reveal different activation patterns do not appear consistent with simple structures activating and deactivating with fixed rates. Individual events exhibit a spectrum of lifetimes before reverting to SR, from seconds to months. This motivates us to assess whether different mechanistic origins of AF are effectively present in the CMP model and how they eventually relate with the progression to persistent AF from paroxysmal AF.

In the following sections, we take up these challenges by removing layers of complexity from the CMP model. This allows us to derive simpler frameworks in which we can examine whether re-entrant circuits have different mechanistic origins and how the features of these activation processes influence the development of AF.

In section 3.5.3, we start with the simplest approach by removing all the spatial elements of the CMP model. This is done by condensing the CMP model into a MF model in which complex critical structures and interactions between re-entrant circuits (i.e., wave collisions) are neglected. This simple framework allows us to study AF under the assumption that fibrillation is exclusively driven by independently activated simple re-entrant circuits. We show that the MF model systematically underestimates the probability of inducing AF and the persistence of AF.

In section 3.5.4 we dissect this discrepancy by reintroducing the spatial elements of the CMP model while carefully controlling the placement of nodes susceptible to conduction block. This prevents the formation of complex critical structures. The main advantage of this controlled CMP model (cCMP) over the simpler MF model is that it allows us to quantify how different activation mechanisms contribute to AF emergence and maintenance. Like the MF model, the cCMP model underestimates the probability of inducing AF and the persistence of AF with respect to the CMP model. However, the cCMP model does not increase the time in AF relative to what is found in the MF model with the exception of very small fluctuations explained by differences in individual event times.

Finally, we confirm that the difference in the probability of inducing AF and the persistence of AF between the CMP and cCMP models stems from the contribution of complex re-entrant circuits which exhibit an asymmetry between the probability of activating and deactivating a re-entrant circuit. These complex structures may only require a single failure from a conduction blocking node to initiate, but multiple failures to terminate, resulting in long individual event times. Additionally, these structures may be coupled as part of a larger critical structure such that the termination of a re-entrant circuit anchored to a specific sub-structure immediately initiates a new re-entrant circuit in a coupled sub-structure. We demonstrate these mechanisms explicitly and show that as the probability that a node is susceptible to conduction block is lowered, the spatial density of conduction blocking nodes falls to the extent that multiple failing nodes are not required for the termination of a re-entrant circuit. As a result, the time the CMP and cCMP models spend in AF collapse onto a single curve. This demonstrates that an increase in the local density of conduction blocking nodes is highly proarrhythmic.

3.5.3 A mean-field representation of the Christensen-Manani-Peters model

Discrete-time Markov chain model

In the CMP model, critical structures activate and deactivate to sustain AF. Initially, the system is in SR as planar waves of excitation released from the SAN (pacemaker) propagate on the lattice. The motion of the planar waves is disrupted now and then by conduction blocks occurring across the grid. At some point in time, a conduction block forms the initial re-entrant circuit. This re-entrant circuit cannot maintain AF indefinitely because it will either self-terminate or be terminated by waves spreading from the surrounding regions. However, its circuitual motion intensifies the model activity, generating disorganized, high-frequency activation wavefronts that spread across the lattice. When the system enters this state, non-planar waves of excitation spreading from the active re-entrant circuit reach dormant critical structures at a much higher frequency than the pacemaker waves. This initiates a chain of asynchronous activations and deactivations of different critical structures located across the lattice, protracting the current AF episode until the complete disappearance of re-entrant circuits brings the system back to SR.

In the CMP model, it is unclear whether these interactions between simple critical structures are the only drivers of AF. In particular, the results discussed in Fig. 3.16 and Fig. 3.17 motivate us to examine whether other activation mechanisms drive AF and how differences between paroxysmal and persistent AF emerge. The simplest approach to this problem is to derive a framework in which fibrillation is solely driven by independently activated simple re-entrant circuits and to compare AF-related statistics against the CMP model.

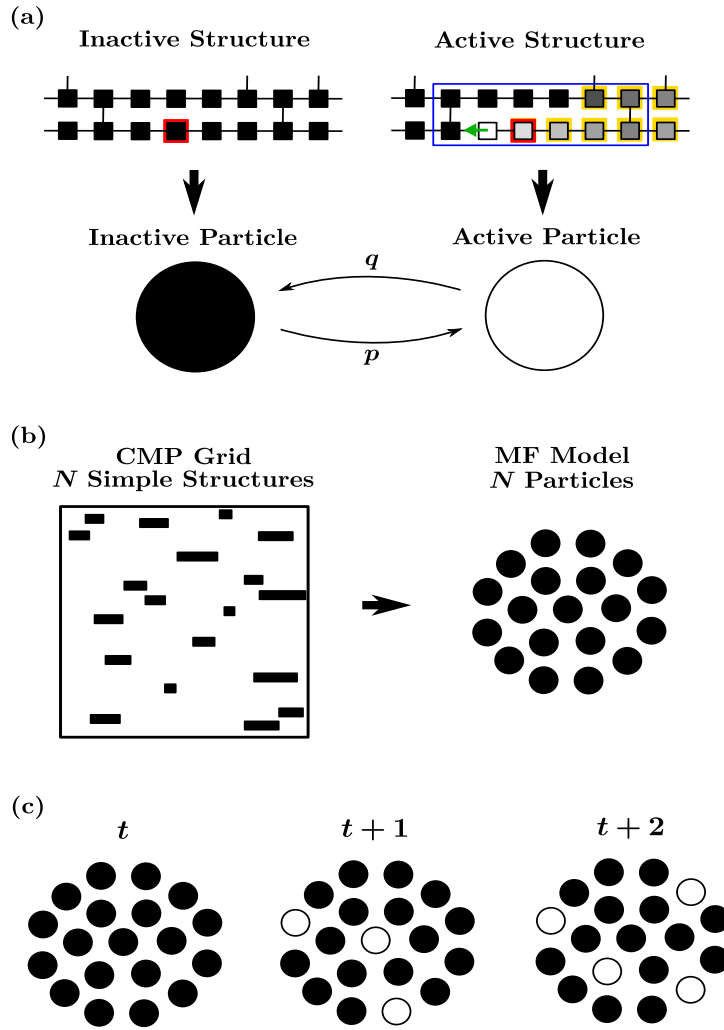


Figure 3.18: **The CMP model is condensed into a mean-field (MF) model of AF.** (a) Simple critical structures are mapped into particles which can take two distinct states: active (i.e., hosting a re-entrant circuit, blue path) or inactive. We enforce the following assumptions: i) the location (spatial positioning) of a particle is irrelevant, ii) all particles activate with rates ϵ/T when the system is in sinus rhythm and $\epsilon/\langle\ell\rangle$ when the system is in AF, iii) all particles deactivate with rate $\epsilon/\langle\ell\rangle$, iv) all particles have the same length $\langle\ell\rangle$ and v) particles can change their states at any time step. (b) Simple critical structures (black filled rectangles) found in the CMP lattice are condensed into particles (black filled circles). (c) The evolution of the MF system is driven by N independent particles that activate and deactivate with probability p , and q respectively, depending on the current state of the particle and the system. This figure has been extracted from [20], see appendix B.1 for details about attributions and permissions.

To do so, we translate the features of the CMP lattice into a simple MF model of AF in which N particles independently turn on and off. For a one-to-one comparison, the number of particles, N , is directly observed from the number of simple critical structures present in the CMP lattice at a given level of coupling. The fact that simple critical structures are characterized by a few well defined architectural features allows us to systematically inspect the grid and detect each region falling into this category.

In the MF model, the system is represented by a simple Markov chain. At a given time t , the state of the chain is the number of active particles $N_a(t)$, such that $t : N_a(t) = \{0, 1, \dots, N\}$. When $N_a(t) = 0$, the system is defined as being in SR where any existing critical structure has a chance to be triggered every T time steps (pacemaker frequency). On the other hand, $N_a(t) \geq 1$ is defined as the MF model exhibiting AF. In this case, the length of active re-entrant circuits sets the frequency (in time steps) at which inactive critical structures can be triggered. For the sake of simplicity, we assume that particles have the same length $\langle \ell \rangle$ corresponding to the average length (in number of nodes) of the simple critical structures tracked across the CMP lattice. At any time step, inactive particles activate with rate p and active particles deactivate with rate q , see Fig. 3.18.

Activation rates change depending on the state of the system, mimicking the fact that the presence of at least one re-entrant circuit significantly increases the frequency at which dormant critical structures can be triggered. It follows that p and q are given by:

$$p = \begin{cases} \frac{\epsilon}{T}, & \text{if } N_a = 0, \\ \frac{\epsilon}{\langle \ell \rangle}, & \text{if } N_a > 0, \end{cases} \quad (3.8a)$$

$$q = \frac{\epsilon}{\langle \ell \rangle}. \quad (3.8b)$$

The probability $P_{i,j}$ of transitioning from i to j active particles is analytically derived,

$$P_{i,j} = \sum_{k=0}^{\min\{i, N-i\}} B(i, k, q) B(N-i, j-i+k, p) \quad \text{if } j \geq i \quad (3.9a)$$

$$P_{i,j} = \sum_{k=i-j}^{\min\{i, N-i\}} B(i, k, q) B(N-i, j-i+k, p) \quad \text{if } j < i \quad (3.9b)$$

where $B(N, k, r) = \binom{N}{k} r^k (1-r)^{N-k}$ is the binomial distribution yielding the probability of getting exactly k successes in N trials when the probability of success is r [296].

This simple model allows us to calculate the same AF-related statistics that one can compute

in simulations of the CMP model. For instance, we can easily adapt Eq. (3.7) to the MF model

$$p_{\text{MF}}^{\text{AF}}(t) = \begin{cases} 1 & \text{if } N_a(t) \geq 1, \\ 0 & \text{otherwise,} \end{cases} \quad (3.10)$$

where $t = 1, \dots, S$ and S is the duration of the experiment (in time steps). In addition, we are interested in measuring the time the system spends in AF as a function of the amount of coupling ν_{\perp} . In the MF model, this statistic corresponds to the ratio between the number of time steps in which at least one particle is active and the duration of the experiment

$$T_{\text{MF}}^{\text{AF}} = S^{-1} \sum_{t=1}^S p_{\text{MF}}^{\text{AF}}(t). \quad (3.11)$$

In the MF model, the spatial elements of the CMP model are neglected to prevent the potential formation of re-entrant circuits from collisions between multiple waves of excitation. Furthermore, the correspondence between the numbers of simple critical structures and system particles excludes any eventual contribution from complex critical structures. The number of tracked simple critical structures reflects, to a good extent, the key architectural properties of the CMP lattice, namely, the amount of coupling, i.e. ν_{\perp} , and the fraction of nodes that are susceptible to conduction block, i.e. δ . Pegging the number of particles to the number of simple critical structures allows us to calibrate the MF model with the CMP model. To compare the MF model with the CMP model, we define the time in AF for the CMP model equivalently to Eq. (3.11),

$$T_{\text{CMP}}^{\text{AF}} = S^{-1} \sum_{t=1}^S p_{\text{CMP}}^{\text{AF}}(t), \quad (3.12)$$

where $a(t)$ is the number of active nodes at time step t . The MF model spends significantly less time in AF than the CMP model, see Fig. 3.19. This may be because the neglected spatial features of critical structures, such as different lengths and asynchronous activation and deactivation, have a significant role in AF emergence and maintenance. However, an enhanced version of the MF model, see next paragraph, reintroduces these omissions and indicates that these changes have no noticeable effect of the time the MF model spends in AF.

Enhanced discrete-time Markov chain model

The phase diagrams discussed in Fig. 3.19 reveal significant differences between the CMP and MF models as the latter underestimates the time in AF. One may assert that this discrepancy

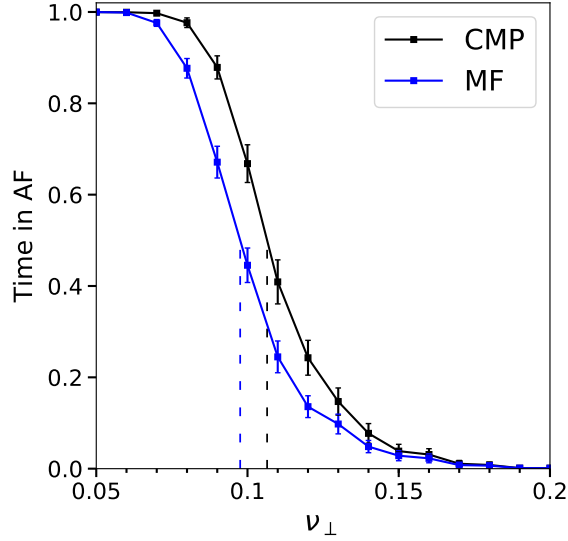


Figure 3.19: **Relationship between the amount of coupling and the time in AF.** Phase diagram of the time in AF as a function of the fraction of transversal connections, ν_{\perp} , for the CMP (black) and MF (blue) models. For each value of ν_{\perp} we perform 200 simulations of the CMP model and measure the time in AF over $S = 10^6$ time steps, see Eq. (3.12). For each simulations of the CMP model we derive the associated MF model, see Fig. 3.18, and compute the time in AF according to Eq. (3.11). The time the system spends in AF is significantly higher in the CMP model (black) than in the MF model (blue). Sharp transitions in the time in AF occur around the threshold values $\nu_{\perp}^* \approx 0.11$ (CMP, black dashed line) and $\nu_{\perp}^* \approx 0.09$ (MF, blue dashed line). This figure has been extracted from [20], see appendix B.1 for details about attributions and permissions.

stems from a poor replication of the interactions between re-entrant circuits, and in particular from the exclusion of the non-spatial features of critical structures (e.g. particles are assumed to have the same length) from the MF model. In this section, we provide further evidence against this hypothesis by showing that modelling various non-spatial features of critical structures does not mitigate the differences between the CMP and MF models. To do so, we introduce an enhanced version of the MF model (eMF) in which each particle retains the length of the associated critical structure and changes its state at specific time steps, depending on the overall configuration of the system. The purpose of the eMF is to indicate that the non-spatial simplifications in the MF model are not responsible for the discrepancy in the time in AF between the MF model and the CMP model.

In the eMF model, the system is represented by the state vector $P(t) = (p_1(t), \dots, p_N(t))$, where $p_j(t) \in \{0, 1\}$, $j = 1, \dots, N$ is the state of the j th particle at time t and N is the number of particles corresponding to the simple critical structures found across the CMP lattice. When $p_j(t) = 1$ ($p_j(t) = 0$), the j th particle is active (inactive) at time t . The number of active particles at time t is

$$N_a(t) = \sum_{j=1}^N p_j(t). \quad (3.13)$$

In line with the original MF model, the system is in SR when $N_a(t) = 0$ and in AF when $N_a(t) > 0$. The j th particle $p_j(t)$ can change its state at a specific time t_j^* . We set the first switching time for each particle as $t_j^* \rightarrow U_j$, where $U_j, j = 1, \dots, N$ is a uniformly distributed integer random variable in $[1, L]$. This mimics the first planar wave front released from the pacemaker reaching critical regions at different time steps due to their different locations. As soon as the simulation time t matches t_j^* , the j th particle changes its state with probability ϵ . Independently of whether the j th particle has changed its state or not, its next switching time t_j^* is updated

$$t_j^* \rightarrow \begin{cases} t_j^* + \min_{p:p(t+1)=1} \ell_p, & \text{if } N_a(t+1) > 0 \text{ and } p_j(t+1) = 0, \\ t_j^* + \ell_j, & \text{if } N_a(t+1) > 0 \text{ and } p_j(t+1) = 1, \\ t_j^* + T, & \text{if } N_a(t+1) = 0, \end{cases} \quad (3.14)$$

where $t+1$ indicates that the update is based on the characteristics of the system observed immediately after the eventual state change of the j th particle. When $N_a(t+1) = 0$, the j th particle will attempt to switch its state in T time steps. This mimics SR in the CMP model where the planar wave front released from the SAN reaches a critical structure every T time steps. When $N_a(t+1) > 0$, particles try to switch their states more frequently. This reflects the intense activity (e.g. number of active nodes per time step) observed in AF episodes occurring in the CMP lattice.

In the eMF model, the length of the shortest active particles dictates the period between two consecutive attempts to activate a dormant region. For instance, the j th particle that turns (or remains) off at time $t_j^* = t$ will attempt to activate again at time

$$t_j^* = t_j^* + \min_{p:p(t+1)=1} \ell_p, \quad (3.15)$$

where the final term is the length of the shortest active particles at time $t+1$. This mimics the fact that in the CMP model the length of a re-entrant circuit determines the frequency at

which nodes forming the hosting critical structure emit waves.

The eMF model enhances the replication of the interactions between simple critical structures by capturing potentially important spatial features that have been excluded from the original simplified MF model. The goal of this framework is to assess the contribution of the non-spatial features of critical structures to the significant discrepancies between the CMP and the MF models, see Fig. 3.19. We find that the phase diagram of the time in AF in the eMF model is perfectly compatible with the one derived from the MF model, see Fig. 3.20. This suggests that adding further layers of complexity to capture every feature of the interactions between simple critical structures is unlikely to reconcile the statistics obtained from the CMP and the MF models.

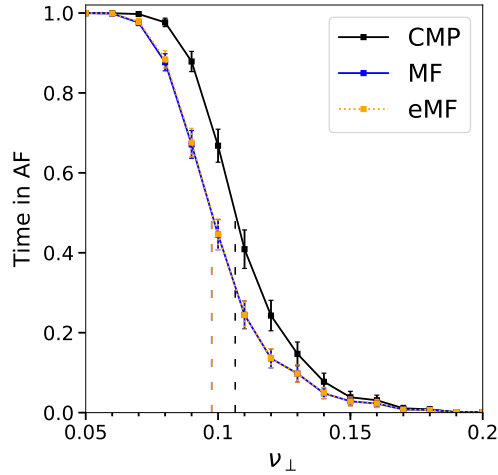


Figure 3.20: **Relationship between the amount of coupling and the time in AF.** Phase diagram of the time in AF as a function of the fraction of transversal connections ν_{\perp} for the CMP (black), MF (blue) and eMF (orange) models. We use the parameters of the CMP model (i.e., N , ϵ , and $\langle \ell \rangle$) and the lengths of the tracked simple critical structures (i.e., $\ell_{p_1}, \dots, \ell_{p_N}$) to calibrate the MF and eMF models. The phase diagrams of the MF and eMF models are perfectly compatible. Both models significantly underestimates the time in AF with respect to the CMP model. These results suggest that the spatial structure of the CMP model is responsible for the excess time the CMP model spends in AF compared to the MF model, and not the non-spatial simplifications of the MF model. Sharp transitions in the time in AF occur around the threshold values $\nu_{\perp}^* \approx 0.11$ (CMP, black dashed line), $\nu_{\perp}^* \approx 0.09$ (MF, blue dashed line; eMF, orange dashed line). This figure has been extracted from [20], see appendix B.1 for details about attributions and permissions.

Continuous approximation

The MF model can be extended to the continuous time case (cMF), providing us with a framework in which the time in AF can be computed analytically. Let $\tilde{p}(k, t)$ be the probability of observing k active simple re-entrant circuits at time t . When the interval between two consecutive time steps Δt is sufficiently small (i.e., $\Delta t \rightarrow 0$), we have at most one event (activation or de-activation) per interval. In these settings, the dynamics of $\tilde{p}(k, t)$ are described by the following master equation

$$\begin{aligned} \frac{d\tilde{p}(k, t)}{dt} = & p(N - k + 1)\tilde{p}(k - 1, t) - p(N - k)\tilde{p}(k, t) \\ & + q(k + 1)\tilde{p}(k + 1, t) - qk\tilde{p}(k, t) \quad \text{for } k > 1 \end{aligned} \quad (3.16a)$$

where the first two terms are associated with an activation process $k - 1 \mapsto k$ and $k \mapsto k + 1$ transitions, respectively, while the last two are associated with $k + 1 \mapsto k$ and $k \mapsto k - 1$ transitions, respectively. Because the activation rate is different when the system has no active particles, see Eq. (3.8a), we need to take special care of the $k = 1$ and $k = 0$ cases. If the term p_0 represents the activation rate when the system has no active particles, then

$$\begin{aligned} \frac{d\tilde{p}(1, t)}{dt} = & p_0 N \tilde{p}(0, t) - p(N - 1)\tilde{p}(1, t) \\ & + 2q\tilde{p}(2, t) - q\tilde{p}(1, t), \quad \text{for } k = 1, \end{aligned} \quad (3.16b)$$

$$\frac{d\tilde{p}(0, t)}{dt} = -p_0 N \tilde{p}(0, t) + q\tilde{p}(1, t), \quad \text{for } k = 0. \quad (3.16c)$$

We enforce the boundary conditions that $\tilde{p}(k, t) = 0$ for $k < 0$ and $k > N$. We will find the steady state solution $\tilde{p}(k) = \lim_{t \rightarrow \infty} \tilde{p}(k, t)$ where the derivatives on the left-hand side of Eq. (3.16) are zero by the ansatz

$$\tilde{p}(k) = \begin{cases} A \binom{N}{k} \left(\frac{q}{p}\right)^{N-k} + B \delta_{k,0} & \text{for } k = 0, 1, \dots, N, \\ 0 & \text{for } k < 0 \text{ or } k > N, \end{cases} \quad (3.17)$$

where $\delta_{i,j}$ is the Kronecker delta function. By inserting the ansatz into Eq. (3.16a), we confirm that it solves the steady state equation for $k > 1$. However, in our case it simplifies further as $p = q = \epsilon/\langle \ell \rangle$, see Eq. (3.8a), so $q/p = 1$. We can determine the two constants A and B by requiring that Eq. (3.17) solves Eqs. (3.16b)-(3.16c) together with the normalization constraint: inserting the ansatz into Eq. (3.16c), recalling $p = q$, we find

$$0 = -p_0 A N - p_0 N B + q A N \quad (3.18)$$

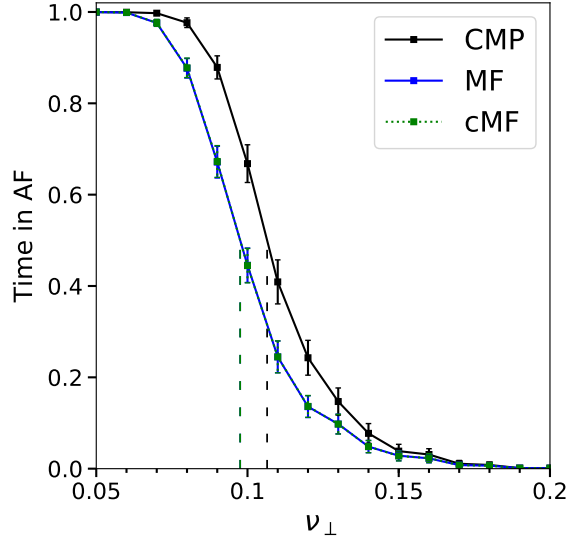


Figure 3.21: **Relationship between the amount of coupling and the time in AF.** Phase diagram of the time in AF as a function of the fraction of transversal connections ν_{\perp} for the CMP (black), the MF (blue) and the cMF (green) models. We use the parameters of the CMP model (i.e., N, ϵ and $\langle \ell \rangle$) to calibrate the cMF model and calculate the time in AF according to Eq. (3.22). The phase diagrams for the MF and the cMF models are perfectly compatible. Both models significantly underestimate the time in AF with respect to the CMP model. Sharp transitions in the time in AF occur around the threshold values $\nu_{\perp}^* \approx 0.11$ (CMP, black dashed line), $\nu_{\perp}^* \approx 0.09$ (MF, blue dashed line) and $\nu_{\perp}^* \approx 0.09$ (cMF, green dashed line). This figure has been extracted from [20], see appendix B.1 for details about attributions and permissions.

implying that

$$B = A \left(\frac{p}{p_0} - 1 \right). \quad (3.19a)$$

Note that $p = p_0 \Rightarrow B = 0$, that is, $\tilde{p}(0)$ does not have a special status but when $p \neq p_0 \Rightarrow B \neq 0$, and B is an extra contribution to $\tilde{p}(0)$, see Eq. (3.17). We now require normalization, that is,

$$1 = \sum_{k=0}^N \tilde{p}(k) = A2^N + B. \quad (3.19b)$$

Solving Eqs. (3.19) for A and B we find

$$A = \frac{1}{2^N + p/p_0 - 1}, \quad (3.20a)$$

$$B = \frac{p/p_0 - 1}{2^N + p/p_0 - 1}, \quad (3.20b)$$

yielding

$$\tilde{p}(0) = \frac{p/p_0}{2^N + p/p_0 - 1}. \quad (3.21)$$

Having obtained the analytical solutions, the fraction of time the system spends in AF for the cMF model is given by

$$1 - \tilde{p}(0) = \frac{2^N - 1}{2^N + p/p_0 - 1}. \quad (3.22)$$

The time in AF for the cMF model is shown in Fig. 3.21. It is interesting to contrast this result with a simple birth-death process where $p = p_0$. The time in AF is shown for the simple birth-death process and for the cMF calibrated to the CMP model, $p/p_0 = T/\tau = 4.4$, in Table 3.1. The results indicate that for $N = 0$, neither model enters AF. As N is increased, the time in AF is initially much higher in the birth-death process than the cMF, but this difference vanishes as N becomes large. Only when $N \rightarrow \infty$ does the model spend 100% of the time in AF. Since N must be finite in the CMP model, this indicates that the cMF cannot explain persistent AF.

N	0	1	2	3	4	5	10	∞
$p/p_0 = 4.4$	0	0.185	0.405	0.614	0.773	0.876	0.996	1
$p/p_0 = 1$	0	0.5	0.75	0.875	0.938	0.969	0.999	1

Table 3.1: **Time in AF in the cMF model for different combinations of p/p_0 and N .** We observe that for small N the time in AF is significantly higher when the ratio p/p_0 is small. These differences vanish as N increases.

3.5.4 The role of complex critical structures

The controlled CMP model

The MF models presented in section 3.5.3 allow us to study AF under the assumption that fibrillation is exclusively driven by independently activated simple re-entrant circuits. We have shown that every MF variant systematically underestimate the probability of inducing AF and the persistence of AF. This result clearly hints at the presence of additional mechanisms through which AF emerges and persists in the original CMP model. The problem of detecting the variety of activation mechanisms and disentangling their roles in the patterns of AF can

be approached in two ways. We may attempt to devise a detection algorithm to identify all simple and complex critical structures located across the lattice and assess their contribution to the phase diagrams in Fig. 3.19. However, the wide variety and complexity of these structures poses a significant challenge with no easy method to verify that all circuits have been detected. A more straightforward approach involves deliberately constructing simple re-entrant circuits by controlling the placement of conduction blocking nodes across the lattice, referred to as the controlled CMP model (cCMP). For simplicity, we achieve this by identifying the isolated segments of length $\geq \tau/2$ in the lattice and note which nodes in the segment, if susceptible to conduction block, would form a simple re-entrant circuit consistent with those simple structures shown in Fig. 3.14. A fraction δ of these nodes are set to be susceptible to conduction block. All other nodes are not susceptible to conduction block. This leads to a special CMP lattice in which AF is driven by simple re-entrant circuits only since conduction blocking nodes are only found in simple critical structures and not across the lattice as a whole.

To compare the cCMP and CMP models, we make a copy of the cCMP lattice and randomly place conduction blocking nodes across the lattice as a whole with probability δ – this model is equivalent to the regular CMP model. We simulate the two models and compare the probability of inducing AF and the time in AF. In this scenario, the eventual differences in AF related statistics quantify the contribution of complex critical structures to AF persistence and maintenance. The probability of inducing AF and the time in AF are significantly higher in the CMP model than in the cCMP model, see Fig. 3.22. This indicates that local regions with complex activation dynamics (e.g. multiple conduction blocks) provide a tangible contribution to AF emergence and maintenance. However, the cCMP and MF models do not show a significant difference in the time spent in AF, with the exception of small fluctuations above and below the critical coupling value, ν_{\perp}^* .

The small differences between the MF and cCMP models can be understood as a consequence of the interaction between multiple active critical structures. By definition, the MF and cCMP models contain the same number of potential critical structures (or particles), N . In the MF model, particles activate independently of any other particles (with the exception of changes in the absolute rate of activation). Conversely, in the cCMP model high frequency waves emitted from a given re-entrant circuit may suppress the activation of new re-entrant circuits. Therefore, at low $\nu_{\perp} < \nu_{\perp}^*$ where there are many simple critical structures, the time spent in AF is slightly higher in the MF model than in the cCMP model since the presence of multiple

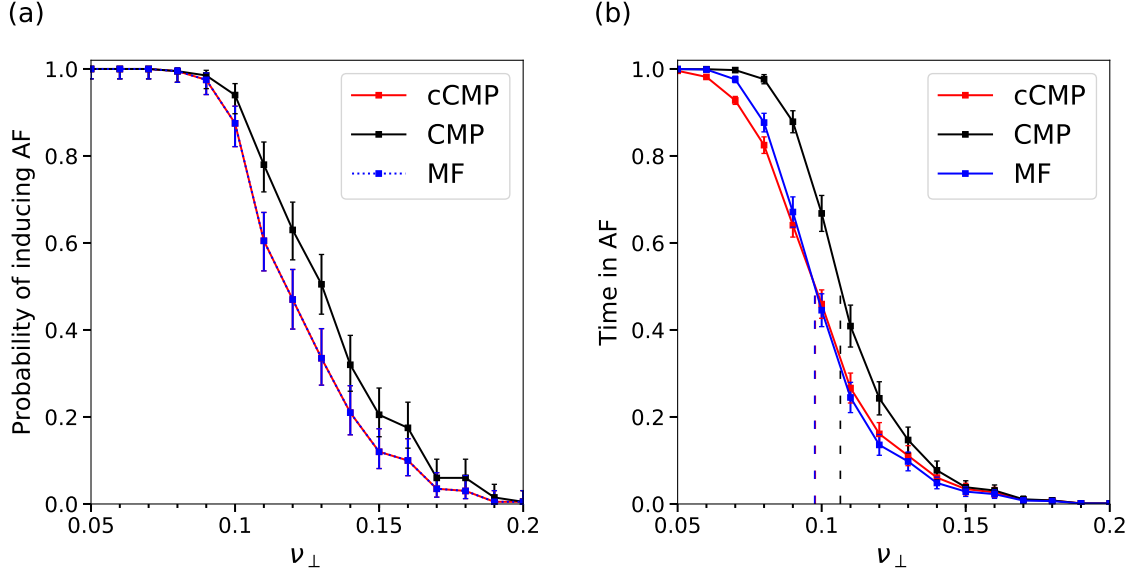


Figure 3.22: **Comparison of the main AF statistics in the cCMP, CMP and MF models.** Phase diagrams of (a) the probability of inducing AF and (b) the time in AF as a function of the fraction of transversal connections, ν_{\perp} , for the CMP (black), cCMP (red) and MF (blue) models. Both statistics are significantly higher in the CMP model than in the cCMP and MF models. The probability of inducing AF is the same in both the cCMP and MF models since the number of particles in the MF model is taken from the cCMP model. Hence, if the cCMP has at least one critical structure, the MF model also has at least one particle. For both the cCMP and MF models, the probability of a structure/particle activating approaches 1 as the simulation time is extended. The time in AF in the MF model is slightly higher than in the cCMP model for $\nu_{\perp} \lesssim 0.1$. In contrast, the cCMP model marginally overtakes the MF model for $\nu_{\perp} \gtrsim 0.1$, see appendix D.4. Sharp transitions in the time in AF occur around the threshold values $\nu_{\perp}^* \approx 0.11$ (CMP, black dashed line), $\nu_{\perp}^* \approx 0.10$ (cCMP, red dashed line) and $\nu_{\perp}^* \approx 0.09$ (MF, blue dashed line). This figure has been extracted from [20], see appendix B.1 for details about attributions and permissions.

simultaneous re-entrant circuits is not suppressed in the MF model, see appendix D.4.

In the reverse case at $\nu_{\perp} > \nu_{\perp}^*$, the cCMP slightly exceeds the MF due to slight differences in the rules of activation and deactivation. More precisely, a critical structure only has one opportunity to activate, or deactivate, in a given pacing cycle with probability ϵ in the cCMP model. However, particles can activate in the MF model every timestep with probability ϵ/T . This results in the cCMP model spending marginally longer in AF if the number of potential simple re-entrant circuits is small, see appendix D.4.

Critical structures with asymmetric activation

Since the spatial components of the CMP model do not account for the difference in the time spent in AF between the MF and CMP models, we note that the only remaining difference between the cCMP and CMP models is the distribution of conduction blocking nodes. By construction, the cCMP and CMP models contain the same number of simple critical structures. Therefore, some higher order critical structures must exist which rely on conduction blocking nodes which cannot form critical circuits by themselves, but which enhance the time spent in AF.

Returning to Fig. 3.17, we draw particular attention to subfigures (b), (c), (d) and (f). In Fig. 3.17(b), we see an isolated number of very short events. Given the duration of the observed AF events, let us assume these dynamics are driven by a simple re-entrant circuit. With $T = 220$, $\tau = 50$ and $\epsilon = 0.05$, the time for a single inactive re-entrant circuit to activate is approximately 4400 time steps. Similarly, once active, the time for a single active re-entrant circuit to deactivate is approximately 1000 time steps. This implies that, on average, from a single simple re-entrant circuit we expect to see a transition from SR to AF and back to SR in approximately 5400 time steps. For a simulation lasting 10^6 time steps, this suggests a single simple re-entrant circuit might generate on the order of ~ 185 individual fibrillatory events. Such behaviour is visible in Fig. 3.17(c), but Fig. 3.17(b) only exhibits 5 events during this time span. This suggests that, although the probability of an active re-entrant circuit terminating is consistent with the presence of a simple re-entrant circuit, the probability of activating a re-entrant circuit is significantly suppressed. This implies the critical structure present in Fig. 3.17(b) requires multiple successive failures of conduction blocking nodes to activate, but only one to fail once active for the circuit to terminate. Examples of complex structures with these properties are described in Fig. 3.14.

We now consider Fig. 3.17(d) where we observe a small number of isolated fibrillatory events similar to those shown in Fig. 3.17(b), implying the presence of a limited number of re-entrant circuits. However, unlike Fig. 3.17(b), the lifetimes of individual fibrillatory events in Fig. 3.17(d) are significantly longer than the ~ 1000 time steps predicted for a single simple re-entrant circuit. This suggests that the re-entrant circuit in Fig. 3.17(d) has both a suppressed activation rate, and a suppressed deactivation rate relative to a simple re-entrant circuit. In these cases, multiple re-entrant circuits must fail simultaneously for AF to be terminated, extending the lifetime of individual episodes. If we assume that the re-entrant circuit in Fig. 3.17(d) requires two successive failures for the circuit to terminate, this would imply an average fibrillatory event duration of ~ 20000 time steps. This demonstrates that a range of different re-entrant circuits can exist, at the same set of model parameters, which result in a spectrum of AF event durations.

The example given in Fig. 3.17(d) requires two successive (in the same activation cycle) failures of conduction blocking nodes. However, we observe that in some cases, such as Fig. 3.17(h) activity persists for durations approaching 10^6 time steps. For fibrillatory events to last this duration, circuits must form which require more than two successive failures of conduction blocking nodes to terminate.

Inspecting the CMP model, we identify two structural mechanisms by which re-entrant circuits can form with asymmetric activation rates such that the probability of entering AF exceeds the probability of returning to sinus rhythm once AF has been initiated. The two mechanisms are as follows: (1) Self-contained critical structures where the number of cell failures required to initiate the structure is less than the number of failures required to terminate the structure. An example of such a structure is shown in Fig. 3.23. (2) Coupled critical structures whereby a fibre can be shared between multiple possible adjacent sub-structures such that when a re-entrant circuit has formed, its termination immediately initiates a new re-entrant circuit in a neighbouring fibre. Depending on the structures coupled, these circuits can require a vast number of cell failures for the activity to be terminated and for SR to be restored. An example of such a structure is shown in Fig. 3.24. In Fig. 3.23, a critical structure is initiated (not from sinus rhythm), which requires the successive failure of two conduction blocking nodes to activate. However, once active, four successive failures are required to terminate the re-entrant circuit. This is because even if a single conduction blocking node fails to excite, secondary pathways exist such that re-entry can move around the conduction blocking region unimpeded.

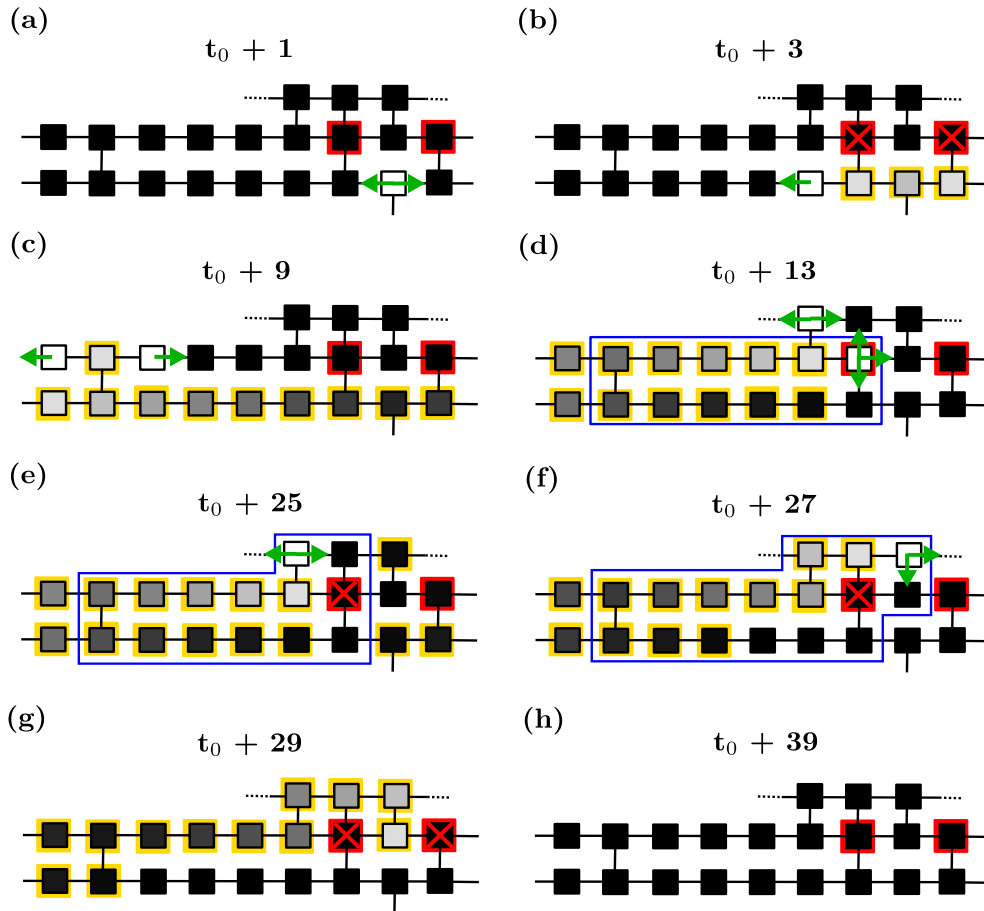


Figure 3.23: **The formation of a complex re-entrant circuit with asymmetric activation and deactivation rates.** (a) An excitation (white cell; not from SR) emerges from below the part of the CMP lattice in question, and propagates in the direction indicated by the green arrows. (b) The excitation is terminated by two conduction blocking nodes (red crosses), but the excitation successfully continues to the left of the lattice region. Refractory cells are shown in grey-scale with a yellow border. (c)-(d) The excitation branches to the adjacent fibre, propagates to the right, and branches back to the lower fibre forming a re-entrant circuit (blue box). (e)-(h) The re-entrant circuit is terminated from the successive failure of four conduction blocking nodes. Hence, this complex circuit requires two failures to initiate and four failures to terminate, resulting in long, persistent AF episodes. The full evolution of this structure is shown in appendix D.2. This figure has been extracted from [20], see appendix B.1 for details about attributions and permissions.

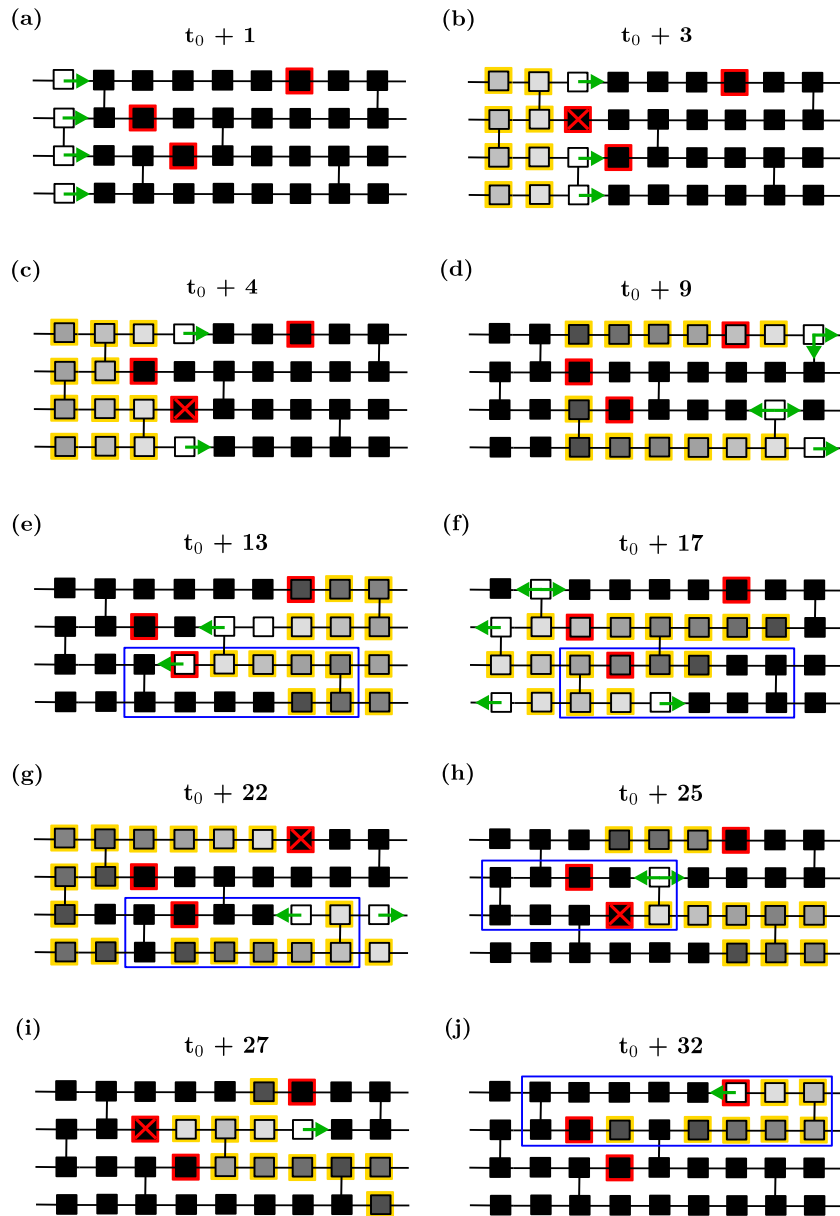


Figure 3.24: **The coupling of multiple re-entrant circuits such that the termination of one circuit immediately activates a secondary circuit.** This coupled behaviour suppresses the probability that activity terminates in the CMP model. Colours as described previously. (a) A wavefront enters a region of the CMP model from SR. (b)-(f) Two successive failures of conduction blocking nodes result in the initiation of a re-entrant circuit in the lower two fibres. (g) Activity propagating through the top fibre is blocked by the failure of a conduction blocking node. (h)-(i) The failure of both conduction blocking nodes in the central fibres allows the wavefront to re-enter the top fibre, forming a new re-entrant circuit. In this process, the termination of the initial re-entrant circuit has initiated a secondary re-entrant circuit, rather than restoring sinus rhythm. In total, two cell failures initiated the re-entrant activity, but activity has not been terminated after three additional cell failures. The full evolution of this structure is shown in appendix D.2. This figure has been extracted from [20], see appendix B.1 for details about attributions and permissions.

Only if all secondary pathways are blocked does the circuit terminate.

In Fig. 3.24, individual critical structures are coupled by sharing common segments. While an individual fibre may not have a higher probability of activation than termination, the coupled structures have the property that if one structure is terminated from a succession of conduction blocks, one of the coupled critical structures in the adjacent fibres can immediately initiate. Note, the probability of any of the sub-structures terminating is not fixed. Some critical structures may require only one cell failure to terminate, whereas other structures may persist in the presence of multiple successive cell failures. Through the inspection of many instances of the CMP model, there does not appear to be any clear limit to how many individual subregions can be coupled together in such a way that the termination of a given sub-structure doesn't initiate a new re-entrant circuit. If a large enough number of critical structures are coupled, and if some of those critical structures have asymmetric activation rates as shown in Fig. 3.23, individual fibrillatory events can become, to all practical purposes, indefinite. In a sample of one hundred simulations at very low coupling, $\nu_{\perp} = 0.05$, every simulation is observed to enter AF, and of those simulations, not a single case returns to sinus rhythm within 10^6 time steps. Such observations suggest that, particularly at low coupling, coupled structures with very low termination probabilities dominate the CMP model.

To emphasise the extent to which these mechanisms can enhance the probability of persistent AF, Fig. 3.25 shows the number of active cells for a simulation which requires a small number of conduction blocks to activate, but at least 5 successive failures to terminate. In such situations, AF can be maintained for durations in excess of 10^9 time steps. This indicates that with simple dynamics and rules, the CMP model is capable of exhibiting fibrillatory events which, if converted into real time, can span anywhere from seconds to months for the same set of model parameters. A common feature in the complex critical structures we have identified is that their activation and deactivation relies on the failure of multiple conduction blocking nodes within a small critical region. This suggests that the formation of these structures should be dependent on the local density of conduction blocking nodes, δ . In Fig. 3.26 we plot the phase diagrams for the probability of inducing AF in the cCMP and CMP models at different values of δ . As δ increases (decreases) the spatial density of conduction blocking nodes in the cCMP and CMP models increases (decreases). Fig. 3.26 demonstrates that at large δ , the CMP model is significantly more likely to enter AF than the cCMP model. However, this difference disappears as the spatial density of conduction blocking nodes is lowered. This indicates that the

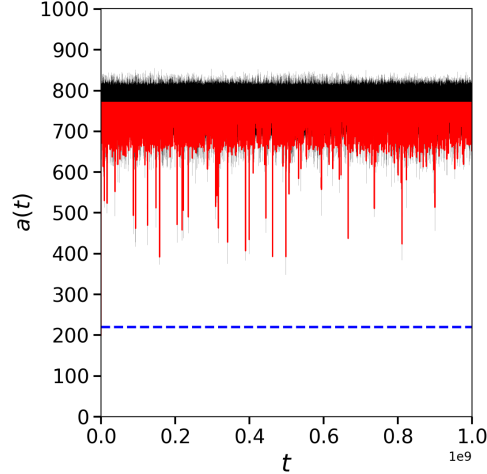


Figure 3.25: **Protracted AF episode.** A simulation of the CMP model for 10^9 timesteps at $\nu_{\perp} = 0.05$. Persistent AF is maintained throughout the simulation. Converted into real time, this corresponds to an AF event of at least 1 month in duration. This figure has been extracted from [20], see appendix B.1 for details about attributions and permissions.

dominant contribution to the difference in the probabilities of inducing AF comes from these special re-entrant circuits with asymmetric activation and termination rates as opposed to the special case shown in Fig. 3.13 where only one failure is required to initiate and terminate a re-entrant circuit.

3.5.5 Discussion and outlook

The persistence of AF is one of the key factors determining the likelihood of a successful ablation [33]. However, at a microstructural level, it is not clear what determines whether a patient will exhibit paroxysmal or persistent AF [307, 305]. Better understanding the causes of persistent AF may, in the future, improve the success rate of ablation or inspire new potential treatment methods.

The CMP model is a simple, percolation based model of AF where re-entrant circuits form when adjacent muscle fibres decouple [25]. The model is not a fully realistic representation of atrial electrophysiology. However, the model, and its extensions, have offered explanations for a number of key observations from clinical AF research. This includes the diversity of AF persistence at comparable levels of fibrosis [304], the distribution of re-entrant circuits in the left and right atria [308], and the observation that re-entrant circuits preferentially form near

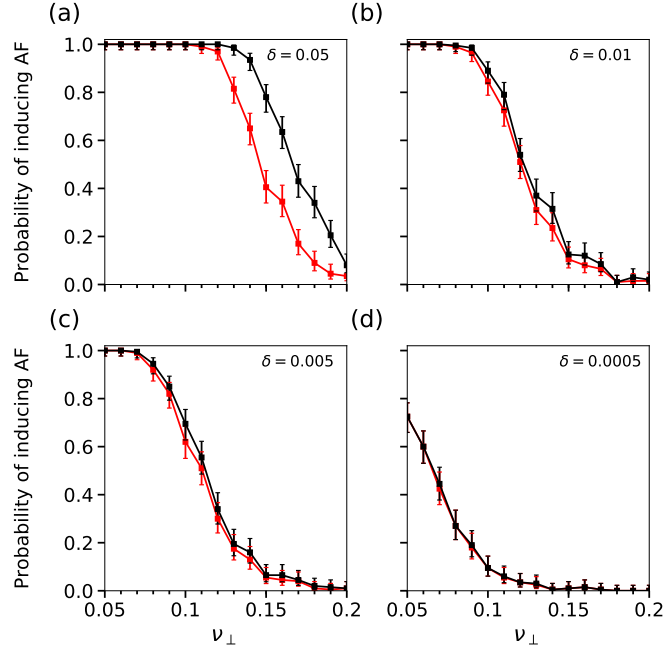


Figure 3.26: **The effect of varying the fraction of nodes that are susceptible to conduction block on the probability of inducing AF.** Phase diagrams for the probability of inducing AF in the CMP model (black) and the cCMP model (red) as a function of the coupling probability, ν_{\perp} . Each subfigure is for a different value of δ , the fraction of nodes that are susceptible to conduction block. In general, the figures indicate that reducing δ reduces the risk of AF. This is consistent with the theoretical risk shown in Eq. (3.6). Additionally, the figures indicate that as δ is reduced, the excess risk of entering AF in the CMP model relative to the cCMP model reduces until both the CMP and cCMP models collapse onto the same curve. This indicates that at high δ , the density of conduction blocking nodes in the lattice is sufficiently high such that complex re-entrant circuits, see Fig. 3.23 and Fig. 3.24, have a noticeable contribution to the risk of entering AF in the CMP model. However, as the density of conduction blocking nodes is reduced, the probability that two conduction blocking nodes are sufficiently close to form a complex re-entrant circuit becomes vanishingly small. As a result, the risk of entering AF is dominated by simple re-entrant circuits that require only a single cell failure to induce AF. Consequently, the risk of entering AF in the model coincides with the cCMP risk where all critical structures are simple re-entrant circuits. This figure has been extracted from [20], see appendix B.1 for details about attributions and permissions.

the endocardium (inner heart wall) rather than the epicardium (outer heart wall) in paroxysmal AF [229, 29]. Additionally, the 3D extension of the CMP model, see section 3.7, suggests a natural explanation for the lowering success rate of ablation as AF becomes more persistent [308]. Despite these findings, the precise dynamics at the microscopic level of the CMP model were not fully elucidated – until now it was not clear how the model is capable of showing the full diversity of AF persistence.

In these sections, we have focused on better understanding the microscopic dynamics of the CMP model, specifically with the aim to understanding which microscopic interactions are responsible for the emergence of persistent AF. By dissecting the model into its constituent parts, we have shown how the formation of complex re-entrant circuits which have a large probability of activating, but a significantly smaller probability of terminating accounts for the difference between the CMP model and the MF/cCMP models. Once activated, these drivers exhibit a wide spectrum of AF event lifetimes from, in real time, a few seconds to months. This spectrum reflects the broad range of AF subtypes exhibited by the model at the same model parameter values, from paroxysmal to persistent AF.

To identify the emergence of persistent re-entrant circuits, we first derived a MF model of AF, neglecting the spatial components of the model and interactions between coexisting drivers. MF approaches are well established in physics for simplifying the study of high dimensional random processes [309]. These models have been used extensively across numerous interdisciplinary fields including in the study of epilepsy in neuroscience [310, 311, 19]. Given the qualitative similarities between epilepsy and cardiac fibrillation, it is surprising that MF models are not widely used in computational cardiac electrophysiology.

Our MF model demonstrates that the essential features of AF remain if spatial structure and driver interactions are neglected. However, the MF model significantly underestimates the time spent in AF relative to the CMP model, and it does not explain the emergence of persistent AF. Only by reintroducing spatial structure can these observations be explained.

Re-introducing spatial structures in the controlled CMP model where we carefully control the initiation of simple re-entrant circuits, we have shown that the density of conduction blocking nodes plays a key role in the time the CMP model spends in AF. At high densities, the CMP model spends significantly more time in AF than the cCMP model. However, as the density of conduction blocking nodes is reduced only simple structures, like those found in the cCMP model, can form in the CMP model. As a result, the time in AF converges for the cCMP and

CMP models.

It is important to stress that the results presented here are for a highly simplified physics model of AF. The scope of the CMP model is highly specific, focusing on the emergence of re-entrant circuits from the accumulation of fibrosis in the atria. We use a cellular automata in our modelling approach which limits the realism of the dynamics in our model, but which recent research has suggested may be preferable to detailed continuous models when studying the effects of local heterogeneity in the cardiac microstructure [312], e.g. due to fibrosis. The model is both structurally and topologically simplified - we do not account for variation in fibre orientation (as in [229]), nor do we consider the real topology of the atria (as in [308]). Additionally, we do not consider variations in the action potential which are present in models which study the ionic currents across gap junctions [313].

However, the value of such a simple model should not be underestimated. Cellular automata are very computationally efficient, allowing for a statistical analysis not easily achieved in more complex models. Likewise, the model has very few key parameters, with re-entrant circuits emerging, and the diversity of AF persistence being explained, by the variation in a single coupling parameter, ν_{\perp} . This gives clarity to any results, avoiding ambiguity as to which model features are responsible for the emergence and maintenance of AF. Finally, although the CMP model itself may not represent a fully realistic atrial electrophysiology, the extensions of the CMP model to 3D and to a real topology are bringing the model closer to clinical relevance. However, naturally, these adaptations complicate model analysis. Hence, understanding the dynamics of simple models is essential to fully understanding the behaviour of the more complicated adaptations for which the CMP model is a precursor. Models such as the CMP model have significant potential in hypothesis generation and will play an increasingly important role in bridging the gap between clinical and computational electrophysiology – such work is already going on in the ElectroCardioMaths centre at Imperial College London, as well as in other groups.

Given that “AF begets AF”, finding ways to treat and prevent persistent AF is a key priority in AF research. In these sections, we have studied the microstructural basis for the emergence of persistent AF in the CMP model. We have shown that persistent AF can arise from the formation of re-entrant circuits with an asymmetry in their probability of activation relative to the probability of termination. These circuits, once active, may drive AF for anywhere from a few seconds to months.

Future work should focus on validating the results obtained here in structurally realistic models of AF, derived from experimentally acquired fibre maps. If successful, this approach may suggest the regions of the atria most susceptible to the formation of persistent re-entrant circuits, and hence, may suggest suitable targets for ablation in persistent AF.

3.6 Increased gap-junction coupling terminates myocardial fibrillation by optimising phase singularity meander - an insilico study

Personal contributions

This section presents the paper “*Increased gap-junction coupling terminates myocardial fibrillation by optimising phase singularity meander - an insilico study*” [26], which we expect to submit in mid 2022. As primary co-author, I played a primary role in every major aspect of this project:

- Understanding the relevant literature.
- Development of the underlying theory.
- Development of the computational infrastructure required to analyse the behavior of the models.
- Management of computer-based simulations and data collection.
- Analysis and interpretation of computer-based simulations.
- Presentation of experimental results.
- Writing of the manuscript.

Note that the phase-singularities detection algorithm was previously described and used in [314].

3.6.1 Context

This section presents the paper “*Increased gap-junction coupling terminates myocardial fibrillation by optimising phase singularity meander - an insilico study*” [26] which is due for submission in mid 2022. Altered gap-junction coupling through the infusion of the experimental drug Rotigaptide has been shown to organise and, in some cases, terminate myocardial fibrillation [27]. The scope of this work is to expand on these clinical evidences in a novel cellular automata model of myocardial fibrillation in which the tissue is modelled as a bi-dimensional lattice and nodes representing cardiac cells may connect longitudinally and diagonally. Using this model, and supported by an experimental rat-model, we demonstrate that the continuous spectrum of myocardial fibrillation can be explained by the interplay of two parameters - (i) the degree and distribution of myocardial fibrosis, and (ii) the sensitivity of cells to depolarisation. Our investigations suggest that a unique region of parameter space exists where the probability of myocardial fibrillation terminating is maximised. In this region, the fraction of excitable myocardial tissue is low, but not minimised. Counter-intuitively, this region is where the fraction of excitable tissue per phase singularity is maximised. Likewise, the meander of the most stable phase singularities in this region is maximised. This suggests that increased coupling terminates myocardial fibrillation by restricting the possible paths of phase singularities in such a way that prevents rotational drivers from stabilising spatially and forces them to meander across the tissue where they collide with other drivers or boundaries.

3.6.2 Introduction

Since the 1960s, multiple mechanisms have been proposed for the maintenance of atrial fibrillation (AF henceforth) and ventricular fibrillation (VF henceforth), with clinical and computational evidence supporting several, seemingly incompatible, hypotheses. Originally, the multiple meandering wavelet hypothesis was introduced whereby depolarising wavefronts break up into wavelets and propagate chaotically throughout the atrial tissue, with no underlying organised drivers of fibrillation [216, 315]. These wavelets generate further wavebreak leading to sustained chaotic activity. In contrast, organised rotational drivers (RDs), anchored to heterogeneities in the myocardial tissue or around phase singularities (PSs), have been proposed as a competing mechanism of myocardial fibrillation [29]. Although both mechanisms have accrued substantial supporting evidence, there is still widespread disagreement in the electrophysiology

community as to the primary mechanism for sustaining myocardial fibrillation [175].

Recently, Handa *et al.* have presented new evidence for a continuous spectrum of fibrillation mechanisms from disorganised multiple wavelets to highly organised RDs in an experimental rat-model [27]. By applying optical mapping techniques to explanted, Langendorff-perfused rat hearts, they demonstrate that by modulating the degree of gap junction (GJ henceforth) coupling and/or the severity and type of fibrosis model, the mechanism of fibrillation can transition between highly disorganised chaotic propagation to highly organised stable re-entry. In the former, where GJ coupling is reduced through the action of carbenoxolone (CBX henceforth) [316], no stable PSs are identified, whereas in the latter, where GJ coupling is increased through the action of rotigaptide (RTG henceforth) [317], a small number of stable PSs dominate the electrical activity of the myocardium with individual drivers persisting for up to 40 rotations. Analogous results are observed in the absence of gap-junction modulation but where the severity of left ventricular fibrosis is varied. At high fibrosis burden ($\sim 25\%$), no stable RDs are observed. Contrastingly, at low fibrosis burden ($\sim < 10\%$), stable, long lived PSs indicate the presence of persistent RDs.

These results suggest that a continuous spectrum of fibrillation maintenance mechanisms exist, spanning disorganised chaotic propagation to organised stable re-entry, mediated by two key electroarchitectural properties, (i) the degree of gap junction coupling, and (ii) the type and severity of accumulated fibrosis in the myocardium.

As part of the investigations into the experimental rat model, it was found that in some cases (5/11 hearts) increasing the degree of GJ coupling at the highest doses of RTG resulted in VF organising to ventricular tachycardia (VT henceforth) before self-terminating. Why VF self-terminates under the action of RTG is not clear. Experimentally answering this question is not easy. The self-termination of VF is a rare event occurring only in a subset of the experimental rat hearts, and taking place on timescales much longer than is feasible using current optical mapping techniques. Experimentally, the self-termination of VF was observed between 5 and 15 minutes after the infusion of RTG, with the duration of the termination event spanning less than 1 second (in some cases less than 0.1 seconds). In contrast, it is difficult to produce optical mapping recordings of explanted Langendorff-perfused hearts lasting longer than 10 seconds. Hence, capturing the self-termination of VF using optical mapping is difficult. This motivates the use of computational modelling to study the termination of VF through the action of RTG. Given the rarity of termination events in myocardial fibrillation, we opt to model increased gap

junction coupling in a phenomenological manner, focusing on the essential properties rather than precise electro-mechanical details. For this reason, the lattice-based models we study produce qualitative rather than quantitative analysis results.

3.6.3 Model

Overview

We have developed a simple phenomenological, lattice-based model of myocardial fibrillation focusing only on the essential qualities of fibrillation dynamics and excluding many higher order effects, following similar approaches developed previously in [25, 295, 28]. The model focuses on the percolation-based discrete propagation of charge through a discontinuous lattice, reminiscent of myocardial tissue decoupled through the action of fibrosis. There is some evidence that models with discrete charge propagation are preferable over more complex models, which assume a functional syncytium, in the case of discontinuous myocardial tissue where fibrosis has decoupled adjacent muscle fibres [312, 277]. Other insilico studies which have used similar, discrete lattice based models include [318, 319, 320] in the context of multiple wavelet reentry ablation, and [321] for the study of the stochastic onset and termination of fibrillation.

The basic rules of the model are summarised in Fig. 3.27. The primary benefit of a lattice-based model is its computational efficiency allowing for the analysis of rare events across large parameter spaces. Critically, the simplicity of this model means that results are qualitative rather than quantitative.

Implementation

Given our continued lack of understanding regarding the action of GJ enhancers like Rotigaptide, we focus on the essential aspects of how conduction is altered under GJ modulation. This is achieved by focusing on two key parameters in our lattice-based model: (i) the cell-to-cell coupling probability, ν , and (ii) the cell excitation threshold charge, Q_{th} . The former models the probability that two neighbouring nodes are electrically connected and is used to simulate the accumulation of diffuse fibrosis. The latter models the excitability of cells, with cells being more likely to depolarise as a function of the input charge as the excitation threshold is reduced. We condense the tissue into a 2-dimensional hexagonal lattice comprising $L_x \times L_y$ nodes representing cardiac cells. Nodes are placed in L_y adjacent fibers and each fiber includes L_y equally

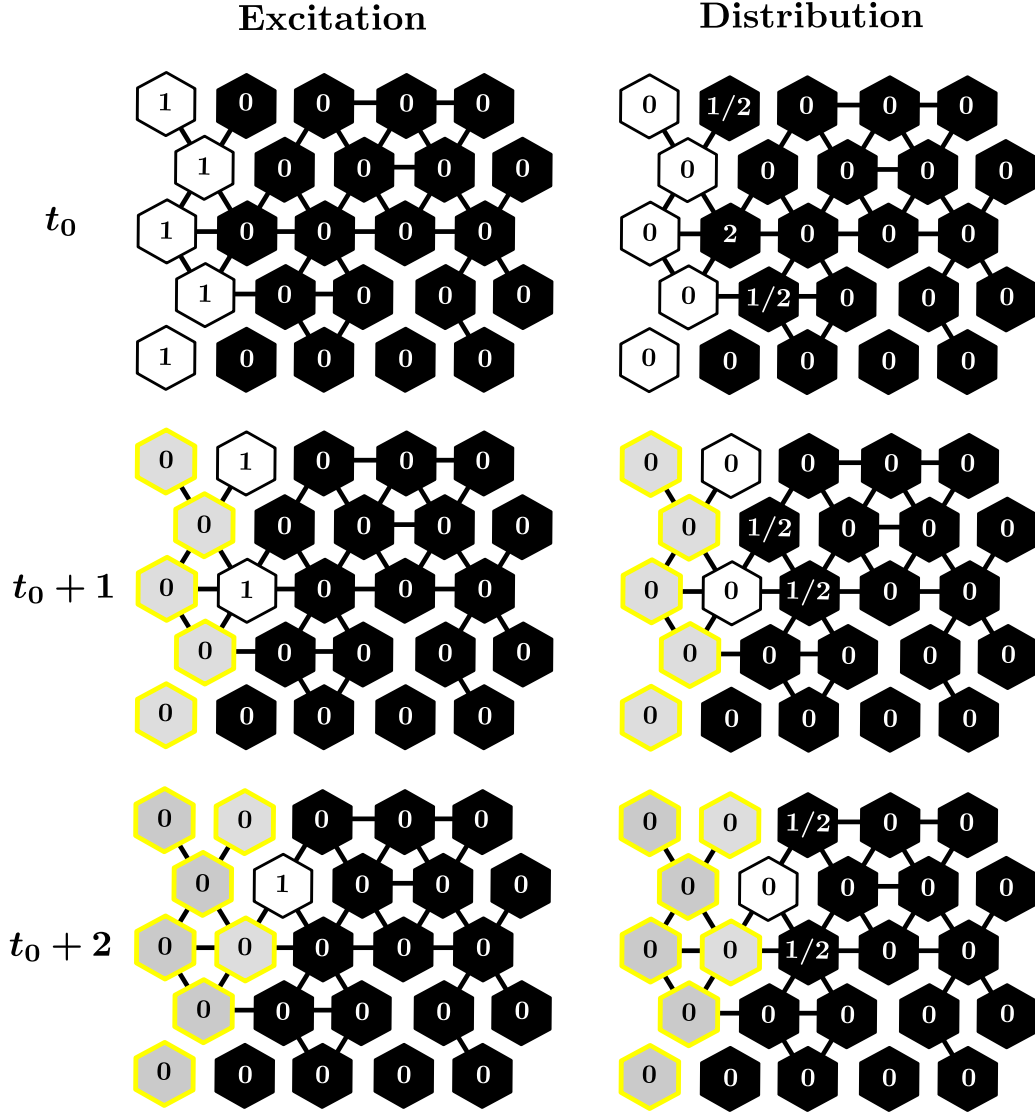


Figure 3.27: A schematic detailing the key rules of the discrete fibrillation model. Each hexagon represents a cell or group of cells. Hexagons are connected to each of their nearest neighbours independently with probability (the static coupling parameter), or disconnected with probability $1 - \nu$. In any given time step a cell is either at rest (black), fully depolarised (white), or repolarising (grey with yellow border). Each active cell in the model splits one unit charge (on an arbitrary scale) equally between each of its connected neighbours at rest. Active and refractory cells receive no charge. Each cell which receives charge will depolarise in the next timestep with probability $\pi(Q, k, Q_{\text{th}})$, which is a function of the received charge, Q , a fixed threshold charge, Q_{th} (the dynamic coupling parameter) and a constant k , see Eq. (3.23). This figure has been extracted from [26], see appendix B.2 for details about attributions and permissions.

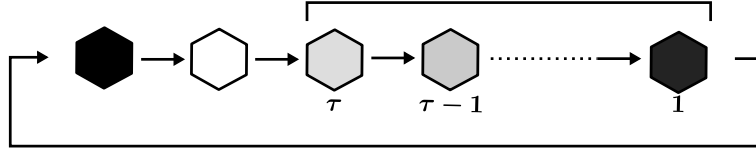


Figure 3.28: **Node states sequence in the hexagonal lattice.** In any given time step a cell is either at rest (black), active (white), or repolarising (grey). This figure has been extracted from [26], see appendix B.2 for details about attributions and permissions.

distanced nodes. In our experiment, the lattice is initialised of size 70×120 cells. This corresponds to approximate tissue dimensions for the rat hearts in lab experiments of $1.4\text{cm} \times 2.4\text{cm}$. Hence, each cell in the model has an approximate linear scale of 0.2mm when converted into real space.

Nodes connect horizontally and diagonally, i.e., north-west, north-east, south-west, south-east, with probability ν . We enforce open boundary conditions on both the left and right edges of the grid and periodic boundary conditions on both the top and bottom edges of the grid. The latter implies that nodes lying in the lowermost (uppermost) fiber can be connected to nodes lying in the uppermost (lowermost) fiber. This setup allows to mimic the cylindrical topology of the real human heart [25]. Nodes can take three different states: resting, excited and refractory. A resting node represents a dormant cell that is able to excite as soon as it is reached by a wave of excitation. A refractory node represents a cell that cannot respond to further stimuli for some time after its last excitation. This cycle mimics the membrane potential pattern of real cardiac cells, see Fig. 3.28. In a given simulation, the lattice is initialised with a fixed value for the cell-to-cell coupling, ν , and the excitation threshold, Q_{th} . This represents a tissue at a fixed point in the gap junction coupling space.

At any time t the (i, j) -th node carries an electrical charge $Q(i, j, t) \geq 0$. The (i, j) -th node that has received a strictly positive charge, i.e., $Q(i, j, t) > Q(i, j, t - 1)$, from neighbouring sites that were active at time $t - 1$ activates with probability:

$$\pi(Q(i, j, t), k, Q_{\text{th}}) = \frac{1}{1 + e^{-k(Q(i, j, t) - Q_{\text{th}})}}, \quad (3.23)$$

where k is a positive constant. When nodes activate, their charge is set to $Q(i, j, t) \rightarrow 1$. An active node transfers its charge $Q(i, j, t) = 1$ to its resting neighbours by distributing it in equal fractions. This implies that as soon as we enter time step $t + 1$, the (i, j) -th node that was active at time t has lost its charge, i.e., $Q(i, j, t + dt) \rightarrow 0$ and enters the refractory state while its resting neighbouring sites have increased their charges by $1/N(i, j, t)$, where $N(i, j, t)$ is the

number of resting neighbours of the (i, j) -th node at time t .

When the (i, j) -th node excites at time t the duration of its next refractory period is

$$\tau(i, j) = \max\{\tau_{\min}, \tau_{\max} \left(1 - \beta e^{-\frac{t - rt(i, j)}{\gamma}}\right)\} + 1, \quad (3.24)$$

where $\tau_{\min}, \tau_{\max}, \beta$ and γ are positive constants and $rt(i, j) < t$ is the last time step in which the (i, j) -th node entered a resting state. This approach was initially proposed in [321] to model the relationship between the current action potential duration and the previous rate of excitation. Each simulation is assigned a unique pseudo-random seed. At time $t = 0$ a wave of excitation is released in the left edge of the lattice. This automatically excites every node lying on this edge, triggering a planar propagation towards right which is governed by the afore discussed charge transferring mechanisms. This wave is then released periodically with time invariant frequency of T time steps. This pacing activity is temporarily intensified to induce fibrillation within the time interval $[t_1^*, t_2^*]$, where $0 < t_1^* < t_2^*$. In this window, the regular pacing from the left edge coexists with a supplementary periodic release of waves spreading from a pre-determined, small region of the lattice with higher pacing frequency T^* . Finally, the regular pacemaking stops at time $t_3^* \geq t_2^*$ and the electrical activity is monitored until spontaneous termination or a final time $t_4^* \geq t_3^*$ if it becomes self-sustained.

For each point in coupling space, if fibrillation can be sustained regularly for short periods after initiation, new simulations are generated until N independent samples exist (each with their own random seed) in which fibrillation is successfully sustained.

For each of the N simulations generated in which fibrillation is sustained, activation maps are generated and phase processed to derive statistics regarding the number, position and behaviour of phase singularities in the tissue. For computational reasons, the time window over which each simulation is phase processed is relatively short (1000 time steps), allowing for a larger total number of simulations.

For each of the phase processed simulations, a second simulation is generated with the identical random seed which is allowed to evolve for up to 10^5 time steps. For each extended simulation, we record whether or not fibrillation self-terminates.

Phase processing is carried out using a custom Matlab (MathWorks, Massachusetts, USA) script as described previously [314]. This method used in silico is identical to the approach used for the experimental rat hearts. For an in depth analysis of the experimental rat model and discussions regarding the spectrum of organisation for myocardial fibrillation, see [27].

Further limitations of our approach are presented in section 3.6.6 while the calibration of the

model parameters is discussed in appendix E.1.

3.6.4 Results

Insilico spectrum of myocardial fibrillation

Fig. 3.29 shows a phase diagram for the gap junction coupling parameters at which fibrillation is inducible in the insilico model. The number of phase singularities, their lifetime, and the degree to which they move across the tissue varies widely across the parameter space. The grey boundary indicates the region of parameter space beyond which the tissue is not sufficiently coupled (either static, low, or dynamic, high Q_{th}) to allow for sustained activation. Note, this boundary can be extended by including a pacemaker-like feature in the insilico model which prevents the model from self-terminating due to the absence of ephaptic coupling. This feature has been omitted in the current work given its lack of relevance to the self-termination of fibrillation at high coupling.

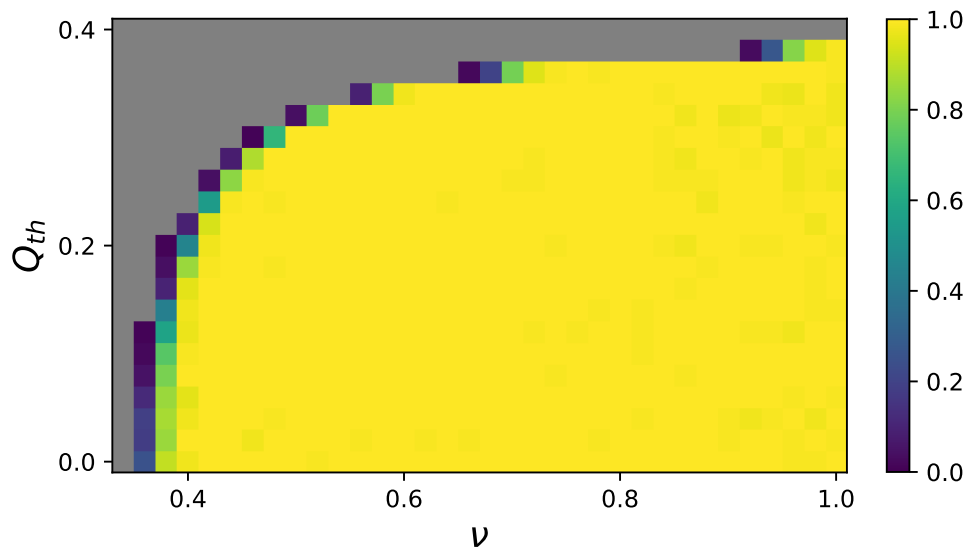


Figure 3.29: **The probability of inducing fibrillation in the insilico model.** Greyscale indicates the region in which fibrillation is not inducible while the colorscale represents the probability of inducing fibrillation across the coupling space (ν, Q_{th}) . This figure has been extracted from [26], see appendix B.2 for details about attributions and permissions.

Close to the percolation boundary, PSs are short lived and move around erratically, implying the

absence of long-lived stable drivers. Conversely, as the degree of static and dynamic coupling in the model is increased, the degree of spatial and temporal organisation of PSs increases in the model. This is summarised in Fig. 3.30 where we present characteristic snapshots of the phase processed activation maps in the insilico model alongside a schematic detailing the spectrum of organisation for myocardial fibrillation. Fig. 3.31 shows the statistics for the phase processed simulations across coupling space. Fig. 3.31(a) shows the average duration of the observed PSs. Fig. 3.31(b) shows the spatial density of the dominant driver frequency in the insilico model (i.e., the fraction of tissue at the modal activation frequency). Fig. 3.31(c) presents the dominant driving frequency of fibrillation while Fig. 3.31(d) presents the total number of PSs identified over the phase processed simulation period. All measures are shown on an arbitrary scale from the minimum to maximum observed value for a specific statistic. Fig. 3.31 demonstrates that

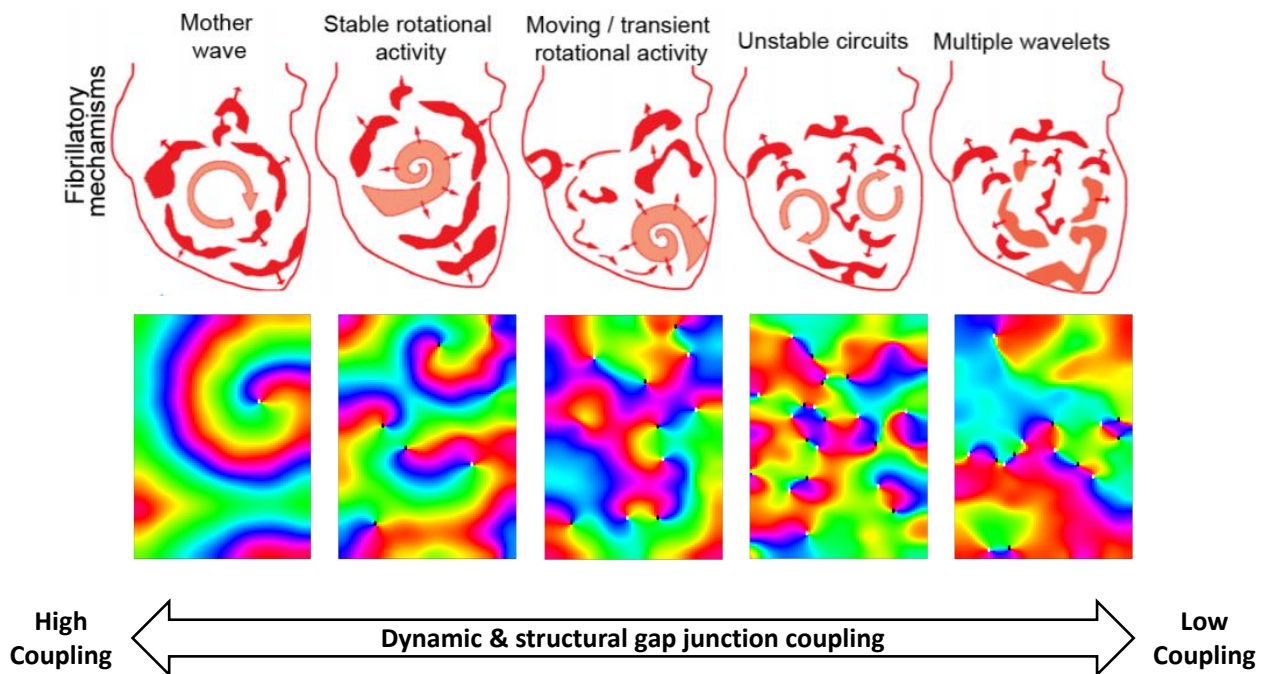


Figure 3.30: **Spectrum of organisation in myocardial fibrillation with corresponding phase processed examples from the insilico model.** The black (white) points indicate clockwise (anticlockwise) phase singularities. This figure has been extracted from [26], see appendix B.2 for details about attributions and permissions. The top illustrative panel has been used with permission from [27], see appendix A for details about attributions and permissions.

as the degree of coupling in the insilico model is increased, PSs become longer lived, dominate a larger fraction of the myocardial tissue, drive at higher frequencies, and reduce in their total number. With the exception of the final observation, these phase singularity statistics

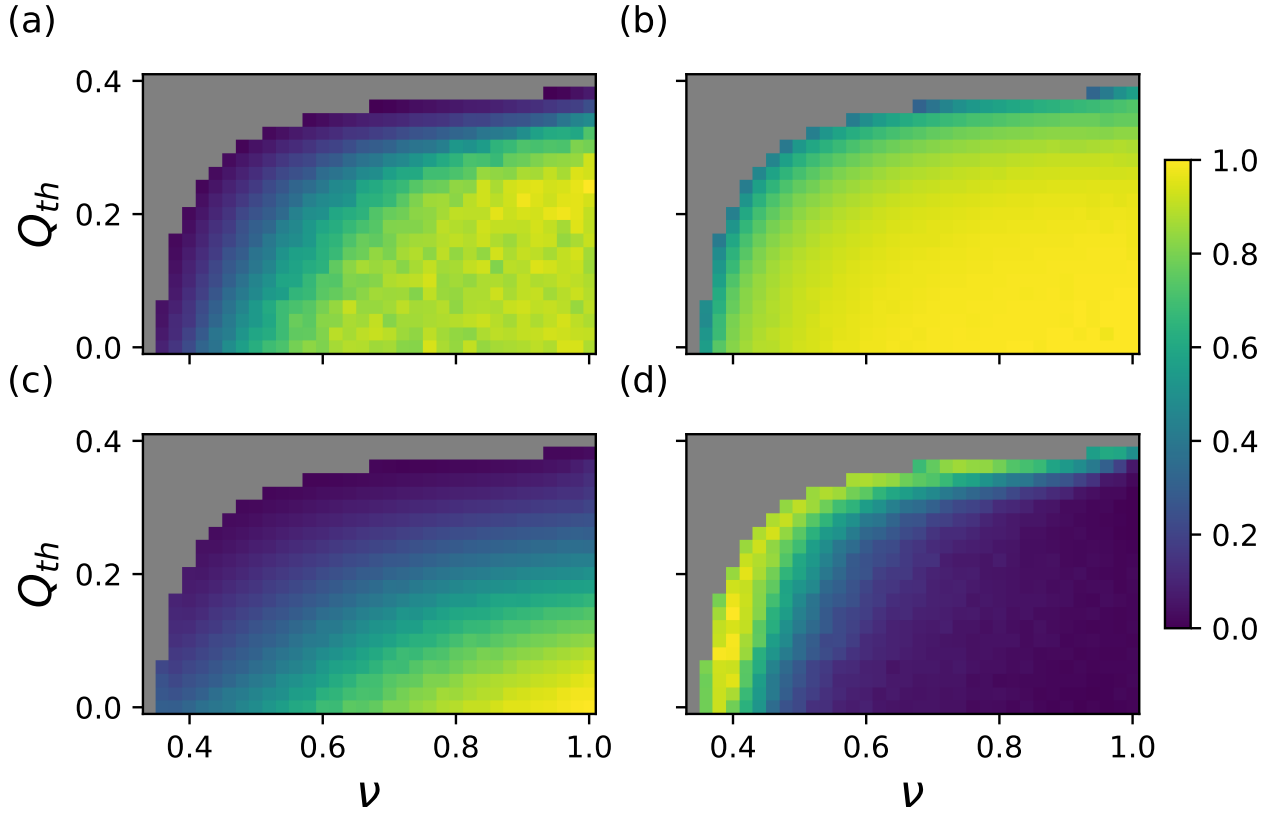


Figure 3.31: **Phase processing statistics from the in the insilico model.** (a) The average lifetime of the recorded phase singularities. (b) The density of the dominant frequency. (c) The dominant frequency. (d) The total number of phase singularities identified over a fixed time window. Scale normalised. Greyscale indicates region where fibrillation is not inducible, see Fig. 3.27. This figure has been extracted from [26], see appendix B.2 for details about attributions and permissions.

correspond well to what is observed experimentally.

Experimental data reports very few PSs at low coupling, before a sharp increase in the number of PSs at moderate coupling. In the insilico model, see Fig. 3.31(d), there is a hint of the initial increase in the number of PSs when moving from low to moderate coupling, however, in general we observe an increased number of PSs as we approach the grey, low coupling percolation boundary. This appears to be in conflict with the experimental findings, however, it is critical to stress that this observable is highly sensitive to the lifetime threshold set for identifying phase singularities. With reference to the average PS lifetimes shown in Fig. 3.31(a), the number of PSs identified at low coupling will increase (decrease) significantly if the lifetime threshold for the identification of a PS is lowered (increased). This accounts for the large number of phase

singularities identified at low coupling in the insilico, but not experimentally.

Combining the observations in Figs. 3.30 and 3.31, the model effectively demonstrates that increasing the degree of gap junction coupling organises fibrillation such that long-lived rotors are the dominant underlying mechanism of fibrillation. In contrast, a reduction in the degree of gap junction coupling disorganises fibrillation such that long lived rotors do not drive fibrillation. In this state, the activity observed more closely resembles the multiple wavelet hypothesis. Between these two states exists a continuous spectrum of myocardial organisation.

Spontaneous termination of myocardial fibrillation at high cell to cell coupling

After initiation, simulations in the insilico model can be extended for long durations to assess the probability of fibrillation spontaneously self-terminating. Fig. 3.32(a) shows the probability that fibrillation is sustained to the end of the simulated period (10^5 time steps, or ca. 40s). This duration can be extended but serves little practical purpose and limits the total number of simulations that can be generated.

Two regions are apparent where the probability of fibrillation terminating is non-zero. The first, bordering the grey, low coupling percolation boundary is associated with conduction block from a lack of cell-to-cell coupling and arises in the model due to the absence of ephaptic coupling [322]. The second region at higher coupling is found at approximately $\nu > 0.7$ and $0.2 < Q_{th} < 0.35$. This region is separated from the low coupling termination region and may be thought of as arising from increased cell-to-cell coupling in the model. The low coupling termination region correlates well with short-lived, unstable PSs as shown in Fig. 3.31. However, the high coupling termination region does not appear to be associated with any of the observables shown in Fig. 3.31, nor with the probability of inducing fibrillation shown in Fig. 3.29.

Figs. 3.32(b) and 3.32(c) show two observables which correlate well with the high coupling termination region, although we note the correspondence is not perfect and other factors likely contribute as well towards spontaneous self-termination of fibrillation. Fig. 3.32(b) shows the fraction of quiescent tissue per phase singularity (FQT/PS) which is maximised in the high coupling termination region. This result is somewhat counterintuitive since this ratio can be maximised by either maximising the amount of quiescent tissue in the model or by minimising the number of phase singularities. The latter is intuitively sensible, however, the former appears to conflict with the critical mass hypothesis which suggests that sustained fibrillation is more likely if the ratio of the refractory wavelength to tissue volume is significantly below one [211],

which is associated with a significant fraction of the tissue being in the quiescent state during fibrillation. However, this initial response oversimplifies the problem. Looking at the fraction of

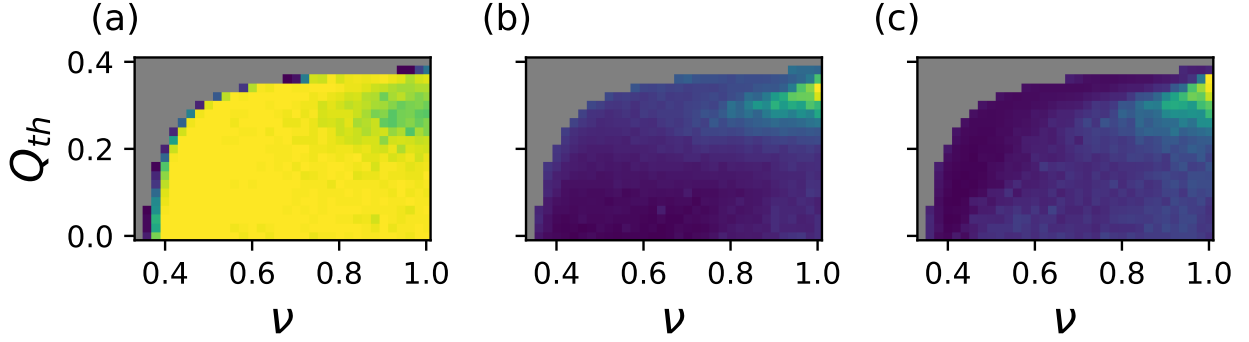


Figure 3.32: **The probability of fibrillation being sustained for the full duration of the extended simulation presented alongside relevant statistics.** (a) The probability that a simulation is sustained for 10^5 time steps (ca. 40s real time). Two regions are identifiable where there is a non-zero probability of fibrillation spontaneously self-terminating. The first is at the boundary of the phase space (bordering grey cells) and is termination associated with the failure of wavefront propagation due to very low cell to cell coupling. The second region of termination is observed for $\nu > 0.7$ and $0.2 < Q_{th} < 0.35$. This region does not appear to correlate with any of the simple statistics presented in Fig. 3.31. The two measured statistics which appear to most accurately predict the region of self-termination from increased coupling are (b) the fraction of quiescent tissue per phase singularity and (c) the degree of phase singularity meander for the most stable PS. See Fig. 3.30 for colormap. This figure has been extracted from [26], see appendix B.2 for details about attributions and permissions.

quiescent tissue (FQT henceforth) at different points in coupling space (see SM), we note that in the high coupling termination region, the FQT is already significantly lower than at the low coupling percolation boundary. However, the FQT is higher than at maximum coupling ($\nu = 1$, $Q_{th} = 0$) where the spontaneous termination of fibrillation is rare. Analogously, the number of PSs observed, see Fig. 3.31, also reduces as coupling is increased. However, the FQT and the number of PSs do not appear to reduce at the same rate with increased coupling. Therefore, since the number of PSs reduces much faster than the FQT in the area approaching the high coupling termination region, the FQT/PS ratio is maximised, despite a low FQT relative to the low coupling region.

This, however, does not explain why the FQT/PS ratio is associated with the spontaneous termination of fibrillation. Fig. 3.32(c) shows the degree of PS meander, measured as the standard

deviation of the PS location coordinate, of the most stable PS, i.e., the PS with the lowest standard deviation for the PS location coordinate, for simulations at different points in coupling phase space. Like Fig. 3.32(b), the minimum PS meander (MinPSM henceforth) correlates well with the high coupling termination region and almost perfectly with the region in which the FQT/PS ratio is maximised. This gives a plausible explanation for why the spontaneous termination of fibrillation is maximised in this region.

Firstly, termination at high coupling is associated with the number of PSs going to zero. Therefore, it follows that a small number of initial PSs are more likely to self-terminate than a larger number. Secondly, if the fraction of depolarised tissue in the model is small, the space into which long-lived PSs can move is highly restricted, offering the PSs a limited number of paths to follow. However, in the region in which the FQT/PS is maximised, the paths which can be followed by PSs are restricted while also covering the largest fraction of myocardial tissue possible relative to other points in phase space. In doing so, PSs are prevented from spatially stabilising, but wavefronts also have insufficient tissue to move into to allow for new wavebreak and the formation of new PSs. As a result, existing PSs meander significantly, colliding with each other or with tissue boundaries, thus terminating fibrillation. However, if the number of PSs and the FQT are both minimised, but in such a way that does not maximise the FQT/PS ratio, PSs are excessively stable and do not meander sufficiently to enable PSs to collide with each other or boundaries, thereby sustaining fibrillation. It is important to note that the MinPSM is used as a predictor rather than the average or maximum PS meander, since this corresponds to the most stable PSs which are the hardest to terminate. All other PSs which are longer lived are like to self-terminate more easily given their greater spatial variance. Although the mean PS meander shows some correlation with the probability of fibrillation self-terminating, this statistic is significantly less discriminatory than the MinPSM. To illustrate these arguments further, Fig. 3.33 shows the survival curves for the probability of sustaining fibrillation over time for (a) the FQT/PS ratio, (b) the MinPSM, and independently, (c) the FQT and (d) the number of PSs. For each panel, simulations have been filtered according to the average PS lifetime (> 300 time steps) to exclude simulations which terminate at the low coupling boundary. Within each panel, the filtered simulations have been split into quartiles, sorted by the statistic of interest. In this respect, the survival curve for quartile 1 in Fig. 3.33(d) includes the 25% of simulations with the smallest number of PSs, and quartile 4 is the survival curve for the 25% of simulations with the largest number of PSs.

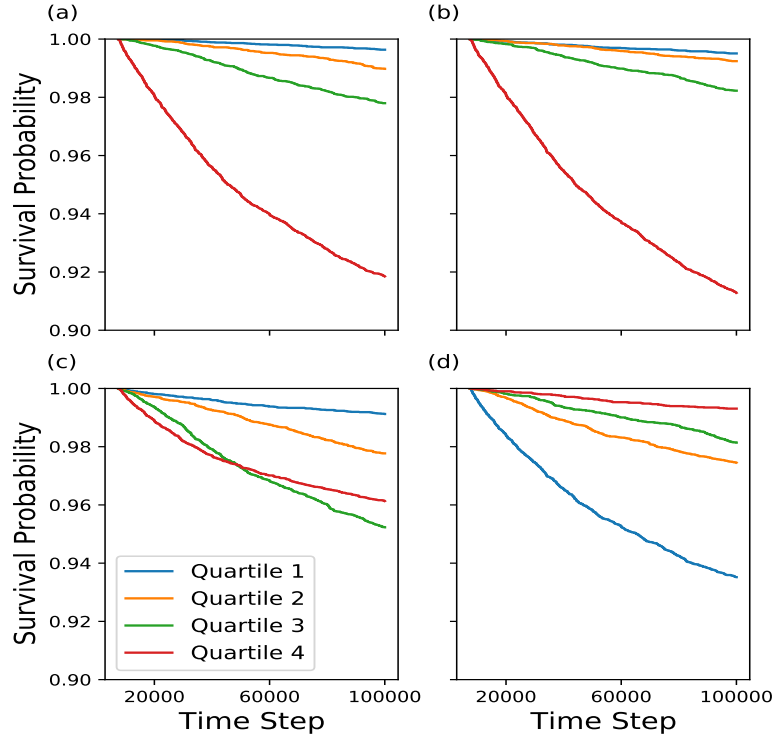


Figure 3.33: **Survival curves for the probability of sustaining fibrillation over time.** The survival curves are grouped by (a) the fraction of quiescent tissue per phase singularity, (b) the minimum phase singularity meander, (c) the fraction of quiescent tissue, and (d) the number of phase singularities. In all panels, simulations have been grouped into quartiles according to the observable in question. This figure has been extracted from [26], see appendix B.2 for details about attributions and permissions.

Fig. 3.33 demonstrates that, in line with the expectation from Fig. 3.32, the survival curves fall off the fastest when the FQT/PS ratio and the MinPSM are maximised. Similarly, Fig. 3.33(d) shows that the self-termination of fibrillation becomes less likely as the number of PSs increases, although the effect is weaker than in Figs. 3.33(a) or 3.33(b). Of most interest is the behaviour observed in Fig. 3.33(c) where we see that the time to termination is maximised at an intermediate value of the FQT.

Fig. 3.34 expands this view by plotting the probability of sustained fibrillation against each of the statistics shown Fig. 3.33. Each point corresponds to a single point in coupling space (averaged over 100 simulations) and is coloured according to the average PS duration to indicate the approximate location of each point on the coupling phase space shown in Fig. 3.31.

Simulations with very low probabilities of being sustained (shown in dark blue) correspond to those which terminate at low coupling due to the lack of ephaptic coupling. In Figs. 3.34(a) and 3.34(b), all points in phase space which sustain fibrillation for all 100 simulations are at low FQT/PS ratios and low MinPSM. Conversely, all points in phase space at larger FQT/PS and MinPSM values have a non-zero probability of fibrillation spontaneously self-terminating. Compare that to Figs. 3.34(c) and 3.34(d) where in both cases, a general trend is observed that the spontaneous termination of fibrillation is more likely as the FQT or the number of PSs is decreased. However, in contrast to Figs. 3.34(a) and 3.34(b), there are points in phase space where spontaneous termination is never observed across the full spectrum of low to high FQT and PS number values.

In summary, the insilico model suggests that the self termination of myocardial fibrillation from increased GJ coupling may be due to Rotigaptide organising fibrillation such that the fraction of quiescent tissue per phase singularity is maximised, but while ensuring that both the fraction of quiescent tissue and the number of observed phase singularities are independently small. This restricts the possible paths into which PSs can move and prevents PSs from stabilising spatially, forcing even the most stable PSs to meander and increasing their probability of a collision with other PSs or tissue boundaries.

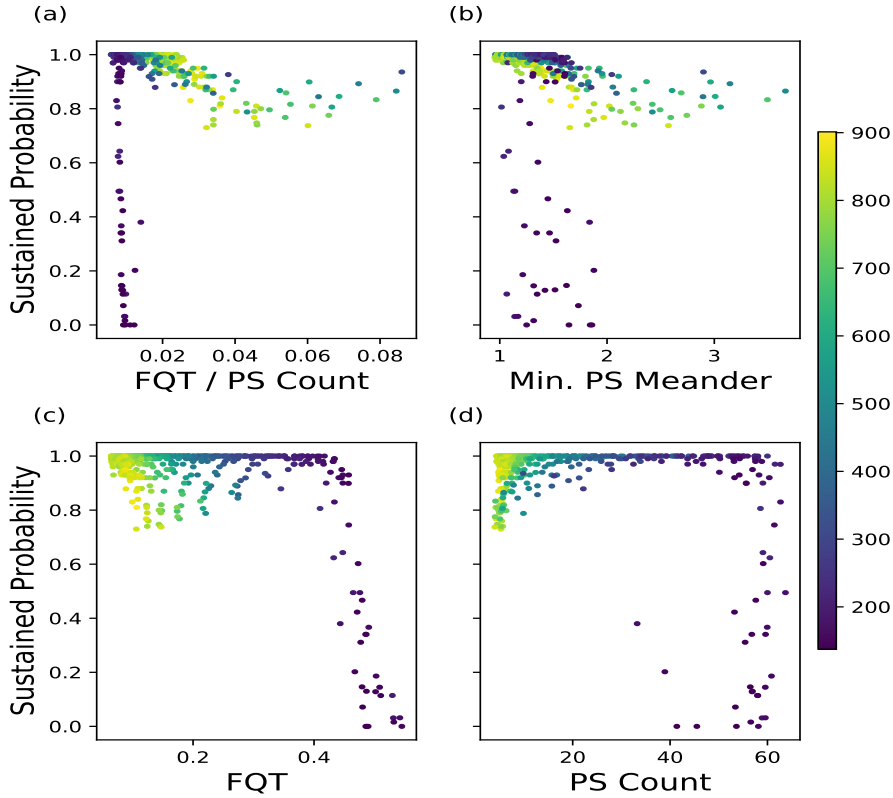


Figure 3.34: **The probability of sustaining fibrillation as a function of different factors.** (a) The fraction of quiescent tissue per phase singularity, (b) the minimum phase singularity meander, (c) the fraction of quiescent tissue, and (d) the total number of phase singularities. Each point represents a set of simulations at fixed ν and Q_{th} . Points are coloured according to the average lifetime of phase singularities to illustrate approximately the position of the simulations on the coupling phase spaces shown in Fig. 3.31. The points marked in dark blue correspond to those simulations where PSs are very short lived and fibrillation terminates due to low cell to cell coupling. This figure has been extracted from [26], see appendix B.2 for details about attributions and permissions.

3.6.5 Discussion

Despite extensive research, there is still significant disagreement in the cardiac electrophysiology community as to the predominant mechanism maintaining myocardial fibrillation. Some researchers argue that fibrillation is driven by the disorganised, chaotic propagation of multiple re-entrant wavelets, whereas others argue that spatially organised (focal) mother rotors drive

fibrillation, with re-entrant wavelets emerging as a secondary consequence of the driving rotor. Both theories have been researched extensively and have accumulated substantial supporting evidence. Therefore, it has been reasonably suggested that both mechanisms may play an important role in fibrillation dynamics and may co-exist, rather than conflict, on a continuous spectrum of spatial and temporal organisation [27].

Conceptually, considering the coexistence of these two mechanisms is important when deciding which ablation strategies are optimal for the treatment of myocardial fibrillation. In the case of the multiple re-entrant wavelet mechanism, ablation strategies inspired by Cox's Maze procedure [236] and informed by the critical mass hypothesis have been developed to maximise the probability of wavelet extinction and collision with tissue boundaries [319, 318]. Although these strategies have been successful in-silico, there is so far little clinical evidence that the addition of linear ablation lines increases ablation success rates in patients with persistent fibrillation over traditional PVI ablation.

In the case of focal drivers of fibrillation, targeted local ablation strategies have been developed which aim to destroy the core of a re-entrant driver, thereby terminating fibrillation [323]. Although these strategies showed promise initially, more recent evidence puts into doubt the effectiveness of these approaches [324].

The failure of mechanism specific ablation strategies for myocardial fibrillation puts us on unsure footing. Evidence exists that both organised and disorganised re-entry are crucial to the maintenance of fibrillation, yet strategies to disrupt these mechanisms have failed. One plausible explanation for this seemingly paradoxical situation may be the apparent failure to consider how treatment strategies for multiple re-entrant wavelets affect the dynamics of focal driver re-entry, and likewise how localised ablation strategies targeting focal drivers may impact the production of new re-entrant wavelets. For example, studies investigating the optimal placement of linear ablation lines often state that ablation lines must connect to a tissue boundary to avoid the creation of a topological hole [319]. By connecting to a tissue boundary, the ablation line increases the rate of wavelet destruction by increasing the ratio of the tissue boundary length to area. However, if a linear ablation line doesn't connect to a tissue boundary, this line can become an anchor for spatially organised macro-reentry [33].

Such considerations suggest that the development of mechanism specific treatment strategies is not complete without a careful consideration of how these treatments will impact other potential mechanisms of fibrillation. It is possible that certain treatment strategies may only be

effective in certain regions of coupling space (and consequently at certain levels of fibrillatory organisation), but that the same strategies will be ineffective after myocardial remodelling.

Pharmacological treatments for fibrillation have the benefit that they are able to alter the electrical properties of the myocardium (albeit for a transient time period) in a manner not achievable by ablation and may terminate myocardial fibrillation without invasively damaging the myocardium. Even if pharmacological cardioversion fails, these treatments may change the electro-phenotype of the fibrillation dynamics and may improve a clinician's ability to identify specific structural substrates to which re-entrant drivers anchor, potentially improving the success rate of ablation in such scenarios.

Numerous drugs have been developed and tested for the prevention and cardioversion of myocardial fibrillation [325], however, these drugs have failed to achieve widespread use due to a combination of a lack of efficacy and serious cardiac and extra-cardiac side effects. In the case of Class I antiarrhythmic agents (sodium channel blockers such as Propafenone and Flecainide), cardioversion is achieved by reducing cell excitability and reducing conduction velocity, thereby (it is believed) destabilising rotors [325]. Similar strategies are deployed by multiple ion channel blockers such as Amiodarone. If cardioversion can be achieved using gap junction enhancement, drugs such as Rotigaptide may avoid some of the dangerous side-effects of existing antiarrhythmic treatments. Initial evidence suggests that Rotigaptide (and its successor Danegaptide) are not associated with the same dangerous side-effects as other pharmacological treatments of fibrillation [317, 326].

In previous studies, Rotigaptide has been investigated for its ability to inhibit the initiation of myocardial fibrillation [327, 328] and its effect on the success of, and energy required for DC cardioversion [329]. However, the potential of Rotigaptide and related gap-junction enhancers for pharmacological cardioversion has not been extensively tested, possibly because the predominant belief so far has been that gap junction enhancement stabilises re-entrant drivers, thereby sustaining fibrillation and preventing the self-termination of individual drivers.

Mechanisms for the stability of reentrant drivers and rotor drift have been investigated extensively [330], although not to our knowledge in the context of gap junction modulation. Two previous studies have noted the spontaneous termination of fibrillation after gap junction enhancement with Rotigaptide [331, 27]. In particular Takemoto *et al.* note that Rotigaptide results in the “considerable meandering and drift [of a reentrant driver] in favor of its early self-termination by collision with the anatomical boundaries” [331]. This is consistent with,

and an important validation of, the insilico results in our current study. However, Takemoto *et al.* offer no clear mechanistic explanation for why Rotigaptide enhances spiral-wave meander and how this mechanism may be affected by the electroarchitectural phenotype of myocardial fibrillation.

In the current study, we have applied a simple insilico model to study the spontaneous termination of myocardial fibrillation. Computational models have a strong history in cardiac electrophysiology research, having played an important role in studying a wide range of different problems. Models have generated new hypotheses for the mechanisms of myocardial fibrillation, such as the original Moe model which illustrates the multiple wavelet hypothesis [216], and have been used for in-silico drug trials to test potential pharmacological treatments for AF and VF [332]. Similarly, recent developments in the creation of personalised heart models [333] have enabled the testing and implementation of personalised ablation strategies based on patient specific fibrosis patterns [286]. Although these models are certainly no replacement for experimental and clinical research, computational modelling is effective at studying problems which, for technological, ethical or economic reasons, may be out of reach using current experimental methods.

Computational models in cardiac electrophysiology span a range of different complexities and purposes. At their most complex, personalised heart models take a fully integrative approach - these models aim to carefully reproduce realistic behaviour at various scales from the subcellular to organ level [333]. For instance, these models may aim to model realistic ion-channel dynamics while also integrating realistic organ topology and tissue deformation. Additionally, patient specific data acquisition, from MRI or otherwise, may be used to integrate realistic fibrosis patterns or tissue defects. However, the complexity of these models comes at great computational cost. As a result, such models are limited in the duration of fibrillatory activity they can study, or the number of simulations they can process for a range of different input parameters [313, 333]. A side effect of such complexity is that these models struggle to study phenomena which take place on much longer timescales than the feasible simulation timescale, often around 30s real time.

An alternative to high complexity personalised models are simple abstract models which simplify several aspects of the electrophysiological problem and focus on understanding the role of a small number of key parameters. These models are limited in their realism and are therefore often not suitable for quantitative problems, but they may still have valuable qualitative in-

sights. A major benefit of these approaches is that their greater simplicity significantly reduces computational complexity. As a result, feasible simulation timescales are much longer and a far wider range of input parameters can be studied [321].

We hypothesise that the spontaneous termination of myocardial fibrillation in our model from increased spiral-wave meander is made possible by simultaneously reducing the number of driving phase singularities and by reducing the fraction of quiescent tissue in the myocardium, but in such a way that maximises the area of quiescent tissue per phase singularity. In doing so, enhanced gap-junction coupling enables spiral wave meander and termination by (i) restricting the possible paths phase singularities can move into by limiting the fraction of quiescent tissue in the myocardium, (ii) preventing the opportunity for new wavebreaks, and (iii) allowing sufficient quiescent tissue such that phase singularities are not able to stabilise spatially. However, perhaps dissapointingly, is this action appears counter-acted if the myocardial substrate is sufficiently fibrotic. Under such conditions, fibrillation rarely self-terminates, with rotational drivers anchoring to lines of block.

Importantly our study highlights that this effect is not achieved with equal efficacy for different electromechanical phenotypes of fibrillation. Qualitatively, we observe significant differences in the probability of spontaneous cardioversion at different fibrosis burdens or gap junction conductances. Unfortunately, a detailed quantitative understanding of how Rotigaptide may induce spontaneous cardioversion is beyond the scope of the current work. Given the safety of Rotigaptide relative to other anti-arrhythmic treatments, prioritising relevant clinical research towards answering these questions should be a key goal for the future.

3.6.6 Limitations

Model Limitations

The insilico model presented here is limited in its physiological realism and should only be used for qualitative insights into fibrillation dynamics. The model focuses on computational efficiency to ensure simulations can be generated which are sufficiently long in real time and cover an appropriate region of parameter space. This also allows an analysis of the robustness of results to changes in the model parameters. To achieve sufficient computational efficiency, the model simplifies a number of features present in electro-physiologically realistic models of fibrillation. For a detailed discussion of the experimental limitations of the rat model, see [27].

Rate-dependent effects

The model simplifies, or omits, a number of rate-dependent features common in other models of cardiac electrophysiology. Firstly, the model does not explicitly account for conduction velocity restitution. This is a limitation of the lattice based approach where the microscopic wavefront velocity is fixed to one lattice spacing per time step [321]. Implicitly, the observed macroscopic conduction velocity in the model is naturally modulated by changes in the coupling parameters such that at very low coupling the observed conduction velocity is significantly slower than at high coupling. At a microscopic level, for the purposes of initiating and sustaining fibrillation, we can qualitatively account for the effect of conduction velocity restitution by merging action potential restitution and conduction velocity restitution into a single curve which simulates the restitution of the refractory wavelength. By doing so, the restitution curve for the refractory wavelength with fixed conduction velocity is treated as identical to the restitution curve for when conduction velocity is variable.

Other rate dependent effects which are not considered in the model are the formation of electrical alternans, or spatial variance in the action potential duration. In the case of the former, such dynamics do not naturally emerge in lattice based models and would require explicitly rules to force cells to produce alternans. This limitation is not easily resolved within the current framework and may be accounted for in future work with more realistic model of fibrillation is such models can achieve sufficient computational efficiency. However, this effect may not be particularly to our current work given that Rotigaptide is known to suppress the formation of electrical alternans [328].

Structural Limitations

The insilico model is a structurally simplified representation of the real myocardium. Topologically, the model tissue is a 2-dimensional pipe with hexagonal lattice cells. This ensures that all regions of the model tissue are treated equally, avoiding bias in the results arising from structural inhomogeneity. Such bias cannot be avoided in a tiling on a topological sphere. Additionally, the tissue does not include orifices to represent key blood vessels, although the pipe topology does ensure that the tissue contains electrically discontinuous boundaries (such as those that may be present at the end of the muscular sleeves extending into the pulmonary veins). Given the focus of this paper on the pharmacological impact of Rotigaptide on fibrillation termination, such simplifications are reasonable. However, investigations into the topological aspects

of reentry must reintroduce these omitted features.

When modelling fibrosis, the approach taken is spatially uniform and probabilistic, with each connection between neighbouring cells exhibiting the same occupation probability across the tissue. This assumption of uniformity is not a fully realistic representation of fibrosis accumulation in the real myocardium, but acceptable as a first approximation for modelling diffuse fibrosis having been used in a number of previous studies [28, 277, 275]. Such an approach is not suitable in the case of highly clustered compact fibrosis. Given the structural simplicity of the model, region specific fibrosis patterns cannot be applied to the model which is topologically simplified. Regarding the spatial inhomogeneity of fibrosis, the probabilistic nature of bond occupation means that there is a small amount of spatial inhomogeneity built into the model. Computationally, it is known that increased inhomogeneity is proarrhythmic, but that qualitatively fibrillation dynamics are similar to more uniform fibrosis deposition [334]. Greater spatial inhomogeneity in the fibrosis distribution can be accounted for in future work.

3.6.7 Conclusion

Despite extensive debate, there is still widespread disagreement in the cardiac electrophysiology community as to the primary mechanism of myocardial fibrillation [33]. Our recent experimental rat model provides evidence that these two mechanisms are in fact not distinct, but lie on a broader spectrum of fibrillatory mechanisms with variable spatial and temporal organisation [27].

In the rat model, the gap junction enhancer Rotigaptide was shown to increase the spatial and temporal organisation of fibrillation and, in some cases, result in the spontaneous termination of fibrillation. Using a simple in-silico model, we have shown that increased structural and dynamic coupling of gap junctions can terminate fibrillation by maximising the meander of the most stable phase singularities.

Given the qualitative nature of these results, it is essential that further experimental evidence is gathered to support these findings and better understand the electro-architectural conditions of the myocardium under which gap-junction enhancement may result in the spontaneous termination of myocardial fibrillation.

3.7 Unified mechanism of local drivers in a percolation model of atrial fibrillation

Personal contributions

This section presents the paper “*Unified mechanism of local drivers in a percolation model of atrial fibrillation*” [28], published in Physical Review E in December 2019. As secondary co-author, I only played a primary role in specific aspects of this project:

- Understanding the relevant literature.
- Development of the underlying theory.
- Writing of specific segments of the manuscript.

I do not take any credit for any other aspect of this project in which I have not played a significant role.

3.7.1 Context

This section presents the paper “*Unified mechanism of local drivers in a percolation model of atrial fibrillation*” [28], published in Physical Review E in December 2019. The main goal of this research is to extend the original CMP model [25] to a three dimensional CAM lattice and assess whether this more complex, yet realistic topology would reveal meaningful insights on the ongoing debate on the mechanisms of AF. Our model shows spontaneous emergence of AF that strongly supports, and gives a theoretical explanation for, the key clinical observations, i.e., diversity of activation, reported by Hansen *et al.* in [29]. We show that the difference in surface activation patterns is a direct consequence of the thickness of the discrete network of heart muscle cells through which electrical signals percolate to reach the imaged surface. In line with the original CMP model, our model naturally follows the clinical spectrum of AF spanning SR, paroxysmal AF, and persistent AF as the decoupling of myocardial cells results in the lattice approaching the percolation threshold. This allows the model to make the prediction that, for paroxysmal AF, re-entrant circuits emerge near the endocardium, but in persistent AF they emerge deeper in the bulk of the atrial wall. If experimentally verified, this may go towards explaining the lowering ablation success rate as AF becomes more persistent.

3.7.2 Introduction

In section 3.3.3 we have discussed a recent work of Hansen *et al.* [29] with “the potential to unify some of the previous discrepant observations” [32] on the mechanisms of AF maintenance. This study has suggested that both focal and re-entrant drivers may be explained by the presence of small re-entrant circuits [29, 33] and that stable transmural re-entrant circuits may project differently onto the endo- and epicardium. These projections typically appear as rotational activity on the endocardium and focal (breakthrough) points on the epicardium. Hence, the apparently incompatible 2d projections onto the atrial walls are consistent with a single underlying mechanism of localised re-entrant circuits in the transmural region [29, 30, 31]. Leading clinicians have called for further work “to confirm and extend these observations” [32]. In the following sections, we develop a percolation based model of AF initiation in pursuit of this goal. Our aim is to understand the origin of the AF mechanism, how it changes as AF becomes more or less persistent, and how this effects the success rate of ablation. We take a physics approach to modelling, focusing on the essential features of the phenomenon as opposed to the fine details. This is much simpler than more biophysically realistic models and allows for concrete predictions based on large scale statistics not accessible in a laboratory setting. The model generates activation wavefronts that propagate in a 3d medium mimicking the complex discrete fibre structure of the atria. AF emerges spontaneously via the formation of spatially stable but temporally intermittent 3d re-entrant circuits when the fibre network decouples, e.g., through fibrosis or fatty infiltration [335]. The model predicts that these circuits should have a minimum length of 12.5 mm, comparable with the 15 mm quoted in [29]. Re-entrant circuits are quasi-1d with isolated fibres that have a width of around 2 mm, making their identification with clinically available mapping technologies difficult [336]. Our results demonstrate how 3d re-entrant circuits emerge and how they are distributed in the heart wall when the coupling between cells is lowered, closely matching key clinical observations reported by Hansen *et al.* in [29]. The observed activation patterns fundamentally change as a function of the depth from the imaged surface to the driving re-entrant circuit. If this depth is large, we observe focal (breakthrough) activity. If this depth is small, we observe re-entrant or rotational activity.

The model predicts that the drivers of paroxysmal AF are located near the endocardium whereas the drivers of persistent AF are uniformly distributed through the atrial wall. Consistent with clinical experience, the former are more easily ablated than the latter. We test this by

numerically simulating focal ablation. We find that ablation lesions that do not penetrate the full depth into the tissue are significantly less likely to destroy a re-entrant circuit in persistent AF than in paroxysmal AF. Additionally, we show that in persistent AF, even if ablation successfully destroys a local source, the existence of multiple co-existing circuits prevents the global termination of AF.

3.7.3 Model definition

We consider a simplified $L_x \times L_y \times L_z$ pipe topology of the atria with open boundaries in x and z , and periodic boundaries in y . Nodes are connected longitudinally to their neighbours in the x direction with spatial frequency ν_{\parallel} and transversely, in the y and z directions, with frequency ν_{\perp} , see Fig. 3.35(a). Once the network is defined at the start of a simulation, it is fixed for the remainder of the simulation.

Each node takes one of three states: resting, where the node can be excited by an active neighbour, excited, or refractory, where for τ time steps after excitation a node cannot be re-excited, see Fig. 3.35(b). We define the SAN as nodes at the boundary, $x = 0$, which excites every T time steps. These settings are identical to those in the original 2D CMP model, see section 3.4.2 and Fig. 3.12. Model parameters $L_x = L_y = 200$, $L_z = 25$, $T = 220$ and $\tau = 50$ are informed by clinically observed values, see section F.1 in appendix F.1. The model results are robust against changes in these parameters. In line with the original CMP model [25], a small fraction of nodes, δ , are susceptible to conduction block. With probability ϵ , these nodes fail to activate when their neighbours excite. When the SAN excites in normal conduction, wavefronts are initiated at $x = 0$ and propagate smoothly in the $+x$ direction and terminate at $x = L_x$. However, re-entrant circuits can form when nodes are sufficiently decoupled, through fibrosis [276, 337], or otherwise, such that the shortest closed loop from a node back to itself is partially isolated from the remaining tissue, and the path length, in units of propagation time, exceeds the refractory period τ , see Fig. 3.36. The formation of these re-entrant circuits drive fibrillatory activity [25, 295].

3.7.4 The spatial distribution of re-entrant circuits

Hansen *et al.* [29] finds that re-entry activity is typically observed on the endocardial surface, whereas focal points are often found on the epicardial surface. Additionally, there is much

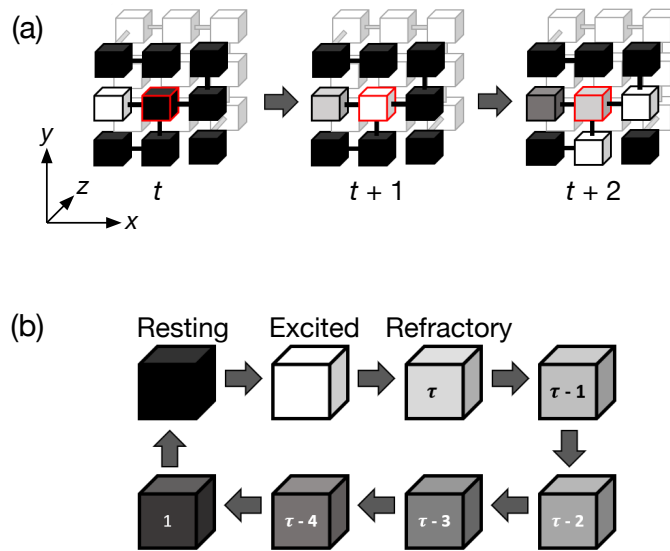


Figure 3.35: **Extending the CMP lattice to three dimensions.** (a) The excitation wave propagates across neighbouring nodes. Nodes are connected longitudinally with frequency ν_{\parallel} and transversally (along y and z directions) with frequency ν_{\perp} . At time t , the red bordered node is resting. At time $t+1$, the node activates in response to the stimulus coming from its neighbour to the left. At time $t+2$, the red bordered node becomes refractory and the excitation wave activates the two nodes in resting state to which it is coupled. The node to the left of the red bordered node cannot be excited as it is in a refractory state. (b) Temporal dynamics of a node. Each node sequentially passes across three distinct states: resting (black), excited (white) and refractory (grey scale). This figure has been extracted from [28], see appendix B.3 for details about attributions and permissions.

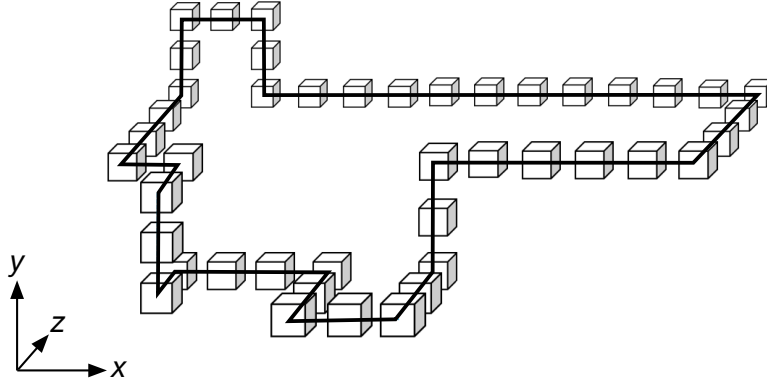


Figure 3.36: **Three-dimensional visualization of an AF driver located in the bulk of the atrial tissue.** The black path represents the connectivity structure between the nodes. In this particular example we observe that longitudinal connections are more frequent than transverse connections (y and z directions), representative of re-entrant circuits that can be observed when ν_{\parallel} is substantially larger than ν_{\perp} . This figure has been extracted from [28], see appendix B.3 for details about attributions and permissions.

stronger longitudinal coupling on the endo- than the epicardial surface. To test whether fibre orientation can account for the distribution of activation patterns observed clinically, we consider a homogeneous and inhomogeneous model. In the homogeneous model all nodes are connected to their neighbours with the same frequencies, ν_{\parallel} and ν_{\perp} . In the inhomogeneous model, the variation in fibre direction changes with depth. Here we fix the average decoupling of nodes, $\bar{\nu} = (2\nu_{\parallel} + 4\nu_{\perp})/6$ and vary linearly the average fibre angle, $\Delta\theta = \tan^{-1}(\nu_{\perp}/\nu_{\parallel})$, in each layer from $\Delta\theta_{\text{ENDO}} = 24^{\circ}$ at the endocardium ($z = 0$) to $\Delta\theta_{\text{EPI}} = 42^{\circ}$ at the epicardium ($z = 24$). These values are taken from clinical data [31]. The introduction of fibre inhomogeneity into the model results in re-entrant circuits preferentially anchoring to the endocardium. An example of this can be seen in Fig. 3.37 which shows a cross-section of the model activation patterns from the endocardium to the epicardium. A re-entrant circuit is shown anchored to the endocardium, with the activation wavefronts propagating from one end of the circuit to the epicardial surface and emerging as a focal breakthrough point. The phase spaces for the risk of entering AF for the homogeneous and inhomogeneous models are shown in Fig. 3.38. For large values of the coupling parameters (no fibrosis) the model exhibits SR indefinitely. As the coupling reduces, a small number of re-entrant circuits can form. Here we observe paroxysmal AF with intermittent episodes of irregular activity. As the coupling is even further reduced,

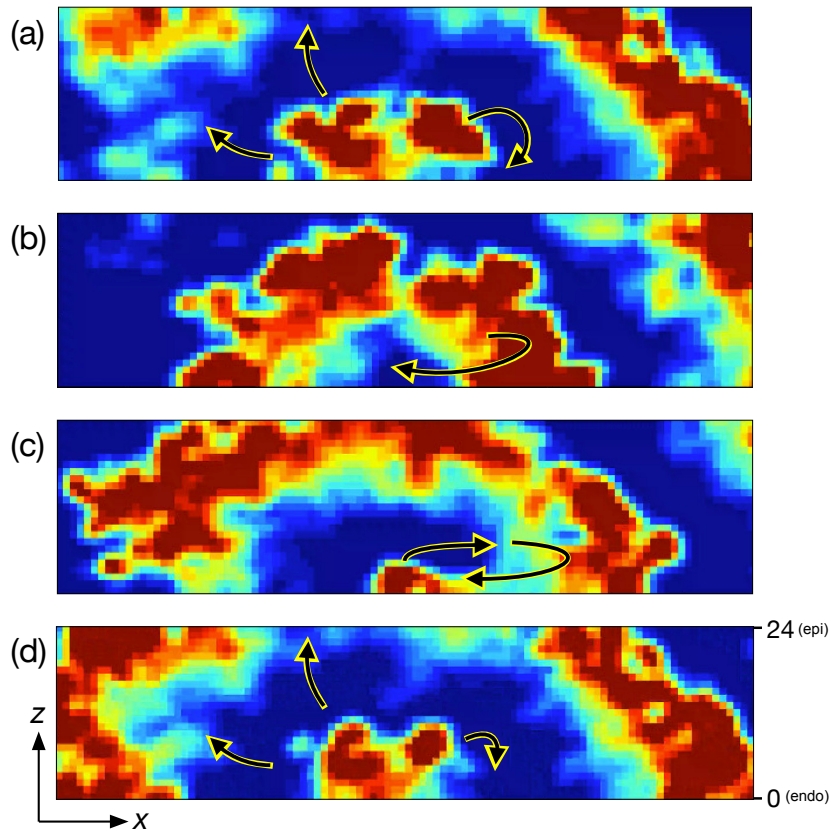


Figure 3.37: **Different projections of the same re-entrant circuit.** A cross-section of the model during AF showing a close-up of the x - z plane (fixed y coordinate). The cross-section has been chosen to align with a re-entrant circuit. Arrows indicate the movement of wavefronts. The top (bottom) surface of each panel corresponds to the epicardium (endocardium). A re-entrant circuit can be seen near the endocardium with (a) activity moving around an isolated fibre, (b/c) re-entering the isolated fibre, and (d) emitting fibrillatory waves from the left end of the isolated fibre. Fibrillatory activity spreads from the endocardium to the epicardium through the complex fibre structure of the model. This results in a wide variety of possible breakthrough patterns on the epicardial surface. When viewed from the endocardium, re-entrant activity will be clearly visible since the isolated fibre lies along the endocardial surface. When viewed from the epicardial surface, the wavefronts propagating from the re-entrant circuit may emerge as a single breakthrough point, or as multiple breakthrough points simultaneously. Scale: 100×25 nodes. This figure has been extracted from [28], see appendix B.3 for details about attributions and permissions.

the model enters persistent AF where, once AF has been initiated, the model will never return to SR without external intervention. These results are consistent with recent evidence showing that local drivers anchor at or near fibrotic lesions [226], with fibrosis increasing the number of re-entrant regions, and the time spent in AF [338]. In the homogeneous model the endo- and

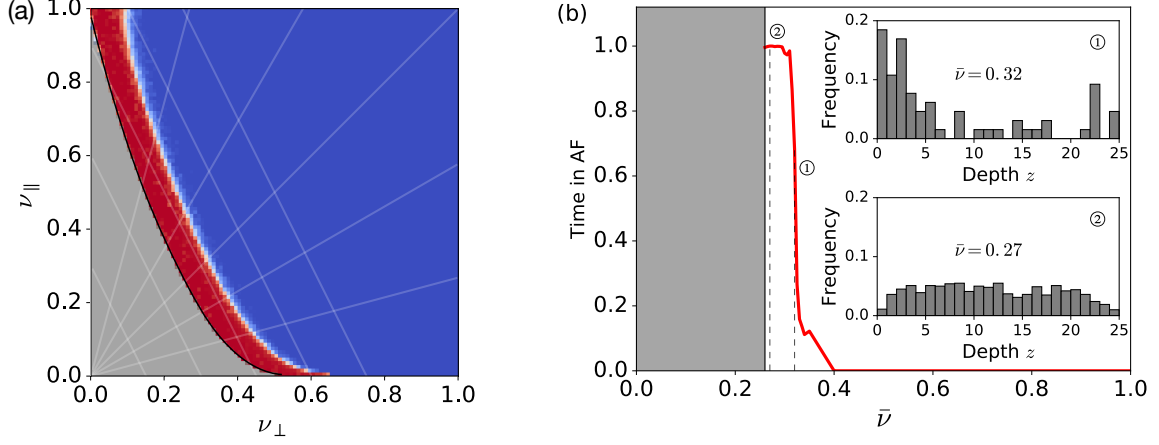


Figure 3.38: **Emergence of AF at different fibrosis burdens.** The average time spent in AF for the (a) homogeneous and (b) inhomogeneous models. Both models show a transition from SR at large coupling (0% AF time) through paroxysmal AF (0% < AF time < 100%) to persistent AF (100% AF time). The grey parameter regions, indicate coupling parameters below the percolation threshold, and are thus irrelevant to clinical AF. (a) Homogeneous coupling parameters, ν_{\parallel} and ν_{\perp} . Blue: SR, red: persistent AF. The white transition region corresponds to paroxysmal AF. Guidelines of positive (negative) gradient indicate constant $\Delta\theta$ ($\bar{\nu}$). (b) Inhomogeneous coupling parameter, $\bar{\nu}$, risk curve (red graph). There is no AF for $\bar{\nu} \gtrsim 0.4$. Decreasing $\bar{\nu}$ associated with decoupling nodes, there is a transition from SR through paroxysmal AF to persistent AF. Inset: Histograms showing the distribution of re-entrant circuits driving AF for paroxysmal AF (top) and persistent AF (bottom) as a function of depth z from the endocardium. Drivers cluster in the sub-endocardial region ($z = 0$) for paroxysmal AF but are uniformly distributed across the bulk for persistent AF. This figure has been extracted from [28], see appendix B.3 for details about attributions and permissions.

epicardium are equivalent, and we find that in paroxysmal AF, the majority of drivers form equivalently on either surface, whereas for persistent AF, the majority of drivers form in the bulk and not on the surfaces, see Fig. F.1 in appendix F.2.

The inhomogeneous model breaks the symmetry between the endo- and epicardium. Here we find that in paroxysmal AF, drivers form preferentially near the endocardial surface, with very

few drivers forming on the epicardial surface and almost none in the bulk of the atria, see Fig. 3.38(b), inset 1. However, in persistent AF, drivers are uniformly distributed throughout the atrial wall, see Fig. 3.38(b), inset 2. Hence, as AF becomes more persistent, the average position of drivers moves away from the endocardium and into the bulk of the atrial wall. The variation in fibre orientation is the only asymmetry between the endo- and epicardium and is therefore responsible for the asymmetry in the re-entrant circuit depths. Because the method by which re-entrant circuits form is fully local [339], the presence of an isolated fibre at one point in the tissue is independent of the tissue elsewhere in the model. Therefore, the results are robust against different choices of fibre orientation and tissue thickness that may be associated with the left or right atria [340], and show that re-entrant circuits will first emerge on the surface with the strongest longitudinal coupling, see Figs. F.2 and H.2 in appendix F.2. Visualizing the activation patterns in the inhomogeneous model on the surfaces at $z = 0$ (endocardium) and $z = 24$ (epicardium), we observe activation patterns consistent with those discussed in [29]. In Fig. 3.39, the left (right) panel shows the activity when viewed from the endocardium (epicardium). For the activation maps, electrical activity spreads across the tissue from point (1) through point (2), but is blocked from reaching the isolated fibre at point (4). The activity loops around the isolated fibre and re-enters the fibre at point (3). This back-propagating excitation passes through point (4) before re-exciting point (1) which sustains the re-entrant circuit. Viewing the same region from the epicardium does not show the same re-entry activity. Instead, the excitation emerges as a point source indicated by a star. The surface activity driven from the atrial bulk will typically appear as a breakthrough point, as opposed to re-entry activity. A cross section of the activation patterns from endo- to epicardium are shown in Fig. 3.37.

3.7.5 The relationship between ablation success rate and fibre coupling

To study the effect of local ablation in the model, we identify the first location at which a re-entrant circuit forms. A new simulation with the identical structure is generated and the nodes at the identified location are destroyed, mimicking focal ablation, up to a prespecified depth, see section F.3 in appendix C for details. This process is repeated until the locations of the first 10 identified re-entrant circuits are ablated. This allows us to study (a) the *global* success rate of ablation as a function of $\bar{\nu}$ by measuring the probability that ablation prevents

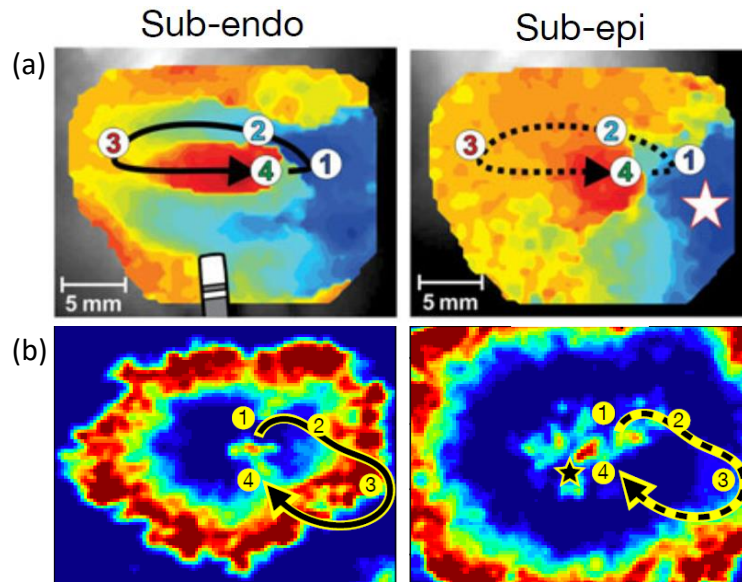


Figure 3.39: **Clinical vs. insilico activation maps from both the endo and epi perspectives.** (a) An activation map adapted with permission from [29] showing re-entry activity from sub-endo imaging and a focal source on the sub-epi side with four marked reference points. (b) The equivalent for our model. Smoothing has been applied to images for clarity. Red: excited nodes, blue: resting nodes, other: refractory nodes. This figure has been extracted from [28], see appendix B.3 for details about attributions and permissions. The top illustrative panels have been used with permission from [29], see appendices A and B.3 for details about attributions and permissions.

AF emerging anywhere in the tissue, and (b) the *local* success rate of ablation as a function of the ablation depth z , by measuring the probability that an ablation, that does not penetrate the full depth into the tissue, destroys the re-entrant circuit at a given location.

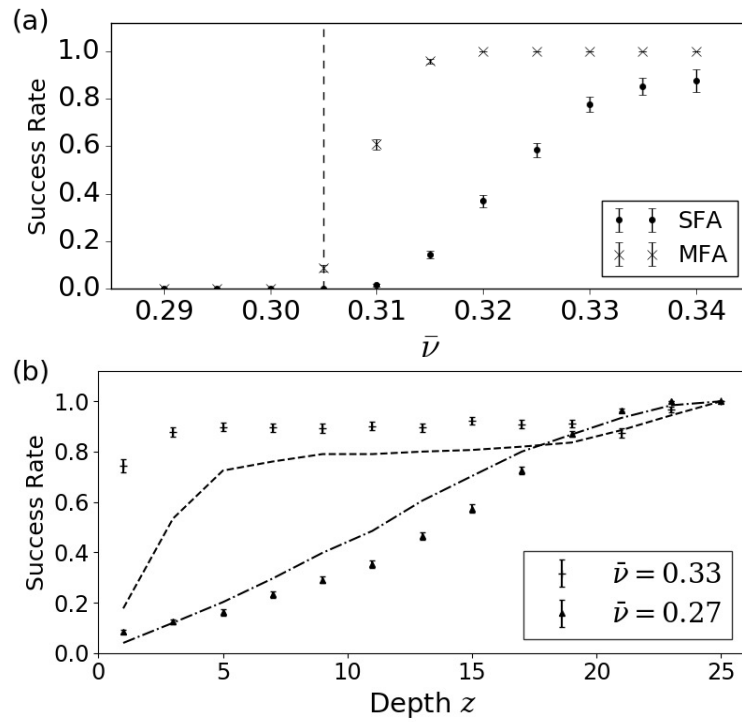


Figure 3.40: **Ablation success rates as a function of fibre coupling and depth.** (a) The global success rate of full depth focal ablation if the first re-entrant circuit location is destroyed (single focal ablation (SFA), circles), and if the first ten locations are destroyed (multiple focal ablations (MFA), crosses) as a function of the coupling parameter, $\bar{\nu}$. The dashed line indicates the coupling value below which all simulated tissues harbour re-entrant circuits. (b) The local success rate of a single focal ablation of destroying re-entrant circuits at the ablation site as a function of the ablation depth, z , for tissues with high coupling, $\bar{\nu} = 0.33$ (plus) and low coupling, $\bar{\nu} = 0.27$ (down triangle). The dashed (dot-dashed) lines correspond to the cumulative sum of the re-entrant circuit depth probabilities for $\bar{\nu} = 0.33$ ($\bar{\nu} = 0.27$). This figure has been extracted from [28], see appendix B.3 for details about attributions and permissions.

Fig. 3.40 shows the global and local success rate of ablation in the model. Globally, Fig. 3.40(a) indicates that the success of ablation exhibits phase transition-like behaviour. At low coupling, focal ablation consistently fails to terminate fibrillation, independent of the number of ablation lesions. Above a transition coupling value, the ablation success rate rapidly increases with increased coupling. The success rate is higher if multiple ablations are applied. The results indicate that focal ablation is increasingly ineffective as AF becomes more persistent. However, despite the fact that ablation fails globally, Fig. 3.40(b) indicates that locally, ablation does

successfully destroy the targeted re-entrant circuits if the ablation is transmural. For non-transmural ablation, ablation has a much higher local success rate at high coupling values - half depth ablation has a success rate of 90% (50%) at high (low) coupling. A direct comparison between transmural and non-transmural ablation is shown in Fig. F.4 in appendix F.3. The activation maps shown demonstrate that for re-entrant circuits anchored to the endocardium, a shallow ablation is sufficient to destroy the re-entrant circuit. However, for re-entrant circuits anchored to the epicardium, non-transmural ablation may fail to destroy the re-entrant circuit driving AF.

3.7.6 Discussion and outlook

These model observations are directly compatible with recent clinical findings that identified rotational activity from endocardial mapping in patients with paroxysmal AF [339, 225], and another clinical observation identifying focal activity in patients with persistent AF from epicardial mapping [224]. Moreover, our model offers a natural explanation why ablation is more successful for paroxysmal than persistent AF. Studies have shown that ablation lesions become smaller as they penetrate further into the tissue from the endocardial surface, and that ablation struggles to penetrate more than 2 mm into the atrial wall [341] which can be up to 7 mm thick [29]. Hence, because the average driver position moves deeper into the atrial wall as AF becomes more persistent, ablation lesions need to be more accurately positioned and they must penetrate further into the tissue, restricting ablation efficacy. The model suggests that if the atria are sufficiently fibrotic, re-entrant circuits are so numerous that focal ablation cannot terminate AF, even with multiple ablation lesions, see Fig. 3.40(a).

Our model is much simpler than alternative biophysically realistic models [313, 333]. We do not account for rate dependent effects in the action potential propagation, although we expect this to play a minimal role in the development and maintenance of structural re-entrant circuits. This has the benefit that we are able to perform unparalleled statistical analyses to fully explore the differences between paroxysmal and persistent AF, but at the cost of electrophysiological realism. As a result, our model focuses purely on the initiation and maintenance of AF from micro-anatomical re-entrant circuits and not on AF initiated or maintained by other methods such as cardiomyocyte automaticity or the formation of rotors and scroll waves. These mechanisms are best studied using alternative models.

In our model, we consider general structural properties such as the difference in fibre orientation

between the endo- and epicardium, but we do not explicitly account for specific anatomical fibre bundles in the real heart or differences between the left and right atria. Therefore, with the current framework, we cannot explain why local drivers are found more frequently in the left atrium than in the right atrium [223, 226]. However, in a proof of concept work where we have adapted the current methods for use with a real atrial fibre map, re-entrant circuits do appear to form preferentially in the left atrium [308]. Additionally, we observe circuits forming in a number of key locations suspected for their role in the formation of local drivers in persistent AF, including the sleeves of the PVs, the posterior atrial wall, and the atrial appendages [342]. To address these limitations and verify the results presented here, we propose a potential experimental test and a number of suggested model developments. Firstly, adapting the model to a realistic atrial topology with an integrated fibre structure will allow us to refine the predictions made here and make concrete statements about different regions of the atria and specific anatomical structures. This includes investigating which atrial regions are especially prone to the formation of re-entrant circuits and testing whether these correlate with known clinical data. We have taken the first steps to adapt the current model to a realistic atrial fibre structure in [308]. Currently, both the model presented here and the adapted model consider the role of local decoupling of muscle fibres, simulating the action of diffuse interstitial fibrosis or fatty infiltration. However, more pronounced global decoupling may occur in regions with compact fibrotic lesions. Future versions of the model should consider a full range of potential fibrosis patterns when analysing the emergence of re-entrant circuits.

As a potential experimental verification of our results, we propose following the methods set out in [29]. Using explanted Langendorff-perfused animal hearts with a diffuse fibrosis model at different levels of fibrotic burden, simultaneous endo- and epicardial optical mapping may be used to assess how the distribution and depth of micro-anatomical re-entrant circuits changes with increasing fibrotic burden. As the fibrotic burden is increased, our model would predict an increase in the number of observed drivers, and a reduction (increase) in the ratio of re-entrant drivers to focal drivers seen on the endocardium (epicardium).

The overarching aim was to create the simplest possible bio-inspired model that displays the variety of clinically observed activation patterns [29], and can exploit large scale statistics to make concrete predictions not accessible in a laboratory setting. The model is consistent with the typical evolution of AF from SR through paroxysmal AF to persistent AF. Moreover, combined with the clinical observations in [29], our model gives substantial evidence for

the proposed unifying mechanism of local drivers in AF, suggesting a potential resolution to long-standing debates. Complementing this finding, we predict that the inhomogeneity in fibre orientation causes the average depth of drivers to move away from the endocardium and into the bulk of the atrial wall as AF becomes more persistent, potentially explaining why ablation is less successful for persistent AF than for paroxysmal AF, if experimentally verified. This insight is the first of its kind and may have key clinical implications.

Work is currently underway on adapting the model to realistic atrial fibre maps with the hope that this may be able to identify re-entrant circuit risk regions clinically on a personalised basis [343, 344].

3.8 Summary of the chapter

Cardiac fibrillation is a diffused arrhythmia in which the healthy planar propagation of electrical waves is disrupted and replaced by fast and disorganized electrical activities drifting across regions of the cardiac tissue [172]. In spite of over a century of research there is no unequivocal consensus on the mechanisms that drive the onset and maintenance of this disease [172, 173, 174, 175, 176, 33], hence the generally poor outcomes of the available surgical treatments [28] and a steadily increasing burden across the globe [172, 194, 195, 196, 197, 198, 199, 200, 201, 202]. In this chapter we have examined the emergence of cardiac fibrillation from the microstructural interplay of cardiac cells, electrical activities and underlying topology. We started from an introduction to the basic structural and functional aspects of the human heart. Next, we discussed the cardiac conduction system and the electrophysiology of cardiac cells. These introductory paragraphs led us to a detailed presentation of atrial fibrillation. In particular, we have discussed its onset, maintenance mechanisms, available treatments and its interactions with and alteration of the cardiac structure. This section is followed by an overview of the major modelling paradigm adopted in cardiac fibrillation research and a deep dive into the Christensen-Manani-Peters model [25], a simple model of atrial fibrillation in which the atrial tissue is conceived as a simple bi-dimensional lattice where nodes mimic cardiac cells connecting longitudinally and eventually transversally and electrical charges periodically propagate across the lattice according to predefined cell-to-cell interactions rules. This work served as a baseline for the novel research presented in the remaining sections of this chapter. First, we discussed the transition from paroxysmal to persistent atrial fibrillation in the Christensen-Manani-Peters model [20]. In this work, we dissected the original model by removing its spatial

component, i.e., the space between critical structures that might host fibrillation-driving activities, and controlling the placement of nodes that are susceptible to conduction block. This led to a mean-field model in which critical structures requiring single conduction blocks are condensed into particles independently activating and deactivating with fixed probability and an intermediate model in which the spatial components are re-introduced while the placement of dysfunctional nodes is controlled to avoid the formation of critical structures that require multiple failures to activate and deactivate [20]. We found that both models underestimate the average time that the original model spends in fibrillation at any degree of fibrotic burden, observing that this discrepancy stems from the fact that the original model allows for the presence of critical structures in which the probability of activation exceeds the probability of deactivation due to peculiar topological features of the surrounding region [20]. This led us to conclude that the activity and interplay of simple critical structures is not sufficient to explain the onset of persistent fibrillation which instead requires “resilient” drivers hosted in regions characterized by asymmetric birth-death probabilities [20].

Second, we have assessed recent clinical evidences [27] highlighting how high dosages of gap-junction enhancer drug Rotigaptide induced a transition from ventricular fibrillation to ventricular tachycardia which culminated in self-termination events in a subset of experimental rat hearts. To do so, we developed a bi-dimensional model of myocardial fibrillation in which nodes may connect longitudinally and diagonally [26]. In this framework, we described the continuous spectrum of fibrillation, i.e., the transition between multiple disorganized circuitual drivers to organized drivers revolving around phase singularities, by studying how the dynamics of the model change within a bi-variate parameters space based on i) the accumulation of fibrosis and ii) the degree of responsiveness of cardiac cells to incoming electrical stimuli [26]. Considering the region in which the probability of termination is maximised, we observed that the fraction of excitable tissue, i.e., responsive to electrical stimuli, per phase singularity and the meander of the most stable phase singularities are also maximised [26]. The topology of this region, being characterized by increased cell-to-cell coupling, mimics the effect of Rotigaptide infusions, thus suggesting that this gap-junction enhancer drug terminates myocardial fibrillation by averting the spatial stabilization of phase singularities which in turn are forced to drift across the tissue and eventually collide with other drivers or tissue boundaries [26].

Finally, we have examined recent clinical evidences supporting a new theory of atrial fibrillation in which long-lasting antagonistic driving mechanisms, i.e., rotational and focal drivers, may

co-exist as mere surface projections of transmural circuital activities [29, 30, 31, 32, 33, 28]. In this context, we introduced a tri-dimensional extension of the Christensen-Manani-Peters model in which the atrial bulk is modelled by a more realistic cubic topology where neighboring nodes may connect longitudinally and transversally, i.e., within the same bi-dimensional sheet, but also to nodes belonging to adjacent sheets [28]. We assessed the dynamics of the tri-dimensional lattice and observed that paroxysmal episodes are driven by rotational activities near the endocardium whereas persistent episodes are driven by activities that are distributed across the entire lattice [28]. In line with the aforementioned clinical evidences, these drivers project as rotational activities when the lattice is observed from the endocardium and as focal point when the lattice is observed from the epicardium [28]. We replicated the effect of ablation procedures on the lattice topology, i.e., by disabling existing connections among neighboring nodes, to find that success rates are related to the fibrotic burden [28]. In particular, iterated lesions hardly terminate fibrillation in highly fibrotic tissues as the uniform spatial distribution of drivers prevents ablation from reaching all the activities that are responsible for the ongoing fibrillatory episode [28]. As coupling increases, drivers tend to concentrate nearby the reachable endocardial surface thus boosting the success rates of ablation procedures [28].

Chapter 4

Emergent correlations and price formation in financial markets

4.1 Introduction

This chapter shifts our attention to financial markets. These systems act as marketplaces where individuals or firms buy and sell a broad range of financial instruments. These interacting participants are remarkably heterogeneous and can be classified according to a broad range of criteria, such as their nature, e.g., humans vs. algorithms, size, e.g., retails vs. institutionals, strategic behavior, e.g., trend-followers vs. arbitragers vs. macro, and goals, e.g., short-term speculations vs. long-term investments. In these days the same financial instrument can be simultaneously traded in several competing venues located across the globes. Furthermore, these venues are likely to adopt different designs and rules, such as trading hours, priority rules for the execution of buy/sell orders bearing the same price, minimum price increment, trading fees, among many others. In this setting, financial markets inevitably form a truly complex ecosystem in which a large number of participants interact across a myriad of venues around the globe while sophisticated technology enables rapid data transmissions and algorithmic-driven fast paced trading. On an academic perspective, such ecosystems raise interesting challenges attracting researchers from different fields.

In my doctoral studies I had the opportunity to investigate financial markets within two different research groups: Prof. Misako Takayasu laboratory at Tokyo Institute of Technology in Japan and Prof. Fabrizio Lillo group at Scuola Normale Superiore in Pisa. At the Prof.

Misako Takayasu laboratory, we have studied how a macroscopic statistical property of foreign exchange markets, i.e., the time-scale dependent cross-correlations between price fluctuations, unfolds from interactions among market participants. We have developed an agent-based model where a market is populated by an arbitrary number of trend-following market makers, i.e., they continuously post a bid and an ask price and re-adjust their pricing according to recent trends [34]. In our ecology we included three independent markets, i.e., market makers acting on a given venue are not affected by events unfolding in other venues, and a special trader, known as the *arbitrager*, who trades opportunistically by submitting buy and sell orders across the three venues to exploit any misprice that guarantee risk free profit [34]. By doing so, the arbitrager causes three synchronous price changes and trend-following market makers will in turn re-adjust their prices in the direction of these changes, thus creating transient and simultaneous price trends across the three venues [34]. Simulations of this ecology shows that the interplay between arbitrage and trend-following strategies generates pronounced cross-correlations between price changes in different markets which resemble those observed in real trading data [34]. These statistical regularities are the consequence of an alteration in the probability of observing two markets moving in the same/opposite direction caused by the transient and iterated synchronizations triggered by the arbitrager [34].

The goal of my collaboration with Prof. Fabrizio Lillo group is the development of new frameworks to better understand the relationships between demand/supply imbalances, market liquidity and price formation. In this thesis I present the first of the two research projects emerged from this collaboration. We introduced a framework in which price fluctuations are characterized by the product of demand/supply imbalances, i.e., the order flow imbalance, and the current liquidity of the market, i.e., the price impact coefficient [37]. In this setting, the price impact coefficient is written as the product of an intraday pattern, a daily level and a stochastic autoregressive component and is estimated via Kalman filter on trading data of multiple securities traded on NASDAQ [37]. This leads to a novel high-frequency state-space model in which price impact is conditionally estimated “on the fly” and price fluctuations are driven by the product of the latest price impact coefficient and the order flow imbalance generated by recent orderbook events [37]. The model suggests that at high frequency time-scales price impact becomes auto-regressive and more dependent on recent orderbook dynamics while the linear relationships between order flow imbalance and price fluctuations established by Cont *et al.* [36] weakens as the discrete nature of price increments becomes more and more relevant

[37].

This chapter is organized as follows. Section 4.2 introduces the reader to the theoretical foundations of financial markets and discusses in detail the two major approaches to the organization of financial trades. Section 4.3 provides an overview of Market Microstructure, an interdisciplinary field focusing on agent-to-agent and agent-to-environment interactions in financial markets. In particular, we expand on the concepts of market liquidity and the price impact of trades. Section 4.4 discusses three important models of financial markets that have influenced and inspired the research presented in this chapter. Section 4.5 presents an agent-based model of the foreign exchange market which describes the formation of cross-currency correlations [34]. Finally, section 4.6 introduces a new statistical model of securities prices which provides insights on the non-trivial relationships between demand/supply imbalances, market liquidity and price formation [37].

Before closing this introductory section, I need to mention two books that have played an important role in my formation as an aspiring financial markets scholar:

- *Trades, quotes and prices: financial markets under the microscope* by J.P.Bouchaud, J.Bonart, J.Donier and M.Gould.
- *Market liquidity* by T.Focault, M.Pagano and A.Röell.

These texts masterfully discuss several topics in Market Microstructure and, more importantly, allow to examine this field under the Physics (Bouchaud *et al.*) and Economics (Focault *et al.*) perspectives. I found these books really enriching for my gradual penetration into this research area, hence, it is not surprising that several introductory paragraphs in the forthcoming sections build on these works.

Note

This chapter includes text and images that have been extracted, with any eventual alteration and extension, from articles I have co-authored [34] and [345]. This material appears in the following subsections:

- 4.2.3 (from [34])
- 4.4.3 (from [34])
- 4.5 and related subsections (from [34])
- 4.6 and related subsections (from [345])

Details on copyrights, permissions and personal contributions to [34] and [345]-[37] are reported in appendices B.4 and B.5, respectively.

Note that for copyrights reasons material appearing in section 4.6 is extracted from [345], which is the latest pre-print preceding [37], i.e., the published version.

4.2 Scopes and organization of financial markets

4.2.1 Introduction

A financial market is a venue in which multiple individuals and firms meet in order to buy and sell, for a variety of reasons, financial instruments such as stocks, bonds, currencies, commodities and other asset classes [21]. A key purpose of financial markets is the facilitation of financial transactions, i.e., a buyer and a seller agree to exchange a financial instrument at a given price, by maintaining and improving infrastructures and tools that allow investors to interact with each other. The dynamics of financial markets are driven by the co-existence of the antagonistic goals of sellers, who aim to sell assets at the highest possible price, and buyers, who aim to buy assets at the lowest possible price [21]. In this setting, it is clear that none of the two sides can attain their optimal outcome. For instance, sellers are very likely to withdraw their requests to sell products if buyers were given the power to set the prices [21]. This matching scheme would be characterized by long lasting negotiations in which the parts would need to adjust their desired prices until a satisfactory compromise is found; delivering a

market characterized by few sporadic transactions resulting from extenuating mediations [21]. Regulators and market designers are tasked with developing and improving the organization, governing rules and infrastructure of financial markets to avoid such an undesirable scenario. In this quest, their goal is the creation and preservation of “high quality” trading activity characterized by the rapid execution of trading requests, low transactions costs and prices that reflect the “fair” value of the traded instruments.

The “ideal market” portrayed in various financial theories is characterized by i) the continuous participation of every participant, i.e., everyone contribute to the formation of the price, ii) prices that fully reflect the “fundamental value” of the traded instrument, i.e., a “theoretical and fair” value that is not affected by exogenous mechanisms, and iii) the absence of any tangible effect of a participant’s activity into other participants [346]. In a recent book [346], Focault *et al.* explain that the unattainability of such a perfect system lies in two “real world” facts that might push actual prices away from the fundamental value. First, only a fraction of potential participants act in the market at any time, hence, prices emerging from the submissions of their buy and sell requests reflect a subset of “views” [346]. As a result, equilibrium prices resulting from the interplay between buy and sell requests of active traders might diverge from the prices that we would have observed under the ideal assumption of complete participation [346]. Second, information is asymmetric in the sense that certain participants might have access to superior information about forthcoming events that will affect the price of a traded instrument [346]. This implies that some orders bear meaningful information, e.g., a trader buys because she has private knowledge about a positive future event, while others do not, e.g., a trader sells because she needs cash to pay the house mortgage, hence, noise and information are entangled in the same order flow [346]. In this setting, participants’ intentions are gradually deciphered by other traders as the trading activity progresses through the day, hence, equilibrium prices emerging when participants are still unable to completely “interpret” the order flow are more likely to diverge from the fundamental value [346].

Stuck in the “real and imperfect” world, regulators and market designers have experimented different approaches to the organization of financial trades, see Fig. 4.1, with the aim of preserving a fair and smooth trading activity [21]. The following paragraphs further expand on this topic by surveying the two most important solutions that exchanges across the globe have adopted to organize financial transactions.

(a)



(b)



Figure 4.1: **Different approaches to the organization of financial interactions.** (a) “Open outcry” is a voice-signs based interaction method used by buyers and sellers who physically operate in a designated arena known as “pit”. The picture portrays the pit at the Chicago Board of Trade, i.e., a Chicago-based trading venue, in the early 90s. (b) In the last decades electronic trading has gradually overtaken physical trading by allowing traders to buy and sell financial instruments through a dedicated online system, often known as *trading platform*. The picture shows a practitioner maneuvering an electronic trading system at the Deutsche Börse, i.e., a Frankfurt-based trading venue. See appendix A for details about attributions and permissions.

4.2.2 Quote driven markets

Until the turn of the millennium a large number of financial markets adopted a quote-driven scheme. In this setting, designated institutions, known as *market makers*, *dealers* or *specialists* depending on the context, provided liquidity to the markets by maintaining buy and sell prices on a broad range of traded instruments [21]. The trading activity proceeds through iterated auctions led by market makers. First, authorized market makers are obliged to *quote*, i.e., publicly reveal, the bid price b_t and ask price a_t at which they are currently committing to buy and sell the traded instrument together with the associated volumes V_t^b and V_t^a , i.e., the maximum number of units they wish to buy/sell at the quoted prices [21]. These commitments are known as *orders* and the distance between quotes $s_t = a_t - b_t$ is known as *bid-ask spread*. The quoting process plays a primary role in these markets as the revealed quotes offer a plausible valuation of the traded instrument that is immediately available to every regular market participant [21]. Traders react to this “signal” by submitting orders bearing prices that are very likely to be aligned with those disclosed by market makers [21]. When demand and supply are revealed, i.e., the market maker and regular traders have posted their orders, the auction enters its sec-

ond phase. In this segment, the market maker mandate is to derive a clearing price p_* and a cleared volume q_* from the current demand and supply and, ultimately, to accept or reject this outcome [21]. Upon acceptance, a subset of submitted orders is satisfied and a total volume of q_* is exchanged at price p_* , thus concluding the auction.

This discussion highlights how a fair and continuous liquidity provision in quote-driven markets is guaranteed through mandates that oblige specific firms, i.e., market makers, to perform these tasks in return for exclusive benefits [21]. In particular, market makers are allowed to set a positive spread between their quotes which compensates them for the risks and costs involved in liquidity provisions, namely, processing costs, inventory risk, i.e., the risk of depreciation of the owned financial instruments, and adverse selection, i.e., the risk of transacting against a trader who has access to superior information on future market dynamics [347].

Fig. 4.2 illustrates the typical organization of quote-driven markets. The outer layer portrays the *retail segment* in which regular market participants interact with designated market makers by submitting buy and sell orders in response to the displayed quotes [346]. The inner layer portrays the *wholesale segment*, also known as *inter-dealer market*, in which market makers manage their inventory exposures by exchanging units of the traded financial instrument with each other [346].

4.2.3 Order driven markets

In the early 1990s the diffusion of computers, together with advancements in the fields of information and communications, prompted exchanges seeking wider participation and lower trading costs to consider electronic platforms, i.e., remote computerized submission of buy and sell requests, as a viable alternative to physical quote driven markets [348]. This drastic shift in the organization of financial trades necessitated a new approach to *price discovery*, i.e., the mechanisms through which a plausible evaluation of the traded instrument is periodically made available to market participants, which has traditionally relied upon market makers' quoting [348]. This call led to the diffusion of online platforms where traders submit buy and sell orders for a certain asset through an online computer program. Unmatched orders, e.g., a request to buy at a certain price that has not found so far a compatible request to sell, *await* for execution in electronic records known as limit order books (LOBs henceforth), see Fig. 4.3. The current state of the LOB can be publicly monitored in real time, hence, the price discovery process is now governed by the interplay of orders submissions, cancellations and matching rather than

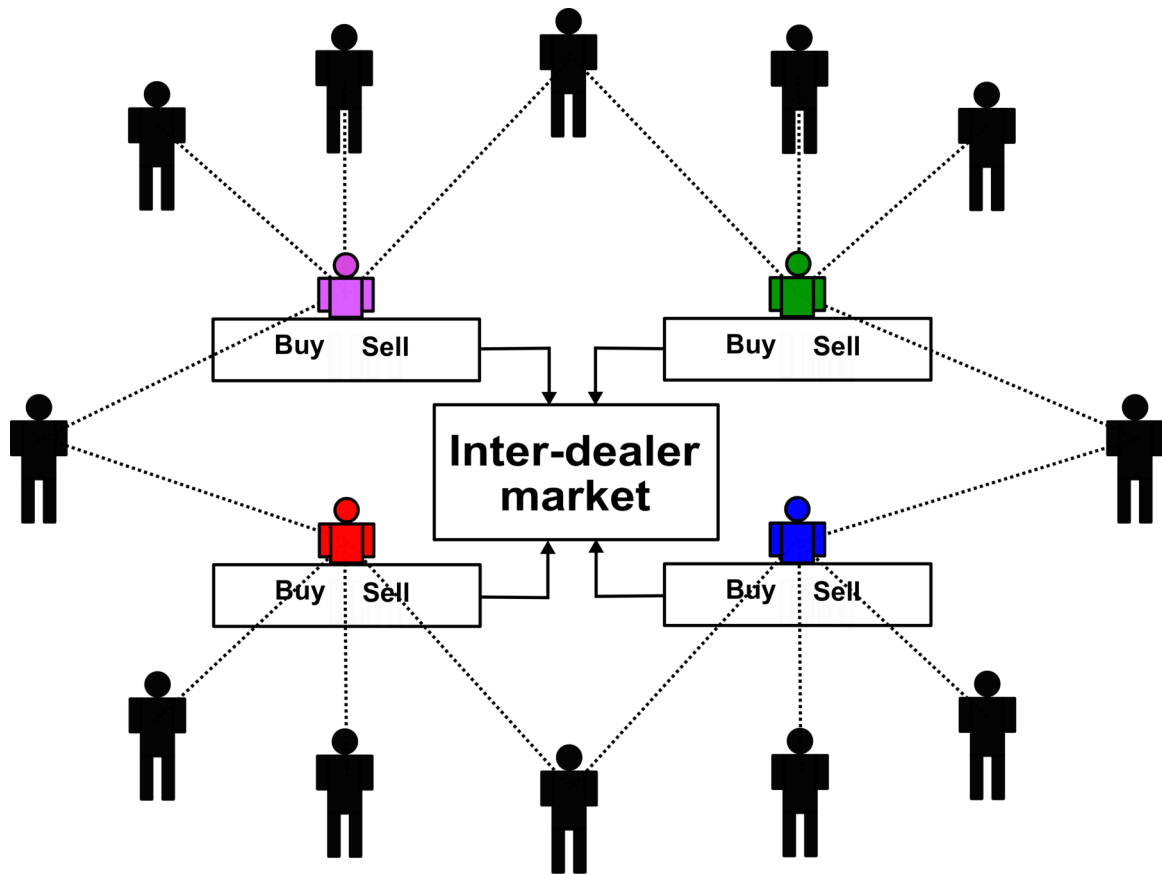


Figure 4.2: **Schematics of a quote-driven market ecology.** Regular market participants (black agents) examine the bid and ask quotes displayed by the designated market makers (colored agents) before picking their favourite dealer and submit their orders (dotted black lines). At the same time, market makers have access to an exclusive “institutional” market, i.e., the inter-dealer market (central rectangle), in which they can manage their inventory by trading with each other. Usually, the exchanged volume, i.e., the number of exchanged units, in inter-dealer markets vastly exceed the one exchanged in retail markets [346].

market makers’ quoting [348]. In this setting, liquidity becomes “*self-organized*” as any market participant can dynamically act as liquidity provider by submitting price-bearing orders, i.e., they post a price at which they buy or sell a number of units of the traded instrument, or as liquidity taker by submitting orders with no specified price, i.e., they immediately match the best available order on the other side of the LOB [349]. This implies that market makers are now more integrated with regular market participants as they maintain and adjust orders on both the buy and sell side of the LOB [21].

By submitting an order, traders pledge to sell (buy) up to a certain quantity of a given asset for a price that is greater (less) than or equal to its limit price [350, 351]. The submission activates

a trade-matching algorithm which determines whether the order can be immediately matched against earlier orders that are still queued in the LOB [351]. A matching occurs anytime a buy (sell) order includes a price that is greater (less) than or equal to the one included in a sell (buy) order, see Fig. 4.4. When this occurs, the owners of the matched orders engage in a transaction. Orders that are completely matched upon entering into the system are called *market orders*. Conversely, orders that are partially matched or completely unmatched upon entering into the system, i.e., *limit orders*, are queued in the LOB until they are completely matched by forthcoming orders or deleted by their owners [351]. The limit order with the best

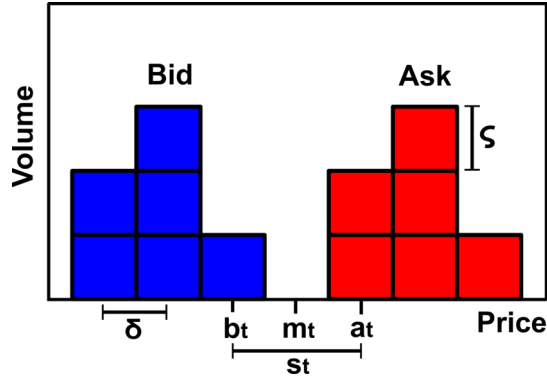


Figure 4.3: **Schematic of a LOB and related terminology.** At any time t the *bid price* b_t is the highest limit price among all the buy limit orders (blue) while the *ask price* a_t is the lowest limit price among all the sell limit orders (red). The bid and ask prices are the *best quotes* of the LOB. The mid point between the best quotes $m_t = (a_t + b_t)/2$ is the *mid price*. The distance between the best quotes $s_t = a_t - b_t$ is the *bid-ask spread*. The volume specified in a limit order must be a multiple of the *lot size* ζ , which is the minimum exchangeable quantity (in units of the traded asset). The price specified in a limit order must be a multiple of the *tick size* δ , which is the minimum price variation imposed by the LOB. The lot size ζ and the tick size δ are known as *resolution parameters* of the LOB [350]. Orders are allocated in the LOB depending on their distance (in multiples of δ) from the current best quote. For instance, a buy limit order with price $b_t - n\delta$ occupies the $(n + 1)$ -th level of the bid side. This figure has been extracted from [34], see appendix B.4 for details about attributions and permissions.

price (i.e., the highest bid or the lowest ask quote) is always the first to be matched against a forthcoming order. The adoption of a minimum price increment δ forces the price to be discretized, hence the same price can be occupied by multiple limit orders at the same time. As a result, exchanges adopt an additional rule to prioritize the execution of orders bearing the

same price. A very common scheme is the *price-time* priority rule which uses the submission time to set the priority among limit orders occupying the same price level, i.e., the order that entered the LOB earlier is executed first [351]. An alternative to this rule is the *pro-rata* priority which assigns a fraction of the matched volume to each limit order involved in the match [21]. The share assigned to each limit order corresponds to the ratio between the volume specified in the order and the total volume queued at that price level [21].

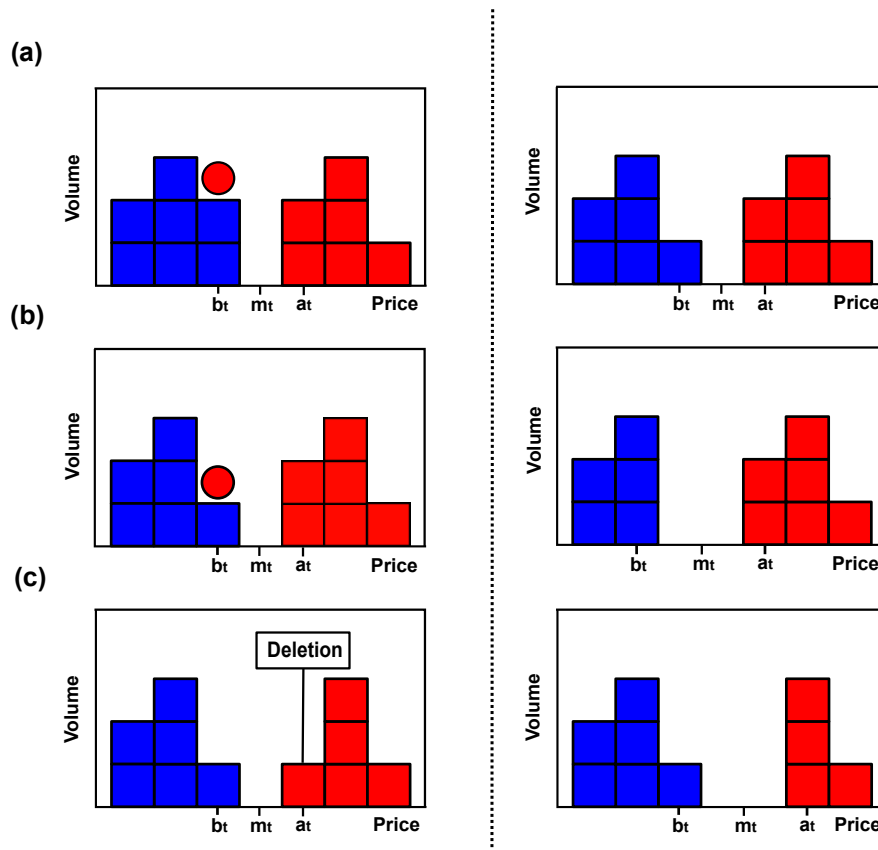


Figure 4.4: **Simple LOB dynamics.** The grid displays different events (left column) and their effects on the LOB (right column). (a) The submission of a sell market order (red circle), i.e., an order which does not include a limit price, prompts an immediate match with the “first in the queue” buy limit order (blue square). This event consumes part of the volume available at the best bid quote but does not alter the current mid price m_t . (b) The same event discussed in (a) occurs when lower volumes are available at the current bid best quote. The match between the sell market order and the last buy limit order available at b_t prompts a negative price change. (c) Order deletions also contribute to the evolution of the LOB. In this example, a positive price change is induced by the deletion of the last sell limit order available at a_t .

4.3 Introduction to Market Microstructure

4.3.1 Overview

Market Microstructure is a rather young discipline which studies the microscopic mechanisms of financial trading, e.g., agent-to-agent or agent-market structure interactions, and offer additional insights on the origins of extensively documented, yet not well understood macroscopic and mesoscopic emergents in financial markets [21]. This definition, which paraphrases the one that Bouchaud *et al.* [21] gave in their recent book, fits very well in the complex systems framework as it emphasises the bottom-up approach, i.e., understand microscopic dynamics to understand macroscopic phenomena, that characterizes this discipline. A more “economics-oriented” definition is the one provided by O’Hara in her 1995 book *Market Microstructure Theory*:

“Market Microstructure the study of the process and outcomes of exchanging assets under explicit trading rules. While much of economics abstracts from the mechanics of trading, microstructure literature analyzes how specific trading mechanisms affect the price formation process.” (M.O’Hara 1995, from [352].)

In this extract we can clearly observe how the author emphasizes the differences between Economics and Market Microstructure, i.e., “*While much of economics abstracts from the mechanics of trading*” [352], and identify the understanding of the price formation process as the key objective of this discipline.

Market Microstructure attracts the interest of people and entities with different backgrounds, mandates and objectives:

- Industry practitioners, such as traders, seeking insights on how to improve and optimize their strategic decisions by better understanding the structure of the environment they operate in [21].
- Regulators and market designers which are responsible for the improvement and preservation of trading venues characterized by “smooth” trading and fair prices [21]. As highlighted by Bouchaud *et al.* [21], the diffusion of algorithmic trading, the relentless pace of the trading activity and the occurrence of sudden extreme price swings, i.e., flash

crashes, are typical examples of contemporary challenges that regulators cannot handle without a comprehensive understanding of Market Microstructure.

- Academics who investigate this field from many different perspectives, such as economists, physicists, mathematicians and computer scientists.

Until the 1990s this nascent field has mostly concentrated on theoretical topics revolving around the relationships between ordinary participants and market makers - a somehow unsurprising fact since the then predominant quote driven markets were driven by the interactions between these two types of agents, see section 4.2.2. For instance, seminal works from this period investigated the factors behind the positive spreads between market makers' buy and sell quotes [347] and introduced models that provide pivotal insights on how prices assimilate information, the impact of the order flow on prices and the influence of adverse selection on market makers' decision [38, 133].

During the years before the turn of the millennium markets began to organize the trading activity in LOBs while computational resources and granular data sets i.e., records of the full sequence of trading events, were becoming more accessible. These dynamics conspired to “revolutionize” Market Microstructure, promoting new research approaches, such as computer-based simulations [22, 35], and raising novel issues that are intimately related to the adoption of LOBs, such as optimal execution [353]. Strikingly, these trends have captured the interest of several research communities that were not traditionally interested in financial markets, thus transforming this discipline into a truly interdisciplinary field lying at the intersection between financial economics, physics, mathematics, statistics and computer science.

In the following sections we introduce some of the most important topics in Market Microstructure. A complete coverage of this field is outside the scope of this dissertation, hence, we limit our discussion to those topics that are related, to different extents, to the original research that is presented in this thesis.

4.3.2 Market liquidity

In the context of financial trading, *liquidity* can be defined as the capability of rapidly satisfying buy and sell requests at prices that are very close to the *consensus* price of the traded instrument [346]. In line with this definition, Wyart *et al.* conceive a liquid market as a venue in which investors “are able to convert cash into stocks and vice-versa nearly instantaneously whenever

they choose to do so” [349].

In practice, one can analyze the costs of trading as a proxy for the “illiquidity” of the market [346]. Trading costs can be split in two groups: i) *explicit costs*, accounting for transaction taxes, brokerage fees, trading fees and other costs, and ii) *implicit costs*, corresponding to the difference between the effective execution price, i.e., the price at which a trader buys or sells an instrument, and a “reference” price at which transactions would have been settled in an ideal, perfectly liquid market [346]. It is common to assume that the the mid price recorded at the submission of the order is a satisfactory proxy for the reference price [346]. As implicit costs are substantially higher than explicit costs, it is sensible to simplify the assessment of market liquidity by focusing on the former and neglecting the latter [346]. The most simple and intuitive approach to the quantification of implicit costs of trading is measuring the current bid-ask spread, i.e., the distance between the current bid and ask quotes or any similar variants, as it informs market participants on what would be the cost of instantaneously buying and re-selling the traded instrument [346]. For instance, the implicit cost of buying is $a_t - m_t$, see Fig. 4.3 for details, while the implicit cost of re-selling is $m_t - b_t$, hence, the sum of these costs equates to the bid-ask spread $s_t = a_t - b_t$. It is easy to observe that the costs of these two actions increase as the effective buy and sell prices, i.e., a_t and b_t , diverge from the reference price m_t . Besides spread-based measures, examples of alternative less trivial metrics for quantifying implicit costs are the volume weighted average price (VWAP henceforth) and price impact-based approaches, i.e., measuring the effect of an order on market prices, see [346] for details. In the previous sections we have seen that positive bid-ask spreads are a fundamental hallmark of both quote driven and order driven markets. This fact indicates that, regardless the rules governing financial interactions, liquidity providers want to be compensated for the risks and costs associated with this task. Hence, wider spreads and lower liquidity gradually emerge as liquidity provision becomes more and more risky. In the next section we further explore this topic by developing a better understanding of the impact that trades have on the price of a financial asset.

4.3.3 Price impact of trades

A basic fact in market microstructure is that market orders contribute to price movements [21]. To better appreciate this, let us consider the idealized LOB displayed in Fig. 4.3 and imagine the arrival of three consecutive sell market orders. This sequence of events would completely

consume the liquidity available at the current best bid quote b_t and partially the one available at the subsequent price level, thus triggering a mid price decrement of $\delta/2$. This trivial experiment illustrates the notion of *price impact*, a central topic for both practitioners and academics that are focused, for a variety of reasons, on modern electronic markets [21]. For instance, a wealth manager that needs to incrementally submit buy orders notice that the price impact of the first segment of the submission, i.e., market orders that trigger price increments by consuming liquidity on the ask side of the LOB, forces subsequent orders to be executed at a worse price, thus generating costs that cannot be neglected [21]. A less discussed, yet similar example can be made for central banks performing large interventions, i.e., purchase and sales of currencies, in the foreign exchange market, see [354].

As illustrated by Bouchaud *et al.* [21], price impact literature is the “battleground” of two contrasting views on this topic and its relation with the *efficiency* of the market, i.e., how well prices reflect the fundamental value of the traded instrument. The first view embraces the assumption of market efficiency, arguing that a subset of informed traders are able to predict the direction of short term price movements and submit orders accordingly [21]. In this “world” uninformed trades, i.e., transactions that are not motivated by superior information held by one of the parts, do not impact prices in the long run whereas informed trades effectively release private information about the fundamental price in what is known in the economics community as the *price discovery* process [21]. On the other hand, the opposite view takes a more “mechanistic” perspective by arguing that the fundamental price does not play any role in the short term and that any trade, regardless of its informative content, impact prices [21]. In this domain the price discovery process is replaced by the *price formation* process, a framework in which price fluctuations are conceived as reactions to the evolution of the order flow, i.e., a sequence of submissions, executions and cancellations of limit orders, independently from the amount of meaningful information revealed by these orders [21].

“If prices move only because of trades, “information revelation” may merely be a self-fulfilling prophecy which would occur even if the fraction of informed traders is zero.” (J.P.Bouchaud 2017, from [355].)

To these days, the debate on an accurate and unequivocal definition of price impact is still open. Bouchaud *et al.* [21] suggest that the major obstacles in this controversy are rooted in the anonymous nature of trades taking place in LOBs and in the intrinsically difficult task of

discerning relevant information from noise.

In practice, the most straightforward approach to the quantification of price impact is the *lag 1 unconditional impact*

$$\mathcal{R}(1) = \langle \epsilon_t(m_{t+1} - m_t) \rangle_t, \quad (4.1)$$

where ϵ_t is the sign of the market order executed at time t , i.e., 1 is a buy and -1 is a sell, m_t is the mid price ex-ante, i.e., before the arrival of the order, and m_{t+1} is the mid price ex-post [21]. A more general version of Eq. (4.4) is the *response function*

$$\mathcal{R}(\tau) = \langle \epsilon_t(m_{t+\tau} - m_t) \rangle_t, \quad (4.2)$$

where $\tau \geq 1$ is an arbitrary lag, i.e., the number of market orders executed from t [21]. A key advantage of these simple approaches is that they allow to estimate price impact through the analysis of basic trading time series, such as best quotes, execution prices and timestamps [21]. However, this simplicity is compensated by an important limitation lying on the fact that limit orders and deletions, despite being important components of the order flow, are not accounted in the response function [21].

In the last two decades, a consistent body of literature reported and examined different empirical facts of price impact [355]. To appreciate some of these observations, let us modify Eq. (4.4) by conditioning the lag-1 impact to the volume of the trade ν

$$\mathcal{R}(\nu, 1) = \langle \epsilon_t(m_{t+1} - m_t) | \nu_t = \nu \rangle_t. \quad (4.3)$$

We can legitimately assume that the impact of market orders increases with their size. This naive assertion holds in both the “fundamental view”, i.e., the information released from a trade is proportional to its size, and the “mechanistic view”, i.e., the liquidity consumed by a trade is proportional to its size [21]. Although trading data provides evidences in support of this intuition, the relationships between the trade size ν and the lag-1 conditional impact $\mathcal{R}(\nu, 1)$ is remarkably sublinear [21]. In their recent book, Bouchaud *et al.* derive the following approximation

$$\mathcal{R}(\nu, 1) \cong c \left(\nu / \langle V^{\text{best}} \rangle \right)^\zeta \langle s \rangle_t, \quad (4.4)$$

where $\langle s \rangle_t$ is the average bid-ask spread, c is a constant of order 1, $\langle V^{\text{best}} \rangle$ is the average volume available at the best quote on the opposite side of the LOB and ζ is a real-valued parameter [21]. Their experiments reveal that the parameter ζ takes values in the range 0 – 0.3, hence Eq. (4.3) is generally characterized by a staunchly concave shape which almost flatten, i.e., the

influence of ν on $\mathcal{R}(\nu, 1)$ is almost negligible, for small tick stocks [21]. The authors identify the origin of this empirical fact in a peculiar market practice known as *selective liquidity taking*, i.e., the tendency of traders to submit market orders of size $\nu \approx V^{\text{best}}$ [21]. This behavior is somehow unsurprising as reducing the size of a large order to the volume available at the opposite best quote would save the trader from the burden of having a fraction of her order executed at worse prices. This implies that large volumes are very likely to be submitted only if the trader perceives that the volume available at the opposite best quote is large enough to “cushion” the impact of her order, hence the remarkably concave shape of Eq. (4.3).

Price impact is a topic of great interest for both practitioners and academics, hence its rapid transformation into one of the most important area in Market Microstructure research [21]. Many notions, empirical laws and topics, such as the impact of *metaorders*, i.e., orders that are split and sequentially submitted in smaller “pieces”, the relationship between autocorrelated order signs and price impact, the Propagator Model and cross asset impacts are outside the scopes of this introductory section. However, a comprehensive and well presented overview of these topics can be found in the recent book of Bouchaud *et al.* [21].

4.4 Models of financial markets

4.4.1 Introduction

Similarly to other disciplines, scientists try to understand the dynamics of financial markets through models. Until the 1980s the dominance of quote driven markets and the relatively poor availability of granular data and computing power favored the development of theoretical models [347, 133, 38] aimed to formalize the mechanisms behind the interactions between market makers and regular traders. From the late 1980s the increasing availability of precise and granular trading records, the diffusion of computers and the gradual adoption of LOBs made financial markets an appealing topic to physicists, computer scientists and mathematicians, among others. This expansion beyond the economics and finance communities introduced new modelling paradigms, such as agent-based models [35, 137, 356, 357], networks [7, 8], zero-intelligence [22, 23, 24], machine learning [358, 359], data exploration [360, 361], and favoured the emergence of novel problems in financial literature, such as understanding the statistical regularities found in financial time series [362, 363, 364, 365, 366] or the mechanisms of market crashes [367, 368, 369].

In the following sections we provide a glimpse of how these diverse communities have positively contributed to the understanding of financial markets by presenting three influential models. Section 4.4.2 examines the Kyle’s Model [38], an early and very influential study of the interactions between a market maker and a trader who can access superior information on the future price of the traded security in a quote driven market. In line with many other works from the *economics approach*, the model encompasses *perfectly rational* agents whose actions aim to maximize their individual utility [350]. Kyle’s work provides important theoretical insights on the importance of adverse selection risk on market makers’ pricing decisions and on how prices assimilate private information [21]. Section 4.4.3 examines the Dealer Model of Yamada *et al.* [35], an agent-based simulation of an order driven artificial market participated by two or more interacting market makers. In this ecology agents sequentially update their bid and ask quotes by taking into the account recent price trends and eventually interact when an agent is willing to buy at a price that matches or exceed the ask price of another agent. Finally, section 4.4.4 discusses the Cont-Kukanov-Stoikov model [36], a simple statistical model of the relationship between supply/demand imbalances in a LOB and price fluctuations. The authors introduce the concept of *order flow imbalance*, a simple metric to measure supply/demand imbalances from the volume supplied and taken by limit order placements, deletions and executions, and construct a linear model in which high frequency price changes are explained by the product between the order flow imbalance and a *price impact coefficient* [36].

4.4.2 The Kyle Model

The Kyle Model [38] is a seminal, yet essential framework in the entire Market Microstructure literature [21]. The model was presented in *Continuous auctions and insider trading* [38], an article published in *Econometrica* in 1985, with the goal of studying how prices incorporate private information that progressively emerge from the actions of informed traders [21]. The model relies on a simple ecology populated by a market maker acting as a liquidity supplier, a trader who has superior information on the traded security and multiple uninformed traders who buy and sell according to individual reasons. The trading activity develops in two simple steps, i.e., t_0 and t_1 . At time t_0 the informed trader obtains private pieces of information on the future value of the traded security p_{t_1} and uses this exclusive advantage to set the direction $\epsilon^I \in \{-1, 1\}$, i.e., 1 is buy and -1 is sell, and the volume q^I , i.e., number of units, of its trade that maximize the expected gain [38, 21]. At the same time, N uninformed traders submit buy

and sell requests generating a net uninformed order flow $\Phi = \sum_{j=1}^N \epsilon_j^{UI} q_j^{UI}$ such that $\Phi \sim \mathcal{N}(0, \Sigma_\Phi^2)$ [38, 21]. As a result, the market maker receives a net buy/sell volume $\Theta = \Phi + \epsilon^I q^I$ and fulfills it with her own inventory, i.e., “stockpiles” of financial instruments, at a clearing price p_* [38, 21]. In the Kyle model, the goal of the market maker is to avoid *ex-post regrets* by choosing the “right” value of p_* [38, 21]. In this setting, the clearing price is determined by the visible net buy/sell volume Θ and a constant λ , i.e., the well known *Kyle’s lambda*

$$p_* = p_{t_0} + \lambda \Theta. \quad (4.5)$$

On the other hand, the informed trader fixes her requested volume

$$q_*^I = \operatorname{argmax}_{q^I} \mathbb{E} [\epsilon^I q^I (p_{t_1} - p_{t_0} - \lambda \Theta)], \quad (4.6a)$$

$$= \operatorname{argmax}_{q^I} \mathbb{E} [\epsilon^I q^I (p_{t_1} - p_*)], \quad (4.6b)$$

$$= (2\lambda)^{-1} (p_{t_1} - p_{t_0}), \quad (4.6c)$$

by maximizing her expected gains $\mathbb{E} [\epsilon^I q^I (p_{t_1} - p_*)]$ in the context of quadratic programming [38, 21]. The lack of private information about p_{t_1} forces the market maker to *estimate* $\epsilon^I q^I$ by knowing i) the total net volume Θ , ii) that the informed trader will try to trade a volume q_*^I that is proportional to $p_{t_1} - p_*$ and iii) that the next price change distribution is $\Delta p = p_{t_1} - p_{t_0} \sim \mathcal{N}(0, \sigma_{\Delta p}^2)$ [38, 21]. It can be shown, see [21] for details, that the expected value of $\epsilon^I q_*^I$ from the market maker perspective is

$$\mathbb{E}[\epsilon^I q_*^I | \Theta] = \frac{\Theta \sigma_{\Delta p}^2}{\sigma_{\Delta p}^2 + 4\lambda^2 \Sigma_\Phi^2}. \quad (4.7)$$

Recalling that Eq. (4.7) is an *estimate* of the quantity derived in Eq. (4.6), equating Eqs. (4.7)-(4.6)(c) allows the market maker to deduce the expected value of p_{t_1}

$$p_* := \mathbb{E} [p_{t_1} | \Theta] = p_{t_0} + 2\lambda \frac{\Theta \sigma_{\Delta p}^2}{\sigma_{\Delta p}^2 + 4\lambda^2 \Sigma_\Phi^2}, \quad (4.8)$$

which is in turn used to fix the clearing price p^* [38, 21]. Finally, λ is found by equating Eqs. (4.8)-(4.5)

$$\lambda = \frac{\sigma_{\Delta p}}{2\Sigma_\Phi}, \quad (4.9)$$

see [21] for detailed calculations.

The Kyle model is a crystalline example of how seminal models of financial markets provided important intuitions on central problems in Market Microstructure. The model shows that

informed trades, i.e., the quantity q_*^I , linearly impact prices, see Eq. (4.5), and that this impact is scaled by the ratio $\lambda = \sigma_{\Delta p}/2\Sigma_{\Phi}$ [21]. The Kyle's lambda captures the contrasting effects of private information and uninformed trading on market prices: the higher the ratio, i.e., $\sigma_{\Delta p}$ is large hence certain traders possess a substantial amount of private information, the larger the impact of q_*^I on the clearing price p_* [21]. This confirms that market makers, perceiving adverse selection, i.e., the risk of trading against a counterpart which can exploit superior information, as a major threat to their profitability, fix a clearing price p_* that compensates them for their exposure to informed traders [21].

4.4.3 The Dealer Model

The Dealer Model [35] was introduced by Yamada *et al.* in 2008 as an artificial agent-based market. This framework relies on a simple market ecology in which N agents interact in a single inter-dealer market where trading is organized in a LOB. For simplicity, the model assumes a continuous price grid, neglecting the role played by the tick size in real financial markets. Agents act as market makers by maintaining buy and sell limit orders through which they provide a bid and an ask quote to the market, see Fig. 4.5. Transactions occur when the i -th agent is willing to buy at a price that matches or exceeds the ask price of the j -th agent (i.e., $b_i \geq a_j$). Trades are settled at the transaction price $p(g_t) = (a_j(t) + b_i(t))/2$, where g_t is the number of transactions occurred in $[0, t[$. It is important to stress that the mid-price $m(t)$ and the transaction price $p(g_t)$ are two different quantities. The former, being the mid point between the best quotes, is the *center* of the LOB and can be tracked at any time step. The latter is sampled whenever two agents engage in a trade.

The Dealer Model assumes that a transaction prompts the entire market to immediately update their dealing prices $z_i(t + dt)$, $i = 1, \dots, N$ to the latest transaction price $p(g_t)$, see Fig. 4.6. In the absence of interactions, agents independently update their dealing prices by adopting a trend-based strategy

$$\frac{dz_i(t)}{dt} = c\langle\Delta p\rangle_n + \sigma\epsilon_i(t), \quad i = 1, \dots, N \quad (4.10)$$

where $\sigma > 0$ and $\epsilon_i(t)$ is a Gaussian white noise. The term

$$\langle\Delta p\rangle_n = \frac{2}{n(n+1)} \sum_{k=0}^{n-1} (n-k)(p(g_t - k) - p(g_t - k - 1)), \quad (4.11)$$

is a weighted average of the last $n < g_t$ changes in the transaction price p .

The real-valued parameter c controls how the current price trend $\langle\Delta p\rangle_n$ influences agents'

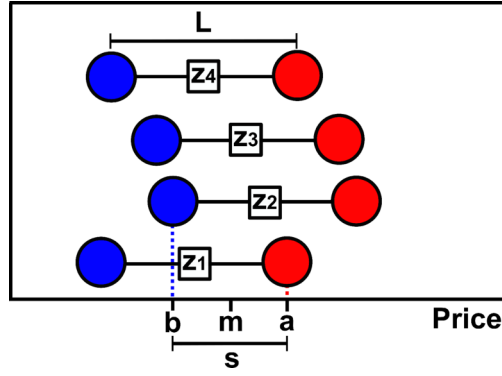


Figure 4.5: **Dealer Model basics.** The market is participated by $N = 4$ agents providing bid $b_i(t)$ (blue circles) and ask $a_i(t)$ (red circles) quotes, $i = 1, \dots, N$. The continuous price grid prevents limit orders to be queued at the same price level. Each limit order includes one unit of the traded currency. The market making spread $L = a_i(t) - b_i(t)$, $i = 1, \dots, N$ is the same for each agent and constant in time, that is, agents only manage their dealing price $z_i(t) = (a_i(t) + b_i(t))/2$, $i = 1, \dots, N$ (white squares) to dynamically adjust their bid and ask quotes $b_i(t) = z_i(t) - L/2$ and $a_i(t) = z_i(t) + L/2$, $i = 1, \dots, N$. The vertical dashed lines mark the best bid $b(t)$ (blue) and ask $a(t)$ (red) quotes. The distance between the best quotes is the current spread $s(t) = a(t) - b(t)$. The current mid price is $m(t) = (a(t) + b(t))/2$. This figure has been extracted from [34], see appendix B.4 for details about attributions and permissions.

strategies. For instance, $c > 0$ represents an agent that tends to adjust its dealing price $z(t)$ in the direction of the price trend (i.e., trend-following). Conversely, $c < 0$ characterizes an agent that tends to adjust its dealing price in the opposite direction of the price trend (i.e., contrarian). In the original work [35] the authors have shown that the Dealer Model accurately reproduces the distributions of price fluctuations and transaction intervals in two major currency markets. In their concluding remarks, the authors propose their model as a simple, intuitive and effective baseline tool to develop more sophisticated variants, e.g., presence of a central bank, large number of agents etc., and perform computer-based simulations to assess the effects of these modifications on the overall behavior of the market [35].

4.4.4 The Cont-Kukanov-Stoikov Model

The Cont-Kukanov-Stoikov Model (CKS henceforth) [36] was introduced in “*The Price Impact of Order Book Events*”, an article published in *Journal of Financial Econometrics* in 2014. Several related studies that preceded this work examined price impact by looking at the rela-

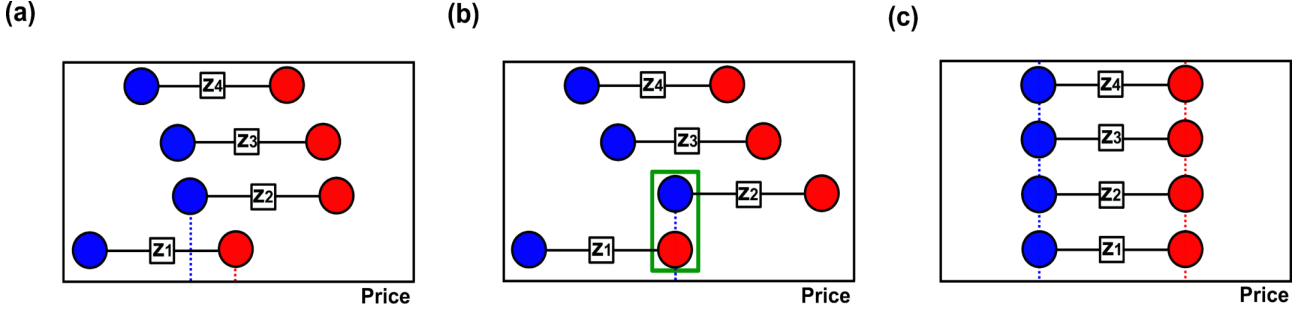


Figure 4.6: **Interactions in the Dealer Model.** (a) Agents are not engaging in transactions as the best bid price (blue dashed line) is smaller than the best ask price (red dashed line). (b) The best bid price matches the best ask price, prompting agents #1 and #2 to exchange one unit of the traded FX rate (green box). The transaction price is the mid point between the two quotes $p = (a_1 + b_2)/2$. (c) This transaction prompts each agent to update its dealing price to the latest transaction price (i.e., $z \rightarrow p$). This figure has been extracted from [34], see appendix B.4 for details about attributions and permissions.

tionships between trades, i.e., execution of limit orders, and price fluctuations, thus overlooking the role of limit order placements and deletions, i.e., “quotes”, in the price formation process [36]. Building on earlier research [370, 371, 372, 373], the authors address this shortfall by introducing a simple linear model of the relationships between price changes and the flow of submissions, executions and deletions that drive the evolution of the LOB.

In the CKS model, the current demand, i.e., at any time t , of the traded instrument is represented by the best bid price b_t and the volume of limit buy orders lying at this price V_t^b [36]. Specularly, the current supply is represented by the best ask price a_t and the volume of limit sell orders lying at this price V_t^a . Changes in demand and supply are driven by submissions, executions and deletions of limit orders as they alter the state of the LOB by adding or removing volumes from the best levels; eventually triggering price changes [36]. It follows that the contribution of the t -th event can be formulated as

$$\eta_t = (V_t^b \mathbb{1}_{\{b_t \geq b_{t-1}\}} - V_{t-1}^b \mathbb{1}_{\{b_t \leq b_{t-1}\}}) + (V_{t-1}^a \mathbb{1}_{\{a_t \geq a_{t-1}\}} - V_t^a \mathbb{1}_{\{a_t \leq a_{t-1}\}}), \quad (4.12)$$

where $\mathbb{1}_A$ is an indicator function of the event A and b_t and a_t are the best bid and ask prices after the t -th event respectively [36]. To better understand Eq. (4.12), we proceed by examples. The placement of a bid limit order at the current best price increases the available buy volume without altering the best quotes, hence $\eta_t = V_t^b - V_{t-1}^b > 0$. Similarly, the deletion or execution, i.e., matching against a forthcoming sell market order, of a buy limit order at the

current best price reduce the available buy volume without altering the best quotes, leading to $\eta_t = V_t^b - V_{t-1}^b < 0$. Finally, the placement of a buy limit order “inside the spread”, i.e., $b_{t-1} < b_t < a_t$, increases the available buy volume while altering the best bid price, hence $\eta_t = V_t^b > 0$. Although one might present other examples, it is now clear that any event in the LOB provide a tangible contribution to the net demand, i.e., when $\eta_t > 0$, or net supply, i.e., when $\eta_t < 0$, of the traded instrument.

In the CKS model, the imbalance between supply and demand in a given time interval $[t_{\ell-1}, t_\ell]$ can be measured by adding up the contributions of individual LOB events recorded between $t_{\ell-1}$ and t_ℓ

$$\phi_\ell = \sum_{i=N(t_{\ell-1})+1}^{N(t_\ell)} \eta_i, \quad (4.13)$$

where $N(t)$ is the number of events recorded until time t [36]. This metric, known as *order flow imbalance* (OFI henceforth), is a major novelty of [36] as it provides a simple and intuitive way to condense the contribution of the entire spectrum of LOB events to supply and demand into a single variable.

Building on the widely accepted idea that imbalances between demand and supply play a pivotal role in price dynamics, the authors describe the relationship between OFI and price fluctuations through a simple linear model

$$\Delta p_\ell = \beta_K \phi_\ell + \epsilon_\ell, \quad (4.14)$$

where $\Delta p_\ell = p_\ell - p_{\ell-1}$ is the price change in a relatively short time window Δ_ℓ , ϕ_ℓ is the OFI defined in Eq. (4.13), ϵ_ℓ is a noise term and β_K is known as “*price impact coefficient*” and is estimated over a longer time window $\Delta_K \gg \Delta_\ell$ [36].

In their analysis, the authors considered one month, i.e., April 2010, of trading activity for 50 randomly selected stocks belonging to the SP 500 index¹ by examining records of the flow of submissions, deletions and executions occurring at the best quotes of the LOB [36]. Price fluctuations and OFI time series are sampled every $\Delta_\ell = 10$ s and split in non-overlapping time windows, i.e., “sub-time series” or “blocks”, every $\Delta_K = 1800$ s [36]. Then, the linear model presented in Eq. (4.14) is fitted to each block. In spite of its simplicity, the model

¹“The SP 500 is widely regarded as the best single gauge of large-cap U.S. equities. There is over USD 11.2 trillion indexed or benchmarked to the index, with indexed assets comprising approximately USD 4.6 trillion of this total. The index includes 500 leading companies and covers approximately 80% of available market capitalization.”, quoted from the Standard and Poor’s webpage [374].

displays a remarkable goodness of fit across the investigated stocks, with average R^2 statistics spanning between 0.35 (CME Group) and 0.79 (Bank of America) [36]. These results provide an important support to the modelling paradigm adopted in this work and, more generally, to the idea that price fluctuations are predominantly driven by events occurring at the best levels of the LOB²[36]. The authors performed further empirical exercises to showcase potential applications of the model, such as monitoring the OFI to manage adverse selection risk in limit order placement, explaining the intraday pattern of price volatility through observable quantities, i.e., OFI and depth, and using the price impact coefficient β as an alternative estimator of the Kyle's Lambda [36].

The CKS model captures important aspects of the impact of LOB events on asset prices with a minimal linear model which turns out to be robust across a spectrum of stocks and sampling frequencies [36]. This remarkable simplicity facilitates the understanding, implementation and assessment of this framework. However, as we have noted in a recent article [37], the CKS model might not be suitable to describe the relationship between OFI and price fluctuations in time-scales that are substantially shorter than those that the authors considered in their analysis. We argue that at higher frequencies variables are autocorrelated and price impact is noisier but more predictable, hence the reduced applicability of static and contemporaneous frameworks like the CKS model [37].

²Note that the definition of OFI provided in Eq. (4.13) only accounts for events occurring at the best bid and ask levels of the LOB.

4.5 The emergence of cross-currency correlations in a simple agent based model of foreign exchange markets

Personal contributions

This section presents the paper “*The microscopic relationships between triangular arbitrage and cross-currency correlations in a simple agent based model of foreign exchange markets*” [34], published in Public Library of Science One in June 2020. As primary co-author, I played a primary role in every major aspect of this project:

- Understanding the relevant literature.
- Development of the underlying theory.
- Development of the computational infrastructure required to analyse the behavior of the models.
- Management of computer-based simulations and data collection.
- Analysis and interpretation of computer-based simulations.
- Presentation of experimental results.
- Writing of the manuscript.

4.5.1 Context

This section presents the paper “*The microscopic relationships between triangular arbitrage and cross-currency correlations in a simple agent based model of foreign exchange markets*” [34], published in Public Library of Science One in June 2020. The main goal of this research is to investigate the microscopic origins of the cross-correlations between price fluctuations in currency markets. We introduce an agent-based model which describes the emergence of cross-currency correlations from the interactions between market makers and an arbitrageur, i.e., a trader who continuously attempt to gain “risk free” profits by exploiting market inefficiencies. The model qualitatively replicates the time-scale vs. cross-correlation diagrams observed in

real trading data, suggesting that triangular arbitrage, i.e., the practice of exploiting a misprice among three related currencies, plays a primary role in the entanglement of the dynamics of different foreign exchange rates. Furthermore, the model shows how the features of the cross-correlation function between two foreign exchange rates, such as its sign and value, emerge from the interplay between triangular arbitrage and trend-following strategies. In particular, the interaction of these trading strategies favors certain combinations of price trend signs across markets, thus altering the probability of observing two foreign exchange rates drifting in the same or opposite direction. Ultimately, this entangles the dynamics of foreign exchange rate pairs, leading to cross-correlation functions that resemble those observed in real trading data.

4.5.2 The foreign exchange market

This thesis presents a model of the foreign exchange (FX henceforth) market. The FX market is characterized by singular institutional features, such as the absence of a central exchange, exceptionally large traded volumes and a declining, yet significant dealer-centric nature [375]. Electronic trading has rapidly emerged as a key channel through which investors can access liquidity in the FX market [375, 376]. For instance, more than 70% of the volume in the FX Spot market is exchanged electronically [376]. A peculiar stylized fact of the FX market is the significant correlation among movements of different currency prices. These interdependencies are time-scale dependent [377, 378], their strength evolves in time and become extremely evident in the occurrence of extreme price swings, known as flash crashes. In these events, various foreign exchange rates related to a certain currency abruptly appreciate or depreciate, affecting the trading activity of several FX markets. A recent example is the large and rapid appreciation of the Japanese Yen against multiple currencies on January 2nd 2019. The largest intraday price changes peaked +11% against Australian Dollar, +8% against Turkish Lira and +4% against US Dollar [379].

Currency prices

In the FX market, the price of a currency is always expressed in units of another currency and it is commonly known as foreign exchange rate (FX rate henceforth). For instance, the price of one Euro (EUR henceforth) in Japanese Yen (JPY henceforth) is denoted by EUR/JPY. The same FX rate can be obtained from the product of two other FX rates, e.g., $\text{EUR/JPY} =$

USD/JPY × EUR/USD, where USD indicates US Dollars. In the former case EUR is purchased directly while in the latter case EUR is purchased indirectly through a third currency (i.e., USD), see Fig. 4.7. At any time t we expect the following equality to hold

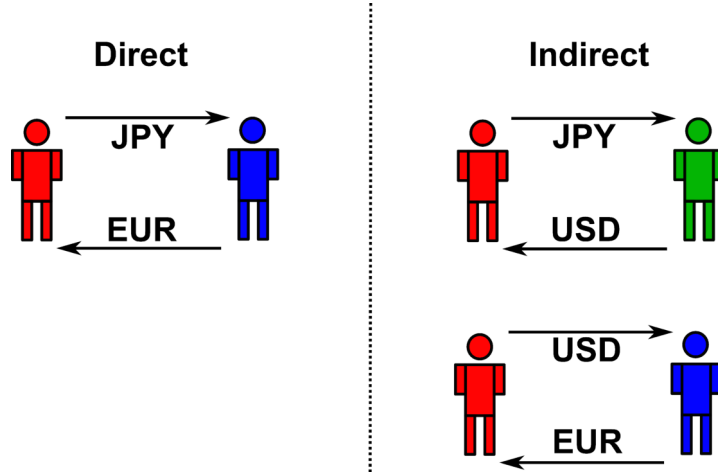


Figure 4.7: **Two ways of obtaining one unit of EUR.** Direct transaction (left panel): agent #1 (red) obtains EUR from agent #2 (blue) in exchange for JPY. Indirect transaction (right panel): agent #1 purchases USD from agent #3 (green) in exchange for JPY. Then, she obtains EUR from agent #2 (blue) in exchange for USD. This figure has been extracted from [34], see appendix B.4 for details about attributions and permissions.

$$\underbrace{\text{EUR/JPY}_t}_{\text{FX rate}} = \underbrace{(\text{USD/JPY}_t) \times (\text{EUR/USD}_t)}_{\text{implied FX cross rate}}, \quad (4.15)$$

that is, the costs of a direct and indirect purchase of the same amount of a given currency must be the same. Clearly, Eq. (4.15) can be generalized to any currency triplet.

Triangular arbitrage

Several datasets [380, 381, 382, 383] reveal narrow time windows in which Eq. (4.15) does not hold. In this scenario, traders might try to exploit one of the following misprices

$$\text{EUR/JPY}_t < (\text{USD/JPY}_t) \times (\text{EUR/USD}_t), \quad (4.16a)$$

$$\text{EUR/JPY}_t > (\text{USD/JPY}_t) \times (\text{EUR/USD}_t), \quad (4.16b)$$

by implementing a triangular arbitrage strategy. For instance, Eq. (4.16b) suggests that a trader holding JPY could gain a risk-free profit by buying EUR indirectly (JPY → USD → EUR) and selling EUR directly (EUR → JPY). Assuming that the arbitrageur completes each

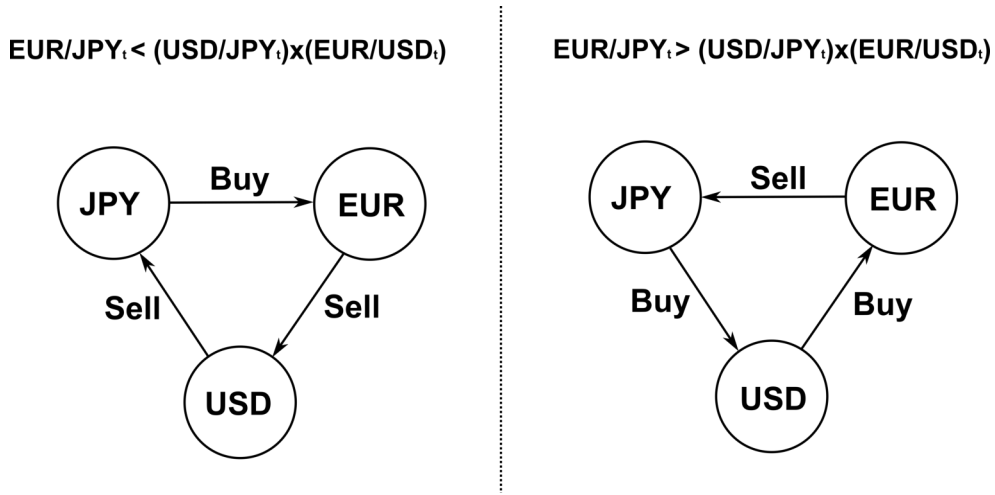


Figure 4.8: **Profitable misprices and associated triangular arbitrage strategies.** Left panel: an agent buys EUR for JPY and sells EUR for JPY through USD. Right panel: an agent sells EUR for JPY and buys EUR for JPY through USD. This figure has been extracted from [34], see appendix B.4 for details about attributions and permissions.

transaction at the best quotes (i.e., sell at the best bid and buy at the best ask) available in the EUR/JPY, USD/JPY and EUR/USD LOBs, any strategy presented in Fig. 4.8 is effectively profitable if the following condition (i.e., Eq. (4.17a) for left panel strategy or Eq. (4.17b) for right panel strategy) is satisfied

$$a_{EUR/JPY}(t) < b_{USD/JPY}(t) \times b_{EUR/USD}(t), \quad (4.17a)$$

$$b_{EUR/JPY}(t) > a_{USD/JPY}(t) \times a_{EUR/USD}(t), \quad (4.17b)$$

where $b_{x/y}(t)$ and $a_{x/y}(t)$ are the best bid and ask quotes available at time t in the x/y market respectively.

Following [380, 384, 382], the presence of triangular arbitrage opportunities is detected whenever one of the following processes

$$\mu^I(t) = \frac{b_{USD/JPY}(t) \times b_{EUR/USD}(t)}{a_{EUR/JPY}(t)}, \quad (4.18a)$$

$$\mu^{II}(t) = \frac{b_{EUR/JPY}(t)}{a_{USD/JPY}(t) \times a_{EUR/USD}(t)}, \quad (4.18b)$$

exceeds the unit. The terms $b_{x/y}(t)$ and $a_{x/y}(t)$ retain the same meaning as in Eq. (4.17).

4.5.3 Introduction

The relationship between triangular arbitrage [380, 382, 385, 383] and cross-currency correlations remains unclear. Mizuno *et al.* [377] observed that the cross-correlation between real and implied prices of Japanese Yen is significantly below the unit on very short time-scales, conjecturing that this counter-intuitive property highlights how the same currency could be purchased and sold at different prices by implementing a triangular arbitrage strategy. Aiba and Hatano [384] proposed an ABM relying on the intriguing idea that triangular arbitrage influences the price dynamics in different currency markets. However, this study fails to explain whether and how reactions to triangular arbitrage opportunities lead to the characteristic shape of the time-scale vs. cross-correlation diagrams observed in real trading data [377, 378].

Building on these observations, this section aims to obtain further insights on the microscopic origins of the correlations among currency pairs by introducing an ABM model in which two species (i.e., market makers and the arbitrageur) interact across three inter-dealer markets where trading is organized in limit order books. The model qualitatively replicates the characteristic shape of the cross-correlation functions between currency pairs observed in real trading data. This suggests that triangular arbitrage is a pivotal microscopic mechanism behind the formation of cross-currency interdependencies. Furthermore, the model elucidates how the features of these statistical relationships, such as the sign and value of the time-scale vs. cross-correlation diagram, stem from the interplay between trend-following and triangular arbitrage strategies.

4.5.4 The Arbitrageur Model

The Arbitrageur Model introduces an ecology which encompasses three co-existing inter-dealer FX markets. The scope of this framework is to mimic the interactions between different trading strategies across multiple FX markets and capture the mechanisms through which these interactions shape the documented cross-correlation among FX rate fluctuations [377, 378]. In the Arbitrageur Model, each market hosts a fixed number of agents who interact by exchanging a given FX rate. Trading is organized in simplified LOBs where prices move in a continuous grid. Agents provide liquidity to the market by adjusting limit orders through which they quote a bid and an ask price, thus acting as market makers. To set these prices, market makers adopt simple trend-based strategies. Furthermore, market makers cannot interact across markets,

that is, they can only trade in the market they have been assigned to. Finally, echoing [384], the ecology hosts a special agent (i.e., the arbitrager) that is allowed to submit market orders in any market to exploit triangular arbitrage opportunities, see Fig. 4.9.

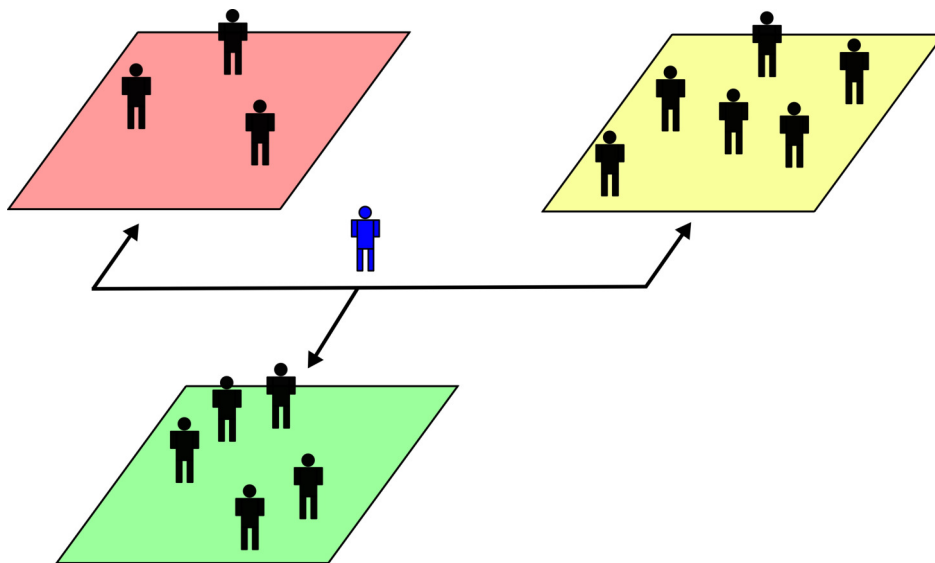


Figure 4.9: **Schematic of the Arbitrager Model ecology.** The ecology comprises three independent FX markets represented by the red, yellow and green areas. For simplicity, each market allows to exchange a major FX rate: USD/JPY, EUR/USD and EUR/JPY. Trading is organized in continuous price grid LOBs as in [35], see section 4.4.3. Market makers (black agents) maintain bid and ask quotes by adopting trend-based strategies. Transactions occur when the best bid matches or exceeds the best ask. Market makers engaging in a trade close the deal at the mid point between the two matching prices (i.e., transaction price), see Fig. 4.10 for details. Finally, an arbitrager (blue agent) exclusively submits market orders across the three markets (black arrows) to exploit triangular arbitrage opportunities emerging now and then, see Fig. 4.11. This figure has been extracted from [34], see appendix B.4 for details about attributions and permissions.

Market makers

The i -th market maker operating in the ℓ -th market actively manages a bid quote $b_{i,\ell}(t)$ and an ask quote $a_{i,\ell}(t)$ separated by a constant spread $L_\ell = a_{i,\ell}(t) - b_{i,\ell}(t)$. To do so, the i -th market maker updates its dealing price $z_{i,\ell}(t)$, which is the mid point between the two quotes

(i.e., $z_{i,\ell}(t) = a_{i,\ell}(t) - L_\ell/2 = b_{i,\ell}(t) + L_\ell/2$), by adopting a trend-based strategy

$$\frac{dz_{i,\ell}(t)}{dt} = c_\ell \phi_{n,\ell}(t) + \sigma_\ell \epsilon_{i,\ell}(t), \quad i = 1, \dots, N_\ell \quad (4.19)$$

where N_ℓ is the number of market makers participating the ℓ -th market, $\sigma_\ell > 0$, and $\epsilon_{i,\ell}(t)$ is a Gaussian white noise. The term

$$\phi_{n,\ell}(t) = \frac{\sum_{k=0}^{n-1} (p_\ell(g_{t,\ell} - k) - p_\ell(g_{t,\ell} - k - 1)) e^{-\frac{k}{\xi}}}{\sum_{k=0}^{n-1} e^{-\frac{k}{\xi}}}, \quad \ell = 1, \dots, d \quad (4.20)$$

is the weighted average of the last $n < g_{t,\ell}$ changes in the transaction price p_ℓ in the ℓ -th market and $g_{t,\ell}$ is the number of transactions occurred in $[0, t[$ in the ℓ -th market. In this average, the weight $e^{-\frac{k}{\xi}}$ decays exponentially fast with characteristic scale $\xi > 0$. The real-valued parameter c_ℓ controls how the current price trend $\phi_{n,\ell}(t)$ influences market makers' strategies. For instance, $c_\ell > 0$ ($c_\ell < 0$) indicates that market makers operating in the ℓ -th market tend to adjust their dealing prices $z(t)$ in the same (opposite) direction of the sign of the price trend $\phi_{n,\ell}(t)$.

Transactions occur when the i -th market maker is willing to buy at a price that matches or exceeds the ask price of the j -th market maker (i.e., $b_{i,\ell} \geq a_{j,\ell}$). Trades are settled at the transaction price $p(g_{t,\ell}) = (a_{j,\ell}(t) + b_{i,\ell}(t))/2$ and only the market makers who have just engaged in a trade adjust their dealing prices $z(t+dt)$ to the latest transaction price $p(g_{t,\ell})$, see Fig. 4.10.

The arbitrageur

The arbitrageur is a liquidity taker (i.e., she does not provide bid and ask quotes like market makers) that can only submit market orders in each market to exploit an existing triangular arbitrage opportunity. Assuming that agents exchange EUR/JPY, EUR/USD and USD/JPY, the arbitrageur monitors the triangular arbitrage processes presented in Eqs. (4.18a) and (4.18b). As soon as one of these processes exceeds the unit, the arbitrageur submits market orders to exploit the current opportunity (predatory market orders henceforth). Contrary to limit orders, market orders trigger an immediate transaction between the arbitrageur and the market maker providing the best quote on the opposite side of the LOB. This implies that transactions involving the arbitrageur are always settled at the bid or ask quote offered by the matched market maker, which are by the definition the current best bid or ask quote of the LOB. Following the post-transaction update rule, the matched market maker adjust its dealing price

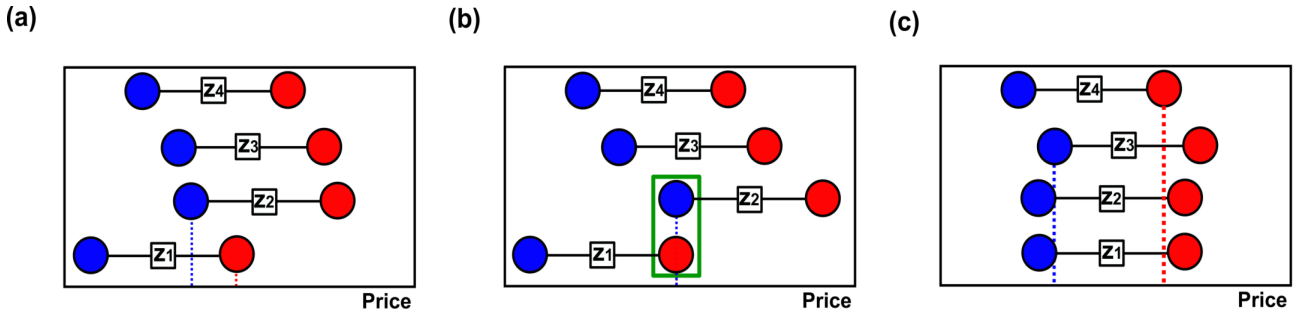


Figure 4.10: **Interactions in the Arbitrager Model.** (a) Market makers are not engaging in transactions as the best bid price (blue dashed line) is smaller than the best ask price (red dashed line). (b) The best bid price matches the best ask price, prompting Market Makers #1 and #2 to exchange one unit of the traded FX rate (green box). The transaction price is the mid point between the two quotes $p = (a_1 + b_2)/2$. (c) This transaction prompts the two transacting market makers to re-adjust their dealing prices z to the latest transaction price p . This figure has been extracted from [34], see appendix B.4 for details about attributions and permissions.

to its own matched bid or ask quote, that is, $z_{i,\ell}(t + dt) \rightarrow a_{i,\ell}(t)$ in case of a buy predatory market order or $z_{i,\ell}(t + dt) \rightarrow b_{i,\ell}(t)$ in case of a sell predatory market order, see Fig. 4.11.

Parameters governing the dynamics of the Arbitrager Model

The evolution of the Arbitrager Model is governed by nine parameters, see table 4.1 Detailed discussions on the calibration of each parameter are provided in appendix G.1.

The Arbitrager Model in context

The Arbitrager Model builds on various existing studies. The structure of each market mimics, with few exceptions, the one introduced in the Dealer Model [35], where a number of autonomous market makers interact in a continuous price-grid LOB by managing limit orders. In the Arbitrager Model, the strategic behavior of market makers is driven by a simple process, see Eq. (4.19), that is reminiscent of those proposed in the Dealer Model [35] and, more recently, in the HFT Model [386]. Finally, the idea of an arbitrager acting as a *connection* between otherwise independent markets was introduced in the Aiba and Hatano Model [384]. In particular, the authors advanced the intriguing comparison between an ecology comprising multiple markets, such as the Arbitrager Model, and a spring-mass system in which the dy-

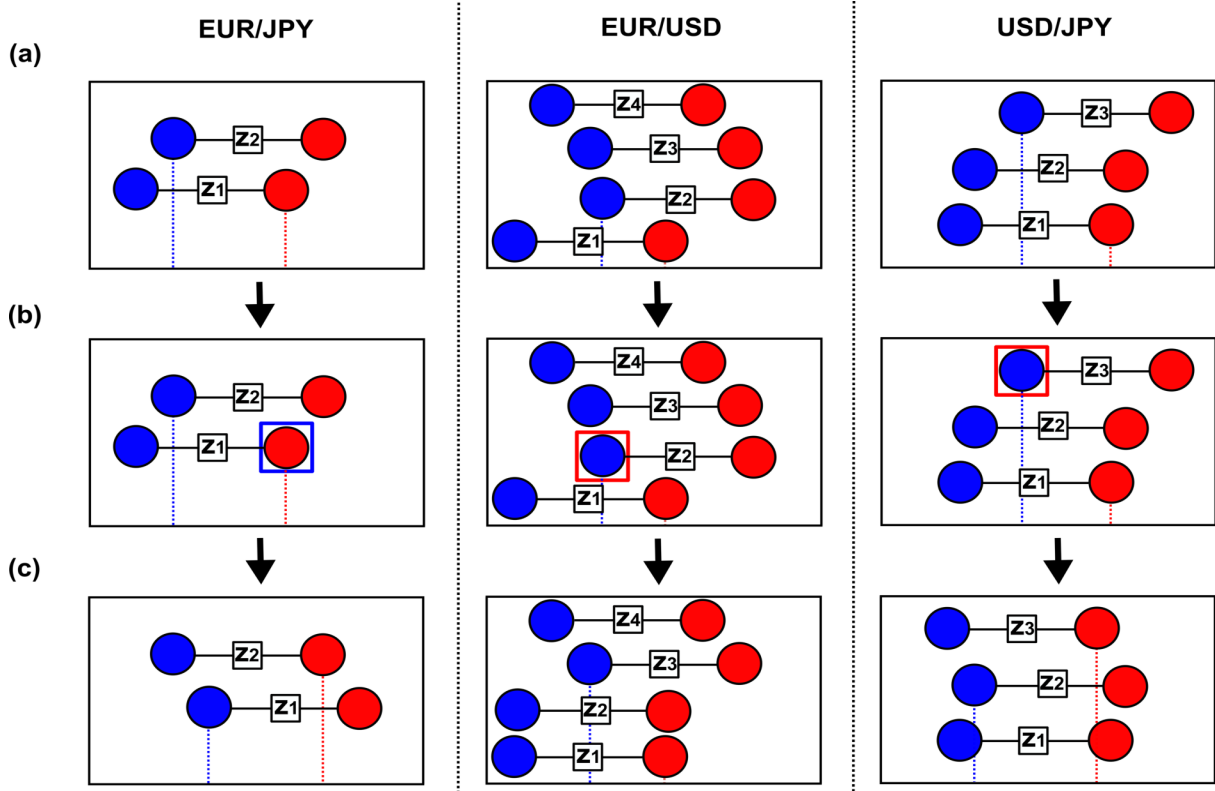


Figure 4.11: **Exploiting a triangular arbitrage opportunity in the Arbitrager Model.**

(a) The states of the three markets before the emergence of an exploitable triangular arbitrage opportunity. (b) When $\mu^I(t) \geq 1$, the arbitrager submits a buy market order (blue square) in the EUR/JPY market and sell market orders (red squares) in the EUR/USD and USD/JPY markets, matching the encapsulated limit orders (i.e., Market Maker # 1 in EUR/JPY, Market Maker # 2 in EUR/USD and Market Maker # 3 in USD/JPY). (c) The transacting market makers re-adjust their dealing prices to the quote matched by the arbitrager's market order (e.g., $z_{1,\text{EUR/JPY}}(t+dt) \rightarrow a_{1,\text{EUR/JPY}}(t)$), causing a mid price change in each market. This figure has been extracted from [34], see appendix B.4 for details about attributions and permissions.

namics of three random walkers (i.e., the markets) are constrained by a restoring force (i.e., the arbitrager) acting on the center of gravity of the system.

The Arbitrager Model presents the main features of the ABM approach [130]. First, it is composed by several actors (i.e., agents) who autonomously evaluate the current state of the system before taking a certain decision, such as re-adjusting their limit orders. Second, the decision making processes, the available trading strategies and the rules governing the interactions among agents retain a remarkable simplicity. This reduces the computational effort required to build and simulate the dynamics of the model and facilitates the understanding

Name	Symbol	Dimension
Initial center of mass	$p_\ell(t_0)$	price
Market making spread	L_ℓ	price
Number of market participants	N_ℓ	dimensionless
Volatility of dealing price updates	σ_ℓ	price/ $\sqrt{\text{time}}$
Average time between transactions	Γ	time (sec)
Discretized time step	Δt	time (sec)
Price changes accounted in $\phi_{n,\ell}(t)$	n	dimensionless
Scaling of the weight function in $\phi_{n,\ell}(t)$	ξ	dimensionless
Trend-following strength	c_ℓ	price/time

Table 4.1: **Parameters governing the dynamics of the Arbitrager Model.** For each parameter, the table reports its nomenclature, symbol and dimension.

and interpretation of its outcomes. Third, the Arbitrager Model does not achieve its goal by directly modelling cross-currency correlations. Instead, this statistical regularity of FX markets is conceived as a macroscopic phenomenon which emerges from the iteration of simple, antagonistic interactions occurring on a more microscopic level.

4.5.5 Cross-correlation diagrams in the Arbitrager Model

Echoing previous empirical studies [377, 378], the cross-correlation function between fluctuations of two foreign exchange rates is

$$\rho_{i,j}(\omega) = \frac{\langle \Delta m_i(t) \Delta m_j(t) \rangle - \langle \Delta m_i(t) \rangle \langle \Delta m_j(t) \rangle}{\sigma_{\Delta m_i} \sigma_{\Delta m_j}}, \quad (4.21a)$$

$$\sigma_{\Delta m_\ell}^2 = \langle \Delta m_\ell(t)^2 \rangle - \langle \Delta m_\ell(t) \rangle^2, \quad (4.21b)$$

where the time-scale ω is the interval (i.e., in seconds) between two consecutive observations of the ℓ -th mid price m_ℓ time series, $\Delta m_\ell(t) \equiv m_\ell(t) - m_\ell(t - \omega)$ is the linear change between consecutive observations, $\sigma_{\Delta m_\ell}$ is the standard deviation of $\Delta m_\ell(t)$ and $\langle \rangle$ denotes average values. In real trading data, the value of the cross-correlation function $\rho_{i,j}(\omega)$ varies with ω on very short time-scales ($\omega < 1$ sec). This time-scale dependency starts to weaken after $\omega \approx 1$ sec and vanishes beyond $\omega \approx 10$ sec, see Fig. 4.12(a). The characteristic shape of $\rho_{i,j}(\omega)$ displayed in Fig. 4.12(a) is compatible with the one found by Mizuno *et al.* [377]. However,

the trading data-based cross-correlation functions presented in this study stabilize on much shorter time-scales. Considering that [377] employed trading data collected in 1999, a period where lower levels of automation imposed a slower trading pace, it is plausible to hypothesize that the time-scale ω beyond which $\rho_{i,j}(\omega)$ stabilizes reflects the speed at which markets react to a given event. Furthermore, $\rho_{i,j}(\omega)$ stabilizes around different levels over the four trading years covered in the present analysis. For instance, the cross-correlation between $\Delta\text{USD}/\text{JPY}$ and $\Delta\text{EUR}/\text{JPY}$, see Fig. 4.12(a), stabilizes around 0.6 in 2011-2012 and 0.3 in 2013-2014. This variability might be related to the different tick sizes adopted by EBS during the four years covered in this empirical analysis, see [387] and table C.2. Detailed investigations on how changes in the design of FX LOBs (e.g., tick size) and the increasing sophistication of market participants (e.g., high frequency traders) affect the characteristic shape of $\rho_{i,j}(\omega)$ are outside the scope of this model, however, such studies will be a very much welcomed addition to the current literature.

The Arbitrager Model satisfactorily replicates the characteristic shape of $\rho_{i,j}(\omega)$, suggesting that triangular arbitrage plays a primary role in the entanglement of the dynamics of currency pairs in real FX markets. However, two quantitative differences between the model-based and data-based characteristic shape of $\rho_{i,j}(\omega)$ emerge in Fig. 4.12. First, $\rho_{i,j}(\omega)$ flattens after $\omega \approx 30$ sec in the model, see Fig. 4.12(b), and $\omega \approx 10$ sec in real trading data, see Fig. 4.12(a). Second, in extremely short time-scales ($\omega \rightarrow 0$ sec) the model-based $\rho_{i,j}(\omega)$ does not converge to zero as in real trading data, see Fig. 4.12(b), but to nearby values. These discrepancies might be rooted in the extreme simplicity of the Arbitrager Model which neglects various practices of real FX markets that contribute, to different degrees, to the shape and features of $\rho_{i,j}(\omega)$ revealed in real trading data. To support this hypothesis, an extended version of the Arbitrager Model which includes additional features of real FX markets is presented and examined in section G.2. This more complex version of the model overcomes the main differences between the curves displayed in Figs. 4.12(a) and 4.12(b), reproducing cross-correlation functions $\rho_{i,j}(\omega)$ that approach zero when $\omega \rightarrow 0$ sec and stabilize on shorter time-scales than those emerged in the baseline model.

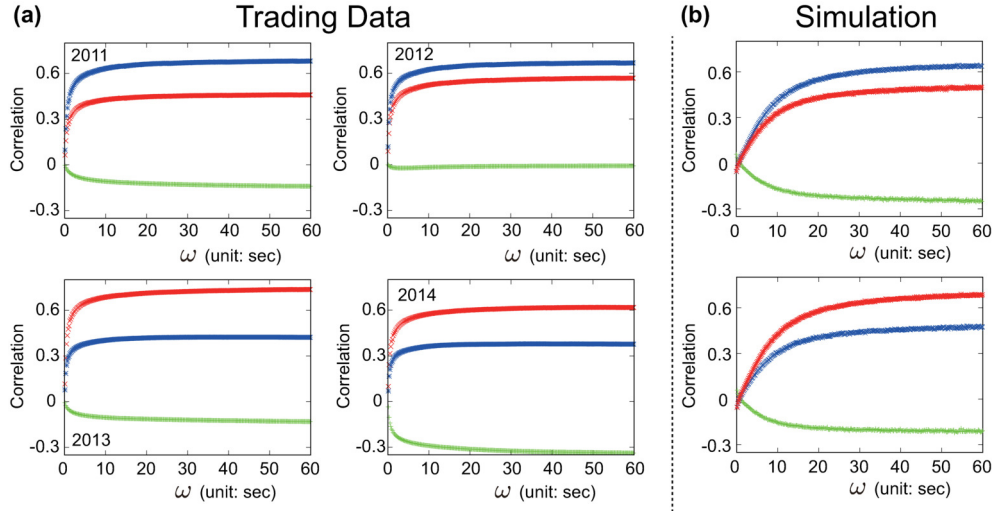


Figure 4.12: **Trading data vs. model based cross-correlation functions.** Cross-correlation function $\rho_{i,j}(\omega)$ for $\Delta\text{USD}/\text{JPY}$ vs. $\Delta\text{EUR}/\text{USD}$ (green), $\Delta\text{EUR}/\text{USD}$ vs. $\Delta\text{EUR}/\text{JPY}$ (blue) and $\Delta\text{USD}/\text{JPY}$ vs. $\Delta\text{EUR}/\text{JPY}$ (red) as a function of the time-scale ω of the underlying time series. (a) Real market data (EBS) across four distinct years (2011-2014). (b) Arbitrager Model simulations. The number of participating market makers ($N_{\text{EUR}/\text{USD}}, N_{\text{USD}/\text{JPY}}, N_{\text{EUR}/\text{JPY}}$) are (35, 45, 25) in the first experiment, see (b) top panel, and (50, 35, 25) in the second experiment, see (b) bottom panel. The trend-following strength parameters are $(c_{\text{EUR}/\text{USD}}, c_{\text{USD}/\text{JPY}}, c_{\text{EUR}/\text{JPY}}) = (0.8, 0.8, 0.8)$ in both experiments. The length of each simulation is 5×10^6 time steps. The price trends $\phi_{n,\ell}$ are calculated over the most recent $n = 15$ changes in the transaction price p and the scaling constant is set to $\xi = 5$, see Eq. (4.20). Details on the initialization of the model and the conversion between simulation time (i.e., time steps) and real time (i.e., sec) are provided in section G.1. This figure has been extracted from [34], see appendix B.4 for details about attributions and permissions.

4.5.6 The microscopic origins of cross-currency correlations in the Arbitrager Model

Introduction

The Arbitrager Model, reproducing the characteristic shape of $\rho_{i,j}(\omega)$, suggests that triangular arbitrage plays a primary role in the formation of the cross-correlations among currencies. However, it is not clear how the features of $\rho_{i,j}(\omega)$, such as its sign and values, stem from the interplay between the different types of strategies adopted by agents operating in the ecology. To

address this key question, we need to examine both the microscopic and mesoscopic dimensions of the system. The former concerns the interactions between the most elementary components of the ecology, i.e., agents adopting different strategies, while the latter concerns the statistical relationships between the three LOBs at the core of the Arbitrager Model environment.

Market states and ecology configurations

The actual state of the j -th market $\nu_j(t)$ is defined as the sign of the current price trend $\text{sgn}(\phi_{n,\ell}(t)) \in \{-, +\}$, see Eq. (4.20). It follows that the current configuration of the ecology $q(t) = \{\nu_1(t), \nu_2(t), \nu_3(t)\}$ is the combination of the states of each market. The Arbitrager Model, considering three markets, admits $2^3 = 8$ different ecology configurations.

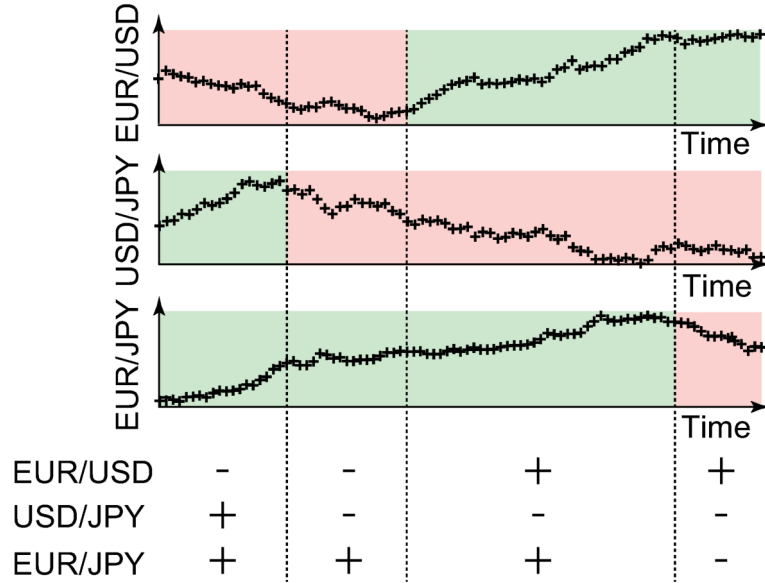


Figure 4.13: **Correspondence between price trend signs and market states.** Simulated price patterns of EUR/USD (top), USD/JPY (mid) and EUR/JPY (bottom). Periods of negative (positive) price trends are denoted by a red (green) background. Vertical dashed lines mark a change in the ecology configuration $q(t)$. Price trends $\phi_{n,\ell}$ are calculated over the most recent $n = 15$ changes in the transaction price and with scaling constant $\xi = 5$. The table below the panels combines the market states to show how the ecology configuration $q(t)$ evolves in time. This figure has been extracted from [34], see appendix B.4 for details about attributions and permissions.

The effect of the arbitrageur presence on the overall behavior of the model

When the arbitrageur is not included in the system, two markets have the same probability of being in the same and opposite state, see first column of Fig. 4.14. This occurs because price trends are driven by transactions triggered by endogenous decisions, that is, events occurring in different markets remain completely unrelated. As a consequence, market states flip independently and at the same rate. It follows that the eight possible combinations of market states share the same appearance probabilities $1/2^3$ and expected lifetimes, see Fig. 4.15. In these settings, the dynamics of the mid price of FX rate pairs do not present any significant correlation, see third column of Fig. 4.14. The inclusion of the arbitrageur has a major impact on the overall behavior of the model. Imbalances in the probability of observing two markets in the same or opposite state emerge in each FX rate pair. For instance, the EUR/USD and EUR/JPY markets have the same state in $\approx 57\%$ of the experiment duration, see Fig. 4.14(b). Movements of FX rate pairs become correlated, revealing cross-correlation functions $\rho_{i,j}(\omega)$ whose shapes qualitatively mimic those found in real trading data. The sign and stabilization levels of these functions are consistent with the sign and size of the probabilities imbalances, suggesting that these two results are two faces of the same coin.

The interplay between triangular arbitrage and trend-following strategies

The statistical properties of the eight ecology configurations shall be examined in order to understand how the findings presented in Fig. 4.14 unfold. The presence of the arbitrageur introduces a degree of heterogeneity in both the expected lifetimes and appearance probabilities of ecology configurations, see Fig. 4.15. This reveals three interesting facts. First, the average lifetime of every ecology configuration is smaller than its counterpart in an arbitrageur-free system. To explain this feature, recall that predatory market orders trigger three simultaneous transactions (i.e., one in each market) altering the current price trends $\phi_{n,\ell}(t)$, see Eq. (4.20). When the latest change in transaction price $p_\ell(g_{t,\ell}) - p_\ell(g_{t,\ell} - 1)$ induced by a predatory market order and $\phi_{n,\ell}(t-dt)$ have opposite signs, the actions of the arbitrageur weaken (i.e., $|\phi_{n,\ell}(t)| < |\phi_{n,\ell}(t-dt)|$) or even flip the sign (i.e., $\phi_{n,\ell}(t)\phi_{n,\ell}(t-dt) < 0$) of the price trend. When this occurs, the arbitrageur weakens the trend-following behaviors of market makers in at least one of the three markets, thus increasing the likelihood of a transition to another ecology configuration. As triangular arbitrage opportunities of both types appear, with different incidences, during any

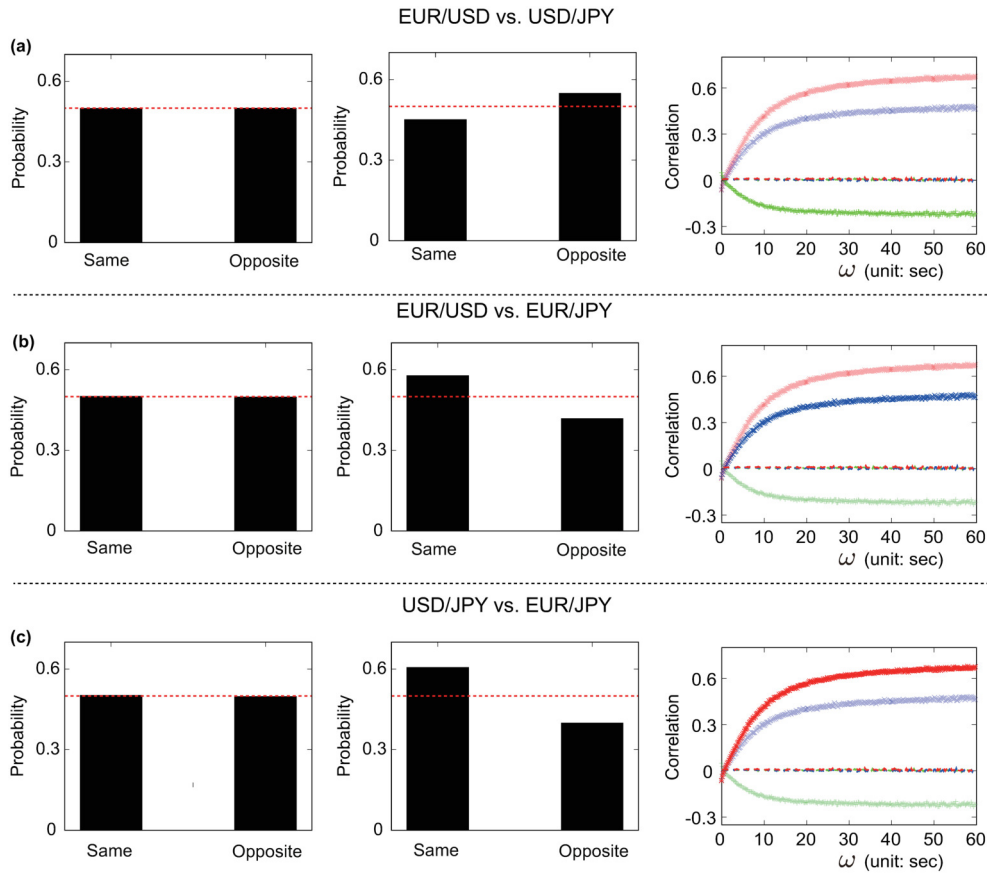


Figure 4.14: **Statistical relationships between different FX markets.** Probability of observing two markets in the same or opposite state in the absence of the arbitrager (left column), with the arbitrager (central column) and the associated cross-correlation functions $\rho_{i,j}(\omega)$ (right column) for (a) $\Delta\text{EUR}/\text{USD}$ vs. $\Delta\text{USD}/\text{JPY}$, (b) $\Delta\text{EUR}/\text{USD}$ vs. $\Delta\text{EUR}/\text{JPY}$ and (c) $\Delta\text{USD}/\text{JPY}$ vs. $\Delta\text{EUR}/\text{JPY}$. The red solid line in the histograms marks the value of 0.5, highlighting the case in which two markets have the same probability of being in the same or opposite state. The lines indicating the value of the cross-correlation function $\rho_{i,j}(\omega)$ are solid (dashed) for experiments including (excluding) the arbitrager. Simulations are performed under the same settings of the experiment presented in Fig. 4.12(b), bottom panel. The inclusion of the arbitrager increases the probability of observing EUR/USD and USD/JPY as well as EUR/USD and EUR/JPY in the same state and USD/JPY and EUR/USD in the opposite state. Furthermore, the active presence of this special agent intertwines the dynamics of different FX rates, creating cross-correlations functions that resemble those emerging in real trading data. This figure has been extracted from [34], see appendix B.4 for details about attributions and permissions.

ecology configuration, see Fig. 4.18, the expected lifetimes of these configurations are, to different extents, shorter than in an arbitrage-free system. Second, certain ecology configurations

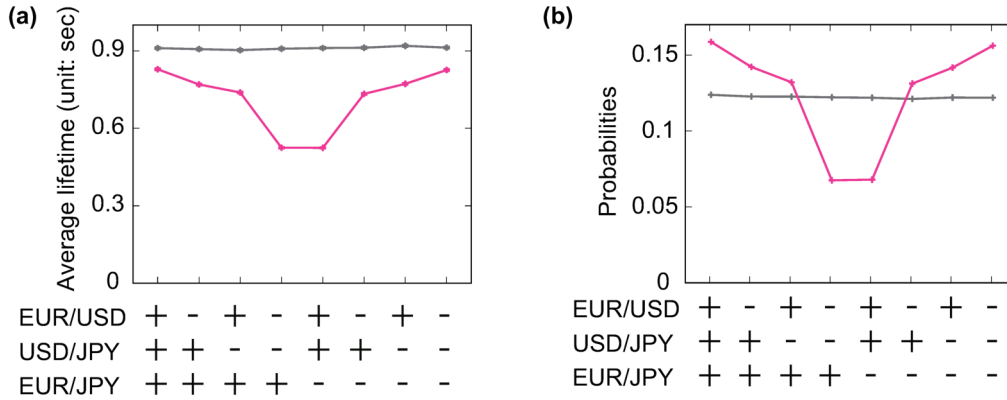


Figure 4.15: **Expected lifetime and appearance probability of the eight ecology configurations.** Statistics are collected from simulations of the Arbitrage Model with active (violet) and inactive (grey) arbitrage. Simulations are performed under the same settings of the experiment presented in Fig. 4.12(b), bottom panel. The presence of an active arbitrage increases the average lifetimes (a) and appearance probabilities (b) of certain configurations and reduces the same statistics for others. Statistics in (a) are expressed in real time (i.e., sec.), details on the conversion between simulation time (i.e., time steps) and real time (i.e., sec) are provided in appendix G.1. This figure has been extracted from [34], see appendix B.4 for details about attributions and permissions.

are expected to last more than others (i.e., single episodes). As reactions to triangular arbitrage opportunities increase the likelihood of flipping a market state, the average lifetime of a given configuration relate to the time required for the first triangular arbitrage opportunity to emerge. For instance, the time between the inception and the first time $\mu^I(t)$ or $\mu^{II}(t)$ becomes larger than one never exceeds 4 sec for $\{-, -, +\}$, which is the configuration with shortest expected lifetime, while it can reach ≈ 6.5 sec for $\{+, +, +\}$, which is the configuration with longest expected lifetime, see Fig. 4.16. This difference can be intuitively explained by looking at the combination of market states. When the ecology configuration is $\{-, -, +\}$, EUR/USD and USD/JPY have the opposite state of EUR/JPY. In this scenario, the implied FX cross rate $\text{EUR/USD} \times \text{USD/JPY}$ moves in the opposite direction of the FX rate EUR/JPY, creating the ideal conditions for a rapid emergence of triangular arbitrage opportunities. Conversely, the three markets share the same state when the ecology configuration is $\{+, +, +\}$. In this case, both the FX rate and the implied FX cross rate move in the same direction, extending

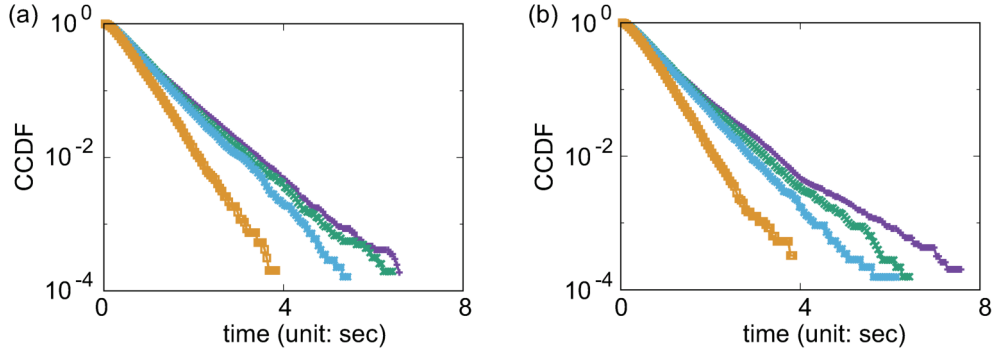


Figure 4.16: **Complementary cumulative distribution function (CCDF) of the time required for the first triangular arbitrage opportunity to emerge.** The CCDFs are presented in two separate panels and each color represents a given configuration: (a) $\{+, +, +\}$ (violet), $\{+, +, -\}$ (cyan), $\{+, -, +\}$ (green) and $\{-, -, +\}$ (orange). (b) $\{-, -, -\}$ (violet), $\{+, -, -\}$ (cyan), $\{-, +, -\}$ (green) and $\{+, +, -\}$ (orange). The y-axis is visualized in the logarithmic scale. Configurations exhibit different tails of the distribution, suggesting that the probability of observing large waiting times between the inception of the configuration and the emergence of the first triangular arbitrage opportunity depends on the current combinations of market states. This figure has been extracted from [34], see appendix B.4 for details about attributions and permissions.

the time required by these prices to create a gap that can be exploited by the arbitrager. The third and final interesting fact emerged in Fig. 4.15 is that certain configurations are more likely to appear than others. To understand this aspect, consider the significant differences between the probabilities of transitioning from a configuration to another, see table 4.2. For instance, assuming that the system is leaving $\{+, +, +\}$, the probabilities of transitioning to $\{-, +, +\}$ and $\{+, +, -\}$ are 35.8% and 22.7%, respectively. This difference can be explained by the fact that it is much easier to flip the state of EUR/USD and move to $\{-, +, +\}$ than flipping EUR/JPY and move to $\{+, +, -\}$. The value of the price trend $\phi_{n,\ell}(t)$ can be intuitively seen as the *resistance* to state changes of the ℓ -th market: the higher its value, the more the transaction price must fluctuate in the opposite direction to flip its sign. For each configuration, the absolute value of this statistics is sampled at the emergence of any triangular arbitrage opportunity. Then, its average is normalized by the initial center of mass $p_\ell(t_0)$, see G.1 Section, to make it comparable with the same quantity measured in other markets. For $\{+, +, +\}$, $\langle |\phi_{n,\ell}(t)| \rangle / p_\ell(t_0)$ is substantially higher for EUR/JPY than EUR/USD and USD/JPY, see Fig. 4.17. As a re-

Configuration	{+, +, +}	{-, +, +}	{+, -, +}	{-, -, +}	{+, +, -}	{-, +, -}	{+, -, -}	{-, -, -}
{+, +, +}		0.358	0.336	0.010	0.227	0.028	0.026	0.014
{-, +, +}	0.375		0.027	0.218	0.011	0.329	0.014	0.026
{+, -, +}	0.364	0.026		0.217	0.012	0.014	0.341	0.026
{-, -, +}	0.035	0.302	0.295		0.006	0.028	0.030	0.305
{+, +, -}	0.304	0.030	0.028	0.007		0.294	0.302	0.035
{-, +, -}	0.026	0.340	0.014	0.012	0.220		0.026	0.363
{+, -, -}	0.028	0.013	0.330	0.011	0.217	0.027		0.374
{-, -, -}	0.015	0.027	0.027	0.226	0.010	0.335	0.359	

Table 4.2: **Transition rates between two configurations.** Rows (Columns) indicate the departed (reached) configuration. These transition rates correspond to the total number of transitions between two specific configurations normalized by the total number of transitions from the departed configuration. The two grey portions of the matrix mark the first (upper-left) and second (lower-right) clusters.

sult, predatory market orders are more likely to set the ground for transitions from $\{+, +, +\}$ to $\{-, +, +\}$ (35.8%) or $\{+, -, +\}$ (33.6%). Looking at these transitions on the opposite direction is even more compelling: $\{+, +, +\}$ is the most likely destination from both $\{-, +, +\}$ (37.5%) and $\{+, -, +\}$ (36.4%). This hints at the presence of a loop in which the ecology transits from $\{+, +, +\}$ to $\{-, +, +\}$ or $\{+, -, +\}$ and then moves back. Such dynamics find an explanation in the fact that the market that has recently flipped its state, causing a departure from $\{+, +, +\}$ towards $\{-, +, +\}$ or $\{+, -, +\}$, can be easily flipped back again before its *resistance* to state changes $\phi_{n,\ell}(t)$ increases in absolute value. This happens when the arbitrageur responds to a type 2 triangular arbitrage opportunity (i.e., $\mu^{II}(t) > 1$) when the ecology configuration is either $\{-, +, +\}$ or $\{+, -, +\}$.

The significant probabilities of returning to $\{+, +, +\}$ stem from the interplay of two elements. First, triangular arbitrage opportunities are more likely to be of type 2 than type 1 in both $\{-, +, +\}$ and $\{+, -, +\}$, see Fig. 4.18. Second, the markets with lowest *resistance* to state changes $\langle |\phi_{n,\ell}(t)| \rangle / p_\ell(t_0)$ are EUR/USD for $\{-, +, +\}$ and USD/JPY for $\{+, -, +\}$, see Fig. 4.17, which are exactly the states that should be flipped to return to $\{+, +, +\}$. The conditional transition probability matrix displayed in 4.2 Table reveals the presence of another configuration triplet (i.e., $\{-, -, -\}$, $\{-, +, -\}$ and $\{+, -, -\}$) exhibiting an analogous behavior while $\{-, -, +\}$ and $\{+, +, -\}$ are the only two configurations that are not part of any loop. Fig. 4.19 shows this mechanism in action by displaying the sequence of ecology configu-

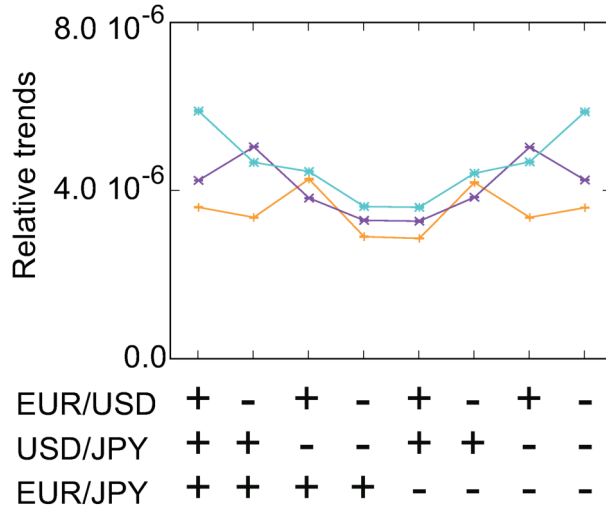


Figure 4.17: **Price trends and changes in market states.** Sample averages of the normalized absolute value of the price trend $\langle |\phi_{n,\ell}(t)|/p_\ell(t_0) \rangle$ for EUR/USD (orange), USD/JPY (violet) and EUR/JPY (cyan). Normalizing by the initial center of mass $p_\ell(t_0)$ allows to compare the price trends across markets with different price magnitudes. The value $|\phi_{n,\ell}(t)|/p_\ell(t_0)$ is exclusively sampled at the emergence of each triangular arbitrage opportunity and each configuration is considered independently. As arbitrageur's market orders alter price trends, the value of $|\phi_{n,\ell}(t)|/p_\ell(t_0)$, where t is the time step when μ^I or μ^{II} exceeds the unit, provides an intuitive measure of how currently hard is to flip the state of the ℓ -th market. For instance, consider $\{+, +, +\}$ and observe that $\langle |\phi_{n,\ell}(t)|/p_\ell(t_0) \rangle$ is much higher in EUR/JPY than in EUR/USD and USD/JPY. This is reflected in the probabilities of transitioning from $\{+, +, +\}$ to other configurations. Flipping EUR/JPY before the other two markets, causing a transition to $\{+, +, -\}$, occurs in 22.7% of the cases. However, flipping EUR/USD or USD/JPY first, causing a transition to $\{-, +, +\}$ or $\{+, -, +\}$, occur in 35.8% and 33.6% of the cases respectively, see table 4.2. This figure has been extracted from [34], see appendix B.4 for details about attributions and permissions.

rations during a segment of the model simulation. It is easy to observe how the system tends to move across configurations belonging to the same looping triplet for long, uninterrupted time windows. Ultimately, this peculiar mechanism increases, to different degrees, the appearance probabilities of configurations involved in these loops at the expenses of $\{-, -, +\}$ and $\{+, +, -\}$.

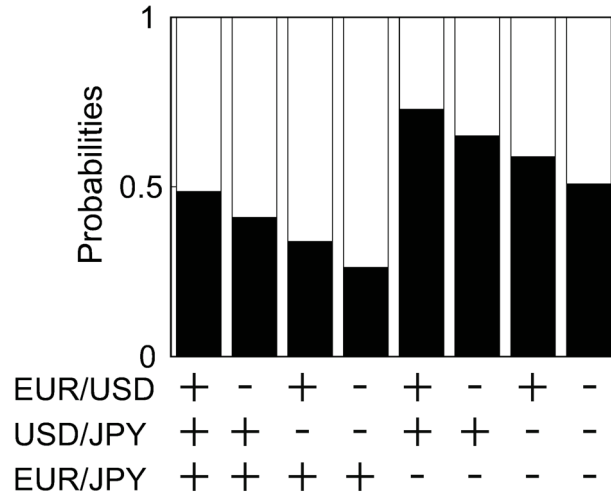


Figure 4.18: **Fraction of triangular arbitrage opportunities of the first and second type in each ecology configuration.** Black bars denote the incidence of type 1 opportunities, see Eq. (4.18a), while white bars represent the incidence of type 2 opportunities, see Eq. (4.18b). These statistics suggest that one type appears more frequently than the other, depending on the considered configuration. This figure has been extracted from [34], see appendix B.4 for details about attributions and permissions.

4.5.7 Summary and outlook

To sum up, the Arbitrager Model elucidates how the interplay between different trading strategies entangles the dynamics of different FX rates, leading to the characteristic shape of the cross-correlation functions observed in real trading data. The Arbitrager Model restricts its focus to the interactions between two types of strategies, namely triangular arbitrage and trend-following. Despite the simplicity of this framework, the interplay between these two strategies alone satisfactorily reproduces the cross-correlation functions observed in real trading data. In particular, trend-following strategies preserve the current combination of market states for some time while reactions to triangular arbitrage opportunities *influence* the behavior of trend-following market makers by altering the price trend signals used in their dealing strategies. The interactions between these two strategies constantly push the system towards certain configurations and away from others through multiple mechanisms. This can be easily seen in Fig. 4.15 as two distinct statistics, the average expected lifetimes and the appearance probability, put the eight configurations in the same order. For instance $\{+, +, +\}$ has the longer expected lifetime but also the highest appearance probability. This *force* shapes the features of the statistical

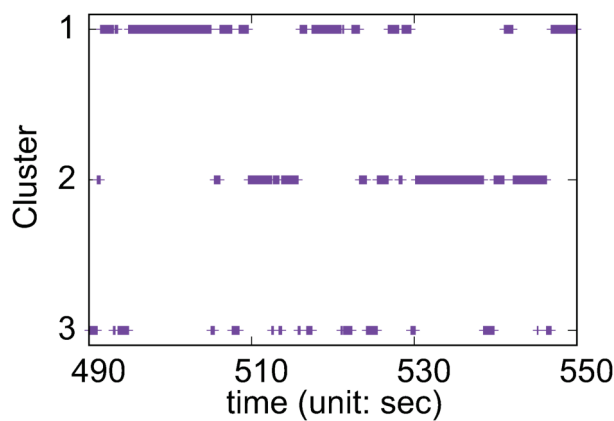


Figure 4.19: **The sequence of transitions between configurations exhibits a clustered behavior.** The x-axis represents an arbitrary time window of the experiment. The y-axis splits the eight ecology configurations in three groups - from top to bottom: (1) cluster 1, (2) cluster 2 and (3) $\{-, -, +\}$ and $\{+, +, -\}$, which are the two configurations that do not belong to any cluster. At each point in time the current ecology configuration is identified and a marker is added to the group it belongs to. A visual inspection of the figure reveals the presence of time windows in which the system moves between configurations belonging to the same cluster, corresponding to the long, uninterrupted lines observed in groups 1 and 2, but not in group 3. These peculiar dynamics favor the appearance of configurations belonging to groups 1 and 2 at the expenses of those belonging to group 3, see Fig. 4.15(b). Details on the conversion between simulation time (i.e., time steps) and real time (i.e., sec) are provided in appendix G.1. This figure has been extracted from [34], see appendix B.4 for details about attributions and permissions.

relationships between currency pairs. FX rates traded in markets that share the same state in configurations with higher (lower) appearance probabilities and longer (shorter) expected lifetimes are more likely to fluctuate in the same (opposite) direction. For instance, consider USD/JPY and EUR/JPY. These two markets have the same states in the four configurations with higher probabilities (i.e., $\{+, +, +\}$, $\{-, +, +\}$, $\{+, -, -\}$ and $\{-, -, -\}$) and opposite states in those with lower probabilities (i.e., $\{+, -, +\}$, $\{-, -, +\}$, $\{+, +, -\}$ and $\{-, +, -\}$). It follows that the probability of observing USD/JPY and EUR/JPY in the same state at a given point in time t is $\approx 60\%$, see Fig. 4.14. In these settings, the mid price dynamics of two FX rates become permanently entangled, leading to the cross-correlation functions displayed in Figs. 4.12(b) and 4.14.

The Arbitrager Model, finding a common ground between previous microscopic ABMs of the FX

market and triangular arbitrage [384, 35, 386], sets a new benchmark for further investigations on the relationships between agent interactions and market interdependencies. In particular, it is the first ABM to provide a complete picture on the microscopic origins of cross-currency correlations.

The outcomes of this work open different research paths and raise new challenges that shall be considered in future studies:

- The Arbitrager Model could be further generalized by including a larger number of currencies, allowing traders to monitor different currency triangles. Extending the number of available currencies could reveal new insights into i) statistical regularities related to the triangular arbitrage processes, such the distributions of $\mu^I(t)$ and $\mu^{II}(t)$, and ii) how the features of the cross-correlation function between two FX rates stem from a much more complex system in which the same FX rate is part of several triangles.
- A potential extension of this model should consider the active presence of special agents operating in FX markets. For instance, simulating public interventions implemented by central banks could be a valuable exercise to understand how the large volumes moved by these entities affect the dynamics of the triangular arbitrage processes $\mu^I(t)$ and $\mu^{II}(t)$ and the local correlations (i.e., in the intervention time window) between currency pairs.
- Another interesting path leads to market design problems. This study advanced the hypothesis that changes in the stabilization levels of the cross-correlation functions $\rho_{i,j}(\omega)$ might be rooted in the different tick sizes adopted by EBS in the period covered by the employed dataset. Calling for further investigations, an extended version of the present model should examine how different tick sizes affect the correlations between FX rates.
- Future works shall also consider established (e.g., AR family models) and novel [388] tools to exploit further properties of FX rates co-movements. Such investigations might reveal additional statistical relationships whose mechanistic origins can be studied in an augmented version of the Arbitrager Model.

The Arbitrager Model could be subject of meaningful extensions and enhancements aimed to turn this framework into a valuable tool that could be used by exchanges, regulators and market designers. In particular, its simple settings would allow these entities to make predictions

on how regulations or design changes could affect the relationships between FX rates and the properties (e.g., frequency, magnitude, duration, etc.) of triangular arbitrage opportunities in a given market. Furthermore, its applicability might attract the attention of other actors operating in the FX market, such as central banks. The ultimate objective of this work and its potential future extensions shall remain the provision of useful means to enhance the understanding of financial market dynamics, assisting the aforementioned entities in conceiving safer and more efficient trading environments.

4.6 Liquidity Fluctuations and the Latent Dynamics of Price Impact

Personal contributions

This section presents the paper “*Liquidity Fluctuations and the Latent Dynamics of Price Impact*” [37], published in *Quantitative Finance* in July 2021. As primary co-author, I played a primary role in every major aspect of this project:

- Understanding the relevant literature.
- Development of the underlying theory.
- Development of the computational infrastructure required to analyse the behavior of the models.
- Management of computer-based simulations and data collection.
- Analysis and interpretation of computer-based simulations.
- Presentation of experimental results.
- Writing of the manuscript.

Note that a seminal version of the model introduced in this paper was proposed by Luca Philippe Mertens in an earlier preprint. We introduce a variety of changes to that model, most notably, the ability to disentangle the intraday pattern of price impact.

4.6.1 Context

This section presents the paper “*Liquidity Fluctuations and the Latent Dynamics of Price Impact*” [37], published in *Quantitative Finance* in July 2021. The current permissions and copyright regulations do not allow us to re-use materials from the published version, therefore, the contents appearing in the following sections and subsections have been extracted from the submitted version of this article.

In this article we propose a dynamical linear price impact model at high-frequency in which the price impact coefficient is a product of a daily, a diurnal, and an auto-regressive stochastic intraday component. We estimate the model using a Kalman filter on order book data for stocks traded on the NASDAQ in 2016. We show that our price changes estimates conditional on order flow imbalance explain, on average, 82% of real price changes variance. Evidence is also provided on the fact that the conditioning on filtered information improves the estimate of the LOB liquidity with respect to the one obtained from a static estimation of the price impact. In addition, an out-of-sample analysis shows that our model provides a superior out-of-sample forecast of price impact with respect to historical estimates.

4.6.2 Introduction

Statistical modeling of LOBs is a well established and active area of research. Central to this topic is the concept of price impact, or “the correlation between an incoming order and the subsequent price change” [355]. Grounded in the economic intuition that price changes should reflect the aggregate imbalance between supply and demand, [36] introduce the *Order Flow Imbalance* (OFI henceforth), the sum of signed volume of all incoming orders at the best quotes over a time interval. The authors prove that, at the minute time-scale, price change is a linear function of the order flow imbalance, and identify the price impact of order book events with the regression coefficient of this linear relationship.

We make two contributions to the price impact literature. First, we provide empirical evidence of the auto-regressive nature of price impact at short time scales. Second, leveraging this statistical feature, we describe an econometric model for *conditional* high frequency estimates of price impact. While the order flow imbalance is a strong predictor of price change at the minute time-scale, at a higher-frequency, the discreteness of the price change variable becomes a dominant feature, weakening the linear relationship between price changes and OFI, and

thus the explanatory power of a simple regression model. We prove that, over short time scales, price impact has a statistically significant auto-correlation, even after controlling for the presence of the intraday pattern. This statistical feature has important consequences for estimation purposes: at a high frequency, price impact has a weaker dependence on OFI, but a higher dependence on recent LOB activity. By using a filtering approach, where price impact is modeled as a latent auto-regressive variable with noisy observations, we can exploit past information to form a prior on the current level of price impact, and lower the estimation error. Precisely, we introduce a model where price impact at time ℓ of day i is determined by the product of three components: a daily price impact component β_i , a deterministic intraday pattern π_ℓ , and a stochastic auto-regressive component $q_{i,\ell}$. This type of modeling is reminiscent of analogous models in the conditional variance literature, see [389] for instance. The resulting price impact process $\beta_{i,\ell}$ describes the time dependent relationship between price change – normalized by the tick size $\delta - \Delta P_{i,\ell}$ and the order flow imbalance $\phi_{i,\ell}$. In particular, our model can be thus written as:

$$\Delta P_{i,\ell} = \beta_{i,\ell} \phi_{i,\ell} + \epsilon_{i,\ell} \quad \epsilon_{i,\ell} \sim \text{NID}(0, \sigma_\epsilon^2) \quad (4.22a)$$

$$\beta_{i,\ell} = \beta_i \pi_\ell q_{i,\ell} \quad (4.22b)$$

$$q_{i,\ell} = 1 + \rho(q_{i,\ell-1} - 1) + \eta_{i,\ell} \quad \eta_{i,\ell} \sim \text{NID}(0, \sigma_\eta^2) \quad (4.22c)$$

In this setting, price impact is linear in the order flow and permanent, but its value at a given day/time of the day is determined by the *price impact process*, see Eqs. (4.22)(b)-(c). The model postulates that even at the time-scale considered in this work, i.e., 1 minute, the contemporaneous OFI is the main determinant of price changes and, in particular, it does not describe the joint dynamics of price changes and OFI. We empirically verify the reliability of this exogeneity assumption on OFI by performing a study following the lines of [390]. Also, the model assumes no commonality in the OFI of assets i and j with $j \neq i$, see [391]). Considering such a factor in our time-varying model represents an interesting direction for future research. Admittedly, the Gaussian assumption in Eq. (4.22)(a) may be suspect because the price change variable may be confined on a discrete price grid. However, we reassure, through some classical diagnostic testing for Kalman filter, that the forecast errors are mostly normal. Finally, the model suggests-and the empirical analysis verifies-that variation in intraday liquidity is not caused only by a deterministic and recurrent diurnal pattern, but also by a stochastic auto-regressive component, which can be associated with transitory phenomena. In other words, the predictable diurnal pattern of market depth [36] is not sufficient to explain all

the auto-correlation of price impact. The model described in Eq. (4.22) has a linear Gaussian state-space representation that can be easily estimated using a Kalman filter [392] and standard maximum-likelihood methods.

Our model has interesting applications for execution. Execution strategies typically slice an order into child orders, which are then executed within a given time window according to a trading schedule. Tactical execution of child orders could benefit from the real-time price impact forecast provided by our model. For example, a trader could defer a trade when the price impact is higher than the expected average level, waiting for market conditions where the likelihood of moving the price against her are lower.

We select five stocks listed on the National Association of Securities Dealers Automated Quotation System (NASDAQ henceforth) 100 index and we filter intraday time-series of price impact estimates. Our analysis leads to the following results: i) the auto-regressive coefficient ρ is statistically significant with an average value of approximately 0.5, suggesting a half-life of 1 minute for the process q ; ii) conditioning on real time information improves the estimate of the LOB liquidity with respect to the one obtained from the deterministic intraday pattern alone. ii) The variance of the price changes explained by $\beta_{i,\ell}\phi_{i,\ell}$ in Eq. (4.22)(a) is significantly larger than the one explained by both a model in which $\beta_{i,l}$ is statically computed and a model in which $\beta_{i,l}$ is book-reconstructed and set equal to half the inverse of the depth as in the stylized LOB model [36]. Moreover, it turns out that the price impact is much higher after the opening auction than during the rest of the trading day in which it exhibits a flat behavior followed by a decline before the closing auction.

4.6.3 Literature review

Market liquidity is one of the key characteristics of financial markets. Given its relevance, both from a theoretical, e.g., for price formation [393, 394], and a practical perspective, e.g., for the optimal liquidation of institutional orders [395, 353], an extensive body of literature has been written in the effort to define, measure, and understand liquidity, see for an authoritative introduction on the subject and its ramifications [346]. Also, market liquidity is a slippery and elusive concept with various dimensions. One of them, which is the focus of this project, is price impact, i.e., the reaction of prices to trades. In his foundational paper [38] Kyle derives an equilibrium solution in a framework where price fluctuations and traded volumes are linearly related. Moreover, he shows that the reciprocal of the coefficient of this linear relationship,

i.e., the notorious Kyle's lambda, is a measure of the depth of the market. Since then, several models of market impact have been proposed [133, 396, 397, 371, 398, 399, 36].

Although price impact can be derived from an equilibrium solution, it can be seen also as the result of the arrival and cancellation of orders in the market. Over the last two decades, the increasing availability of high quality granular data has motivated a stream of studies focused on the modeling and measurement of the price impact of orders. The impact of market orders has been extensively investigated in [400, 401], where the connection between the state of the LOB and price fluctuations has been elucidated. Moreover, it has been shown that limit orders and cancellations also have a significant price impact [402, 403].

Our model builds on [36] and brings the following innovations: i) the price impact coefficient is considered a latent and dynamical variable; ii) we are able to disentangle and quantify the contribution of the different components (daily component, time-of-the-day pattern and intra-day variance) of the price impact coefficient estimates; iii) we can describe the statistical properties of the stochastic intraday component $q_{i,\ell}$, such as its persistence. We point out that a previous version of this model appeared in a preprint written by one of us. Here we add several changes to that model, the most important one is the disentangling of the periodic intraday component, which is responsible of a significant fraction of the persistence in price impact. Our model is broadly in line with the class of History Dependent Impact Models (HDIM henceforth) [365, 402] in which the price impact is permanent but variable. Indeed, although in our methodology the price impact is not explicitly history dependent, i.e., it does not depend explicitly on previous values of the OFI, its dynamics is filtered out through the use of Kalman Filter. As a consequence of this procedure, it becomes dependent on previous values of the OFI.

Finally, we notice that the assumption of time varying liquidity is consistent with various theoretical and empirical works in the literature [404, 405, 406] for which price impact varies according to the underlying economic environment. Moreover, other authors in the financial literature postulate an auto-regressive dynamics for the price impact coefficient [407, 408, 409, 406]. However, while models for high-frequency intra-day conditional variance of financial returns are well-explored [410, 411, 412, 413, 389, 414], to the best of our knowledge, price impact models in which the price impact has an its own unobserved dynamics have not been subject of deep investigations. The main contribution of our study is the introduction of an enhanced methodology for the characterization of security price dynamics within the state-

space models framework. Broader finance applications would include liquidity effects on asset pricing, optimal trading strategies, or market design. Still, the latter applications may represent an interesting direction for future research.

4.6.4 The Cont-Kukanov-Stoikov Model on different time scales

The estimation of the model proposed by [36], see section 4.4.4 for a detailed overview, relies on two distinct time scales: Δ_K , which is the time interval over which a single β is estimated, see Eq. (4.14), and Δ_ℓ , with $\Delta_\ell < \Delta_K$, which is the frequency at which single realizations of price changes and order flow imbalance are sampled. We use the following notation: days are indexed by $i = 1, \dots, N$ and the trading day is divided in multiple non-overlapping intervals, i.e., bins, indexed by $\ell = 0, \dots, L$.

In the original paper the authors divided each day in 13 non-overlapping intervals of $\Delta_K = 1800$ s minutes and considered time-series of Δp and ϕ with sampling frequency $\Delta_\ell = 10$ s. Since we are interested in modeling liquidity at a significantly higher frequencies, i.e., $\Delta_K = 60$ s, we conduct an empirical analysis in order to test the performance of the Cont-Kukanov-Stoikov model over different time scales. We estimate Eq. (4.14) for different values of Δ_K and for different values of Δ_ℓ given a fixed Δ_K . Qualitatively, the results obtained from different stocks are highly comparable, allowing us to display MSFT as a representative of the entire pool.

The left panel of Fig. 4.20 shows the estimated value of β when Δ_K is fixed and equal to 1800s and Δ_ℓ varies from 300 to 0.5s. The right panel displays a contour plot of the coefficients of determination as a function of the length (in seconds) of the regression window Δ_K and of the sampling frequency Δ_ℓ . Reported statistics have been averaged across 100 days, starting from January 4th 2016. The left panel shows that the average value of β weakly depends on Δ_ℓ . A mildly divergence from this behavior occurs when Δ_ℓ is equal to 300s. In line with [36], the R^2 strongly depends on Δ_ℓ . For a fixed Δ_K , R^2 is a non monotonic function of Δ_ℓ , i.e., it initially increases and reaches a maximum around $\Delta_\ell = 10 - 30$ s, which is the time-scale used in [36]. Moreover, it is a monotonically decreasing function of Δ_K for a fixed Δ_ℓ . Fig. 4.20 indicates that at short time scales the regression is less accurate, thus suggesting that the estimation of the price impact at a higher frequencies is likely to be quite noisy. To overcome this problem, we propose a dynamical model of price impact, see section 4.6.5, where β is a latent variable estimated through a Kalman filter approach, over intervals of one minute. Before introducing our model, we perform a standard regression analysis under the following settings: i) β is

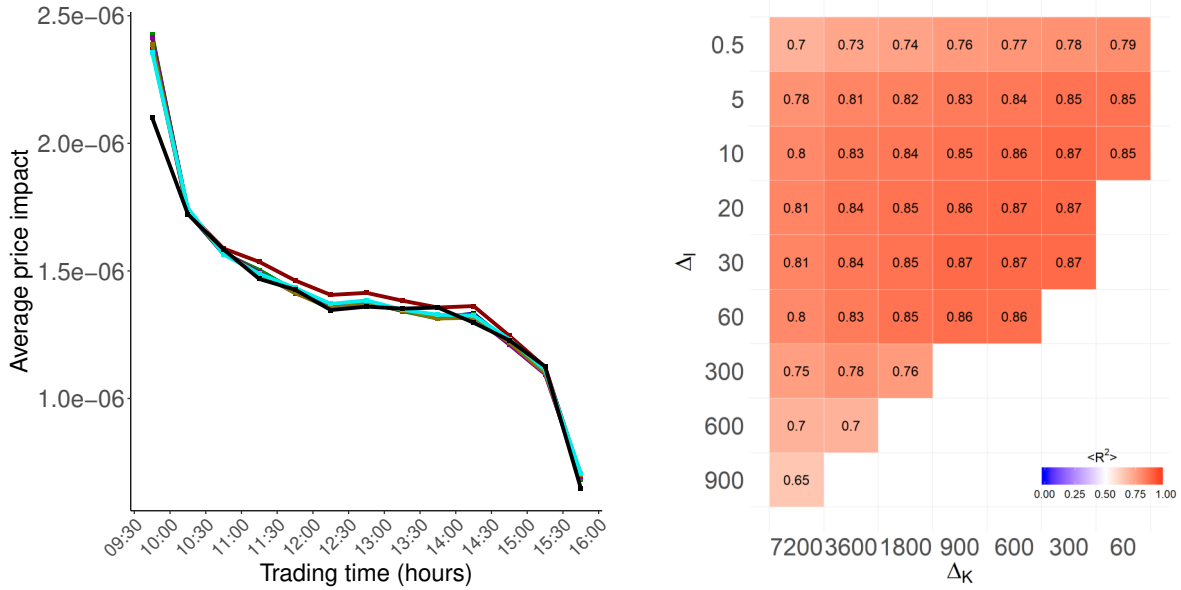


Figure 4.20: **The Cont-Kukanov-Stoikov on different time scales.** Left panel represents averages across days of the price impact coefficient estimates $\hat{\beta}_k$ as in Eq. (4.14) for MSFT as a function of the time of the day for $\Delta_K = 1800\text{s}$ and $\Delta_\ell = 0.5\text{s}$ (red), 5s (blue), 10s (green), 20s (magenta), 30s (gold), 60s (cyan) and 300s (black). Right panel represents the contour plot of the averages R^2 across days as a function of the regression window Δ_K and sampling frequency Δ_ℓ . This figure has been extracted from [345], see appendix B.5 for details about attributions and permissions.

estimated over a window $\Delta_K = 60\text{s}$ and ii) time series of ϕ and Δp are sampled with frequency $\Delta_\ell = 0.5\text{s}$. The goal of this exercise is to obtain further insights on the type of dynamical modeling that is appropriate for empirical data. Results are summarized in Fig. 4.21.

The top-left panel of Fig. 4.21 plots the histogram of the values $\hat{\beta}_i$, $i = 1, \dots, N$ obtained by averaging, in each generic day i , $\hat{\beta}_{i,\ell}$ over ℓ . The significant variability range of $\hat{\beta}_{i,\ell}$, i.e., between 2 and 4, calls for the introduction of a parameter that accounts for the average liquidity on a given day i . Therefore, a proper account of the factors governing price impact must incorporate its average daily level. The intuition behind our assertion is that there are some days in which the market is globally more “liquid” than others.

The top-right panel of Fig. 4.21 displays the estimated price impact intraday pattern $\hat{\beta}_\ell$, $\ell = 1, \dots, L$. In the same spirit of [36], we retrieve the pattern by averaging the estimated price impact across the trading days. In agreement with the empirical findings of [36], the price impact exhibits a pronounced intraday periodic component. This calls for a model specification

that explicitly takes into the account this feature. A first visual inspection of the intraday pattern of price impact reveals a characteristic shape. The largest price impact occurs at the open trade. Then, it gradually tapers through the interior period and rapidly falls at the end of the trading day.

Let $\hat{\beta}_{i,\ell}$ be the estimates in Eq. (4.14) relative to day i and to the ℓ -th one-minute slot. We compute for each intraday one-minute interval the sample mean and the sample standard deviation of the estimates across days and relate these quantities in the scatter plots presented in the bottom-left panel of Fig. 4.21. The panel clearly shows a positive relationship between these two statistics. This type of relationship, common for families of random variables with positive support, e.g. the Gamma, the log-normal, and the Weibull are parametric families of random variables with this property, calls for a multiplicative process for market impact.

Finally, we rescale each $\hat{\beta}_{i,\ell}$ by the intraday pattern. We perform this further step in order to eliminate the risk of accounting for spurious auto-correlations. We plot the ACF of this normalized quantity, see the bottom-right panel of Fig. 4.21, on May 12nd 2016 to detect some short-lived dependencies. What type of phenomena can lead to these dependencies? We interpret this result as being symptomatic of transient phenomena, which are not captured by the “predictable” intraday pattern of the price impact [36]. In particular, these phenomena should exhibit different statistical properties with respect to the time-of-the day effect. We claim that these *fluctuations* around the average level of price impact should be unobserved, i.e., *latent*, similarly to what is assumed for the volatility of price returns in the volatility literature. In summary, we have identified four main dynamical properties that we will incorporate in the model proposed in section 4.6.5:

1. Price impact varies across days, thus a global level characterizes the average liquidity.
2. There is a pronounced intraday pattern³.
3. There is a linear relation between the mean and standard deviation of price impact, suggesting that the price impact should be modeled by a multiplicative process.

³In addition to the previous effects, price impact may exhibit large, sudden shifts around the release of important economic news, such as macroeconomic information, see [411] for instance. Should the price impact *explicitly* accounts for economic announcements, one would multiply the price impact coefficient for an additional factor representing the scheduled announcement effects. This further modelling is beyond the scopes of this project, however, we strongly encourage this analysis in future works.

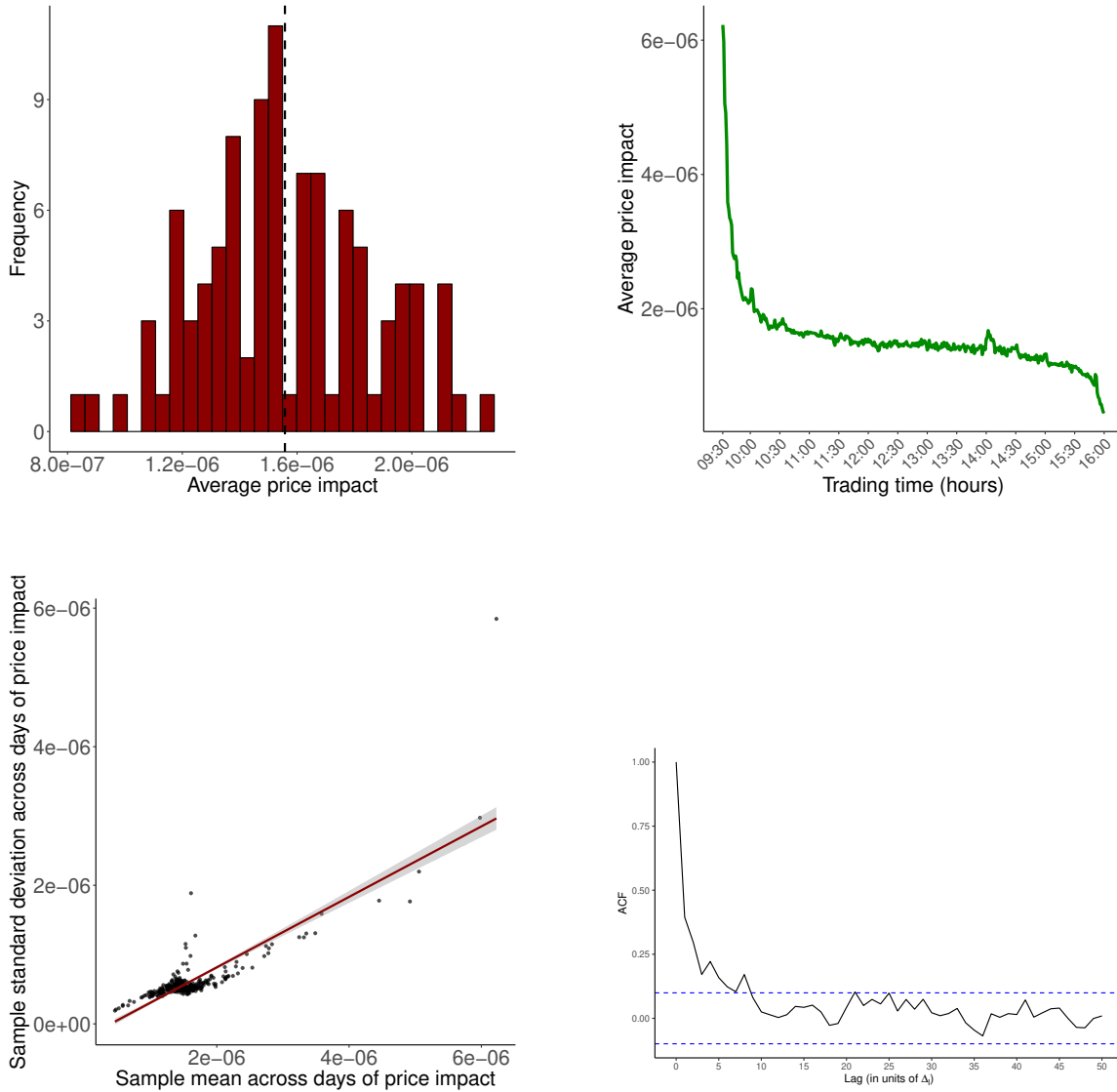


Figure 4.21: **Statistical properties of the price impact coefficient estimates.** (top-left) Histograms of the average daily level of price impact; (top-right) estimates of the intraday pattern of price impact coefficient computed according to [36] at a time-scale of $\Delta_K = 60\text{s}$, $\Delta_\ell = 0.5\text{s}$; (bottom-left) scatter plot of the sample mean vs. the sample standard deviation computed in each intraday one-minute interval across the days included in the sample; (bottom-right) average autocorrelation (ACF) across days as a function of the lag, i.e., 1 minute bin. This figure has been extracted from [345], see appendix B.5 for details about attributions and permissions.

4. Price impact exhibits short-range autocorrelation.

4.6.5 A dynamical market impact model

Overview

Intraday equity returns on a given day i and at time-of-the-day ℓ are described by the following process:

$$\Delta P_{i,\ell} = \beta_{i,\ell} \phi_{i,\ell} + \epsilon_{i,\ell}, \quad \epsilon_{i,\ell} \sim \text{NID}(0, \sigma_\epsilon^2) \quad (4.23a)$$

$$\beta_{i,\ell} = \beta_i \pi_t q_{i,\ell}, \quad (4.23b)$$

$$q_{i,\ell} = 1 + \rho(q_{i,\ell-1} - 1) + \eta_{i,\ell}, \quad \eta_{i,\ell} \sim \text{NID}(0, \sigma_\eta^2) \quad (4.23c)$$

where $\epsilon_{i,\ell}$ and $\eta_{i,\ell}$ are NIID and mutually independent with mean zero and variance respectively equal to σ_{ϵ}^2 and σ_{η}^2 . The process π_ℓ , which is allowed to change within the day but is otherwise time-invariant across days, captures the diurnal effect. β_i is the daily average price impact component on day i , while $q_{i,\ell}$ denotes the remaining, potentially correlated, stochastic price impact component which is described through a latent mean-reverting process. Note that, without additional restrictions, the components of Eq. (4.23)(b) are not separately identified hence the assumption $\sum_{\ell=1}^L \pi_\ell = L$. Setting $\alpha_{i,\ell} \equiv q_{i,\ell} - 1$, i.e. $\alpha_{i,\ell}$ measures the stochastic component of the price impact deviation from the average level, we define a *price impact fluctuation* to be a non-zero conditional expected value of the process $\beta_i \pi_\ell \alpha_{i,\ell}$. The dynamics presented in Eq. (4.23) form a latent variable model which can be estimated through Kalman Filter.

Estimation

Following the general state-space representation in [392], we denote the value of a generic variable X , e.g. price impact coefficient or hyper-parameter, at day i and bin ℓ as $X_{i,\ell}$, $i = 1, \dots, N$ and $\ell = 1, \dots, L$. Our methodology is independently applied to each day of the sample, therefore, for the sake of simplicity, the index i will be replaced by \cdot . We denote the set of observations of the price adjustment up to time $\ell - 1$ with $\mathcal{P}_{\cdot,\ell-1} = \{\Delta P_{\cdot,1}, \dots, \Delta P_{\cdot,\ell-1}\}$ and the hyper-parameters vector with $\Theta = (\beta_\cdot, \rho_\cdot, \sigma_{\cdot,\epsilon}, \sigma_{\cdot,\eta})$. Adapting this notation to Eq. 4.23 we

obtain

$$\Delta P_{.,\ell} = q_{.,\ell} \beta. \pi_{\ell} \phi_{.,\ell} + \epsilon_{.,\ell}, \quad \epsilon_{.,\ell} \sim \text{NID}(0, \sigma_{.,\epsilon}^2) \quad (4.24a)$$

$$q_{.,\ell+1} = (1 - \rho.) + \rho. q_{.,\ell} + \eta_{.,\ell}, \quad \eta_{.,\ell} \sim \text{NID}(0, \sigma_{.,\eta}^2) \quad (4.24b)$$

which has a linear Gaussian state-space representation. This has two important implications: i) the model can be treated with Kalman filter and ii) the log-likelihood function can be written in a closed form. Denoting by $\mathbf{q}_{.,\ell|\ell}$ and $\mathbf{P}_{.,\ell|\ell}$ the conditional mean and variance of $q_{.,\ell}$ given $\mathcal{P}_{.,\ell}$, and by $\mathbf{q}_{.,\ell+1}$ and $\mathbf{P}_{.,\ell+1}$ the conditional mean and variance of $q_{.,\ell+1}$ given $\mathcal{P}_{.,\ell}$, the Kalman filter recursions [392] can be written as follows

$$v_{.,\ell} = \Delta P_{.,\ell} - Z_{.,\ell} \mathbf{q}_{.,\ell} \quad (4.25a)$$

$$Z_{.,\ell} = \beta. \pi_{\ell} \phi_{.,\ell} \quad (4.25b)$$

$$F_{.,\ell} = Z_{.,\ell}^2 \mathbf{P}_{.,\ell} + \sigma_{.,\epsilon}^2 \quad (4.25c)$$

$$\mathbf{q}_{.,\ell|\ell} = \mathbf{q}_{.,\ell} + \mathbf{P}_{.,\ell} Z_{.,\ell} F_{.,\ell}^{-1} v_{.,\ell} \quad (4.25d)$$

$$\mathbf{P}_{.,\ell|\ell} = \mathbf{P}_{.,\ell} - (\mathbf{P}_{.,\ell} Z_{.,\ell})^2 F_{.,\ell}^{-1} \quad (4.25e)$$

$$\mathbf{q}_{.,\ell+1} = \rho. \mathbf{q}_{.,\ell|\ell} + (1 - \rho.) \quad (4.25f)$$

$$\mathbf{P}_{.,\ell+1} = \rho.^2 \mathbf{P}_{.,\ell|\ell} + \sigma_{.,\eta}^2 \quad (4.25g)$$

Once $\mathbf{q}_{.,\ell}$, $\mathbf{P}_{.,\ell}$, $\mathbf{q}_{.,\ell|\ell}$ and $\mathbf{P}_{.,\ell|\ell}$ are retrieved, one can compute the Kalman smoothing equations [392] by backward recursion

$$\mathbf{q}_{.,\ell|L} = \mathbf{q}_{.,\ell|\ell} + J_{.,\ell}(\mathbf{q}_{.,\ell+1|L} - \mathbf{q}_{.,\ell+1}) \quad (4.26a)$$

$$\mathbf{P}_{.,\ell|L} = \mathbf{P}_{.,\ell|\ell} + (J_{.,\ell})^2 (\mathbf{P}_{.,\ell+1|L} - \mathbf{P}_{.,\ell+1}) \quad (4.26b)$$

$$J_{.,\ell} = \mathbf{P}_{.,\ell|\ell} F_{.,\ell}^{-1} \mathbf{P}_{.,\ell+1} \quad (4.26c)$$

Given the Kalman filter recursions in Eq. (4.26), the log-likelihood function

$$\log L(\Delta P_{.,1}, \dots, \Delta P_{.,L}) = \sum_{\ell=1}^L \log p(\Delta P_{.,\ell} | \mathcal{P}_{.,\ell-1}), \quad (4.27a)$$

can be computed in the prediction error decomposition form:

$$\log L(\Delta P_{.,1}, \dots, \Delta P_{.,L}) = -\frac{L}{2} \log 2\pi - \frac{1}{2} \sum_{\ell=1}^L (\log F_{.,\ell} + (v_{.,\ell})^2 F_{.,\ell}^{-1}). \quad (4.28a)$$

As the diurnal pattern is not practically observable, we propose a “two-stage” approach. In the first stage, the diurnal factor is pre-estimated. In the second stage, the estimator is included in

the estimation procedure. In the conditional variance literature there are several methodologies that capture the intraday unobservable pattern. For instance, [410] and [411] employ Fourier transform techniques, whereas [415] use functional data analysis methods. The approach that we propose in this work can be related to the one introduced by [389]⁴.

In our setting, the daily price impact component β_i belongs to the hyper-parameters vector Θ , i.e., it is an output of the estimation procedure. To capture π_ℓ , $\ell = 1, \dots, L$, we proceed as follows. First, we set $\pi_\ell = 1$ for each $\ell = 1, \dots, L$ and we run the Kalman filter for each day i in our sample to obtain a first estimation of both the hyper-parameters vector $\Theta^{(I)}$ and the smoothed state process $\mathbf{Q} \doteq \mathbf{q}_{i,\ell|L}^{(I)}$ with $i = 1, \dots, N$ and $\ell = 1, \dots, L$. At this point, the state process also incorporates the diurnal price impact pattern, i.e., \mathbf{Q} is actually equal to $\mathbf{Q} \equiv \mathbf{q}_{i,\ell|L}^{(I)} \widehat{\pi}_\ell$. Thus, $\widehat{\pi}_\ell$ turns out to be

$$\mathbb{E}[\mathbf{q}_{i,\ell|L}^{(I)} \widehat{\pi}_\ell] = \mathbb{E}[\mathbf{q}_{i,\ell|L}^{(I)}] \widehat{\pi}_\ell = \widehat{\pi}_\ell. \quad (4.29a)$$

In the second step, $\widehat{\pi}_\ell$ is embedded into the Kalman filter recursions in Eq. (4.25), leading to the final estimates.

4.6.6 Empirical results

We estimate the model in Eq. (4.24) by applying the procedure presented in section 4.6.5 to the dataset described in appendix C.1.2. We recall that our dataset contains the order book activity of five NASDAQ 100 Index stocks over 125 days. We split each trading day in $L = 390$ non overlapping time windows from which we sample the mid-price change and OFI time series. We divide the available data into a training set of 100 days and a test set of the subsequent 25 days.

In-sample analysis

The analysis on the training set is carried out by estimating the model via maximum likelihood estimation (MLE henceforth) through the two-steps procedure discussed in section 4.6.5.

⁴[389] propose a model for high-frequency intraday financial returns, $r_{i,\ell}$. They decompose the conditional variance of the latter as a multiplicative product of daily, h_i , diurnal, s_ℓ , and stochastic, $q_{i,\ell}$ with $q_{i,\ell} = 1$, intraday volatility. To proxy the daily variance component h_i , authors use commercially available volatility forecast. Thus, once a proxy for h_i is obtained, they simply calculate s_ℓ as the variance of returns in each bin after deflating by the daily variance.

Hyper-parameter estimates of the training set are used to construct the empirical distribution of the hyper-parameters vector Θ . Table 4.3 reports hyper-parameter estimates after the second stage. Overall, estimates are statistically significant and their inter-quantile ranges indicates that estimates have a small statistical dispersion.

We now focus on the parameter ρ describing the persistence of price impact. Coherently with the preliminary descriptive investigation presented in section 4.6.4 and with the numerical exercise displayed in appendix H.3.3, we note that the proposed two-steps procedure successfully captures and filters out the auto-regressive stochastic dynamics from the intraday pattern. The auto-regressive coefficient ρ at stage two is significantly smaller than the one estimated at stage one, see table 4.4. The difference highlights that ignoring the pervasive diurnal effect of the market impact would turn q_ℓ in an almost integrated process, see table 4.4. In particular, this would support the statement that the price impact is *strongly* auto-correlated. When the intraday pattern is properly taken into account, the value of ρ significantly decreases. Nonetheless, estimates remain statistically significant. The reduction of the auto-correlation coefficient has notable implications for the persistence of liquidity fluctuations. For instance, while values for ρ around 0.98 and 0.99 represent a process with half-life ranging between 30 minutes and 1 hour, values of ρ below 0.5 suggest that the process has a half-life of 60s. Thus, the liquidity fluctuations predicted by our model are, on average, short lived but significant.

Fig. 4.22 displays the estimates $\beta_{,\ell}$, $\ell = 1, \dots, L$, averaged across days. Panels show the price impact process for five stocks, i.e, from top to bottom and left to right: CMCSA, MSFT, INTC, CSCO, AAPL. The dynamics of price impact is interesting and presents a clear intraday pattern. It peaks right after the opening auction, then it quickly decreases to lower levels where it hovers around an average value for most of the trading day and, finally, it decreases again right before the closing auction. The shape of the pattern has an intuitive explanation: the high level of market impact at the beginning of the day is likely to be the consequence of heterogeneity of traders' opinions and adverse selection. The low levels observed at the end of the day can be linked to the market practice of requesting the completion of a parent order within the trading day, a phenomenon that increases the available liquidity right before the closing auction.

Fig. 4.23 provides a closer look at the dynamics of the price impact process. It combines Kalman smoothed estimates of price impact, i.e., black line, Kalman filtered estimates of price impact, i.e., green line, and averages across days of the price impact process $\beta_{,\ell}$, $\ell = 1, \dots, L$,

Parameter: β					
Ticker	Median	Mean	Average t-statistic	Q_1	Q_3
CSCO	3.883×10^{-5}	3.835×10^{-5}	41.07	3.414×10^{-5}	4.368×10^{-5}
INTC	6.455×10^{-5}	6.515×10^{-5}	35.06	5.285×10^{-5}	7.979×10^{-5}
MSFT	1.404×10^{-4}	1.443×10^{-4}	40.95	1.213×10^{-4}	1.613×10^{-4}
CMCSA	3.022×10^{-4}	3.124×10^{-4}	37.36	2.576×10^{-4}	3.522×10^{-4}
AAPL	3.392×10^{-4}	3.472×10^{-4}	46.32	2.974×10^{-4}	4.015×10^{-4}
Parameter: ρ					
Ticker	Median	Mean	Average t-statistic	Q_1	Q_3
CSCO	0.3323	0.3505	11.62	0.1167	0.5084
INTC	0.2714	0.3553	12.13	0.1232	0.5271
MSFT	0.4016	0.4603	14.10	0.2419	0.7513
CMCSA	0.3287	0.3855	11.57	0.147	0.6463
AAPL	0.4122	0.4262	14.01	0.1700	0.6203
Parameter: σ_ϵ					
Ticker	Median	Mean	Average t-statistic	Q_1	Q_3
CSCO	0.0035	0.0036	17.52	0.0027	0.0045
INTC	0.0045	0.0050	20.21	0.0039	0.0056
MSFT	0.0096	0.0115	19.34	0.0080	0.0133
CMCSA	0.0103	0.0135	15.05	0.00870	0.0150
AAPL	0.0274	0.0316	20.58	0.0200	0.0400
Parameter: σ_η					
Ticker	Median	Mean	Average t-statistic	Q_1	Q_3
CSCO	0.2547	0.3364	10.29	0.1958	0.3341
INTC	0.2561	0.2941	16.36	0.1942	0.3611
MSFT	0.2752	0.2666	21.06	0.1736	0.3496
CMCSA	0.3091	0.2981	18.79	0.2002	0.3758
AAPL	0.4089	0.3753	24.64	0.2889	0.4639

Table 4.3: **Summary of estimates of the model in Eq. (4.24).** The model is estimated on order book data of five NASDAQ 100 Index stock over 100 days in 2016. For each parameter we report the median (second column), the mean (third column), the average t-statistic (fourth column) and the lower and the upper quartile (fifth and sixth columns, respectively).

Parameter: ρ						
Ticker	Median	Mean	Average t-statistic	Q_1	Q_3	
CSCO	0.8671	0.7771	32.73	0.6983	0.9470	
INTC	0.9218	0.8513	43.51	0.8491	0.9627	
MSFT	0.8880	0.8198	40.76	0.7818	0.9548	
CMCSA	0.9163	0.8597	48.07	0.8406	0.9598	
AAPL	0.6507	0.6109	20.62	0.3744	0.8758	

Table 4.4: **Estimates of the parameter ρ after the first stage.** We report median (second column), mean (third column), average t-statistic (fourth column), and the lower and the upper quartile (fifth and sixth column, respectively).

i.e., blue line, normalized by the average daily level. The top panel displays CSCO on January 27th 2016, the middle panel displays INTC on April 27th 2016 while the bottom panel displays AAPL on June 15th. In these days three different meetings of the Federal Open Market Committee (FOMC henceforth) took place. The behavior of the price impact significantly diverges from the average price impact around 1400 EST, which is the time in which economic information is released, showing how investors promptly react to the announcement by updating their positions. This empirical result suggests that our model successfully captures real time variations of price impact.

Out-of-sample performance

We now discuss the out-of-sample performance of our model. As a benchmark for the true price impact on a given day we select the *ex-post* smoothed estimates of market impact. Note that Kalman smoothing estimates are computed by using the hyper-parameters estimated from real trading data for the considered day; hence they represent the best *ex-post* estimates of market impact.

We perform two out-of-sample exercises. In the first one, we show that the conditioning on real time information improves the estimates of the LOB liquidity with respect to the one obtained from the deterministic intra-day pattern alone. We first estimate our model over an in-sample period of 100 days. Fig. 4.24 presents Kalman filtering performed on out-of-sample data. The hyper-parameters values are set equal to the median values of the hyper-parameter

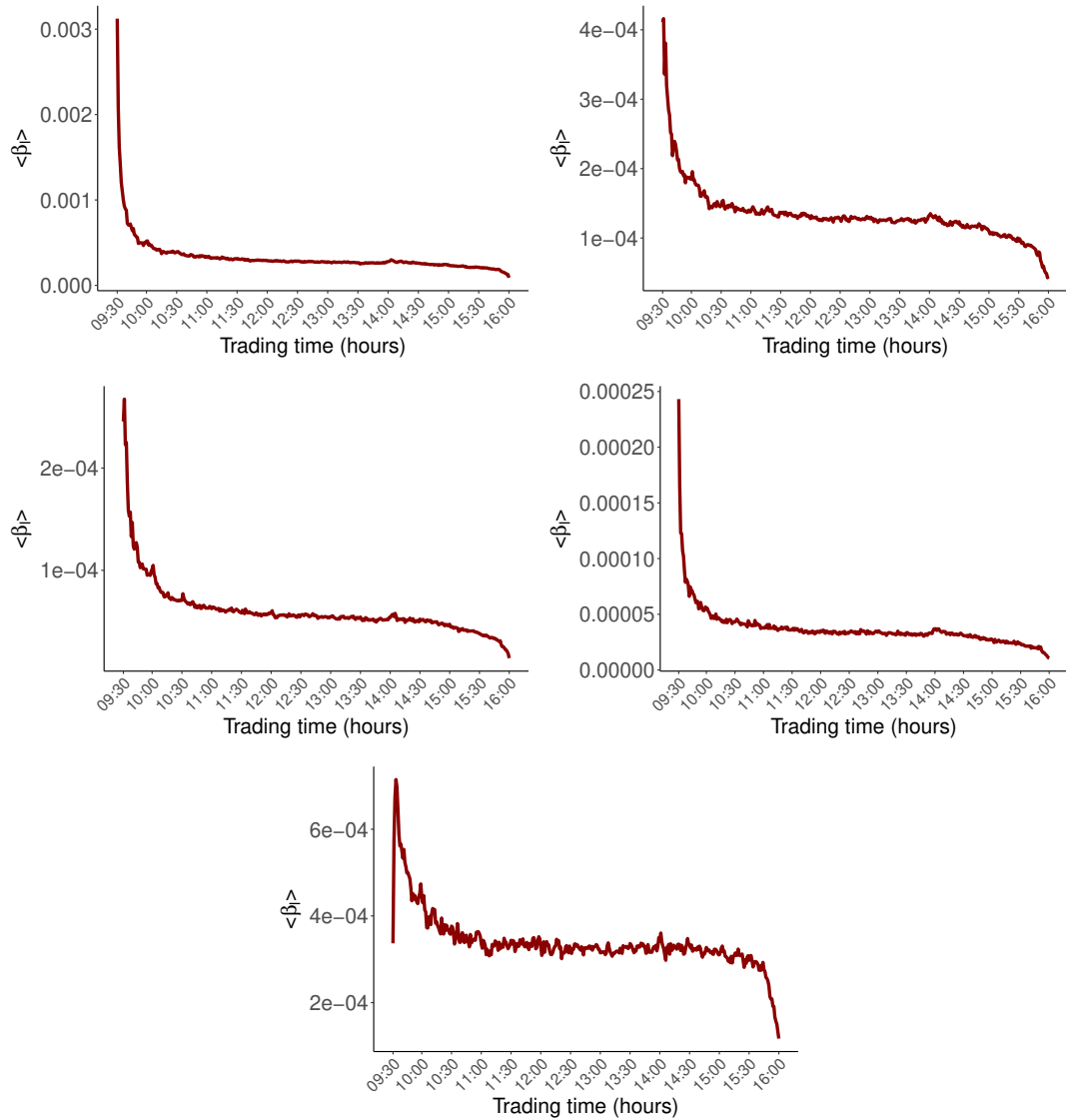


Figure 4.22: **Price impact estimates average patterns through the trading day.** Price impact process $\beta_{.,\ell}$, $\ell = 1, \dots, L$, averaged across days for CMCSA (top-left), MSFT (top-right), INTC (mid-left), CSCO (mid-right), AAPL (bottom). This figure has been extracted from [345], see appendix B.5 for details about attributions and permissions.

distributions computed in the in-sample analysis. Blue lines represent the historical average market impact, green lines the filtered real-time estimation of market impact and black lines represent the *ex-post* smoothed estimates of market impact. The picture clearly shows that the filter successfully captures the intraday dynamic of market impact. To support our statement, we compute i) the mean squared error (MSE henceforth) of the historical marked impact (resp. of the filtered estimates) with respect to the smoothed one, which is denoted by MSE_1 (resp. by MSE_2) and ii) the “gain” in signal extraction as $(\text{MSE}_1 - \text{MSE}_2)/\text{MSE}_1$. Table 4.5 reports

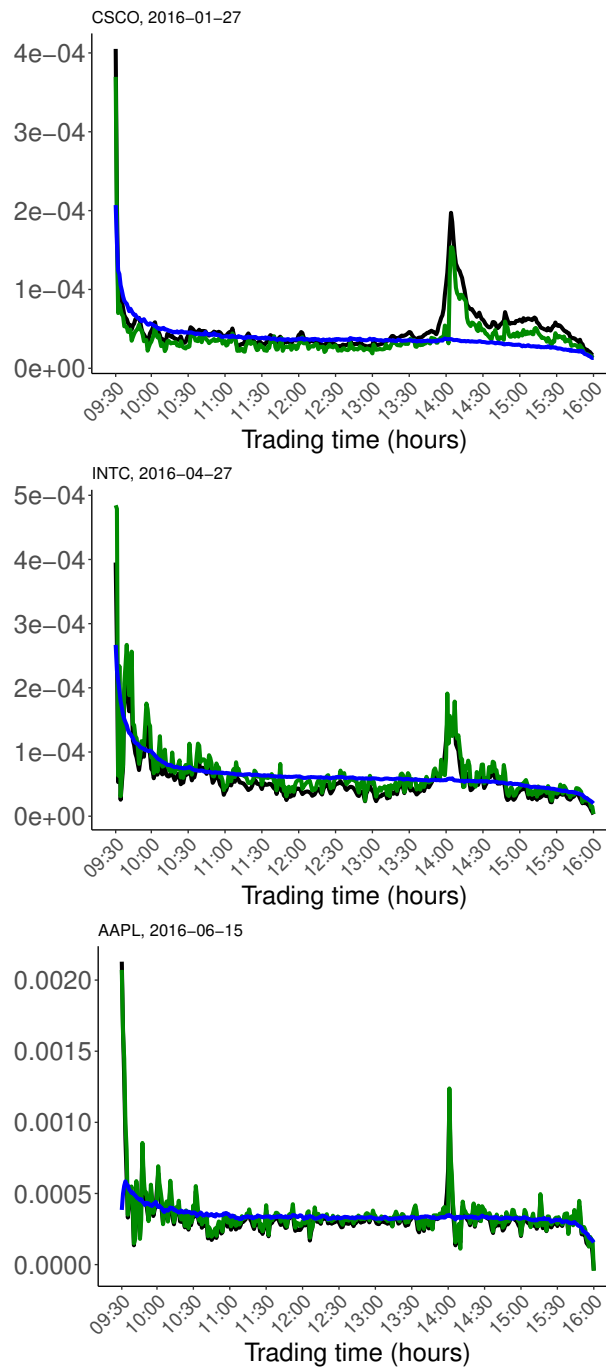


Figure 4.23: **Price impact estimates average patterns on FOMC meeting days.** Black lines represent Kalman smoothing estimates of the price impact process for CSCO on January 27th 2016 (top), INTC on April 27th 2016 (middle) and AAPL on June 15th 2016 (bottom). The corresponding Kalman filtered estimates are plotted in green while averages across days over the in-sample period are plotted in blue. This figure has been extracted from [345], see appendix B.5 for details about attributions and permissions.

the average gain, i.e., Average Gain 1, across the 25 out-of-sample days. On average, real-time monitoring reduces the MSE of market impact by a factor ranging between 0.22-0.83.

In the second experiment we show the importance of the filtering procedure by comparing

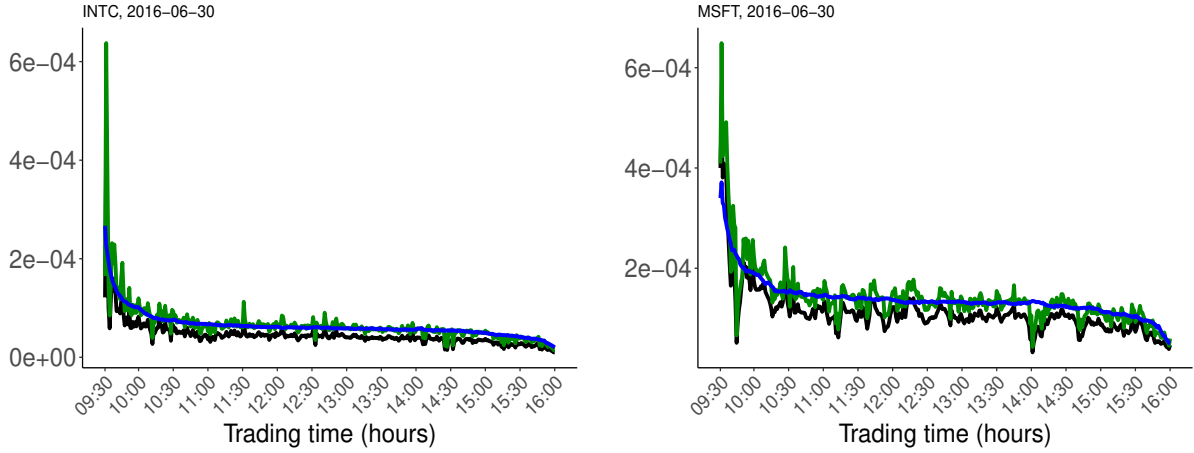


Figure 4.24: **Out-of-sample Kalman filtering of market impact process.** Panels (INTC left and MSFT right) display the average market impact (blue), the real-time filtered market impact (green) and the ex-post smoothed market impact (black). This figure has been extracted from [345], see appendix B.5 for details about attributions and permissions.

our model with the static model of [36], see yellow line in Fig. 4.25. For our model, we use the estimates over the in-sample period of 100 days to estimate the diurnal pattern. This pattern is allowed to change within the day but it is otherwise time-invariant across days. Then, for each of the subsequent 25 days we compute the mean squared error of the filtered estimates of price impact with respect the smoothed one, i.e., MSE_2 . The diurnal pattern used in all the out-of-sample period is estimated over the in-sample period, i.e., it is not updated as the experiment proceeds beyond the 100-th day, whereas the values of the hyper-parameters in each day are the one obtained in the previous day. We compare this mean square error with the one of the static model of [36] with respect to the Kalman smoothing, i.e., MSE_1 . In particular, we estimate in each of the out-of-sample days the model of [36] with $\Delta_k = 60s$ and $\Delta_\ell = 0.5s$. It is important to emphasize the difference between the two modelling approaches. The Kalman approach uses the predictive filter, i.e. the expected value of q_ℓ conditional to the past history up to $\ell - 1$ and for the daily average β_i we use the daily average price impact from the previous day β_{i-1} . For the static model we fit the regression at each interval ℓ to obtain β without performing an estimation. The second column of table 4.5 shows that the MSE for Kalman filter is smaller

than the one obtained from the static approach. Fig. 4.25 suggests that Kalman estimates might be biased due to the use of the previous day level β_i as the average impact in a specific day can be quite different from the one measured in the previous day. The static estimates present a high variance due to fluctuations which significantly affect the MSE. One could easily improve the performances of the filtering approach by estimating the hyper-parameters in the earlier hours of the trading day and then use it afterwards. This is expected to reduce the afore discussed bias without increasing the variance. This exercise is beyond the scope of this project and we will not be investigated further.

Next, we investigate the correlation between the dynamic and the static measure of price impact. We compute the Pearson correlation between the dynamic $\beta_{\ell,K} = q_{i,\ell}\beta_i\pi_\ell$, where $q_{i,\ell}$ are the filtered estimates, and the static market $\beta_{\ell,K}$ from [36], with $\Delta_k = 60s$ and $\Delta_\ell = 0.5s$, over the in-sample period of $i = 1, \dots, 100$ days. Fig. 4.26 displays the box-plots of these correlations for each stock included in our sample. The two measures of market impact are moderately correlated, i.e., the correlation coefficient is around 60%. This might be symptomatic of the fact that in our model price impact becomes history dependent because of Kalman filter and, as a consequence, it captures different dimensions of the price impact.

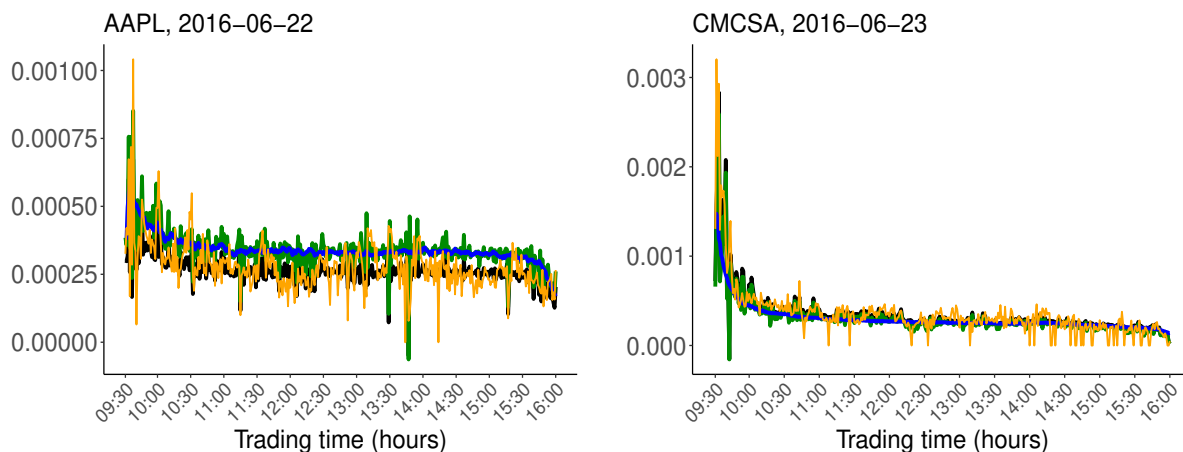


Figure 4.25: **Out-of-sample Kalman filtering of market impact.** Panels (AAPL left and CMCSA right) display the average market impact (blue), the real-time filtered market impact (green), the ex-post smoothed market impact (black), and the static market impact of [36]. This figure has been extracted from [345], see appendix B.5 for details about attributions and permissions.

Ticker	Average gain 1	Average gain 2
CSCO	0.40	0.51
INTC	0.28	0.10
MSFT	0.22	0.02
CMCSA	0.83	0.28
AAPL	0.37	0.35

Table 4.5: **Performances comparison.** Average gain 1 is defined as $(\text{MSE}_1 - \text{MSE}_2)/\text{MSE}_1$, where MSE_1 is the mean squared error of the historical market impact with respect to the smoothed market impact and MSE_2 is the mean squared error of the filtered estimates with respect to the smoothed market impact. Average gain 2 is defined as $(\text{MSE}_1 - \text{MSE}_2)/\text{MSE}_1$, where MSE_1 is the mean squared error of the static model [36] with respect to the smoothed market impact and MSE_2 is the mean squared error of the filtered estimates with respect to the smoothed market impact. These metrics are computed across the out-of-sample window, i.e., 25 days.

Price impact and market depth

At this point we analyse the relationship between the proposed price impact measure and market depth. The baseline for Eq. (4.23)(a) is the *stylized order book* model which describes the relation between price impact and market depth as

$$\beta_\ell = \frac{c}{D_\ell^\lambda} + \nu_\ell, \quad (4.30)$$

where $c = 1/2$, $\lambda = 1$ and ν_ℓ is a noise term. One can straightforwardly set $\beta_\ell = 1/(2D_\ell)$ to reconstruct the price impact directly from the market depth, see appendix H.1 for details. Cont *et al.* [36] computed price impact estimates through linear regressions of price fluctuations on the OFI. Relying on a large spectrum of stocks, they find that $\hat{c} = 0.56$ and $\hat{\lambda} = 1.08$ assuming $\Delta_K = 1800\text{s}$ and $\Delta_\ell = 10\text{s}$, see Eqs. (17)-(18) in [36], obtaining values that are comparable to those predicted by the stylized order book model. At this point, we want to assess how \hat{c} and $\hat{\lambda}$ vary when we may either use different time-scales Δ_K and Δ_ℓ or Kalman-filtered price impact time series.

First, we estimate c and λ in Eq. (4.30) by deriving price impact from the static model of Cont *et al.* [36] under two different time-scales: $(\Delta_K = 1800\text{s}, \Delta_\ell = 10\text{s})$ and $(\Delta_K = 60\text{s}, \Delta_\ell = 0.5\text{s})$.

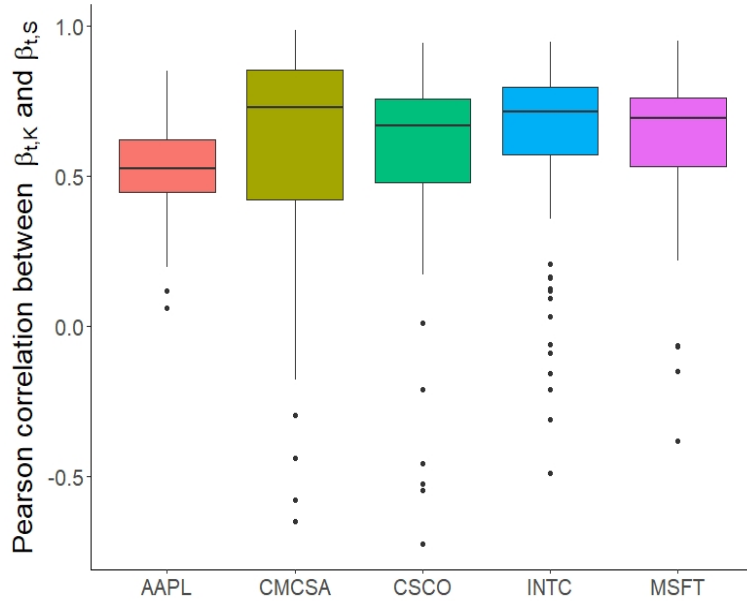


Figure 4.26: **Box-plot of the Pearson correlation between the compared models.** We compare the dynamics vs. static model assuming $\Delta_k = 60\text{s}$ and $\Delta_\ell = 1\text{s}$. The correlation coefficients are computed in each of the 100 days covered in the in-sample period. This figure has been extracted from [345], see appendix B.5 for details about attributions and permissions.

Considering that $\approx 10\%$ of the estimates turned out to be negative, we fit Eq. (4.30) with a non-linear regression model by robust methods, i.e. by using iterated re-weighted least squares⁵. Table 4.6 reports the average values of \hat{c} and $\hat{\lambda}$. The grand mean and median, see second and third column, are in line with the values reported by Cont *et al.* [36]⁶. This confirms that at time-scales like $(\Delta_K = 1800\text{s}, \Delta_\ell = 10\text{s})$ there is a tight relation between price impact and the reciprocal of the market depth, as suggested by the stylized order book model. Furthermore, estimates reported in the fourth and fifth column indicate that the stylized order book model is still a good approximation for this relationships even at the shorter time-scale $(\Delta_K = 60\text{s}, \Delta_\ell = 0.5\text{s})$. The sixth and seventh columns report the estimates when $\beta_{i,\ell}$ is derived through Kalman filtering. These figures suggest that Eq. (4.30) does not adequately capture the relationships between market depth and price impact when $c = 1/2$ and $\lambda = 1$. This suggests that the price impact dynamic cannot be solely explained by a deterministic function of quote size alone.

⁵We also implement the two-step linear regressions proposed in [36] after ignoring negative estimates. We confirm that no significant differences in the estimates emerged from this exercise

⁶Their data set covers trading data collected in April 2010

We assert that this might be linked to the auto-regressive nature of our price impact measure, which captures different dimensions of the price impact beyond market depth. To support this assertion, we look at the goodness of fit of Eq. (4.23)(a) at a time scale of 60s for three different proxies of price impact $\beta_{i,\ell}$: i) the book-reconstructed price impact $\beta_{i,\ell} = 1/(2D_{i,\ell})$, ii) the *static* price impact when $(\Delta_K = 60\text{s}, \Delta_\ell = 0.5\text{s})$, iii) the Kalman filtered estimates of price impact. We run regressions of the returns $\Delta P_{i,\ell}$ on $\beta_{i,\ell}$, $i = 1, \dots, N$ and $\ell = 1, \dots, L$:⁷

$$\Delta P_{i,\ell} = \alpha + \gamma \beta_{i,\ell} \phi_{i,\ell} + \nu_{i,\ell}, \quad (4.31)$$

where $\nu_{i,\ell}$ is a random error term. Table 4.7 reports the outcomes of this exercise. In the stylized model introduced by Cont. *et al.* [36] price changes are a mechanical consequence of the provision and depletion of volume at the best quotes. This allows to express price impact as a function of the size of the best quotes, see Eq. (4.30). If this approach was accurate, alternative estimation methods would be exclusively justified in the absence of order book data. The superior results, i.e., higher R^2 coefficients, obtained from price impact estimates based on both price fluctuations and OFI suggest that price impact dynamics cannot be exclusively explained by quote sizes. The model of Cont *et al.* [36] already captures some of the variations not explained by quote sizes, but further significant improvements can be achieved by modelling the dynamics of price impact as in the framework proposed in this section.

4.6.7 Concluding remarks

In this section we introduced a model in which price impact is linear and permanent, but the price impact coefficient is a latent state of the limit order book governed by its own dynamics. We defined the price impact coefficient as the product of a daily price impact level, a deterministic intraday pattern and a stochastic auto-regressive component.

A peculiar feature of this model is that the price impact components are not studied in isolation. This feature is critical for real-time analysis and decision making. On a practical perspective, practitioners should recognise and quantify the interactions and contributions of the various price impact components as they simultaneously affect the dynamics of the price. More generally, such decomposition is necessary as factors display widely different statistical properties.

We calibrated the model on five stocks traded on NASDAQ using a 60s binning scheme. We

⁷This regression includes the intercept hence the $\hat{\gamma}$ coefficient $\neq 1$ in the static model.

	Cont <i>et al.</i> (1800s, 10s)		Cont <i>et al.</i> (60s, 0.5s)		Kalman filter	
Parameter: \hat{c}	Mean	Median	Mean	Median	Mean	Median
AAPL	0.251	0.216	0.283	0.158	0.008	0.006
CMCSA	0.64	0.71	0.92	0.93	0.07	0.06
CSCO	0.18	0.17	0.35	0.40	0.048	0.045
INTC	0.19	0.21	0.29	0.32	0.04	0.04
MSFT	0.126	0.125	0.157	0.170	0.018	0.016
Grand mean	0.456		0.289		0.02	

	Cont <i>et al.</i> (1800s, 10s)		Cont <i>et al.</i> (60s, 0.5s)		Kalman filter	
Parameter: $\hat{\lambda}$	Mean	Median	Mean	Median	Mean	Median
AAPL	0.985	0.990	0.987	0.938	0.47	0.46
CSCO	0.97	0.96	1.06	1.04	0.82	0.81
CMCSA	1.14	1.17	1.209	1.213	0.818	0.810
INTC	0.97	0.99	1.03	1.05	0.799	0.806
MSFT	0.91	0.91	0.94	0.96	0.66	0.64
Grand mean	0.91		0.83		0.50	

Table 4.6: **Estimates of the parameters c and λ in Eq. (4.30).** We fit Eq. (4.30) on a monthly basis by using $\beta_{i,\ell}$ time series derived from the model of Cont *et al.* with $(\Delta_K = 1800s, \Delta_\ell = 10s)$ (first and second columns), the model of Cont *et al.* with $(\Delta_K = 60s, \Delta_\ell = 0.5s)$ (third and fourth columns) and the state-space model presented in this section (fifth and sixth column). We report the mean and median of each estimate for every model considered in this analysis.

shown that i) market impact dynamics should be taken into the account on out-of-sample estimation performances and ii) the history dependent nature of our price impact measure captures different dimensions of the price impact beyond market depth. We observed that our model does not imply a square-root relation between price changes and trading volume [21]. This statement also holds in the model of Cont *et al.* when the considered time-scales are signifi-

Ticker	book-reconstructed			Static $\beta_{i,\ell}$			Kalman filtered $\beta_{i,\ell}$		
	$\hat{\alpha}$	$\hat{\gamma}$	R^2	$\hat{\alpha}$	$\hat{\gamma}$	R^2	$\hat{\alpha}$	$\hat{\gamma}$	R^2
AAPL	$4.72 \cdot 10^{-3}$	0.29	0.48	$5.84 \cdot 10^{-3}$	0.800	0.64	$4.14 \cdot 10^{-3}$	1.063	0.82
	(22.09)	(212.26)		(32.52)	(289.31)		(32.9)	(467.4)	
CSCO	6.7210^{-4}	0.44	0.83	4.7410^{-4}	0.94	0.86	3.7610^{-4}	1.01	0.96
	(21.81)	(488.43)		(16.95)	(544.62)		(24.59)	(1055.29)	
CMCSA	2.0510^{-3}	0.46	0.64	1.8910^{-3}	0.92	0.69	1.4310^{-3}	1.03	0.89
	(18.71)	(294.07)		(18.68)	(331.71)		(23.9)	(635.9)	
INTC	8.3410^{-4}	0.41	0.80	6.0610^{-4}	0.95	0.85	4.6110^{-4}	1.02	0.96
	(20.13)	(437.41)		(17.06)	(526.22)		(23.6)	(1013.1)	
MSFT	2.1610^{-3}	0.39	0.74	1.8010^{-3}	0.91	0.81	1.4110^{-3}	1.02	0.91
	(25.86)	(366.00)		(25.14)	(445.67)		(29.07)	(700.08)	

Table 4.7: **Estimates of the parameters α and γ in Eq. (4.31).** We fit Eq. (4.31) by using $\beta_{i,\ell}$ time series derived from book reconstruction (first, second and third columns), the model of Cont *et al.* with ($\Delta_K = 60s, \Delta_\ell = 0.5s$) (fourth, fifth and sixth columns) and the state-space model presented in this section (seventh, eight and ninth columns.). For each approach we report the estimates $\hat{\alpha}, \hat{\beta}$ and the coefficient of determination R^2 . T-statistics for the reported estimates are displayed in the even rows of the table.

cantly smaller than those adopted in the original work [36]. Moreover, our approach to market impact estimation explained a greater dispersion of price fluctuations when compared to other proxies, see table 4.7. In the out-of-sample exercise we shown that the MSE for Kalman filter is smaller than the one obtained when using the static approach of [36]. In the static model the average daily level of market impact was automatically determined by the estimation. On the other hand, the Kalman approach used the predictive filter while the daily average market impact levels were extracted from the previous day. In spite of this disadvantage, we obtained a reduction in the MSE which was primarily caused by lower variances in the dynamic estimates. As a by-product, our investigation allowed us to estimate the intraday pattern of price impact. We observed that price impact peaks right after the opening auction before descending into an average daily level which is preserved until a final steep drop around the closing auction. We

interpreted this characteristic shape as a symptom of higher opinion dispersion and adverse selection at the opening of the market, which translates in lower order book liquidity, or equivalently, in higher market impact. As trading begins, the price discovery process takes place and liquidity gradually reverts from this initial shock to an equilibrium level, lowering market impact.

In summary, the main contribution of this project is the introduction of an improved methodology for characterizing security price dynamics within the family of models covered in this section. Broader finance applications would include liquidity effects on asset pricing, optimal trading strategies, or market design. Still, these applications may also serve as interesting directions for future research.

4.7 Summary of the chapter

Financial markets are hubs in which heterogeneous agents, such as individuals and firms, exchange financial instruments. Participants can be characterised by different degrees of sophistication, e.g., retail vs. high frequency trading firms, while the underlying infrastructure sustain a truly global and interconnected network of trading venues in which events occurring in a specific market reverberate across the entire system. This complexity inevitably pose interesting and arduous challenges for practitioners, academics and regulators seeking to understand the dynamics of these systems.

In this chapter we examined two distinct problems in the foreign exchange and stock markets. We started from an introduction to the scopes and organization of financial markets. In this segment, we focused on the features and differences between quote-driven markets, i.e., venues in which designated agents pledged to continuously provide liquidity in exchange for specific benefits, and order-driven markets, i.e., venues in which liquidity is organized in electronic limit order book and trading does not necessarily require the presence of special agents. Next, we introduced market microstructure and discussed in detail the concepts of market liquidity and price impact of trades. These introductory sections were followed by an overview of three models that influenced, to different extents, the research presented in this chapter: the Kyle Model [38], the Dealer Model [35] and the Cont-Kukanov-Stoikov Model [36]. This led us to the two final sections in which we presented two independent research projects. First, we examined how the time-scale dependent cross-correlations between price fluctuations emerge from interactions among heterogeneous market participants. We developed an agent-based model of the foreign

exchange markets in which three independent inter-dealer markets are populated by trend-following market makers that transact with each other every now and then [34]. We included a special agent, known as the *arbitrager*, who solely trade to exploit triangular arbitrage opportunities across the three venues [34]. We simulated the dynamics of this ecology and observed that the interplay between arbitrage and trend-following strategies generates pronounced cross-correlations between price changes resembling those observed in real trading data [34]. A deep analysis of the model dynamics suggested that these statistical regularities are the consequence of an alteration in the probability of observing two markets moving in the same/opposite direction as price trajectories are transiently synchronized by the simultaneous price changes caused by the arbitrager's orders and the subsequent response of trend-following traders [34]. Second, we introduced a new framework to investigate the relationships between demand/supply imbalances, market liquidity and price formation. In this model, we described price fluctuations as the product of demand/supply imbalances, i.e., the order flow imbalance, and the current liquidity of the market, i.e., the price impact coefficient [37]. We modelled the price impact coefficient as the product of an intraday pattern, a daily level and a stochastic autoregressive component and estimated the model through Kalman Filtering on NASDAQ trading data [37]. We observed that the linear relationships between order flow imbalance and price fluctuations established in [36] weakens when price series are sampled at high-frequency timescales as the discreteness of price increments becomes a constraint to price movements [37]. In addition, we also found that at high frequency time-scales price impact becomes auto-regressive and more dependent on recent orderbook dynamics [37].

Chapter 5

Conclusion

5.1 Summary and achievements of this thesis

In this thesis I have examined two seemingly unrelated physical systems, the human heart and financial markets. I have mainly approached these systems from a complexity science perspective, i.e., by modelling the interactions between their components and studying how they generate and affect structures and patterns involving the system as a whole, with the notable exception of section 4.6 in which I have used methods that are more relatable to data analytics and statistics. The driving motivations of this dissertation and, more generally, of my doctoral studies, were my curiosity towards different topics and my desire to learn new things by exploring open problems, diving into experiments and collaborating with likeminded people. In retrospective, the gradual expansions of my research horizons towards topics that were not planned at the beginning of this long journey have been a positive game changing factor on the personal and academic outcomes of this experience. I have been extremely fortunate to meet, discuss and collaborate with brilliant people from different academic backgrounds and interests. This helped me in appreciating the benefits of approaching a problem from multiple angles and the importance of engaging, rather than competing, with different academic communities and work together towards a common goal, which is the essence of complexity science.

My research has examined several open questions across different systems. This thesis reflects a significant portion of this effort as it presents multiple academic manuscripts in which I, together with my collaborators, sought to provide a meaningful contribution to the following problems:

1. The mechanisms behind the transition from paroxysmal atrial fibrillation to persistent atrial fibrillation.
2. The termination of myocardial fibrillation through drug-induced optimization of phase singularities meander.
3. The debate on the driving mechanisms of atrial fibrillation and a novel theory with “the potential to unify some of the previous discrepant observations” [32]
4. The emergence of cross-currency correlations from the interactions between heterogeneous strategic agents.
5. The relationships between price fluctuations, market liquidity and order flow imbalance.

Having reached the end of my doctoral studies, I finally reflect on the academic achievements of the research presented in this thesis.

First, this thesis shows that the transition from paroxysmal to persistent atrial fibrillation requires specific regions of the tissue characterized by a tangible imbalance in the probability of triggering and killing any circuitual electrical activity that may stabilize and revolve around them [20], see section 3.5. This result, in spite of being confined to a simplified insilico model of fibrillation, calls for further replications on clinically relevant models as it might provide insights on how to detect those areas of the cardiac tissue that are more likely to drive persistent fibrillation and should eventually be targeted by ablation procedures [20].

Second, this thesis offers a potential explanation for the self-termination of fibrillation observed in certain Langendorff-perfused rat hearts that were subjected to Rotigaptide infusions, see [27]. Large-scale simulations of the model presented in section 3.6 identified specific topological features, i.e., high coupling and moderate resistivity to depolarisation, that are associated with increased probability of self-termination [26]. In this topological setup, which is compatible with the effect of Rotigaptide on the structure of the cardiac tissue, the fraction of excitable tissue and meander per phase singularity are maximised - creating a scenario in which drivers tend to drift across the tissue and ultimately collide with other drivers or boundaries to eventually terminate fibrillation [26].

Third, this thesis offers a model-based assessment of recent clinical evidence supporting a new theory of atrial fibrillation in which long-lasting antagonistic driving mechanisms, i.e., rotational and focal drivers, may co-exist as mere surface projections of transmural circuitual

activities [29, 30, 31, 32, 33]. Section 3.7 presented a tri-dimensional cellular automata model of atrial fibrillation in which the atrial bulk is modelled by a cubic topology where neighboring nodes may also connect to adjacent sheets [28]. Simulations of this model reveal that paroxysmal episodes are driven by rotational activities acting near the endocardium whereas persistent episodes are driven by activities that are distributed across the entire bulk [28]. These circuitual drivers project as rotational activities when the lattice is observed from the endocardium and as focal points when the lattice is observed from the epicardium, providing model-based support to the aforementioned clinical evidence [28].

Fourth, this thesis provides a potential explanation of the origins of cross-currency correlations observed in real trading data. To address this problem, section 4.5 introduced an agent-based model of currency markets in which agents acting as liquidity providers trade in three independent markets, i.e., their pricing decisions are not affected by events taking place in other markets, while a special agent known as the *arbitrager* trades opportunistically to exploit any cross-market misprice that guarantees risk free profit [34]. In this setting, the sole mechanism through which prices across markets might temporarily synchronize is the interplay between different trading strategies, i.e., the arbitrager simultaneously submits orders across exchanges and the subsequent price changes prompt trend-following market makers to adjust their quotes in the same direction of the latest uptick/downtick caused by the arbitrager [34]. Market makers, despite reacting to price actions taking place in the market they are trading on, are effectively re-adjusting their prices in the same/opposite direction of market makers trading in other markets as the arbitrager orders cause simultaneous price changes across every market, resulting in a transient synchronization of price dynamics across the ecology [34]. This mechanism breaks the 50/50 probability of observing two markets moving in the same/opposite direction that one would have had in an arbitrager-free ecology, producing synthetic price time series characterized by cross-correlations that are qualitatively compatible to those found on real trading data [34].

Fifth, this thesis offers insights on the relationships between price fluctuations, market liquidity and order flow imbalance. In section 4.6 we examined this problem by presenting a state space model in which the price impact of orderbook events is written as the product of an intraday pattern, a daily level and a stochastic autoregressive component while price fluctuations are driven by the interplay between order flow imbalance and the price impact coefficient [37]. The model is calibrated on real trading data through Kalman filtering, offering a novel approach

for the dynamic estimation of price impact at high frequency time-scales [37]. Building on the work of Cont *et al.* [36], we observed that the linear relationships between order flow imbalance and price fluctuations established in that work weakens when price series are sampled at high-frequency timescales as the discrete nature of price increments becomes more and more relevant [37]. Furthermore, we also found that at high frequency time-scales price impact becomes auto-regressive and more dependent on recent orderbook dynamics [37].

5.2 Future work

This closing section offers a general outlook of the research directions that can be pursued from the outcomes of the works presented in this thesis. The cellular automata models introduced in sections 3.5.3, 3.6 and 3.7 are simple, yet powerful and computationally efficient frameworks designed to reproduce the dynamics of cardiac fibrillation over relatively long timescales. Their scope is to offer qualitative insights and to formulate hypotheses on specific issues as their intrinsic simplicity does not allow for any direct clinical application. Building from this observation, a major research direction is the validation of the results presented in the aforementioned sections in more clinically relevant models. For instance, fibre structures data collected in real hearts can be used to derive maps of atrial topologies which can be used as baseline of novel frameworks inspired by the simple insilico models discussed in this dissertation [20, 26, 28]. This approach would not only allow us to reproduce the results presented here in a more realistic setting but also examine how the predictions made by these models are affected by diversity of fiber maps, e.g., samples with similar fibrotic burdens but different distributions of fibrotic regions [28]. The ElectroCardioMaths research initiative at Imperial College London is already working in this direction by developing computational models that can be “fit” to real atrial fibre maps in order to identify regions of the cardiac muscle that are susceptible to the formation of re-entry drivers on a patient-by-patient basis, see [416].

The agent-based model of the foreign exchange market introduced in section 4.5 is a simple, proof-of-concept model of the interactions between heterogeneous market participants across multiple trading venues [34]. In line with the models of cardiac fibrillation presented in chapter 3, this tool is designed to reproduce the evolution of this complex system over long timescale and to generate qualitative insights and hypotheses on the mechanisms that govern interactions and emergents. Unsurprisingly, the intrinsic simplicity of these models remains a major hurdle for their practical implementation as short term decision making algorithms, e.g., the optimal

execution of a large order or the systematic exploitation of triangular arbitrage opportunities. In this context, future research building on the Arbitrager Model should aim to extract new insights and hypotheses on the mechanisms of financial markets rather than looking at more practical applications in financial trading. A first potential research path is extending the model to $N > 3$ markets such that the arbitrager can choose to exploit different “triangles” [34]. In particular, it would be interesting to assess how the increased complexity introduced by the inclusion of a larger number of sub-systems affects the cross-currency correlation diagrams generated by the model [34]. A second research path is the inclusion of special players of the currency markets, such as a central bank [34]. In this setting, one can simulate large intervention actions, e.g., a central bank performing a large purchase of foreign currency as part of its monetary policy, and assess how these unique events affect the presence of triangular arbitrage opportunities and, in turn, the cross-correlations structures among the affected currencies [34]. Finally, another intriguing direction is the inclusion of market design features [34]. For instance, one may discretize the price movements to model the effect of the different tick sizes adopted by EBS during the period covered in the analyses presented in section 4.5 and assess how these microstructural constraints affect the interactions among agents and, ultimately, the cross-correlations among currencies [34].

The statistical model presented in section 4.6 introduces a new framework in which price fluctuations are described as the product of order flow imbalance and price impact coefficient, i.e., the co-action of supply/demand imbalances and market liquidity, and the price impact coefficient is conceived as a latent variable governed by the interplay of three components, i.e., a diurnal level, a deterministic intraday pattern and an autoregressive component [37]. The scope of this model is not aligned to the ones of the other models presented in this thesis as the problem of modelling one of more aspect of a complex system, i.e., in this case the evolution of securities prices, is not approached from a complexity science perspective but rather from a fine-detailed and data driven statistical one. As a result, this model is more suitable for i) practical financial markets applications and ii) to gather insights in support of the development of more theoretical frameworks aimed to describe the dynamics of securities markets in a broader sense [37]. A potential extension of such framework is the inclusion of cross-asset impact in the characterization of price dynamics in order to model how events taking place in other orderbooks affect the price of a given security, see [417, 418] for details.

Bibliography

- [1] Ernest G. Ehlert and Simeon Potter. Phase, 2019.
- [2] Mark EJ Newman. Complex systems: A survey. *arXiv preprint arXiv:1112.1440*, 2011.
- [3] Yaneer Bar-Yam. *Dynamics of complex systems*. CRC Press, 2019.
- [4] Brigitte Gay and Bernard Dousset. Innovation and network structural dynamics: Study of the alliance network of a major sector of the biotechnology industry. *Research policy*, 34(10):1457–1475, 2005.
- [5] Yuya Kajikawa, Yoshiyuki Takeda, Ichiro Sakata, and Katsumori Matsushima. Multiscale analysis of interfirm networks in regional clusters. *Technovation*, 30(3):168–180, 2010.
- [6] Hayato Goto, Hideki Takayasu, and Misako Takayasu. Empirical analysis of firm-dynamics on japanese interfirm trade network. In *Proceedings of the International Conference on Social Modeling and Simulation, plus Econophysics Colloquium 2014*, pages 195–204. Springer, Cham, 2015.
- [7] Takayuki Mizuno, Hideki Takayasu, and Misako Takayasu. Correlation networks among currencies. *Physica A: Statistical Mechanics and its Applications*, 364:336–342, 2006.
- [8] Jarosław Kwapien, Sylwia Gworek, Stanisław Drożdż, and Andrzej Górski. Analysis of a network structure of the foreign currency exchange market. *Journal of Economic Interaction and Coordination*, 4(1):55, 2009.
- [9] Mark EJ Newman. Coauthorship networks and patterns of scientific collaboration. *Proceedings of the national academy of sciences*, 101(suppl 1):5200–5205, 2004.

- [10] Wolfgang Glänzel and András Schubert. Analysing scientific networks through co-authorship. In *Handbook of quantitative science and technology research*, pages 257–276. Springer, 2004.
- [11] Emre Sarigöl, René Pfitzner, Ingo Scholtes, Antonios Garas, and Frank Schweitzer. Predicting scientific success based on coauthorship networks. *EPJ Data Science*, 3(1):9, 2014.
- [12] Mariagrazia Dotoli and Maria Pia Fanti. An urban traffic network model via coloured timed petri nets. *Control Engineering Practice*, 14(10):1213–1229, 2006.
- [13] Kok Mun Ng, Mamun Bin Ibne Reaz, and Mohd Alauddin Mohd Ali. A review on the applications of petri nets in modeling, analysis, and control of urban traffic. *IEEE Transactions on Intelligent Transportation Systems*, 14(2):858–870, 2013.
- [14] AA van Ballegooijen, ER Priest, and DH Mackay. Mean field model for the formation of filament channels on the sun. *The Astrophysical Journal*, 539(2):983, 2000.
- [15] William Ogilvy Kermack and Anderson G McKendrick. A contribution to the mathematical theory of epidemics. *Proceedings of the royal society of london. Series A, Containing papers of a mathematical and physical character*, 115(772):700–721, 1927.
- [16] Herbert W Hethcote and James A Yorke. *Gonorrhea transmission dynamics and control*, volume 56. Springer, 2014.
- [17] Andreas Schadschneider and Michael Schreckenberg. Car-oriented mean-field theory for traffic flow models. *Journal of Physics A: Mathematical and General*, 30(4):L69, 1997.
- [18] Takashi Nagatani. Dynamical transition and scaling in a mean-field model of pedestrian flow at a bottleneck. *Physica A: Statistical Mechanics and Its Applications*, 300(3-4):558–566, 2001.
- [19] Frank Marten, Serafim Rodrigues, Oscar Benjamin, Mark P Richardson, and John R Terry. Onset of polypike complexes in a mean-field model of human electroencephalography and its application to absence epilepsy. *Philosophical Transactions of the Royal Society A: Mathematical, Physical and Engineering Sciences*, 367(1891):1145–1161, 2009.

- [20] Alberto Ciacci, Max Falkenberg, Kishan A Manani, Tim S Evans, Nicholas S Peters, and Kim Christensen. Understanding the transition from paroxysmal to persistent atrial fibrillation. *Physical Review Research*, 2(2):023311, 2020.
- [21] Jean-Philippe Bouchaud, Julius Bonart, Jonathan Donier, and Martin Gould. *Trades, quotes and prices: financial markets under the microscope*. Cambridge University Press, 2018.
- [22] Marcus G Daniels, J Doyne Farmer, László Gillemot, Giulia Iori, and Eric Smith. Quantitative model of price diffusion and market friction based on trading as a mechanistic random process. *Physical review letters*, 90(10):108102, 2003.
- [23] Eric Smith, J Doyne Farmer, L szl Gillemot, Supriya Krishnamurthy, et al. Statistical theory of the continuous double auction. *Quantitative finance*, 3(6):481–514, 2003.
- [24] J Doyne Farmer, Paolo Patelli, and Ilija I Zovko. The predictive power of zero intelligence in financial markets. *Proceedings of the National Academy of Sciences*, 102(6):2254–2259, 2005.
- [25] Kim Christensen, Kishan A Manani, and Nicholas S Peters. Simple model for identifying critical regions in atrial fibrillation. *Physical review letters*, 114(2):028104, 2015.
- [26] Max Falkenberg, Alberto Ciacci, Gwyneth Matthews, Jack Way, Balvinder Handa, Li Xinyang, Nicholas S Peters, Fu Siong Ng, and Kim Christensen. Increased gap-junction coupling terminates myocardial fibrillation by optimising phase singularity meander - an insilico study. *In completion*, 2021.
- [27] Balvinder S Handa, Xinyang Li, Nicoleta Baxan, Caroline H Roney, Anastasia Shchendrygina, Catherine A Mansfield, Richard J Jabbour, David S Pitcher, Rasheda A Chowdhury, Nicholas S Peters, et al. Ventricular fibrillation mechanism and global fibrillatory organization are determined by gap junction coupling and fibrosis pattern. *Cardiovascular research*, 117(4):1078–1090, 2021.
- [28] Max Falkenberg, Andrew J Ford, Anthony C Li, Robert Lawrence, Alberto Ciacci, Nicholas S Peters, and Kim Christensen. Unified mechanism of local drivers in a percolation model of atrial fibrillation. *Physical Review E*, 100(6):062406, 2019.

- [29] Brian J. Hansen, Jichao Zhao, Thomas A. Csepe, Brandon T. Moore, Ning Li, Laura A. Jayne, Anuradha Kalyanasundaram, Praise Lim, Anna Bratasz, K. A. Powell, et al. Atrial fibrillation driven by micro-anatomic intramural re-entry revealed by simultaneous sub-epicardial and sub-endocardial optical mapping in explanted human hearts. *Eur. Heart J.*, 36(35):2390–2401, 2015.
- [30] Brian J. Hansen, Thomas A. Csepe, Jichao Zhao, Anthony J. Ignozzi, John D. Hummel, and Vadim V. Fedorov. Maintenance of Atrial Fibrillation: Are Reentrant Drivers with Spatial Stability the Key? *Circ. Arrhythm. Electrophysiol.*, 9(10):e004398, oct 2016.
- [31] Thomas A. Csepe, Brian J. Hansen, and Vadim V. Fedorov. Atrial fibrillation driver mechanisms: Insight from the isolated human heart. *Trends Cardiovas. Med.*, 27(1):1–11, January 2017.
- [32] Stanley Nattel, Feng Xiong, and Martin Aguilar. Demystifying rotors and their place in clinical translation of atrial fibrillation mechanisms. *Nat. Rev. Cardiol.*, 14(9):509–520, 2017.
- [33] Hugh Calkins, Gerhard Hindricks, Riccardo Cappato, Young-Hoon Kim, Eduardo B Saad, Luis Aguinaga, Joseph G Akar, Vinay Badhwar, Josep Brugada, John Camm, et al. 2017 HRS/EHRA/ECAS/APHRS/ SOLAECE expert consensus statement on catheter and surgical ablation of atrial fibrillation. *Heart Rhythm*, 14(10):e275–e444, 2017.
- [34] Alberto Ciacci, Takumi Sueshige, Hideki Takayasu, Kim Christensen, and Misako Takayasu. The microscopic relationships between triangular arbitrage and cross-currency correlations in a simple agent based model of foreign exchange markets. *PLOS ONE*, 15(6):1–19, 06 2020.
- [35] Kenta Yamada, Hideki Takayasu, Takatoshi Ito, and Misako Takayasu. Solvable stochastic dealer models for financial markets. *Physical Review E*, 79(5):051120, 2009.
- [36] Rama Cont, Arseniy Kukanov, and Sasha Stoikov. The price impact of order book events. *Journal of financial econometrics*, 12(1):47–88, 2014.
- [37] Luca Philippe Mertens, Alberto Ciacci, Fabrizio Lillo, and Giulia Livieri. Liquidity fluctuations and the latent dynamics of price impact. *Quantitative Finance*, pages 1–21, 2021.

- [38] Albert S Kyle. Continuous auctions and insider trading. *Econometrica: Journal of the Econometric Society*, pages 1315–1335, 1985.
- [39] Jan Hodicky. *Modelling and Simulation for Autonomous Systems: Second International Workshop, MESAS 2015, Prague, Czech Republic, April 29-30, 2015, Revised Selected Papers*, volume 9055. Springer, 2015.
- [40] Russell M Lawson et al. *Science in the ancient world: an encyclopedia*. ABC-CLIO, 2004.
- [41] G Galileo. Sidereus nuncius. translated and prefaced by albert van helden, 1989.
- [42] Paolo Palmieri. Galileo and the discovery of the phases of venus. *Journal for the History of Astronomy*, 32(2):109–129, 2001.
- [43] Nick Wilding. Galileo and the stain of time. *California Italian Studies*, 2(1), 2011.
- [44] C Cenkalska and B Biéłowska. *The Scientific World of Copernicus: On the Occasion of the 500th Anniversary of His Birth 1473–1973*. Springer Science & Business Media, 2012.
- [45] Arnab Rai Choudhuri. *Nature’s third cycle: a story of sunspots*. OUP Oxford, 2015.
- [46] Maurice A Finocchiaro. The essential galileo. 2018.
- [47] Wilbur Applebaum. *Encyclopedia of the scientific revolution: from Copernicus to Newton*. Routledge, 2003.
- [48] Bruce Stephenson. *Kepler’s physical astronomy*, volume 13. Springer Science & Business Media, 2012.
- [49] Jennifer L Hicks, Thomas K Uchida, Ajay Seth, Apoorva Rajagopal, and Scott L Delp. Is my model good enough? best practices for verification and validation of musculoskeletal models and simulations of movement. *Journal of biomechanical engineering*, 137(2), 2015.
- [50] Bryan A Tolson and Christine A Shoemaker. Dynamically dimensioned search algorithm for computationally efficient watershed model calibration. *Water Resources Research*, 43(1), 2007.
- [51] Leonid V Kantorovich. The mathematical method of production planning and organization. *Management Science*, 6(4):363–422, 1939.

- [52] Institute for Numerical Analysis (US). *Problems for the Numerical Analysis of the Future*, volume 15. US Government Printing Office, 1951.
- [53] George B Dantzig. Origins of the simplex method. In *A history of scientific computing*, pages 141–151. 1990.
- [54] John von Neumann. Discussion of a maximum problem. *John von Neumann Collected Works*, 6:89–95, 1947.
- [55] WC Davidon. Variable metric method for minimization. Technical report, Argonne National Lab., Lemont, Ill., 1959.
- [56] Charles G Broyden. Quasi-newton methods and their application to function minimisation. *Mathematics of Computation*, 21(99):368–381, 1967.
- [57] Philipp Hennig and Martin Kiefel. Quasi-newton method: A new direction. *Journal of Machine Learning Research*, 14(Mar):843–865, 2013.
- [58] John A Nelder and Roger Mead. A simplex method for function minimization. *The computer journal*, 7(4):308–313, 1965.
- [59] Scott Kirkpatrick, C Daniel Gelatt, and Mario P Vecchi. Optimization by simulated annealing. *science*, 220(4598):671–680, 1983.
- [60] Dimitris Bertsimas, John Tsitsiklis, et al. Simulated annealing. *Statistical science*, 8(1):10–15, 1993.
- [61] Bruce Hajek. Cooling schedules for optimal annealing. *Mathematics of operations research*, 13(2):311–329, 1988.
- [62] Lester Ingber. Simulated annealing: Practice versus theory. *Mathematical and computer modelling*, 18(11):29–57, 1993.
- [63] Marco Dorigo, Vittorio Maniezzo, and Alberto Colomi. The ant system: An autocatalytic optimizing process. 1991.
- [64] Marco Dorigo, Vittorio Maniezzo, and Alberto Colomi. Ant system: optimization by a colony of cooperating agents. *IEEE Transactions on Systems, Man, and Cybernetics, Part B (Cybernetics)*, 26(1):29–41, 1996.

- [65] Marco Dorigo, Gianni Di Caro, and Luca M Gambardella. Ant algorithms for discrete optimization. *Artificial life*, 5(2):137–172, 1999.
- [66] Russell Eberhart and James Kennedy. A new optimizer using particle swarm theory. In *MHS'95. Proceedings of the Sixth International Symposium on Micro Machine and Human Science*, pages 39–43. Ieee, 1995.
- [67] Alec Banks, Jonathan Vincent, and Chukwudi Anyakoha. A review of particle swarm optimization. part i: background and development. *Natural Computing*, 6(4):467–484, 2007.
- [68] Alec Banks, Jonathan Vincent, and Chukwudi Anyakoha. A review of particle swarm optimization. part ii: hybridisation, combinatorial, multicriteria and constrained optimization, and indicative applications. *Natural Computing*, 7(1):109–124, 2008.
- [69] Fred Glover. Future paths for integer programming and links to artificial intelligence. *Computers operations research*, 13(5):533–549, 1986.
- [70] Fred Glover. Tabu search—part i. *ORSA Journal on computing*, 1(3):190–206, 1989.
- [71] Fred Glover. Tabu search—part ii. *ORSA Journal on computing*, 2(1):4–32, 1990.
- [72] Cynthia Rudin. Stop explaining black box machine learning models for high stakes decisions and use interpretable models instead. *Nature Machine Intelligence*, 1(5):206–215, 2019.
- [73] Yaman Barlas. Formal aspects of model validity and validation in system dynamics. *System Dynamics Review: The Journal of the System Dynamics Society*, 12(3):183–210, 1996.
- [74] Lisa Jean Bair and Andreas Tolk. Towards a unified theory of validation. In *2013 Winter Simulations Conference (WSC)*, pages 1245–1256. IEEE, 2013.
- [75] Chollet François. *Deep learning with python*, 2017.
- [76] Tim Miller. Explanation in artificial intelligence: Insights from the social sciences. *Artificial Intelligence*, 267:1–38, 2019.
- [77] Christoph Molnar. *Interpretable machine learning*. Lulu. com, 2020.

- [78] Or Biran and Courtenay Cotton. Explanation and justification in machine learning: A survey. In *IJCAI-17 workshop on explainable AI (XAI)*, volume 8, 2017.
- [79] Rebecca Wexler. When a computer program keeps you in jail: How computers are harming criminal justice. *New York Times*, 13, 2017.
- [80] Michael McGough. How bad is sacramento’s air, exactly? google results appear at odds with reality, some say. *Sacramento Bee*, 7, 2018.
- [81] Kush R Varshney and Homa Alemzadeh. On the safety of machine learning: Cyber-physical systems, decision sciences, and data products. *Big data*, 5(3):246–255, 2017.
- [82] Eric R Kandel, James H Schwartz, Thomas M Jessell, Department of Biochemistry, Molecular Biophysics Thomas Jessell, Steven Siegelbaum, and AJ Hudspeth. *Principles of neural science*, volume 4. McGraw-hill New York, 2000.
- [83] Paul Cilliers. *Complexity and Postmodernism: Understanding Complex Systems*. Psychology Press, 1998.
- [84] Dan C Marinescu. *Complex systems and clouds: a self-organization and self-management perspective*. Morgan Kaufmann, 2016.
- [85] Aristotle. *Metaphysics*. translated by w. d. ross, 1981.
- [86] Timothy O’Connor and Hong Yu Wong. Emergent properties. In Edward N. Zalta, editor, *The Stanford Encyclopedia of Philosophy*. Metaphysics Research Lab, Stanford University, spring 2020 edition, 2020.
- [87] R Keith Sawyer. *Social emergence: Societies as complex systems*. Cambridge University Press, 2005.
- [88] J.S. Mill. *The Collected Works of John Stuart Mill: Utilitarianism, The Subjection of Women, On Liberty, Principles of Political Economy, A System of Logic, Ratiocinative and Inductive, Memoirs. . . .* e-artnow, 2017.
- [89] David Blitz. *Emergent evolution: qualitative novelty and the levels of reality*, volume 19. Springer Science & Business Media, 2013.
- [90] Jeffrey Goldstein. *Emergence in Complex Systems*, pages 65–78. Sage Publications, 2011.

- [91] Andrea Parravicini. Pragmatism and emergentism. *European Journal of Pragmatism and American Philosophy*, (2), 2019.
- [92] Jeffrey Goldstein. Emergence as a construct: History and issues. *Emergence*, 1(1):49–72, 1999.
- [93] Nino Boccarda. *Modeling complex systems*. Springer Science & Business Media, 2010.
- [94] Francis Heylighen. *Complexity and self-organization*. 2008.
- [95] Marc Bekoff. Vigilance, flock size, and flock geometry: information gathering by western evening grosbeaks (aves, fringillidae). *Ethology*, 99(1-2):150–161, 1995.
- [96] David B Bahr and Marc Bekoff. Predicting flock vigilance from simple passerine interactions: modelling with cellular automata. *Animal Behaviour*, 58(4):831–839, 1999.
- [97] Stephen Wolfram. Statistical mechanics of cellular automata. *Reviews of modern physics*, 55(3):601, 1983.
- [98] Jarkko Kari. Theory of cellular automata: A survey. *Theoretical computer science*, 334(1-3):3–33, 2005.
- [99] Kamalika Bhattacharjee, Nazma Naskar, Souvik Roy, and Sukanta Das. A survey of cellular automata: Types, dynamics, non-uniformity and applications. *Natural Computing*, pages 1–29, 2018.
- [100] John Von Neumann, Arthur W Burks, et al. Theory of self-reproducing automata. *IEEE Transactions on Neural Networks*, 5(1):3–14, 1966.
- [101] Lawrence Gray, A New, et al. A mathematician looks at wolfram’s new kind of science. In *Notices of the American Mathematical Society 50 (2)(2003) 200–211*, URL <http://www.ams.org/notices/200302/fea-gray.pdf>. URL <http://www.ams.org/notices/200302/fea-gray.pdf>. Citeseer, 2003.
- [102] Eric W Weisstein. von neumann neighborhood. from mathworld—a wolfram web resource. 2013.
- [103] Edward F Moore. The shortest path through a maze. In *Proc. Int. Symp. Switching Theory, 1959*, pages 285–292, 1959.

- [104] Eric W Weisstein. Moore neighborhood. *From MathWorld—A Wolfram Web Resource*. <http://mathworld.wolfram.com/MooreNeighborhood.html>, 2005.
- [105] Martin Gardner. Mathematical games: on cellular automata, self-reproduction, the garden of eden and the game of 'life'. *Sci. Am.*, 224:112–117, 1971.
- [106] Giuseppe A Trunfio. Predicting wildfire spreading through a hexagonal cellular automata model. In *International Conference on Cellular Automata*, pages 385–394. Springer, 2004.
- [107] L Hernández Encinas, S Hoya White, A Martín Del Rey, and G Rodríguez Sánchez. Modelling forest fire spread using hexagonal cellular automata. *Applied mathematical modelling*, 31(6):1213–1227, 2007.
- [108] Irfan Siap, Hasan Akin, and Selman Uğuz. Structure and reversibility of 2d hexagonal cellular automata. *Computers & Mathematics with Applications*, 62(11):4161–4169, 2011.
- [109] Katsunobu Imai and Kenichi Morita. A computation-universal two-dimensional 8-state triangular reversible cellular automaton. *Theoretical Computer Science*, 231(2):181–191, 2000.
- [110] Ryan K Hopman and Michael J Leamy. Triangular cellular automata for computing two-dimensional elastodynamic response on arbitrary domains. *Journal of Applied Mechanics*, 78(2), 2011.
- [111] Kenichi Morita. Universality of 8-state reversible and conservative triangular partitioned cellular automata. In *International Conference on Cellular Automata*, pages 45–54. Springer, 2016.
- [112] William J Stewart, Karim Atif, and Brigette Plateau. The numerical solution of stochastic automata networks. *European Journal of Operational Research*, 86(3):503–525, 1995.
- [113] Marco Tomassini. Generalized automata networks. In *International Conference on Cellular Automata*, pages 14–28. Springer, 2006.
- [114] Eric Goles and Servet Martínez. *Neural and automata networks: dynamical behavior and applications*, volume 58. Springer Science & Business Media, 2013.

- [115] Sukumar Nandi, Biswajit K Kar, and P Pal Chaudhuri. Theory and applications of cellular automata in cryptography. *IEEE Transactions on computers*, 43(12):1346–1357, 1994.
- [116] Franciszek Sereczynski, Pascal Bouvry, and Albert Y Zomaya. Cellular automata computations and secret key cryptography. *parallel computing*, 30(5-6):753–766, 2004.
- [117] Marcin Sereczynski and Pascal Bouvry. Block cipher based on reversible cellular automata. *New Generation Computing*, 23(3):245–258, 2005.
- [118] Enrico Formenti, Katsunobu Imai, Bruno Martin, and Jean-Baptiste Yunès. Advances on random sequence generation by uniform cellular automata. In *Computing with New Resources*, pages 56–70. Springer, 2014.
- [119] Kolin Paul, D Roy Choudhury, and P Pal Chaudhuri. Cellular automata based transform coding for image compression. In *International Conference on High-Performance Computing*, pages 269–273. Springer, 1999.
- [120] Sartra Wongthanavasuu and R Sadananda. A ca-based edge operator and its performance evaluation. *Journal of Visual Communication and Image Representation*, 14(2):83–96, 2003.
- [121] Paul L Rosin. Training cellular automata for image processing. *IEEE transactions on image processing*, 15(7):2076–2087, 2006.
- [122] Erica Jen. Invariant strings and pattern-recognizing properties of one-dimensional cellular automata. *Journal of statistical physics*, 43(1-2):243–265, 1986.
- [123] Parimal Pal Chaudhuri, Dipanwita Roy Chowdhury, Sukumar Nandi, and Santanu Chattopadhyay. *Additive cellular automata: theory and applications*, volume 43. John Wiley & Sons, 1997.
- [124] Sukanta Das, Sukanya Mukherjee, Nazma Naskar, and Biplab K Sikdar. Characterization of single cycle ca and its application in pattern classification. *Electronic Notes in Theoretical Computer Science*, 252:181–203, 2009.
- [125] Biswanath Sethi and Sukanta Das. On the use of asynchronous cellular automata in symmetric-key cryptography. In *International Symposium on Security in Computing and Communication*, pages 30–41. Springer, 2016.

- [126] Christian Burks and Doyne Farmer. Towards modeling dna sequences as automata. *Physica D: nonlinear phenomena*, 10(1-2):157–167, 1984.
- [127] S Mitra, S Das, P Pal Chaudhuri, and Sukumar Nandi. Architecture of a vlsi chip for modelling amino acid sequence in proteins. In *Proceedings of 9th international conference on VLSI design*, pages 316–317. IEEE, 1996.
- [128] Soumyabrata Ghosh, Nirmalya S Maiti, and Parimal Pal Chaudhuri. Theory and application of restricted five neighborhood cellular automata (r5nca) for protein structure prediction. In *International Conference on Cellular Automata*, pages 360–369. Springer, 2012.
- [129] Brian Heath, Raymond Hill, and Frank Ciarallo. A survey of agent-based modeling practices (january 1998 to july 2008). *Journal of Artificial Societies and Social Simulation*, 12(4):9, 2009.
- [130] Eric Bonabeau. Agent-based modeling: Methods and techniques for simulating human systems. *Proceedings of the national academy of sciences*, 99(suppl 3):7280–7287, 2002.
- [131] Nigel Gilbert. *Agent-based models*, volume 153. Sage Publications, Incorporated, 2019.
- [132] J Doyne Farmer, Eric Smith, and Martin Shubik. Economics: the next physical science? *arXiv preprint physics/0506086*, 2005.
- [133] Lawrence R Glosten and Paul R Milgrom. Bid, ask and transaction prices in a specialist market with heterogeneously informed traders. *Journal of financial economics*, 14(1):71–100, 1985.
- [134] Christine A Parlour. Price dynamics in limit order markets. *The Review of Financial Studies*, 11(4):789–816, 1998.
- [135] Thierry Foucault. Order flow composition and trading costs in a dynamic limit order market1. *Journal of Financial markets*, 2(2):99–134, 1999.
- [136] Herbert A Simon. *Models of man; social and rational*. 1957.
- [137] PW Anderson, KJ Arrow, and D Pines. The economy as an evolving complex system addison-wesley. *Redwood City*, 1988.

- [138] Thomas C Schelling. Dynamic models of segregation. *Journal of mathematical sociology*, 1(2):143–186, 1971.
- [139] James M Sakoda. The checkerboard model of social interaction. *The Journal of Mathematical Sociology*, 1(1):119–132, 1971.
- [140] Junfu Zhang. A dynamic model of residential segregation. *Journal of Mathematical Sociology*, 28(3):147–170, 2004.
- [141] Amy H Auchincloss, Rick L Riolo, Daniel G Brown, Jeremy Cook, and Ana V Diez Roux. An agent-based model of income inequalities in diet in the context of residential segregation. *American journal of preventive medicine*, 40(3):303–311, 2011.
- [142] Guillaume Deffuant. Comparing extremism propagation patterns in continuous opinion models. *Journal of Artificial Societies and Social Simulation*, 9(3), 2006.
- [143] Ingo Wolf, Tobias Schröder, Jochen Neumann, and Gerhard de Haan. Changing minds about electric cars: An empirically grounded agent-based modeling approach. *Technological forecasting and social change*, 94:269–285, 2015.
- [144] Mateu Llas, Pablo M Gleiser, Juan M López, and Albert Díaz-Guilera. Nonequilibrium phase transition in a model for the propagation of innovations among economic agents. *Physical Review E*, 68(6):066101, 2003.
- [145] Hideki Takayasu, Hitoshi Miura, Tadashi Hirabayashi, and Koichi Hamada. Statistical properties of deterministic threshold elements—the case of market price. *Physica A: Statistical Mechanics and its Applications*, 184(1-2):127–134, 1992.
- [146] Rama Cont and Jean-Philippe Bouchaud. Herd behavior and aggregate fluctuations in financial markets. *Macroeconomic Dynamics*, 4(2):170–196, 2000.
- [147] T Garel and H Orland. Mean-field model for protein folding. *EPL (Europhysics Letters)*, 6(4):307, 1988.
- [148] David Boris and Michael Rubinstein. A self-consistent mean field model of a starburst dendrimer: dense core vs dense shell. *Macromolecules*, 29(22):7251–7260, 1996.
- [149] P Bialas, Zdzisław Burda, and D Johnston. Phase diagram of the mean field model of simplicial gravity. *Nuclear Physics B*, 542(1-2):413–424, 1999.

- [150] H Shen and H Toki. Quark mean field model for nuclear matter and finite nuclei. *Physical Review C*, 61(4):045205, 2000.
- [151] Roberta Amato, Nikos E Kouvaris, Maxi San Miguel, and Albert Díaz-Guilera. Opinion competition dynamics on multiplex networks. *New Journal of Physics*, 19(12):123019, 2017.
- [152] Wai-Ki Ching and Michael K Ng. Markov chains. *Models, algorithms and applications*, 2006.
- [153] Karl Sigman. Continuous-time markov chains (notes for the course ieor 6711 at columbia university), 2009.
- [154] Sven Banisch, Ricardo Lima, and Tanya Araújo. Agent based models and opinion dynamics as markov chains. *Social Networks*, 34(4):549–561, 2012.
- [155] Gabriele Valentini, Mauro Birattari, and Marco Dorigo. Majority rule with differential latency: An absorbing markov chain to model consensus. In *Proceedings of the European Conference on Complex Systems 2012*, pages 651–658. Springer, 2013.
- [156] Rama Cont, Sasha Stoikov, and Rishi Talreja. A stochastic model for order book dynamics. *Operations research*, 58(3):549–563, 2010.
- [157] Frédéric Abergel and Aymen Jedidi. A mathematical approach to order book modeling. *International Journal of Theoretical and Applied Finance*, 16(05):1350025, 2013.
- [158] Rama Cont and Adrien De Larrard. Price dynamics in a markovian limit order market. *SIAM Journal on Financial Mathematics*, 4(1):1–25, 2013.
- [159] Nir Nossenson and Hagit Messer. Modeling neuron firing pattern using a two state markov chain. In *2010 IEEE Sensor Array and Multichannel Signal Processing Workshop*, pages 41–44. IEEE, 2010.
- [160] Lars Buesing, Johannes Bill, Bernhard Nessler, and Wolfgang Maass. Neural dynamics as sampling: a model for stochastic computation in recurrent networks of spiking neurons. *PLoS Comput Biol*, 7(11):e1002211, 2011.

- [161] Guoqiang Yu, Jianming Hu, Changshui Zhang, Like Zhuang, and Jingyan Song. Short-term traffic flow forecasting based on markov chain model. In *IEEE IV2003 Intelligent Vehicles Symposium. Proceedings (Cat. No. 03TH8683)*, pages 208–212. IEEE, 2003.
- [162] Shiliang Sun, Guoqiang Yu, and Changshui Zhang. Short-term traffic flow forecasting using sampling markov chain method with incomplete data. In *IEEE Intelligent Vehicles Symposium, 2004*, pages 437–441. IEEE, 2004.
- [163] Sergio Gómez, Alexandre Arenas, Javier Borge-Holthoefer, Sandro Meloni, and Yamir Moreno. Discrete-time markov chain approach to contact-based disease spreading in complex networks. *EPL (Europhysics Letters)*, 89(3):38009, 2010.
- [164] Renaud Lambiotte, Martin Rosvall, and Ingo Scholtes. From networks to optimal higher-order models of complex systems. *Nature physics*, 15(4):313–320, 2019.
- [165] Mark EJ Newman. The structure and function of complex networks. *SIAM review*, 45(2):167–256, 2003.
- [166] M. Newman. *Networks: An Introduction*. OUP Oxford, 2010.
- [167] Giacomo Livan, Fabio Caccioli, and Tomaso Aste. Excess reciprocity distorts reputation in online social networks. *Scientific reports*, 7(1):1–11, 2017.
- [168] Ray Rivers, Carl Knappett, and Tim Evans. Network models and archaeological spaces. *Computational approaches to archaeological spaces*, pages 99–126, 2011.
- [169] Tim S Evans, Ray J Rivers, and C Knappett. Interactions in space for archaeological models. *Advances in Complex Systems*, 15(01n02):1150009, 2012.
- [170] Luce Prignano, Ignacio Morer, and Albert Díaz-Guilera. Wiring the past: a network science perspective on the challenge of archeological similarity networks. *Frontiers in Digital Humanities*, 4:13, 2017.
- [171] Oleguer Josep Sagarra Pascual, Michael Szell, Paolo Santi, Albert Díaz-Guilera, and Carlo Ratti. Supersampling and network reconstruction of urban mobility. *PLoS One*, 2015, vol. 10, num. 8, p. e0134508, 2015.
- [172] Stanley Nattel. New ideas about atrial fibrillation 50 years on. *Nature*, 415(6868):219–226, 2002.

- [173] U. Schotten, D. Dobrev, P. G. Platonov, H. Kottkamp, and G. Hindricks. Current controversies in determining the main mechanisms of atrial fibrillation. *J. Intern. Med.*, 279(5):428–438, 2016.
- [174] Vadim V. Fedorov and Brian J. Hansen. Now you see a rotor, now you don't. *JACC: Clin. Electrophysiol.*, 4(1):84 – 86, 2018.
- [175] Stanley Nattel and Dobromir Dobrev. Controversies about atrial fibrillation mechanisms: aiming for order in chaos and whether it matters. *Circ. Res.*, 120(9):1396–1398, 2017.
- [176] Ian Mann, Belinda Sandler, Nick Linton, and Prapa Kanagaratnam. Drivers of atrial fibrillation: Theoretical considerations and practical concerns. *Arrhythm. Electrophysiol. Rev.*, 7:49–54, 04 2018.
- [177] Anthony J Weinhaus and Kenneth P Roberts. Anatomy of the human heart. In *Handbook of cardiac anatomy, physiology, and devices*, pages 51–79. Springer, 2005.
- [178] Heart. *Encyclopaedia Britannica*, 2020. <https://www.britannica.com/science/heartref174619>.
- [179] HW Vliegen, A Van der Laarse, CJ Cornelisse, and F Eulderink. Myocardial changes in pressure overload-induced left ventricular hypertrophy: A study on tissue composition, polyploidization and multinucleation. *European heart journal*, 12(4):488–494, 1991.
- [180] Patrizia Camelliti, Thomas K Borg, and Peter Kohl. Structural and functional characterisation of cardiac fibroblasts. *Cardiovascular research*, 65(1):40–51, 2005.
- [181] Frederic Martini et al. *Anatomy and Physiology'2007 Ed.* Rex Bookstore, Inc., 2006.
- [182] Jeremy Pinnell, Simon Turner, and Simon Howell. Cardiac muscle physiology. *Continuing Education in Anaesthesia Critical Care Pain*, 7(3):85–88, 05 2007.
- [183] Tariq MA Saxton A and Bordoni B. *Anatomy, thorax, cardiac muscle*, 2020.
- [184] Ahmad S Amin, Hanno L Tan, and Arthur AM Wilde. Cardiac ion channels in health and disease. *Heart Rhythm*, 7(1):117–126, 2010.
- [185] Habo J Jongsma and Ronald Wilders. Gap junctions in cardiovascular disease. *Circulation research*, 86(12):1193–1197, 2000.
- [186] Johann P Braithwaite and Yasir Al Khalili. *Physiology, muscle myocyte*. 2019.

- [187] David S Park and Glenn I Fishman. Development and function of the cardiac conduction system in health and disease. *Journal of cardiovascular development and disease*, 4(2):7, 2017.
- [188] Hue-Teh Shih. Anatomy of the action potential in the heart. *Texas Heart Institute Journal*, 21(1):30, 1994.
- [189] Jeanne M Nerbonne and Robert S Kass. Molecular physiology of cardiac repolarization. *Physiological reviews*, 85(4):1205–1253, 2005.
- [190] Sophie Kussauer, Robert David, and Heiko Lemcke. hiPSCs derived cardiac cells for drug and toxicity screening and disease modeling: what micro-electrode-array analyses can tell us. *Cells*, 8(11):1331, 2019.
- [191] Mayo Clinic. Electrocardiogram (ecg or ekg). <https://www.mayoclinic.org/tests-procedures/ekg/about/pac-20384983>.
- [192] Daniel E Becker. Fundamentals of electrocardiography interpretation. *Anesthesia progress*, 53(2):53–64, 2006.
- [193] SJ Enna and David B Bylund. xpharm: the comprehensive pharmacology reference, 2008.
- [194] Dennis H Lau, Stanley Nattel, Jonathan M Kalman, and Prashanthan Sanders. Modifiable risk factors and atrial fibrillation. *Circulation*, 136(6):583–596, 2017.
- [195] Won Chan Lee, Gervasio A Lamas, Sanjeev Balu, James Spalding, Qin Wang, and Chris L Pashos. Direct treatment cost of atrial fibrillation in the elderly american population: a medicare perspective. *Journal of medical economics*, 11(2):281–298, 2008.
- [196] Michael H Kim, Stephen S Johnston, Bong-Chul Chu, Mehul R Dalal, and Kathy L Schulman. Estimation of total incremental health care costs in patients with atrial fibrillation in the united states. *Circulation: Cardiovascular Quality and Outcomes*, 4(3):313–320, 2011.
- [197] Sumeet S Chugh, Rasmus Havmoeller, Kumar Narayanan, David Singh, Michiel Rienstra, Emelia J Benjamin, Richard F Gillum, Young-Hoon Kim, John H McAnulty Jr, Zhi-Jie Zheng, et al. Worldwide epidemiology of atrial fibrillation: a global burden of disease 2010 study. *Circulation*, 129(8):837–847, 2014.

- [198] Fu Siong Ng, Balvinder S. Handa, Xinyang Li, and Nicholas S. Peters. Toward mechanism-directed electrophenotype-based treatments for atrial fibrillation. *Frontiers in Physiology*, 11:987, 2020.
- [199] Philip A Wolf, Emelia J Benhamin, Albert J Belanger, William B Kannel, Daniel Levy, and Ralph B D’Agostino. Secular trends in the prevalence of atrial fibrillation: The framingham study. *American heart journal*, 131(4):790–795, 1996.
- [200] Jonathan P Piccini, Bradley G Hammill, Moritz F Sinner, Paul N Jensen, Adrian F Hernandez, Susan R Heckbert, Emelia J Benjamin, and Lesley H Curtis. Incidence and prevalence of atrial fibrillation and associated mortality among medicare beneficiaries: 1993–2007. *Circulation: Cardiovascular Quality and Outcomes*, 5(1):85–93, 2012.
- [201] Alan S Go, Elaine M Hylek, Kathleen A Phillips, YuChiao Chang, Lori E Henault, Joe V Selby, and Daniel E Singer. Prevalence of diagnosed atrial fibrillation in adults: national implications for rhythm management and stroke prevention: the anticoagulation and risk factors in atrial fibrillation (atria) study. *Jama*, 285(18):2370–2375, 2001.
- [202] Nileshkumar J Patel, Abhishek Deshmukh, Sadip Pant, Vikas Singh, Nilay Patel, Shilpkumar Arora, Neeraj Shah, Ankit Chothani, Ghanshyambhai T Savani, Kathan Mehta, et al. Contemporary trends of hospitalization for atrial fibrillation in the united states, 2000 through 2010: implications for healthcare planning. *Circulation*, 129(23):2371–2379, 2014.
- [203] Robert G Hart and Jonathan L Halperin. Atrial fibrillation and stroke: concepts and controversies. *Stroke*, 32(3):803–808, 2001.
- [204] Anne M Gillis, Atul Verma, Mario Talajic, Stanley Nattel, Paul Dorian, CCS Atrial Fibrillation Guidelines Committee, et al. Canadian cardiovascular society atrial fibrillation guidelines 2010: rate and rhythm management. *Canadian Journal of Cardiology*, 27(1):47–59, 2011.
- [205] Charles Antzelevitch and Alexander Burashnikov. Overview of basic mechanisms of cardiac arrhythmia. *Cardiac electrophysiology clinics*, 3(1):23–45, 2011.

- [206] AL Wit and MR Rosen. After depolarizations and triggered activity. en: Fozzard ha, haber e, jennings rb, katz am, morgan he, editores. the heart and cardiovascular system, 1986.
- [207] Hai Huang, Michael K Pugsley, Bernard Fermini, Michael J Curtis, John Koerner, Michael Accardi, and Simon Authier. Cardiac voltage-gated ion channels in safety pharmacology: review of the landscape leading to the cipa initiative. *Journal of Pharmacological and Toxicological Methods*, 87:11–23, 2017.
- [208] Alfred G Mayer. Scientific books: Rhythmical pulsations in scyphomedusoe. *Science*, 25:821–822, 1907.
- [209] George Ralph Mines. On dynamic equilibrium in the heart. *The Journal of physiology*, 46(4-5):349, 1913.
- [210] George Ralph Mines. On circulating excitations in heart muscle and their possible relation to tachycardia and fibrillation. *Trans R Soc Can*, 8:43–52, 1914.
- [211] Kedar K Aras, Ndeye Rokhaya Faye, Brianna Cathey, and Igor R Efimov. Critical volume of human myocardium necessary to maintain ventricular fibrillation. *Circulation: Arrhythmia and Electrophysiology*, 11(11):e006692, 2018.
- [212] Walter E Garrey. The nature of fibrillary contraction of the heart.—its relation to tissue mass and form. *American Journal of Physiology-Legacy Content*, 33(3):397–414, 1914.
- [213] Maurits A Allessie, Felix IM Bonke, and Francien JG Schopman. Circus movement in rabbit atrial muscle as a mechanism of tachycardia. *Circulation research*, 33(1):54–62, 1973.
- [214] MAURITS A Allessie, FI Bonke, and FJ Schopman. Circus movement in rabbit atrial muscle as a mechanism of tachycardia. iii. the” leading circle” concept: a new model of circus movement in cardiac tissue without the involvement of an anatomical obstacle. *Circulation research*, 41(1):9–18, 1977.
- [215] P Comtois, J Kneller, and S Nattel. Of circles and spirals: bridging the gap between the leading circle and spiral wave concepts of cardiac reentry. *EP Europace*, 7(s2):S10–S20, 2005.

- [216] Gordon K Moe, Werner C Rheinboldt, and JA Abildskov. A computer model of atrial fibrillation. *American heart journal*, 67(2):200–220, 1964.
- [217] Maurits A Allesie, Wim JEP Lammers, Felix IM Bonke, and Jan Hollen. Cardiac electrophysiology and arrhythmias isbn 0-8089-1691-2. *Cardiac Electrophysiology and Arrhythmias*, page 265, 1985.
- [218] Jens Eckstein, Stef Zeemering, Dominik Linz, Bart Maesen, Sander Verheule, Arne van Hunnik, Harry Crijns, Maurits A Allesie, and Ulrich Schotten. Transmural conduction is the predominant mechanism of breakthrough during atrial fibrillation: evidence from simultaneous endo-epicardial high-density activation mapping. *Circulation: Arrhythmia and Electrophysiology*, 6(2):334–341, 2013.
- [219] Michel Haissaguerre, Frank I Marcus, Bruno Fischer, and Jacques Clementy. Radiofrequency catheter ablation in unusual mechanisms of atrial fibrillation: report of three cases. *Journal of cardiovascular electrophysiology*, 5(9):743–751, 1994.
- [220] Pierre Jaïs, Michel Haissaguerre, Dipen C Shah, Salah Chouairi, Laurent Gencel, Méléze Hocini, and Jacques Clémenty. A focal source of atrial fibrillation treated by discrete radiofrequency ablation. *Circulation*, 95(3):572–576, 1997.
- [221] Michel Haissaguerre, Pierre Jaïs, Dipen C Shah, Atsushi Takahashi, Méléze Hocini, Gilles Quiniou, Stéphane Garrigue, Alain Le Mouroux, Philippe Le Métayer, and Jacques Clémenty. Spontaneous initiation of atrial fibrillation by ectopic beats originating in the pulmonary veins. *New England Journal of Medicine*, 339(10):659–666, 1998.
- [222] Hugh Calkins, Karl Heinz Kuck, Riccardo Cappato, Josep Brugada, A John Camm, Shih-Ann Chen, Harry JG Crijns, Ralph J Damiano Jr, D Wyn Davies, John DiMarco, et al. 2012 hrs/ehra/ecas expert consensus statement on catheter and surgical ablation of atrial fibrillation: recommendations for patient selection, procedural techniques, patient management and follow-up, definitions, endpoints, and research trial design: a report of the heart rhythm society (hrs) task force on catheter and surgical ablation of atrial fibrillation. developed in partnership with the european heart rhythm association (ehra), a registered branch of the european society of cardiology (esc) and the european cardiac arrhythmia society (ecas); and in collaboration with the american college of cardiology (acc), american heart association (aha), the asia pacific heart rhythm society (aphrs), and

the society of thoracic surgeons (sts). endorsed by the governing bodies of the american college of cardiology foundation, the american heart association, the european cardiac arrhythmia society, the european heart rhythm association, the society of thoracic surgeons, the asia pacific heart rhythm society, and the heart rhythm society. *Europace*, 14(4):528–606, 2012.

- [223] Kalyanam Shivkumar, Kenneth A Ellenbogen, John D Hummel, John M Miller, and Jonathan S Steinberg. Acute termination of human atrial fibrillation by identification and catheter ablation of localized rotors and sources: first multicenter experience of focal impulse and rotor modulation (firm) ablation. *J. Cardiovasc. Electrophysiol.*, 23(12):1277–1285, 2012.
- [224] Seungyup Lee, Jayakumar Sahadevan, Celeen M. Khrestian, Ivan Cakulev, Alan Markowitz, and Albert L. Waldo. Simultaneous Bi-Atrial High Density (510 - 512 electrodes) Epicardial Mapping of Persistent and Long-Standing Persistent Atrial Fibrillation in Patients: New Insights into the Mechanism of Its Maintenance. *Circulation*, 132(22):2108–2117, dec 2015.
- [225] Sanjiv M Narayan, David E Krummen, Paul Clopton, Kalyanam Shivkumar, and John M Miller. Direct or coincidental elimination of stable rotors or focal sources may explain successful atrial fibrillation ablation. *J. Am. Coll. Cardiol.*, 62(2):138–147, 2013.
- [226] Michel Haïssaguerre, Meleze Hocini, Arnaud Denis, Ashok J. Shah, Yuki Komatsu, Seigo Yamashita, Matthew Daly, Sana Amraoui, Stephan Zellerhoff, Marie-Quitterie Picat, et al. Driver domains in persistent atrial fibrillation. *Circulation*, 130(7):530–538, 2014.
- [227] Sanjiv M. Narayan, Mohan N. Vishwanathan, Christopher A. B. Kowalewski, Tina Baykaner, Miguel Rodrigo, Junaid A. B. Zaman, and Paul J. Wang. The continuous challenge of af ablation: From foci to rotational activity. *Rev. Port. Cardiol.*, 36(Suppl 1):9–17, nov 2017.
- [228] Tina Baykaner, Albert J. Rogers, Gabriela L. Meckler, Junaid A. B. Zaman, Rachita Navara, Miguel Rodrigo, Mahmood Alhousseini, Christopher A. B. Kowalewski, Mohan N. Viswanathan, Sanjiv M. Narayan, et al. Clinical implications of ablation of drivers for atrial fibrillation: A systematic review and meta-analysis. *Circ. Arrhythm. Electrophysiol.*, 11(5):e006119, 2018.

- [229] Max Falkenberg, Andrew J. Ford, Anthony C. Li, Robert Lawrence, Alberto Ciacci, Nicholas S. Peters, and Kim Christensen. Unified mechanism of local drivers in a percolation model of atrial fibrillation. *Phys. Rev. E*, 100:062406, Dec 2019.
- [230] VI Krinskii. Spread of excitation in an inhomogeneous medium (state similar to cardiac fibrillation). *Biophysics*, 11(4):776–784, 1966.
- [231] Arthur T Winfree and John J Tyson. When time breaks down: The three-dimensional dynamics of electrochemical waves and cardiac arrhythmias. *PhT*, 41(12):107, 1988.
- [232] Sandeep V Pandit and José Jalife. Rotors and the dynamics of cardiac fibrillation. *Circulation research*, 112(5):849–862, 2013.
- [233] Atrial Fibrillation Follow-up Investigation of Rhythm Management (AFFIRM) Investigators. A comparison of rate control and rhythm control in patients with atrial fibrillation. *New England Journal of Medicine*, 347(23):1825–1833, 2002.
- [234] Yen-Sin Ang, Sridharan Rajamani, Saptarsi M Haldar, and Jörg Hüser. A new therapeutic framework for atrial fibrillation drug development. *Circulation Research*, 127(1):184–201, 2020.
- [235] Katherine Kearney, Rowan Stephenson, Kevin Phan, Wei Yen Chan, Min Yin Huang, and Tristan D Yan. A systematic review of surgical ablation versus catheter ablation for atrial fibrillation. *Annals of cardiothoracic surgery*, 3(1):15, 2014.
- [236] James L Cox, Richard B Schuessler, Harry J D’Agostino Jr, Constance M Stone, Byung-Chul Chang, Michael E Cain, Peter B Corr, and John P Boineau. The surgical treatment of atrial fibrillation: Iii. development of a definitive surgical procedure. *The Journal of thoracic and cardiovascular surgery*, 101(4):569–583, 1991.
- [237] Lucas VA Boersma, Manuel Castella, Wimjan van Boven, Antonio Berruezo, Alaaddin Yilmaz, Mercedes Nadal, Elena Sandoval, Naiara Calvo, Josep Brugada, Johannes Kelder, et al. Atrial fibrillation catheter ablation versus surgical ablation treatment (fast) a 2-center randomized clinical trial. *Circulation*, 125(1):23–30, 2012.
- [238] Martin EW Hemels, Youlan L Gu, Anton E Tuinenburg, Piet W Boonstra, Ans CP Wiesfeld, Maarten P van den Berg, Dirk J Van Veldhuisen, and Isabelle C Van Gelder.

Favorable long-term outcome of maze surgery in patients with lone atrial fibrillation. *The Annals of thoracic surgery*, 81(5):1773–1779, 2006.

- [239] Laura Rottner, Barbara Bellmann, Tina Lin, Bruno Reissmann, Tobias Tönnis, Ruben Schleberger, Moritz Nies, Christiane Jungen, Leon Dinshaw, Niklas Klatt, et al. Catheter ablation of atrial fibrillation: State of the art and future perspectives. *Cardiology and Therapy*, pages 1–14, 2020.
- [240] Lung National Heart and Blood Institute. Catheter ablation. <https://www.nhlbi.nih.gov/health-topics/catheter-ablation>.
- [241] Amit Noheria, Abhishek Kumar, John V Wylie, and Mark E Josephson. Catheter ablation vs antiarrhythmic drug therapy for atrial fibrillation: a systematic review. *Archives of internal medicine*, 168(6):581–586, 2008.
- [242] Stephanie Brooks, Andreas Metzner, Peter Wohlmuth, Tina Lin, Erik Wissner, Roland Tilz, Andreas Rillig, Shibu Mathew, Ardan Saguner, Christian Heeger, et al. Insights into ablation of persistent atrial fibrillation: Lessons from 6-year clinical outcomes. *Journal of cardiovascular electrophysiology*, 29(2):257–263, 2018.
- [243] Lung Mayo Clinic, National Heart and Biosense Webster Inc. Blood Institute (NHLBI), Abbott Medical Devices. Catheter ablation vs anti-arrhythmic drug therapy for atrial fibrillation trial (cabana). <https://clinicaltrials.gov/ct2/show/study/NCT00911508>.
- [244] Douglas L Packer, Daniel B Mark, Richard A Robb, Kristi H Monahan, Tristram D Bahnson, Jeanne E Poole, Peter A Noseworthy, Yves D Rosenberg, Neal Jeffries, L Brent Mitchell, et al. Effect of catheter ablation vs antiarrhythmic drug therapy on mortality, stroke, bleeding, and cardiac arrest among patients with atrial fibrillation: the cabana randomized clinical trial. *Jama*, 321(13):1261–1274, 2019.
- [245] Larissa Fabritz, Eduard Guasch, Charalambos Antoniades, Isabel Bardinet, Gerlinde Benninger, Tim R Betts, Eva Brand, Günter Breithardt, Gabriela Bucklar-Suchankova, A John Camm, et al. Expert consensus document: defining the major health modifiers causing atrial fibrillation: a roadmap to underpin personalized prevention and treatment. *Nature Reviews Cardiology*, 13(4):230–237, 2016.

- [246] Paulus Kirchhof and Hugh Calkins. Catheter ablation in patients with persistent atrial fibrillation. *European heart journal*, 38(1):20–26, 2017.
- [247] Maurits C.E.F. Wijffels, Charles J.H.J. Kirchhof, Rick Dorland, and Maurits A. Allessie. Atrial fibrillation begets atrial fibrillation. *Circulation*, 92(7):1954–1968, 1995.
- [248] Michael R Franz, Pamela L Karasik, Cuilan Li, Jean Moubarak, and Mary Chavez. Electrical remodeling of the human atrium: similar effects in patients with chronic atrial fibrillation and atrial flutter. *Journal of the American College of Cardiology*, 30(7):1785–1792, 1997.
- [249] Emile G Daoud, Frank Bogun, Rajiva Goyal, Mark Harvey, K Ching Man, S Adam Strickberger, and Fred Morady. Effect of atrial fibrillation on atrial refractoriness in humans. *Circulation*, 94(7):1600–1606, 1996.
- [250] Tomos E. Walters, Ashley Nisbet, Gwilym M. Morris, Gabriel Tan, Megan Mearns, Eliza Teo, Nigel Lewis, AiVee Ng, Paul Gould, Geoffrey Lee, Stephen Joseph, Joseph B. Morton, Dominica Zentner, Prashanthan Sanders, Peter M. Kistler, and Jonathan M. Kalman. Progression of atrial remodeling in patients with high-burden atrial fibrillation: Implications for early ablative intervention. *Heart Rhythm*, 13(2):331 – 339, 2016.
- [251] Brett Burstein and Stanley Nattel. Atrial fibrosis: mechanisms and clinical relevance in atrial fibrillation. *Journal of the American College of Cardiology*, 51(8):802–809, 2008.
- [252] Kai Friedrichs, Stephan Baldus, and Anna Klinke. Fibrosis in Atrial Fibrillation - Role of Reactive Species and MPO. *Frontiers in physiology*, 3:214, jun 2012.
- [253] Pyotr G. Platonov, Lubov B. Mitrofanova, Victoria Orshanskaya, and Siew Yen Ho. Structural abnormalities in atrial walls are associated with presence and persistency of atrial fibrillation but not with age. *Journal of the American College of Cardiology*, 58(21):2225 – 2232, 2011.
- [254] Ping Kong, Panagiota Christia, and Nikolaos G Frangogiannis. The pathogenesis of cardiac fibrosis. *Cellular and molecular life sciences*, 71(4):549–574, 2014.
- [255] Marieke Rienks, Anna-Pia Papageorgiou, Nikolaos G Frangogiannis, and Stephane Heymans. Myocardial extracellular matrix: an ever-changing and diverse entity. *Circulation research*, 114(5):872–888, 2014.

- [256] Saroja Bharati and Maurice Lev. Cardiac conduction system involvement in sudden death of obese young people. *American heart journal*, 129(2):273–281, 1995.
- [257] Juan Asbun and Francisco J Villarreal. The pathogenesis of myocardial fibrosis in the setting of diabetic cardiomyopathy. *Journal of the American College of Cardiology*, 47(4):693–700, 2006.
- [258] Bradford C Berk, Keigi Fujiwara, and Stephanie Lehoux. Ecm remodeling in hypertensive heart disease. *The Journal of clinical investigation*, 117(3):568–575, 2007.
- [259] Bob N Bernaba, Jessica B Chan, Chi K Lai, and Michael C Fishbein. Pathology of late-onset anthracycline cardiomyopathy. *Cardiovascular pathology*, 19(5):308–311, 2010.
- [260] Sanne De Jong, Toon AB van Veen, Harold VM van Rijen, and Jacques MT de Bakker. Fibrosis and cardiac arrhythmias. *Journal of cardiovascular pharmacology*, 57(6):630–638, 2011.
- [261] Gordon A Begg, Arun V Holden, Gregory YH Lip, Sven Plein, and Muzahir H Tayebjee. Assessment of atrial fibrosis for the rhythm control of atrial fibrillation. *International journal of cardiology*, 220:155–161, 2016.
- [262] Pyotr G Platonov. Atrial fibrosis: an obligatory component of arrhythmia mechanisms in atrial fibrillation? *Journal of geriatric cardiology: JGC*, 14(4):233, 2017.
- [263] Svenja Hinderer and Katja Schenke-Layland. Cardiac fibrosis—a short review of causes and therapeutic strategies. *Advanced drug delivery reviews*, 146:77–82, 2019.
- [264] Natalia A Trayanova. Mathematical approaches to understanding and imaging atrial fibrillation: significance for mechanisms and management. *Circulation research*, 114(9):1516–1531, 2014.
- [265] Raimond L Winslow, Natalia Trayanova, Donald Geman, and Michael I Miller. Computational medicine: translating models to clinical care. *Science translational medicine*, 4(158):158rv11–158rv11, 2012.
- [266] Alan L Hodgkin and Andrew F Huxley. A quantitative description of membrane current and its application to conduction and excitation in nerve. *The Journal of physiology*, 117(4):500, 1952.

- [267] Anders Nygren, Céline Fiset, Ludwik Firek, John W Clark, Douglas S Lindblad, Robert B Clark, and Wayne R Giles. Mathematical model of an adult human atrial cell: the role of K^+ currents in repolarization. *Circulation research*, 82(1):63–81, 1998.
- [268] Marc Courtemanche, Rafael J Ramirez, and Stanley Nattel. Ionic mechanisms underlying human atrial action potential properties: insights from a mathematical model. *American Journal of Physiology-Heart and Circulatory Physiology*, 275(1):H301–H321, 1998.
- [269] Eleonora Grandi, Sandeep V Pandit, Niels Voigt, Antony J Workman, Dobromir Dobrev, José Jalife, and Donald M Bers. Human atrial action potential and Ca^{2+} model: sinus rhythm and chronic atrial fibrillation. *Circulation research*, 109(9):1055–1066, 2011.
- [270] Mary M Maleckar, Joseph L Greenstein, Wayne R Giles, and Natalia A Trayanova. K^+ current changes account for the rate dependence of the action potential in the human atrial myocyte. *American Journal of Physiology-Heart and Circulatory Physiology*, 297(4):H1398–H1410, 2009.
- [271] David E Krummen, Jason D Bayer, Jeffrey Ho, Gordon Ho, Miriam R Smetak, Paul Clopton, Natalia A Trayanova, and Sanjiv M Narayan. Mechanisms of human atrial fibrillation initiation: clinical and computational studies of repolarization restitution and activation latency. *Circulation: Arrhythmia and Electrophysiology*, 5(6):1149–1159, 2012.
- [272] Rüdiger Thul, Stephen Coombes, H Llewelyn Roderick, and Martin D Bootman. Sub-cellular calcium dynamics in a whole-cell model of an atrial myocyte. *Proceedings of the National Academy of Sciences*, 109(6):2150–2155, 2012.
- [273] Niels Voigt, Jordi Heijman, Qiongling Wang, David Y Chiang, Na Li, Matthias Karck, Xander HT Wehrens, Stanley Nattel, and Dobromir Dobrev. Cellular and molecular mechanisms of atrial arrhythmogenesis in patients with paroxysmal atrial fibrillation. *Circulation*, 129(2):145–156, 2014.
- [274] Daniel D Correa de Sa, Nathaniel Thompson, Justin Stinnett-Donnelly, Pierre Znojkwicz, Nicole Habel, Joachim G Müller, Jason HT Bates, Jeffrey S Buzas, and Peter S Spector. Electrogram fractionation: the relationship between spatiotemporal variation of tissue excitation and electrode spatial resolution. *Circulation: Arrhythmia and Electrophysiology*, 4(6):909–916, 2011.

- [275] Sergio Alonso and Markus Bär. Reentry near the percolation threshold in a heterogeneous discrete model for cardiac tissue. *Physical review letters*, 110(15):158101, 2013.
- [276] Edward Vigmond, Ali Pashaei, Sana Amraoui, Hubert Cochet, and Michel Haïssaguerre. Percolation as a mechanism to explain atrial fractionated electrograms and reentry in a fibrosis model based on imaging data. *Heart Rhythm*, 13(7):1536–1543, 2016.
- [277] Danuta Makowiec, Joanna Wdowczyk, and Zbigniew R Struzik. Heart rhythm insights into structural remodeling in atrial tissue: timed automata approach. *Frontiers in Physiology*, 9:1859, 2019.
- [278] Edward J Vigmond, Rachel Ruckdeschel, and Natalia Trayanova. Reentry in a morphologically realistic atrial model. *Journal of cardiovascular electrophysiology*, 12(9):1046–1054, 2001.
- [279] L Dang, N Virag, Z Ihara, V Jacquemet, J-M Vesin, J Schlaepfer, P Ruchat, and L Kapfenberger. Evaluation of ablation patterns using a biophysical model of atrial fibrillation. *Annals of biomedical engineering*, 33(4):465–474, 2005.
- [280] Jan Freudenberg, Thomas Schiemann, Ulf Tiede, and Karl Heinz Höhne. Simulation of cardiac excitation patterns in a three-dimensional anatomical heart atlas. *Computers in biology and medicine*, 30(4):191–205, 2000.
- [281] Matthias Reumann, Julia Bohnert, Gunnar Seemann, Brigitte Osswald, and Olaf Dossel. Preventive ablation strategies in a biophysical model of atrial fibrillation based on realistic anatomical data. *IEEE Transactions on Biomedical Engineering*, 55(2):399–406, 2008.
- [282] RA Gray and J Jalife. Ventricular fibrillation and atrial fibrillation are two different beasts. *Chaos: An Interdisciplinary Journal of Nonlinear Science*, 8(1):65–78, 1998.
- [283] Edward J Vigmond, Vincent Tsoi, Samuel Kuo, Hermenegild Arevalo, James Kneller, Stanley Nattel, and Natalia Trayanova. The effect of vagally induced dispersion of action potential duration on atrial arrhythmogenesis. *Heart Rhythm*, 1(3):334–344, 2004.
- [284] Kathleen S McDowell, Fijoy Vadakkumpadan, Robert Blake, Joshua Blauer, Gernot Plank, Rob S MacLeod, and Natalia A Trayanova. Methodology for patient-specific modeling of atrial fibrosis as a substrate for atrial fibrillation. *Journal of electrocardiology*, 45(6):640–645, 2012.

- [285] Kathleen S McDowell, Fijoy Vadakkumpadan, Robert Blake, Joshua Blauer, Gernot Plank, Rob S MacLeod, and Natalia A Trayanova. Mechanistic inquiry into the role of tissue remodeling in fibrotic lesions in human atrial fibrillation. *Biophysical journal*, 104(12):2764–2773, 2013.
- [286] Patrick M Boyle, Tarek Zghaib, Sohail Zahid, Rheeda L Ali, Dongdong Deng, William H Franceschi, Joe B Hakim, Michael J Murphy, Adityo Prakosa, Stefan L Zimmerman, et al. Computationally guided personalized targeted ablation of persistent atrial fibrillation. *Nature biomedical engineering*, 3(11):870–879, 2019.
- [287] David M Harrild and Craig S Henriquez. A computer model of normal conduction in the human atria. *Circulation research*, 87(7):e25–e36, 2000.
- [288] Gunnar Seemann, Christine Höper, Frank B Sachse, Olaf Dössel, Arun V Holden, and Henggui Zhang. Heterogeneous three-dimensional anatomical and electrophysiological model of human atria. *Philosophical Transactions of the Royal Society A: Mathematical, Physical and Engineering Sciences*, 364(1843):1465–1481, 2006.
- [289] Victor M Spitzer and David G Whitlock. The visible human dataset: the anatomical platform for human simulation. *The Anatomical Record: An Official Publication of the American Association of Anatomists*, 253(2):49–57, 1998.
- [290] Vincent Jacquemet, Nathalie Virag, and Lukas Kappenberger. Wavelength and vulnerability to atrial fibrillation: Insights from a computer model of human atria. *EP Europace*, 7(s2):S83–S92, 2005.
- [291] Marc-Etienne Ridler, Mike Lee, David McQueen, Charles Peskin, and Edward Vigmond. Arrhythmogenic consequences of action potential duration gradients in the atria. *Canadian Journal of Cardiology*, 27(1):112–119, 2011.
- [292] Nazem Akoum, Marcos Daccarett, Chris McGann, Nathan Segerson, Gaston Vergara, Suman Kuppahally, Troy Badger, Nathan Burgon, Thomas Haslam, Eugene Kholmovski, et al. Atrial fibrosis helps select the appropriate patient and strategy in catheter ablation of atrial fibrillation: A de-mri guided approach. *Journal of cardiovascular electrophysiology*, 22(1):16–22, 2011.

- [293] Robert A Luke and Jeffrey E Saffitz. Remodeling of ventricular conduction pathways in healed canine infarct border zones. *The Journal of clinical investigation*, 87(5):1594–1602, 1991.
- [294] Sander Verheule, Emily Wilson, Thomas Everett IV, Sujata Shanbhag, Catherine Golden, and Jeffrey Olgin. Alterations in atrial electrophysiology and tissue structure in a canine model of chronic atrial dilatation due to mitral regurgitation. *Circulation*, 107(20):2615–2622, 2003.
- [295] Max Falkenberg McGillivray, William Cheng, Nicholas S. Peters, and Kim Christensen. Machine learning methods for locating re-entrant drivers from electrograms in a model of atrial fibrillation. *Roy. Soc. Open Sci.*, 5(4):172434, 2018.
- [296] Kishan A Manani. Structure and dynamics in atrial fibrillation: a model for cardiac excitation. *Imperial College London PhD Thesis*, 2016.
- [297] Roberto M Lang, Michelle Bierig, Richard B Devereux, Frank A Flachskampf, Elyse Foster, Patricia A Pellikka, Michael H Picard, Mary J Roman, James Seward, Jack S Shanewise, et al. Recommendations for chamber quantification: a report from the american society of echocardiography’s guidelines and standards committee and the chamber quantification writing group, developed in conjunction with the european association of echocardiography, a branch of the european society of cardiology. *Journal of the American Society of Echocardiography*, 18(12):1440–1463, 2005.
- [298] Alicia M Maceira, Juan Cosín-Sales, Michael Roughton, Sanjay K Prasad, and Dudley J Pennell. Reference left atrial dimensions and volumes by steady state free precession cardiovascular magnetic resonance. *Journal of cardiovascular magnetic resonance*, 12(1):65, 2010.
- [299] Koki Nakamura, Nobusada Funabashi, Masae Uehara, Marehiko Ueda, Taichi Murayama, Hiroyuki Takaoka, and Issei Komuro. Left atrial wall thickness in paroxysmal atrial fibrillation by multislice-ct is initial marker of structural remodeling and predictor of transition from paroxysmal to chronic form. *International journal of cardiology*, 148(2):139–147, 2011.
- [300] Balvinder Handa, Xinyang Li, Nicoleta Baxan, Caroline Roney, Anastasia Shchendrygina, Catherine A. Mansfield, Richard Jabbour, David Pitcher, Rasheda A. Chowdhury,

- Nicholas S. Peters, and Fu S. Ng. The electrophenotype spectrum in myocardial fibrillation: a unifying hypothesis for mechanisms sustaining fibrillation. *Unpublished*, 2019.
- [301] Mihail G. Chelu, Jordan B. King, Eugene G. Kholmovski, Junjie Ma, Pim Gal, Qussay Marashly, Mossab A. AlJuaid, Gagandeep Kaur, Michelle A. Silver, Kara A. Johnson, Promporn Suksaranjit, Brent D. Wilson, Frederick T. Han, Arif Elvan, and Nassir F. Marrouche. Atrial fibrosis by late gadolinium enhancement magnetic resonance imaging and catheter ablation of atrial fibrillation: 5-year follow-up data. *Journal of the American Heart Association*, 7(23):e006313, 2018.
- [302] Teresa SM Tsang, Marion E Barnes, Kent R Bailey, Cynthia L Leibson, Samantha C Montgomery, Yasuhiko Takemoto, Pauline M Diamond, Marisa A Marra, Bernard J Gersh, David O Wiebers, et al. Left atrial volume: important risk marker of incident atrial fibrillation in 1655 older men and women. In *Mayo Clinic Proceedings*, volume 76, pages 467–475. Elsevier, 2001.
- [303] Madison S Spach and John P Boineau. Microfibrosis produces electrical load variations due to loss of side-to-side cell connections; a major mechanism of structural heart disease arrhythmias. *Pacing and clinical electrophysiology*, 20(2):397–413, 1997.
- [304] Kishan A. Manani, Kim Christensen, and Nicholas S. Peters. Myocardial architecture and patient variability in clinical patterns of atrial fibrillation. *Phys. Rev. E*, 94:042401, Oct 2016.
- [305] Hans Kottkamp. Human atrial fibrillation substrate: towards a specific fibrotic atrial cardiomyopathy. *European Heart Journal*, 34(35):2731–2738, 06 2013.
- [306] RA Veasey, C Sugihara, K Sandhu, G Dhillon, N Freemantle, SS Furniss, and AN Sulke. The natural history of atrial fibrillation in patients with permanent pacemakers: is atrial fibrillation a progressive disease? *Journal of Interventional Cardiac Electrophysiology*, 44(1):23–30, 2015.
- [307] Conn Sugihara, Rick Veasey, Nick Freemantle, Steve Podd, Steve Furniss, and Neil Sulke. The development of AF over time in patients with permanent pacemakers: objective assessment with pacemaker diagnostics demonstrates distinct patterns of AF. *EP Europace*, 17(6):864–870, 05 2015.

- [308] M. Falkenberg, D. Hickey, L. Terrill, A. Ciacci, N. S. Peters, and K. Christensen. Identifying potential re-entrant circuit locations from atrial fibre maps. In *2019 Computing in Cardiology (CinC)*, pages 1–4, 2019.
- [309] K. Christensen and Nicholas R. Moloney. *Complexity and Criticality*. Imperial College Press, 2005.
- [310] Ivan Soltesz and Kevin Staley. *Computational neuroscience in epilepsy*. Academic Press, 2011.
- [311] Serafim Rodrigues, David Barton, Robert Szalai, Oscar Benjamin, Mark P Richardson, and John R Terry. Transitions to spike-wave oscillations and epileptic dynamics in a human cortico-thalamic mean-field model. *Journal of computational neuroscience*, 27(3):507–526, 2009.
- [312] Tanmay A. Gokhale, Eli Medvescek, and Craig S. Henriquez. Modeling dynamics in diseased cardiac tissue: Impact of model choice. *Chaos*, 27(9):093909, 2017.
- [313] R H Clayton, Olivier Bernus, E M Cherry, Hans Dierckx, F H Fenton, L Mirabella, A V Panfilov, Frank B Sachse, G Seemann, and H Zhang. Models of cardiac tissue electrophysiology: progress, challenges and open questions. *Prog. Biophys. Mol. Bio.*, 104(1):22–48, 2011.
- [314] Balvinder S Handa, Caroline H Roney, Charles Houston, Norman A Qureshi, Xinyang Li, David S Pitcher, Rasheda A Chowdhury, Phang Boon Lim, Emmanuel Dupont, Steven A Niederer, et al. Analytical approaches for myocardial fibrillation signals. *Computers in biology and medicine*, 102:315–326, 2018.
- [315] Dhani Dharmaprani, Madeline Schopp, Pawel Kuklik, Darius Chapman, Anandaroop Lahiri, Lukah Dykes, Feng Xiong, Martin Aguilar, Benjamin Strauss, Lewis Mitchell, et al. Renewal theory as a universal quantitative framework to characterize phase singularity regeneration in mammalian cardiac fibrillation. *Circulation: Arrhythmia and Electrophysiology*, 12(12):e007569, 2019.
- [316] Pipin Kojodjojo, Prapa Kanagaratnam, Oliver R Segal, Wajid Hussain, and Nicholas S Peters. The effects of carbenoxolone on human myocardial conduction: a tool to inves-

- investigate the role of gap junctional uncoupling in human arrhythmogenesis. *Journal of the American College of Cardiology*, 48(6):1242–1249, 2006.
- [317] Anne Louise Kjølbye, Ketil Haugan, James K Hennen, and Jørgen S Petersen. Pharmacological modulation of gap junction function with the novel compound rotigaptide: a promising new principle for prevention of arrhythmias. *Basic & clinical pharmacology & toxicology*, 101(4):215–230, 2007.
- [318] Peter S Spector, Daniel D Correa de Sa, Ethan S Tischler, Nathaniel C Thompson, Nicole Habel, Justin Stinnett-Donnelly, Bryce E Benson, Philipp Bielau, and Jason HT Bates. Ablation of multi-wavelet re-entry: general principles and in silico analyses. *Europace*, 14(suppl_5):v106–v111, 2012.
- [319] Richard T Carrick, Bryce Benson, Nicole Habel, Oliver RJ Bates, Jason HT Bates, and Peter S Spector. Ablation of multiwavelet re-entry guided by circuit-density and distribution: maximizing the probability of circuit annihilation. *Circulation: Arrhythmia and Electrophysiology*, 6(6):1229–1235, 2013.
- [320] Peter Spector, Richard T Carrick, Bryce E Benson, and Oliver Bates. Competitive drivers of atrial fibrillation: The interplay between focal drivers and multiwavelet reentry. *Frontiers in Physiology*, 12:292, 2021.
- [321] Yen Ting Lin, Eugene TY Chang, Julie Eatock, Tobias Galla, and Richard H Clayton. Mechanisms of stochastic onset and termination of atrial fibrillation studied with a cellular automaton model. *Journal of the Royal Society Interface*, 14(128):20160968, 2017.
- [322] Joyce Lin and James P Keener. Ephaptic coupling in cardiac myocytes. *IEEE Transactions on Biomedical Engineering*, 60(2):576–582, 2013.
- [323] Sanjiv M Narayan, Tina Baykaner, Paul Clopton, Amir Schricker, Gautam G Lalani, David E Krummen, Kalyanam Shivkumar, and John M Miller. Ablation of rotor and focal sources reduces late recurrence of atrial fibrillation compared with trigger ablation alone: extended follow-up of the confirm trial (conventional ablation for atrial fibrillation with or without focal impulse and rotor modulation). *Journal of the American College of Cardiology*, 63(17):1761–1768, 2014.

- [324] Eric Buch, Michael Share, Roderick Tung, Peyman Benharash, Parikshit Sharma, Jayanthi Koneru, Ravi Mandapati, Kenneth A Ellenbogen, and Kalyanam Shivkumar. Long-term clinical outcomes of focal impulse and rotor modulation for treatment of atrial fibrillation: A multicenter experience. *Heart Rhythm*, 13(3):636–641, 2016.
- [325] Ursula Ravens. Novel pharmacological approaches for antiarrhythmic therapy, 2010.
- [326] Thomas Engstrøm, Lars Nepper-Christensen, Steffen Helqvist, Lene Kløvgaard, Lene Holmvang, Erik Jørgensen, Frants Pedersen, Kari Saunamaki, Hans-Henrik Tilsted, Adam Steensberg, et al. Danegaptide for primary percutaneous coronary intervention in acute myocardial infarction patients: a phase 2 randomised clinical trial. *Heart*, 104(19):1593–1599, 2018.
- [327] Akiko Shiroshita-Takeshita, Masao Sakabe, Ketil Haugan, James K Hennen, and Stanley Nattel. Model-dependent effects of the gap junction conduction-enhancing antiarrhythmic peptide rotigaptide (zp123) on experimental atrial fibrillation in dogs. *Circulation*, 115(3):310–318, 2007.
- [328] Yu-Cheng Hsieh, Jiunn-Cherng Lin, Chen-Ying Hung, Cheng-Hung Li, Shien-Fong Lin, Hung-I Yeh, Jin-Long Huang, Chu-Pin Lo, Ketil Haugan, Bjarne D Larsen, et al. Gap junction modifier rotigaptide decreases the susceptibility to ventricular arrhythmia by enhancing conduction velocity and suppressing discordant alternans during therapeutic hypothermia in isolated rabbit hearts. *Heart rhythm*, 13(1):251–261, 2016.
- [329] Guo-Ying Su, Jing Wang, Zhen-Xing Xu, Xiao-Jun Qiao, Jing-Quan Zhong, and Yun Zhang. Effects of rotigaptide (zp123) on connexin43 remodeling in canine ventricular fibrillation corrigendum in/mmr/12/6/8327. *Molecular medicine reports*, 12(4):5746–5752, 2015.
- [330] María S Guillem, Andreu M Climent, Miguel Rodrigo, Francisco Fernández-Avilés, Felipe Atienza, and Omer Berenfeld. Presence and stability of rotors in atrial fibrillation: evidence and therapeutic implications. *Cardiovascular research*, 109(4):480–492, 2016.
- [331] Yoshio Takemoto, Hiroki Takanari, Haruo Honjo, Norihiro Ueda, Masahide Harada, Sara Kato, Masatoshi Yamazaki, Ichiro Sakuma, Tobias Opthof, Itsuo Kodama, et al. Inhibition of intercellular coupling stabilizes spiral-wave reentry, whereas enhancement of

- the coupling destabilizes the reentry in favor of early termination. *American Journal of Physiology-Heart and Circulatory Physiology*, 303(5):H578–H586, 2012.
- [332] Thomas Brennan, Martin Fink, and Blanca Rodriguez. Multiscale modelling of drug-induced effects on cardiac electrophysiological activity. *European Journal of Pharmaceutical Sciences*, 36(1):62–77, 2009.
- [333] Steven A Niederer, Joost Lumens, and Natalia A Trayanova. Computational models in cardiology. *Nat. Rev. Cardiol.*, 16(2):100–111, 2019.
- [334] Ivan V Kazbanov, Kirsten HWJ Ten Tusscher, and Alexander V Panfilov. Effects of heterogeneous diffuse fibrosis on arrhythmia dynamics and mechanism. *Scientific reports*, 6(1):1–14, 2016.
- [335] Christopher X. Wong, Anand N. Ganesan, and Joseph B. Selvanayagam. Epicardial fat and atrial fibrillation: current evidence, potential mechanisms, clinical implications, and future directions. *European Heart Journal*, 38(17):1294–1302, 03 2016.
- [336] Caroline H Roney, Chris D Cantwell, Jason D Bayer, Norman A Qureshi, Phang Boon Lim, Jennifer H Tweedy, Prapa Kanagaratnam, Nicholas S Peters, Edward J Vigmond, and Fu Siong Ng. Spatial resolution requirements for accurate identification of drivers of atrial fibrillation. *Circ. Arrhythm. Electrophysiol.*, 10(5):e004899, 2017.
- [337] Madison S. Spach and John P. Boineau. Microfibrosis produces electrical load variations due to loss of side-to-side cell connections; a major mechanism of structural heart disease arrhythmias. *Pacing Clin. Electrophysiol.*, 20(2):397–413, 2006.
- [338] Hubert Cochet, Rémi Dubois, Seigo Yamashita, Nora Al Jefairi, Benjamin Berte, Jean-Marc Sellal, Darren Hooks, Antonio Frontera, Sana Amraoui, Adlane Zemoura, et al. Relationship Between Fibrosis Detected on Late Gadolinium-Enhanced Cardiac Magnetic Resonance and Re-Entrant Activity Assessed With Electrocardiographic Imaging in Human Persistent Atrial Fibrillation. *JACC: Clin. Electrophysiol.*, 4(1):17–29, jan 2018.
- [339] Vijay Swarup, Tina Baykaner, Armand Rostamian, James P Daubert, John Hummel, David E Krummen, Rishi Trikha, John M Miller, Gery F Tomassoni, and Sanjiv M Narayan. Stability of rotors and focal sources for human atrial fibrillation: focal impulse

- and rotor mapping (firm) of af sources and fibrillatory conduction. *J. Cardiovasc. Electr.*, 25(12):1284–1292, 2014.
- [340] R. O. Y. Beinart, Suhny Abbara, Andrew Blum, Maros Ferencik, Kevin Heist, Jeremy Ruskin, and Moussa Mansour. Left atrial wall thickness variability measured by ct scans in patients undergoing pulmonary vein isolation. *J. Cardiovasc. Electrophysiol.*, 22(11):1232–1236, 2011.
- [341] Saurabh Kumar, Chirag R Barbhaiya, Samuel Balindger, Roy M John, Laurence M Epstein, Bruce A Koplan, Usha B Tedrow, William G Stevenson, and Gregory F Michaud. Better lesion creation and assessment during catheter ablation. *J. Atr. Fibrillation*, 8(3):1189, 2015.
- [342] Arunashis Sau, Sayed Al-Aidarous, James Howard, Joseph Shalhoub, Afzal Sohaib, Matthew Shun-Shin, Paul G Novak, Rick Leather, Laurence D Sterns, Christopher Lane, et al. Optimum lesion set and predictors of outcome in persistent atrial fibrillation ablation: a meta-regression analysis. *EP Europace*, 21(8):1176–1184, 05 2019.
- [343] Jichao Zhao, Timothy D. Butters, Henggui Zhang, Andrew J. Pullan, Ian J. LeGrice, Gregory B. Sands, and Bruce H. Smaill. An image-based model of atrial muscular architecture: Effects of structural anisotropy on electrical activation. *Circ. Arrhythm. Electrophysiol.*, 5(2):361–370, 2012.
- [344] Yufeng Wang, Zhaohan Xiong, Aaqel Nalar, Brian J. Hansen, Sanjay Kharche, Gunnar Seemann, Axel Loewe, Vadim V. Fedorov, and Jichao Zhao. A robust computational framework for estimating 3d bi-atrial chamber wall thickness. *Computers in Biology and Medicine*, 114:103444, 2019.
- [345] Luca Mertens, Alberto Ciacci, Fabrizio Lillo, and Giulia Livieri. Liquidity fluctuations and the latent dynamics of price impact. *Available at SSRN 3214744*, 2019.
- [346] Thierry Foucault, Marco Pagano, Ailsa Roell, and Ailsa Röell. *Market liquidity: theory, evidence, and policy*. Oxford University Press, 2013.
- [347] Hans R Stoll. The supply of dealer services in securities markets. *The Journal of Finance*, 33(4):1133–1151, 1978.

- [348] Mark Paddrik, Roy Hayes, William Scherer, and Peter Beling. Effects of limit order book information level on market stability metrics. *Journal of Economic Interaction and Coordination*, 12(2):221–247, 2017.
- [349] Matthieu Wyart, Jean-Philippe Bouchaud, Julien Kockelkoren, Marc Potters, and Michele Vettorazzo. Relation between bid–ask spread, impact and volatility in order-driven markets. *Quantitative finance*, 8(1):41–57, 2008.
- [350] Martin D Gould, Mason A Porter, Stacy Williams, Mark McDonald, Daniel J Fenn, and Sam D Howison. Limit order books. *Quantitative Finance*, 13(11):1709–1742, 2013.
- [351] Julius Bonart and Fabrizio Lillo. A continuous and efficient fundamental price on the discrete order book grid. *Physica A: Statistical Mechanics and its Applications*, 503:698–713, 2018.
- [352] Maureen O’hara. *Market microstructure theory*. Wiley, 1997.
- [353] Robert Almgren and Neil Chriss. Optimal execution of portfolio transactions. *Journal of Risk*, 3:5–40, 2001.
- [354] Ian W Marsh. Order flow and central bank intervention: An empirical analysis of recent bank of japan actions in the foreign exchange market. *Journal of International Money and Finance*, 30(2):377–392, 2011.
- [355] Jean-Philippe Bouchaud. Price impact. *Encyclopedia of quantitative finance*, 2010.
- [356] Marco Raberto, Silvano Cincotti, Sergio M Focardi, and Michele Marchesi. Agent-based simulation of a financial market. *Physica A: Statistical Mechanics and its Applications*, 299(1-2):319–327, 2001.
- [357] Iacopo Mastromatteo, Bence Toth, and Jean-Philippe Bouchaud. Agent-based models for latent liquidity and concave price impact. *Physical Review E*, 89(4):042805, 2014.
- [358] Alec N Kercheval and Yuan Zhang. Modelling high-frequency limit order book dynamics with support vector machines. *Quantitative Finance*, 15(8):1315–1329, 2015.
- [359] Arthur le Calvez and Dave Cliff. Deep learning can replicate adaptive traders in a limit-order-book financial market. In *2018 IEEE Symposium Series on Computational Intelligence (SSCI)*, pages 1876–1883. IEEE, 2018.

- [360] Bruno Biais, Pierre Hillion, and Chester Spatt. An empirical analysis of the limit order book and the order flow in the paris bourse. *the Journal of Finance*, 50(5):1655–1689, 1995.
- [361] Jonathan Donier and Julius Bonart. A million metaorder analysis of market impact on the bitcoin. *Market Microstructure and Liquidity*, 1(02):1550008, 2015.
- [362] Rama Cont. Empirical properties of asset returns: stylized facts and statistical issues. 2001.
- [363] Xavier Gabaix, Parameswaran Gopikrishnan, Vasiliki Plerou, and H Eugene Stanley. A theory of power-law distributions in financial market fluctuations. *Nature*, 423(6937):267–270, 2003.
- [364] J Doyne Farmer, Fabrizio Lillo, et al. On the origin of power-law tails in price fluctuations. *Quantitative Finance*, 4(1):7–11, 2004.
- [365] Fabrizio Lillo and J Doyne Farmer. The long memory of the efficient market. *Studies in nonlinear dynamics & econometrics*, 8(3), 2004.
- [366] Anirban Chakraborti, Ioane Muni Toke, Marco Patriarca, and Frédéric Abergel. Econophysics review: I. empirical facts. *Quantitative Finance*, 11(7):991–1012, 2011.
- [367] Didier Sornette, Anders Johansen, and Jean-Philippe Bouchaud. Stock market crashes, precursors and replicas. *Journal de Physique I*, 6(1):167–175, 1996.
- [368] Jonathan Donier and Jean-Philippe Bouchaud. Why do markets crash? bitcoin data offers unprecedented insights. *PloS one*, 10(10):e0139356, 2015.
- [369] Didier Sornette. *Why stock markets crash: critical events in complex financial systems*, volume 49. Princeton University Press, 2017.
- [370] Peter J Knez and Mark J Ready. Estimating the profits from trading strategies. *The Review of Financial Studies*, 9(4):1121–1163, 1996.
- [371] Jean-Philippe Bouchaud, Yuval Gefen, Marc Potters, and Matthieu Wyart. Fluctuations and response in financial markets: the subtle nature of ‘random’ price changes. *Quantitative finance*, 4(2):176–190, 2004.

- [372] Philipp Weber and Bernd Rosenow*. Order book approach to price impact. *Quantitative Finance*, 5(4):357–364, 2005.
- [373] Jim Gatheral. No-dynamic-arbitrage and market impact. *Quantitative finance*, 10(7):749–759, 2010.
- [374] SP Global Inc. Sp 500, 2020.
- [375] Dagfinn Rime and Andreas Schrimpf. The anatomy of the global fx market through the lens of the 2013 triennial survey. *BIS Quarterly Review, December*, 2013.
- [376] Bank for International Settlements (BIS). Monitoring of fast-paced electronic markets, report submitted by a study group established by the market committee, 2018.
- [377] Takayuki Mizuno, Shoko Kurihara, Misako Takayasu, and Hideki Takayasu. Time-scale dependence of correlations among foreign currencies. In *The Application of Econophysics*, pages 24–29. Springer, 2004.
- [378] Gang-Jin Wang, Chi Xie, Yi-Jun Chen, and Shou Chen. Statistical properties of the foreign exchange network at different time scales: evidence from detrended cross-correlation coefficient and minimum spanning tree. *Entropy*, 15(5):1643–1662, 2013.
- [379] Mr Fei Han and Mr Niklas J Westelius. *Anatomy of Sudden Yen Appreciations*. International Monetary Fund, 2019.
- [380] Yukihiro Aiba, Naomichi Hatano, Hideki Takayasu, Kouhei Marumo, and Tokiko Shimizu. Triangular arbitrage as an interaction among foreign exchange rates. *Physica A: Statistical Mechanics and its Applications*, 310(3-4):467–479, 2002.
- [381] Ben Marshall, Sirimon Treepongkaruna, and Martin Young. Exploitable arbitrage opportunities exist in the foreign exchange market. *American Finance Association Annual Meeting, New Orleans*, 2008.
- [382] Daniel J Fenn, Sam D Howison, Mark McDonald, Stacy Williams, and Neil F Johnson. The mirage of triangular arbitrage in the spot foreign exchange market. *International Journal of Theoretical and Applied Finance*, 12(08):1105–1123, 2009.
- [383] Thierry Foucault, Roman Kozhan, and Wing Wah Tham. Toxic arbitrage. *The Review of Financial Studies*, 30(4):1053–1094, 2016.

- [384] Yukihiro Aiba and Naomichi Hatano. A microscopic model of triangular arbitrage. *Physica A: Statistical Mechanics and its Applications*, 371(2):572–584, 2006.
- [385] Roman Kozhan and Wing Wah Tham. Execution risk in high-frequency arbitrage. *Management Science*, 58(11):2131–2149, 2012.
- [386] Kiyoshi Kanazawa, Takumi Sueshige, Hideki Takayasu, and Misako Takayasu. Derivation of the boltzmann equation for financial brownian motion: Direct observation of the collective motion of high-frequency traders. *Physical Review Letters*, 120(13):138301, 2018.
- [387] Soheil Mahmoodzadeh and Ramazan Gençay. Tick size change in the wholesale foreign exchange market. Technical report, 2014.
- [388] José Pedro Ramos-Requena, Juan Evangelista Trinidad-Segovia, and Miguel Ángel Sánchez-Granero. An alternative approach to measure co-movement between two time series. *Mathematics*, 8(2):261, 2020.
- [389] Robert F Engle and Magdalena E Sokalska. Forecasting intraday volatility in the us equity market. multiplicative component garch. *Journal of Financial Econometrics*, 10(1):54–83, 2012.
- [390] Joel Hasbrouck. Measuring the information content of stock trades. *The Journal of Finance*, 46(1):179–207, 1991.
- [391] Francesco Capponi and Rama Cont. Multi-asset market impact and order flow commonality. Available at SSRN, 2020.
- [392] James Durbin and Siem Jan Koopman. *Time series analysis by state space methods*. Oxford university press, 2012.
- [393] Vinay T Datar, Narayan Y Naik, and Robert Radcliffe. Liquidity and stock returns: An alternative test. *Journal of financial markets*, 1(2):203–219, 1998.
- [394] Kee H Chung and Chairat Chuwonganant. Market volatility and stock returns: The role of liquidity providers. *Journal of Financial Markets*, 37:17–34, 2018.
- [395] Dimitris Bertsimas and Andrew W Lo. Optimal control of execution costs. *Journal of Financial Markets*, 1(1):1–50, 1998.

- [396] Lawrence R Glosten and Lawrence E Harris. Estimating the components of the bid/ask spread. *Journal of financial Economics*, 21(1):123–142, 1988.
- [397] Ananth Madhavan, Matthew Richardson, and Mark Roomans. Why do security prices change? a transaction-level analysis of nyse stocks. *The Review of Financial Studies*, 10(4):1035–1064, 1997.
- [398] Joel Hasbrouck. *Empirical market microstructure: The institutions, economics, and econometrics of securities trading*. Oxford University Press, 2007.
- [399] Jean-Philippe Bouchaud, J Doyne Farmer, and Fabrizio Lillo. How markets slowly digest changes in supply and demand. In *Handbook of financial markets: dynamics and evolution*, pages 57–160. Elsevier, 2009.
- [400] Fabrizio Lillo, J Doyne Farmer, and Rosario N Mantegna. Master curve for price-impact function. *Nature*, 421(6919):129–130, 2003.
- [401] J Doyne Farmer 5, Laszlo Gillemot, Fabrizio Lillo, Szabolcs Mike, and Anindya Sen. What really causes large price changes? *Quantitative finance*, 4(4):383–397, 2004.
- [402] Zoltan Eisler, Jean-Philippe Bouchaud, and Julien Kockelkoren. The price impact of order book events: market orders, limit orders and cancellations. *Quantitative Finance*, 12(9):1395–1419, 2012.
- [403] Nikolaus Hautsch and Ruihong Huang. The market impact of a limit order. *Journal of Economic Dynamics and Control*, 36(4):501–522, 2012.
- [404] Gideon Saar. Price impact asymmetry of block trades: An institutional trading explanation. *The Review of Financial Studies*, 14(4):1153–1181, 2001.
- [405] Chiraphol N Chiyachantana, Pankaj K Jain, Christine Jiang, and Robert A Wood. International evidence on institutional trading behavior and price impact. *The Journal of Finance*, 59(2):869–898, 2004.
- [406] Joao Pedro Pereira and Harold H Zhang. Stock returns and the volatility of liquidity. *Journal of Financial and Quantitative Analysis*, 45(4):1077–1110, 2010.
- [407] Yakov Amihud and Haim Mendelson. Asset pricing and the bid-ask spread. *Journal of financial Economics*, 17(2):223–249, 1986.

- [408] L'uboš Pástor and Robert F Stambaugh. Liquidity risk and expected stock returns. *Journal of Political economy*, 111(3):642–685, 2003.
- [409] Viral V Acharya and Lasse Heje Pedersen. Asset pricing with liquidity risk. *Journal of financial Economics*, 77(2):375–410, 2005.
- [410] Torben G Andersen and Tim Bollerslev. Intraday periodicity and volatility persistence in financial markets. *Journal of empirical finance*, 4(2-3):115–158, 1997.
- [411] Torben G Andersen and Tim Bollerslev. Deutsche mark–dollar volatility: intraday activity patterns, macroeconomic announcements, and longer run dependencies. *the Journal of Finance*, 53(1):219–265, 1998.
- [412] Tim Bollerslev, Jun Cai, and Frank M Song. Intraday periodicity, long memory volatility, and macroeconomic announcement effects in the us treasury bond market. *Journal of empirical finance*, 7(1):37–55, 2000.
- [413] Pierre Giot. Market risk models for intraday data. *The European Journal of Finance*, 11(4):309–324, 2005.
- [414] Jonathan R Stroud and Michael S Johannes. Bayesian modeling and forecasting of 24-hour high-frequency volatility. *Journal of the American Statistical Association*, 109(508):1368–1384, 2014.
- [415] Hans-Georg Müller, Rituparna Sen, and Ulrich Stadtmüller. Functional data analysis for volatility. *Journal of Econometrics*, 165(2):233–245, 2011.
- [416] Max Falkenberg, James A Coleman, Sam Dobson, David J Hickey, Louie Terrill, Alberto Ciacci, Belvin Thomas, Nicholas S Peters, Arunashis Sau, Fu Siong Ng, et al. Identifying locations susceptible to micro-anatomical reentry using a spatial network representation of atrial fibre maps. *bioRxiv*, 2021.
- [417] Michael Benzaquen, Iacopo Mastromatteo, Zoltan Eisler, and Jean-Philippe Bouchaud. Dissecting cross-impact on stock markets: An empirical analysis. *Journal of Statistical Mechanics: Theory and Experiment*, 2017(2):023406, 2017.
- [418] Michael Schneider and Fabrizio Lillo. Cross-impact and no-dynamic-arbitrage. *Quantitative Finance*, 19(1):137–154, 2019.

- [419] Markets Committee et al. Monitoring of fast-paced electronic markets. *MC Papers*, (10), 2018.
- [420] Matteo Aquilina, Eric B Budish, and Peter O’Neill. Quantifying the high-frequency trading “arms race”: A simple new methodology and estimates. *Chicago Booth Research Paper*, (20-16), 2020.
- [421] Ruihong Huang and Tomas Polak. Lobster: Limit order book reconstruction system. *Available at SSRN 1977207*, 2011.
- [422] CME Group. Ebs platforms. <https://www.cmegroup.com/trading/market-tech-and-data-services/ebs/platforms.html>, 2019.
- [423] CME Group. Ebs ultra. <https://www.cmegroup.com/trading/market-tech-and-data-services/ebs/data-analytics.html#live-ultra>, 2020.
- [424] LOBSTER. what is lobster?, 2020.
- [425] CME Group. Ebs. <https://www.cmegroup.com/trading/market-tech-and-data-services/ebs.html>, 2019.
- [426] Fabrizio Lillo and J Doyne Farmer. The key role of liquidity fluctuations in determining large price changes. *Fluctuation and Noise Letters*, 5(02):L209–L216, 2005.
- [427] Raphael P Martins, Kuljeet Kaur, Elliot Hwang, Rafael J Ramirez, B Cicero Willis, David Filgueiras-Rama, Steven R Ennis, Yoshio Takemoto, Daniela Ponce-Balbuena, Manuel Zarzoso, Ryan P O’Connell, Hassan Musa, Guadalupe Guerrero-Serna, Uma Mahesh R Avula, Michael F Swartz, Sandesh Bhushal, Makarand Deo, Sandeep V Pandit, Omer Berenfeld, and José Jalife. Dominant frequency increase rate predicts transition from paroxysmal to long-term persistent atrial fibrillation. *Circulation*, 129(14):1472–1482, apr 2014.
- [428] Kiyoshi Kanazawa, Takumi Sueshige, Hideki Takayasu, and Misako Takayasu. Kinetic theory for financial brownian motion from microscopic dynamics. *Physical Review E*, 98(5):052317, 2018.
- [429] Takumi Sueshige, Kiyoshi Kanazawa, Hideki Takayasu, and Misako Takayasu. Ecology of trading strategies in a forex market for limit and market orders. *PloS one*, 13(12):e0208332, 2018.

- [430] Yoshihiro Yura, Hideki Takayasu, Didier Sornette, and Misako Takayasu. Financial brownian particle in the layered order-book fluid and fluctuation-dissipation relations. *Physical Review Letters*, 112(9):098703, 2014.
- [431] Piet Sercu. *International finance: Theory into practice*. Princeton University Press, 2009.
- [432] James Hamilton. *Time series econometrics*, 1994.
- [433] Martin D Gould and Julius Bonart. Queue imbalance as a one-tick-ahead price predictor in a limit order book. *Market Microstructure and Liquidity*, 2(02):1650006, 2016.

Appendices

Appendix A

External images: attributions and permissions

- Fig. 2.1

- **Content:** the figure includes two images from Pixabay, an online community where users share images and videos without copyright
- **Source 1:** <https://pixabay.com/photos/nature-animal-world-grass-snake-2727199/>
- **Source 2:** <https://pixabay.com/photos/snake-forest-gad-grass-snake-4344421/>
- **License:** Pixabay license.
- **License url:** <https://pixabay.com/service/license/>
- **Alterations to original files:** none.
- **Permission:** not required.

- Fig. 2.3

- **Content:** the figure includes three images from Pixabay, an online community where users share images and videos without copyright
- **Source 1:** <https://pixabay.com/illustrations/solar-system-planet-planetary-system-11111/>
- **Source 2:** <https://pixabay.com/illustrations/nerve-cell-neuron-brain-neurons-2213009/>
- **Source 3:** <https://pixabay.com/illustrations/pay-stock-exchange-negotiation-4852537/>

- **License:** Pixabay license.
 - **License url:** <https://pixabay.com/service/license/>
 - **Alterations to original files:** none.
 - **Permission:** not required.
- Fig. 2.4
 - **Content:** the figure includes two images from Pixabay, an online community where users share images and videos without copyright
 - **Source 1:** <https://pixabay.com/illustrations/solar-system-planet-planetary-system-11111/>
 - **Source 2:** <https://pixabay.com/illustrations/nerve-cell-neuron-brain-neurons-2213009/>
 - **License:** Pixabay license.
 - **License url:** <https://pixabay.com/service/license/>
 - **Alterations to original files:** none.
 - **Permission:** not required.
- Fig. 2.5
 - **Content:** the figure includes an image from Wikimedia Commons, a large database of media files.
 - **Source:** https://commons.wikimedia.org/wiki/File:Flock_of_birds_on_a_watch.jpg
 - **License:** Creative Commons Attribution 4.0 International license.
 - **License url:** <https://creativecommons.org/licenses/by/4.0/deed.en>
 - **Alterations to original file:** none.
 - **Permission:** not required.
- Fig. 3.1
 - **Content:** the figure includes an image from Wikimedia Commons, a large database of media files.
 - **Source:** https://commons.wikimedia.org/wiki/File:Blausen_0470_HeartWall.png

- **License:** Creative Commons Attribution 3.0 Unported license.
 - **License url:** <https://creativecommons.org/licenses/by/3.0/deed.en>
 - **Alterations to original file:** minor.
 - **Permission:** not required.
- Fig. 3.2
 - **Content:** the figure includes two images from Wikimedia Commons, a large database of media files.
 - **Source 1:** https://commons.wikimedia.org/wiki/File:Blausen_0462_HeartAnatomy.png
 - **Source 2:** https://commons.wikimedia.org/wiki/File:Blausen_0452_Heart_BloodFlow.png
 - **License:** Creative Commons Attribution 3.0 Unported license.
 - **License url:** <https://creativecommons.org/licenses/by/3.0/deed.en>
 - **Alterations to original files:** minor.
 - **Permission:** not required.
- Fig. 3.3
 - **Content:** the figure includes two images from Wikimedia Commons, a large database of media files.
 - **Source 1:** https://commons.wikimedia.org/wiki/File:Blausen_0801_SkeletalMuscle.png
 - **Source 2:** <https://commons.wikimedia.org/wiki/File:Sarcomere.jpg>
 - **License 1:** Creative Commons Attribution 3.0 Unported license.
 - **License 1 url:** <https://creativecommons.org/licenses/by/3.0/deed.en>
 - **License 2:** Creative Commons Attribution 2.5 Generic license.
 - **License 2 url:** <https://creativecommons.org/licenses/by/2.5/>
 - **Alterations to original files:** none.
 - **Permission:** not required.
- Fig. 3.4
 - **Content:** the figure includes an image from Wikimedia Commons, a large database of media files.

- **Source:** <https://commons.wikimedia.org/wiki/File:Conductionsystemoftheheart.png>
- **License :** Creative Commons Attribution 3.0 Unported license.
- **License url:** <https://creativecommons.org/licenses/by/3.0/deed.en>
- **Alterations to original file:** none.
- **Permission:** not required.

- Fig. 3.5

- **Content:** an altered version of Fig.2(a) from [190].
- **Original article:** <https://doi.org/10.3390/cells8111331>. This article was published in Cells, Vol 8, Issue 11, Authors: Sophie Kussauer, Robert David and Heiko Lemcke, Title of article: hiPSCs Derived Cardiac Cells for Drug and Toxicity Screening and Disease Modeling: What Micro- Electrode-Array Analyses Can Tell Us, Copyright MDPI (2019).
- **License:** Creative Common CC BY license.
- **License url:** <https://creativecommons.org/licenses/by/4.0/>
- **Alterations to original file:** none. Note that we use only one of the three panels of the original figure.
- **Permission:** not required as per the MDPI Open Access Information and Policy webpage, see <https://www.mdpi.com/openaccess>

- Fig. 3.6

- **Content:** the figure includes two images from Wikimedia Commons, a large database of media files.
- **Source 1:** <https://commons.wikimedia.org/wiki/File:SinusRhythmLabels.svg#/media/File:SinusRhythmLabels.svg>
- **Source 2:** https://commons.wikimedia.org/wiki/File:Normal_Sinus_Rhythm_Unlabeled.jpg
- **License 1:** public domain.
- **License 2:** Creative Commons Attribution-Share Alike 3.0 Unported license.

- **License 2 url:** <https://creativecommons.org/licenses/by-sa/3.0/deed.en>
 - **Alterations to original files:** significant alterations have been applied to the figure appearing in panel (b).
 - **Permission:** not required.
- Fig. 3.7
 - **Content:** The figure includes images appearing in Fig. 3(a)-(b) from [207].
 - **Original article:** <https://doi.org/10.1016/j.vascn.2017.04.002>. This article was published in Journal of Pharmacological and Toxicological Methods, Vol 87, Authors: Hai Huang, Michael K.Pugsley, Bernard Fermini, Michael J.Curtis, John Kerner, Michael Accardi and Simon Authier, Title of article: Cardiac voltage-gated ion channels in safety pharmacology: Review of the landscape leading to the CiPA initiative, Page Nos: 11-23, Copyright Elsevier (2017).
 - **License:** Creative Commons Attribution-Non Commercial-No Derivatives License (CC BY NC ND)
 - **License url:** <https://creativecommons.org/licenses/by-nc-nd/4.0/>
 - **Alterations to original file:** minor. We split the original figure into two distinct figures and removed some textual elements.
 - **Permission:** permission obtained from Elsevier on June 11st 2021.
 - Fig. 3.11
 - **Content:** The figure includes two images appearing in the graphical abstract of [263].
 - **Original article:** <https://doi.org/10.1016/j.addr.2019.05.011>. This article was published in Advanced Drug Delivery Reviews, Vol 146, Authors: Svenja Hinderer and Katja Schenke-Layland, Title of article: Cardiac fibrosis – A short review of causes and therapeutic strategies, Page Nos: 77-82, Copyright Elsevier (2019).
 - **License:** Creative Commons CC-BY license.
 - **License url:** <https://creativecommons.org/licenses/by/4.0/>

- **Alterations to original file:** major. Note that we have extracted the two close-in images from the graphical abstract, i.e., displaying tissues with different fibrotic burdens, and re-arranged them into a two adjacent panels figure.
- **Permission:** permission obtained from Elsevier on June 14th 2021.

- Fig. 3.15

- **Content:** The figure originally appeared in [304] and was used in Fig.15 in [20].
- **Original article:** <https://doi.org/10.1103/PhysRevE.94.042401>. This article was published in Physical Review E, Vol 94, Issue 4, Authors: Kishan A. Manani, Kim Christensen, and Nicholas S. Peters, Title of article: Myocardial architecture and patient variability in clinical patterns of atrial fibrillation, Copyright American Physical Society (2016).
- **License:** Creative Commons Attribution 3.0 license.
- **License url:** <https://creativecommons.org/licenses/by/3.0/>
- **Alterations to original file:** none.
- **Permission:** the license associated with the original manuscript [304] allowed us to re-use this figure without additional permissions.

- Fig. 3.30

- **Content:** The figure originally appeared in [27] and was used in Fig.3 (top panel) in [26].
- **Original article:** <https://doi.org/10.1093/cvr/cvaa141>. This article was published in Cardiovascular Research, Vol 117, Issue 4, Authors: Balvinder S Handa, Xinyang Li, Nicoleta Baxan, Caroline H Roney, Anastasia Shchendrygina, Catherine A Mansfield *et al.*, Title of article: Ventricular fibrillation mechanism and global fibrillatory organization are determined by gap junction coupling and fibrosis pattern, Page Nos: 1078-1090, Copyright Oxford University Press (2020).
- **License:** Creative Commons CC BY license.
- **License url:** <https://creativecommons.org/licenses/by/4.0/>
- **Alterations to original file:** significant as we only retained the sequence of five heart schematics and the closest textual elements.

- **Permission:** the license associated with the original manuscript [27] allowed us to re-use this figure without additional permissions.
- Fig. 3.39
 - **Content:** The images forming panel (a) of this figure originally appeared in [29] and were used as part of Fig. 4 in [28].
 - **Original article:** <https://doi.org/10.1093/eurheartj/ehv233>. This article was published in European Heart Journal, Vol 36, Issue 35, Authors: Brian J. Hansen and Jichao Zhao, Title of article: Atrial fibrillation driven by micro-anatomic intramural re-entry revealed by simultaneous sub-epicardial and sub-endocardial optical mapping in explanted human hearts, Page Nos: 2390-2401, Copyright Oxford University Press (2015).
 - **License number:** CCC Rightslink license number 5197210170082.
 - **Alterations to original file:** minor as the colorbar at the bottom of the two figures extracted from Fig. 5 in [29] was removed before including these files in Fig. 4 in [28]. In addition, the space between the two panel was reduced and the Sub-endo and Sub-epi labels were rewritten in black.
 - **Permission:** permission obtained from Copyright Clearance Center on November 27th 2021.
 - Fig. 4.1
 - **Content:** the figure includes two images from Wikimedia Commons, a large database of media files.
 - **Source 1:** https://commons.wikimedia.org/wiki/File:Chicago_bot.jpg
 - **Source 2:** <https://commons.wikimedia.org/wiki/File:Deutsche-boerse-parkett-ffm008.jpg>
 - **License 1:** public domain.
 - **License 2:** Creative Commons Attribution-Share Alike 3.0 Unported license.
 - **License 2 url:** <https://creativecommons.org/licenses/by-sa/3.0/deed.en>
 - **Alterations to original files:** none.
 - **Permission:** not required.

Appendix B

Published work: contributions and permissions

B.1 Understanding the transition from paroxysmal to persistent atrial fibrillation

- **Authors:** Alberto Ciacci, Max Falkenberg, Kishan A Manani, Tim S Evans, Nicholas S Peters, Kim Christensen.
- **Journal:** Physical Review Research, 2 (2), 2020.
- **DOI:** <https://doi.org/10.1103/PhysRevResearch.2.023311>
- **Personal contributions:** As primary co-author, I provided a broad contribution to this project by focusing on several major tasks such as the development of the underlying theory, the development of computational models and tools, computer-based simulations, presentation of the experimental results and writing of the manuscript. Note that an initial version of the mean-field model was introduced by Kishan Manani in [296] while its continuous extension was derived by Tim Evans.
- **Sections and subsections containing text from this work:** 3.3.3, 3.3.5, 3.4.2, 3.5 and related subsections, appendix D and related sections and subsections.

- **Figures extracted from this work:** 3.12, 3.13, 3.14, 3.15 (used with permission from [304]), 3.16, 3.17, 3.18, 3.19, 3.20, 3.21, 3.22, 3.23, 3.24, 3.25, 3.26, D.1, D.2, D.3, D.4, D.5, D.6, D.7, D.8, D.9, D.10, D.11, D.12, D.13, D.14, D.15, D.16
- **License:** Creative Commons Attribution 4.0 International license.
- **License url:** <https://creativecommons.org/licenses/by/4.0/>
- **Alterations to original article:** The ordering of sections and subsections have been altered to fit the structure of this dissertation. Text from the original article has been amended to fit the structure, notations and other aspects of this dissertation.
- **Permissions for reusing text and images:** It is not necessary to obtain permission to reuse this article or its components as it is available under the terms of the Creative Commons Attribution 4.0 International license. This license permits unrestricted use, distribution, and reproduction in any medium, provided attribution to the author(s) and the published article's title, journal citation, and DOI are maintained. Please note that some figures may have been included with permission from other third parties. It is your responsibility to obtain the proper permission from the rights holder directly for these figures. (statement extracted from the Physical Review Research webpage of this article).

B.2 Increased gap-junction coupling terminates myocardial fibrillation by optimising phase singularity meander-an insilico study

- **Authors:** Max Falkenberg, Alberto Ciacci, Gwyneth Matthews, Jack Way, Balvinder Handa, Li Xinyang, Nicholas S Peters, Fu Siong Ng, Kim Christensen.
- **Journal:** The manuscript is about to be submitted to a scientific journal.
- **Personal contributions:** As primary co-author, I provided a broad contribution to this project by focusing on several major tasks such as the development of the underlying theory, the development of computational models and tools, computer-based simulations, presentation of the experimental results and writing of the manuscript. Note that the phase-singularities detection algorithm was previously described and used in [314].

- **Sections and subsections containing text from this work:** 3.6 and related subsections, appendix E and related sections and subsections.
- **Figures extracted from this work:** 3.27, 3.28, 3.29, 3.30 (used with permission from [27]), 3.31, 3.32, 3.33, 3.34, E.1.
- **Alterations to original article:** The ordering of sections and subsections have been altered to fit the structure of this dissertation. Text from the original article has been amended to fit the structure, notations and other aspects of this dissertation.
- **Permissions for reusing text and images:** No permission is required as the manuscript is about to be submitted to a scientific journal. A notable exception is the upper panel of Fig. 3.30, which includes material from [27], see appendix A for details about this specific permission.

B.3 Unified mechanism of local drivers in a percolation model of atrial fibrillation

- **Authors:** Max Falkenberg, Andrew J Ford, Anthony C Li, Robert Lawrence, Alberto Ciacci, Nicholas S Peters, Kim Christensen.
- **Journal:** Physical Review E, 100 (6), 2019.
- **DOI:** <https://doi.org/10.1103/PhysRevE.100.062406>
- **Personal contributions:** As secondary co-author, I specifically focused on the theoretical foundations of the model and the writing of certain segments of the manuscript.
- **Sections and subsections containing text from this work:** 3.3.3, 3.7 and related subsections, appendix F and related sections and subsections.
- **Figures extracted from this work:** 3.35, 3.36, 3.37, 3.38, 3.39 (used with permission from [29]), 3.40, F.1, F.2, H.2, F.4.
- **License:** Creative Commons Attribution 4.0 International license.
- **License url:** <https://creativecommons.org/licenses/by/4.0/>

- **Alterations to original article:** The ordering of sections and subsections have been altered to fit the structure of this dissertation. Text from the original article has been amended to fit the structure, notations and other aspects of this dissertation.
- **Permissions for reusing text and images:** It is not necessary to obtain permission to reuse this article or its components as it is available under the terms of the Creative Commons Attribution 4.0 International license. This license permits unrestricted use, distribution, and reproduction in any medium, provided attribution to the author(s) and the published article's title, journal citation, and DOI are maintained. Please note that some figures may have been included with permission from other third parties. It is your responsibility to obtain the proper permission from the rights holder directly for these figures (statement extracted from the Physical Review E webpage of this article).

B.4 The microscopic relationships between triangular arbitrage and cross-currency correlations in a simple agent based model of foreign exchange markets

- **Authors:** Alberto Ciacci, Takumi Sueshige, Hideki Takayasu, Kim Christensen, Misako Takayasu.
- **Journal:** PLoS one, 15 (6), 2020.
- **DOI:** <https://doi.org/10.1371/journal.pone.0234709>
- **Personal contributions:** As primary co-author, I provided a broad contribution to this project by focusing on several major tasks such as the development of the underlying theory, the development of computational models and tools, computer-based simulations, presentation of the experimental results and writing of the manuscript.
- **Sections and subsections containing text from this work:** 4.2.3, 4.4.3, 4.5 and related subsections, section C.1.1 and related subsections in appendix C and appendix G and related sections and subsections.

- **Figures extracted from this work:** 4.3, 4.5, 4.6, 4.7, 4.8, 4.9, 4.10, 4.11, 4.12, 4.13, 4.14, 4.15, 4.16, 4.17, 4.18, 4.19, C.1, G.1, G.2, G.3, G.4, G.5, G.6.
- **License:** Creative Commons Attribution 4.0 International license.
- **License url:** <https://creativecommons.org/licenses/by/4.0/>
- **Alterations to original article:** The ordering of sections and subsections have been altered to fit the structure of this dissertation. Text from the original article has been amended to fit the structure, notations and other aspects of this dissertation.
- **Permissions for reusing text and images:** This is an open access article distributed under the terms of the Creative Commons Attribution License, which permits unrestricted use, distribution, and reproduction in any medium, provided the original author and source are credited (statement extracted from the PLoS One webpage of this article).

B.5 Liquidity Fluctuations and the Latent Dynamics of Price Impact

- **Authors:** Luca Philippe Mertens, Alberto Ciacci, Fabrizio Lillo, Giulia Livieri.
- **Journal:** Quantitative Finance, 1-21, 2021.
- **Journal website:** <https://www.tandfonline.com/>
- **Required Acknowledgment:**

“This is an ‘Original Manuscript’ of an article published by Taylor & Francis Group in Quantitative Finance on 19 Jul 2021, available online: <https://doi.org/10.1080/14697688.2021.1947511>”

- **Personal contributions:** As primary co-author, I provided a broad contribution to this project by focusing on several major tasks such as the development of the underlying theory, the development of computational models and tools, computer-based simulations, presentation of the experimental results and writing of the manuscript. Note that a seminal version of the model introduced in this paper was proposed by Luca Philippe Mertens in an earlier preprint. We introduce a variety of changes to that model, most notably, the ability to disentangle the intraday pattern of price impact.

- **Sections and subsections containing text from this work:** 4.6 and related subsections, section C.1.2 and related subsections in appendix C and appendix H and related section and subsections.
- **Figures extracted from this work:** 4.20, 4.21, 4.22, 4.23, 4.24, 4.25, 4.26, H.1, H.2, H.3
- **Alterations to original article:** The ordering of sections and subsections have been altered to fit the structure of this dissertation. Text from the original article has been amended to fit the structure, notations and other aspects of this dissertation. These modifications do not alter the results and the overall message of the original article.
- **Permissions for reusing text and images:** I forwarded a formal request to Taylor & Francis to obtain the required permissions to re-use the contents of this article. My request was followed by direct discussions in which I obtained permissions to re-use and amend the most recent submitted version, i.e., the “Original Manuscript”. The official license terms reported below:

We will be pleased to grant permission to reproduce your article as it was originally submitted to the journal on the condition that you make the following acknowledgement:

“This is an ‘Original Manuscript’ of an article published by Taylor & Francis Group in Quantitative Finance on 19 Jul 2021, available online:

<https://doi.org/10.1080/14697688.2021.1947511>”

You will also need to obtain permission from any co-author’s of this article.

Please note we are unable to grant you permission to include the final accepted version within the 18 month embargo period.

Please note: This does not allow the use of the Version of Record (VoR) to be posted online, however you may include the VoR as an Appendix to the printed version of your thesis / dissertation. (The Version of Record (VoR) is the final, definitive, citable version of your paper, which has been copyedited, typeset, had metadata applied, and has been allocated a DOI; the PDF version on Taylor Francis Online)

Using a DOI to link to the VoR on Taylor Francis Online means that downloads, Altmetric data, and citations can be tracked and collated – data you can use

to assess the impact of your work.

This permission does not cover any third party copyrighted work which may appear in the material requested.

Appendix C

Data description and access

Note

This appendix includes text and images that have been extracted, with any eventual alteration and extension, from articles I have co-authored [34] and [345]. This material appears in the following subsections:

- C.1.1 (from [34])
- C.1.2 (from [345])

Details on copyrights, permissions and personal contributions to [34] and [345] are reported in appendices B.4 and 4.6, respectively.

Note that for copyrights reasons material appearing in appendix C.1.2 is extracted from [345], which is the latest pre-print preceding [37], i.e., the published version.

C.1 Introduction

Modern financial markets are extremely complex systems in which a myriad of agents exchange financial instruments by submitting buy and sell orders in an electronic queueing system, i.e., the LOB. In a recent report [419], Bank of International Settlement (BIS henceforth) report that the price discovery process in equity, futures and certain segments of currency and bond markets is substantially driven by sophisticated and fast algorithmic strategies that actively interact with the LOB. These systems rely on fast data feeds and are capable of reacting to

the most recent market event, e.g., by deleting or submitting a limit order, in extremely short time windows. To put this into context, a restricted pool of participants in the EBS market, i.e., an important inter-dealer market for currency spot trading, are able to receive feed updates every 5ms (milliseconds) since early 2017 [419] while recent data reveals that *high frequency trading* firms (HFTs henceforth), i.e., companies adopting state-of-art technology to support extremely fast trading, are able to act within time windows that are substantially shorter than $100\mu\text{s}$ (microseconds) [420].

The afore discussed scenario clearly suggest that a significant fraction of financial ecosystems are populated by sophisticated agents interacting at a very intense pace. The characteristic time scales of contemporary electronic trading are way beyond human perception, hence, these systems cannot be analyzed without accessible records of the long sequence of events, e.g., a submission of a limit order, that govern the regular trading activity across the globe [421]. Luckily, the technological progresses of the last decades have significantly weakened various barriers in the collection, processing and distribution of granular trading data, thus offering practitioners, academics and regulators the possibility of examining the microscopic dynamics of financial markets.

As discussed in the LOBSTER white paper [421], a practicable, yet non-trivial approach to the construction of a ready-to-use limit order book dataset consists in i) obtaining compressed raw message streams data, such as the ITCH protocol, reporting the entire flow of orders submissions, executions and deletions and ii) embarking in the arduous challenge of reconstructing the dynamics of the LOB from this data stream. A typical layout of the outcome of this procedure include a *message file* in which the i -th row reports an event, e.g., a buy limit order execution of k units at time t , and an *orderbook file* in which the i -th row displays the state of the LOB, e.g., best bid price b_t with volume V_t^b and best ask price a_t with volume V_t^a , before or after the i -th event, see [421] for example. The terms of the agreement between providers and their clients regulate the amount of information that end-users can access from reconstructed LOB data. The quality and costs of this product are the resultant of many underlying variables, such as the overall correctness of the reported information, the number of available markets and products, the covered time window and the available depth, i.e., the number of LOB levels. In the following appendices we introduce two LOB data sets that have been used in the analyses presented in this dissertation. Appendix C.1.1 examines the Electronic Broking Services Ultra, a real-time feed of foreign exchange spot prices recorded in the Electronic Broking Services

Market, i.e., a longstanding and dominant platform for accessing liquidity in several currency markets [422, 423]. Appendix C.1.2 discusses LOBSTER, an online data provider specializing in the reconstruction of NASDAQ Historical TotalView-ITCH files¹ into accessible data sets reporting the flow of limit order submissions, cancellations and executions and the event-by-event evolution of the LOB state for every stock traded on the NASDAQ [424].

C.1.1 The Electronic Broking Services market dataset

Overview

Electronic Broking Services (EBS henceforth) is an important inter-dealer electronic platform for FX spot trading [376]. Trading is organized in LOBs and estimates suggest that approximately 70% of the orders are posted by algorithms [376]. The empirical analysis presented in this thesis is based on highly granular LOB data provided by EBS. We cover three major FX rates, USD/JPY, EUR/USD and EUR/JPY, across four years of trading activity (2011-2014). The EBS dataset provides a 24-7 coverage of the trading activity (from 00:00:00.000 GMT Monday to 23:59:59.999 GMT Sunday included), thus offering a complete and uninterrupted record of the flow of submissions, executions and deletions occurring in the first ten price levels of the bid and ask sides of the LOB, see table C.1 for further details. The shortest time

Date	Timestamp	Market	Event	Direction	Depth	Price	Volume
2011-05-10	09.00.00.000	USD/JPY	Deal	Buy	1st	100.000	1
⋮	⋮	⋮	⋮	⋮	⋮	⋮	⋮
2011-10-21	21.00.00.000	EUR/USD	Quote	Ask	3rd	0.8000	5

Table C.1: **EBS dataset structure.** Each record (i.e., row) corresponds to a specific market event. Records are reported in chronological order (top to bottom) and include the following details: i) date (yyyy-mm-dd), ii) timestamp (GMT), iii) the market in which the event took place, iv) event type (submission (Quote) or execution (Deal) of visible or hidden limit orders), v) direction of limit orders (Buy/Sell for deals and Bid/Ask for quotes), vi) depth (number of occupied levels) between the specified price and the best price, vii) price and viii) units specified in the limit order.

¹For further details see <http://nasdaqtrader.com/Trader.aspx?id=ITCH>

window between consecutive records is 100 millisecond (ms). Events occurring within 100 ms are aggregated and recorded at the nearest available timestamp. The tick size has changed two times within the considered four years window, see [387] and table C.2 for further details. The EBS dataset, in virtue of its features, is a reliable source of granular market data. First,

Initial Month	USD/JPY	EUR/USD	EUR/JPY
2011-03	0.01	0.0001	0.01
2012-09	0.001	0.00001	0.001
-	0.005	0.00005	0.005

Table C.2: **Tick sizes adopted in the EBS market.** EBS has changed the tick size twice in the period between January 1st 2011 and December 31st 2014. The table reports the initial month (yyyy-mm) of each implementation period (first column) and the corresponding tick size in the USD/JPY (second column), EUR/USD (third column) and EUR/JPY (fourth column) markets. See [387] for further details.

EBS directly collects data from its own trading platform. This prevents the common issues associated to the presence of third parties during the recording process, such as interpolations of missing data and input errors (e.g., incorrect timestamps or order types). Second, the EBS dataset offers a continuous record of LOB events across a wide spectrum of currencies, thus becoming a natural choice for cross-sectional studies (e.g., triangular arbitrage or correlation networks). Third, in spite of the increasing competition, the EBS platform has remained a key channel for accessing FX markets for more than two decades by connecting traders across more than 50 countries [425, 422]. The enduring relevance of this platform has been guaranteed by the fairness and the competitiveness of the quoted prices.

Access

The raw data used in appendices C.1.1 and G and section 4.5 was purchased from EBS Service Company Limited, with no special access privileges. Since EBS Service Company Limited created this dataset for sales purpose, the contract between EBS Service Company Limited and the authors does not allow to distribute data samples. Those researchers interested in analyzing historical data of the EBS Market are advised to contact EBS Service Company Limited at the following website: <https://www.cmegroup.com/tools-information/contacts-list/ebs-support.html>.

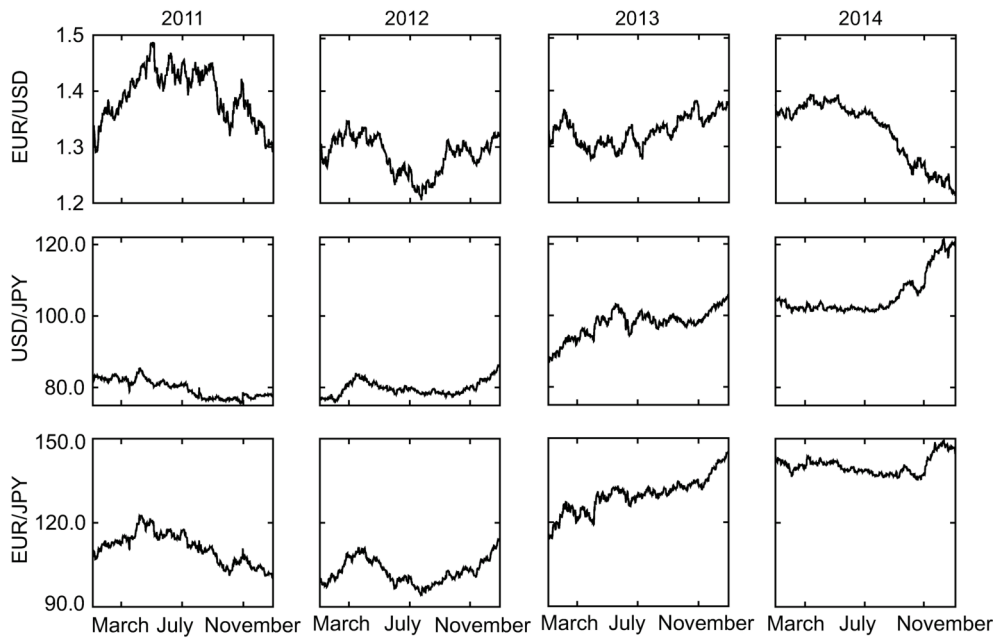


Figure C.1: **Mid price patterns.** The panels show the dynamics of the mid price between January 1st 2011 and December 31st 2014 in the EUR/USD (top panels), USD/JPY (middle panels) and EUR/JPY (bottom panels) markets. This figure has been extracted from [34], see appendix B.4 for details about attributions and permissions.

To access the dataset employed in appendices C.1.1 and G and section 4.5, researchers should discuss the availability and sales of historical limit order book data of the EUR/USD, USD/JPY and EUR/JPY EBS spot FX markets between January 1st 2011 and December 31st 2014.

C.1.2 LOBSTER dataset

Overview

We use data collected from the NASDAQ Historical TotalView-ITCH and extracted through LOBSTER [421]. The dataset contains the history of all trades, orders and cancellations submitted at the best quotes to the NASDAQ stock exchange during standard trading hours². On the NASDAQ platform each stock is traded in a separate LOB with price-time priority and a tick size of $\delta = \$0.01$. Although this tick size is the same for all stocks, the prices of different stocks vary across several orders of magnitude. As it is customary on the financial literature, we refer to *large-tick stocks* if the ratio between δ and the average stock price, i.e. the *relative*

²NASDAQ standard trading hours are between 09:30 and 16:00 EST.

tick size, is large and to *small-tick stocks* if this quantity is small. The model of Cont *et al.* [36] is particularly suitable for large-tick assets because small tick assets are characterized by small queues and sparse LOB [401, 426]. Thus, all our developments are illustrated on five specific examples of large-tick stocks from the NASDAQ 100 index: Microsoft Corp (MSFT henceforth), Comcast Corp (CMCSA henceforth), Intel Corp (INTC henceforth), Cisco System Inc (CSCO henceforth), Apple Inc. (AAPL henceforth). The relative tick sizes spans between 4.27 and 1.36 basis points. Dates range from January 4th 2016 to June 30th 2016, for a total of 125 days. The average mid-price of each stock along with its standard deviation over the sample period is reported in the third column of table C.3. The fifth and seventh column of table C.3 outline time-weighted bid-ask spreads in dollars and as a percentage of the prevailing quoted midpoint³. Table C.4 presents more detailed summary statistics for the covered LOBs. Limit orders, market orders and cancellations are reported both in terms of number of events, i.e., #Ev., and of average volume, i.e., Avg.Vol. We observe higher activities in limit orders and cancellations than in market orders. Moreover the activity on the ask and the bid side of the LOBs is quite symmetric.

Stock	Ticker	Mid-price		Spread		Relative Spread	
		Avg.	Std	Avg.	Std	Avg.	Std
Cisco System Inc	CSCO	26.910	1.870	0.011	0.000	4.27	0.35
Intel Corp	INTC	30.994	1.209	0.012	0.000	3.74	0.21
Microsoft Corp	MSFT	52.150	1.819	0.012	0.000	2.35	0.10
Comcast Corp	CMCSA	59.779	2.896	0.013	0.000	2.10	0.14
Apple Inc.	AAPL	99.502	5.463	0.013	0.001	1.36	0.11

Table C.3: **Descriptive statistics for the investigated NASDAQ prices time series.** The sample period spans between January 4th 2016 to June 30th 2016. Mid-price and Spread are reported in dollar unit (\$). The Relative Spread is reported in basis point unit. Stocks are sorted by average price or by spread, i.e. inversely by relative tick size.

³We note, however, that spreads calculated on displayed liquidity may overestimate the effective spreads actually paid or received due to non-displayed orders. On NASDAQ non-displayed orders are not visible until executed.

Symbol	Bid $Q_{1,\ell}$		Ask $Q_{1,\ell}$	
	#Ev.	Avg.Vol.	#Ev.	Avg.Vol.
CSCO	83746.38	1004.59	85574.85	1018.82
INTC	107735.19	1027.75	109450.99	1052.25
MSFT	190464.74	1776.54	190903.58	1755.47
CMCSA	90841.02	715.31	91874.22	724.14
AAPL	206612.51	2460.25	210055.42	2507.16

Symbol	Bid $Q_{1,c}$		Ask $Q_{1,c}$	
	#Ev.	Avg.Vol.	# Ev.	Avg.Vol.
CSCO	69306.98	809.28	71667.87	823.32
INTC	89663.46	824.30	91820.30	849.24
MSFT	154535.32	1351.72	156275.93	1355.95
CMCSA	74455.99	561.90	76142.54	575.87
AAPL	183007.70	2091.56	185826.46	2137.03

Symbol	Bid $Q_{1,m}$		Ask $Q_{1,m}$	
	#Ev.	Avg.Vol.	#Ev.	Avg.Vol.
CSCO	7481.11	54.04	10983.63	70.47
INTC	9429.46	60.24	12460.66	76.54
MSFT	18022.72	141.13	23296.63	196.48
CMCSA	9460.17	62.16	11637.26	80.69
AAPL	21011.42	247.76	25953.06	320.13

Table C.4: **Sample statistics for the investigated NASDAQ limit order books.** The sample period spans between January 4th 2016 to June 30th 2016. Top table: the amount of limit orders at the best bid (Bid $Q_{1,\ell}$) and ask (Ask $Q_{1,\ell}$). Mid table: the amount of cancellations of bid limit orders (Bid $Q_{1,c}$) and ask limit orders (Ask $Q_{1,c}$). Bottom table: the amount of sell market orders (Bid $Q_{1,m}$) and buy market orders (Ask $Q_{1,m}$). Quantities are characterized in term of both number of events (#Ev.) and average volume (Avg.Vol.) measured in number of shares.

Access

The raw data used in appendices C.1.2 and H and section 4.6 was provided by the CFM-Imperial Institute of Quantitative Finance at Imperial College London. To access the dataset employed in appendices C.1.2 and H and section 4.6, researchers should contact the the CFM-Imperial Institute of Quantitative Finance, see <https://www.imperial.ac.uk/quantitative-finance/>, or the data provider LOBSTER, see <https://lobsterdata.com/>.

Appendix D

Supplementary materials for sections 3.4.2 and 3.5

Note

This appendix includes text and images that have been extracted, with any eventual alteration and extension, from an article I have co-authored [20]. This material appears in the following sections:

- D.1
- D.2
- D.3
- D.4.

Details on copyrights, permissions and personal contributions to [20] are reported in appendix B.1.

D.1 Activation maps for critical structures appearing in Fig. 3.14

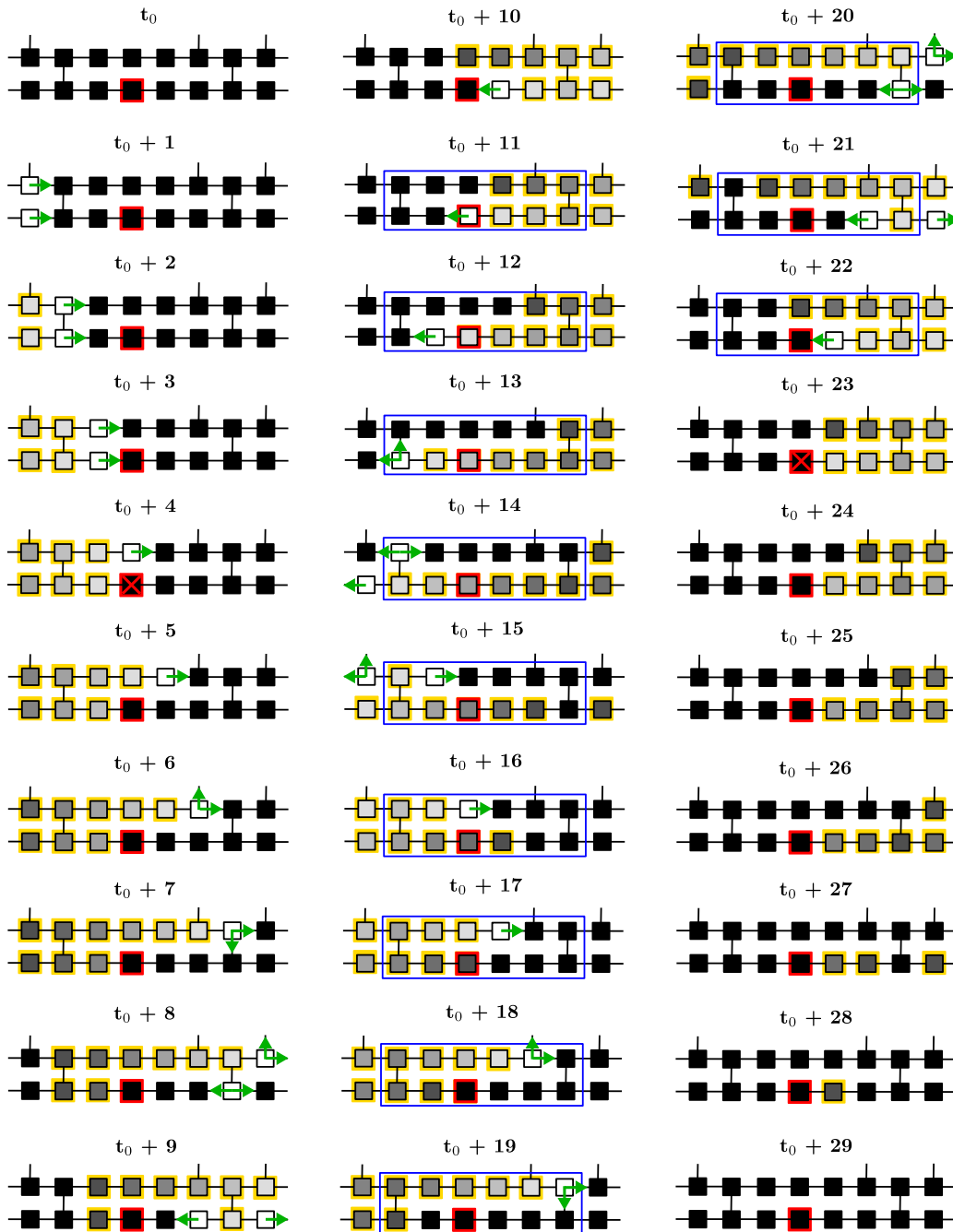


Figure D.1: **Activation and deactivation of the critical structure presented in Fig. 3.14 (a).** Resting cells are shown in black. Excited cells are shown in white. Refractory cells are shown in grey-scale with a yellow border. Green arrows indicate the movement of the excitation wavefront. Red bordered cells are susceptible to conduction block. A red cross indicates that a cell susceptible to conduction block has failed to activate when prompted to do so by a neighbour. The blue box indicates the region corresponding to an active re-entrant circuit. This figure has been extracted from [20] see appendix B.1 for details about attributions and permissions.



Figure D.2: **Activation and deactivation of the critical structure presented in Fig. 3.14 (b).** Resting cells are shown in black. Excited cells are shown in white. Refractory cells are shown in grey-scale with a yellow border. Green arrows indicate the movement of the excitation wavefront. Red bordered cells are susceptible to conduction block. A red cross indicates that a cell susceptible to conduction block has failed to activate when prompted to do so by a neighbour. The blue box indicates the region corresponding to an active re-entrant circuit. This figure has been extracted from [20], see appendix B.1 for details about attributions and permissions.

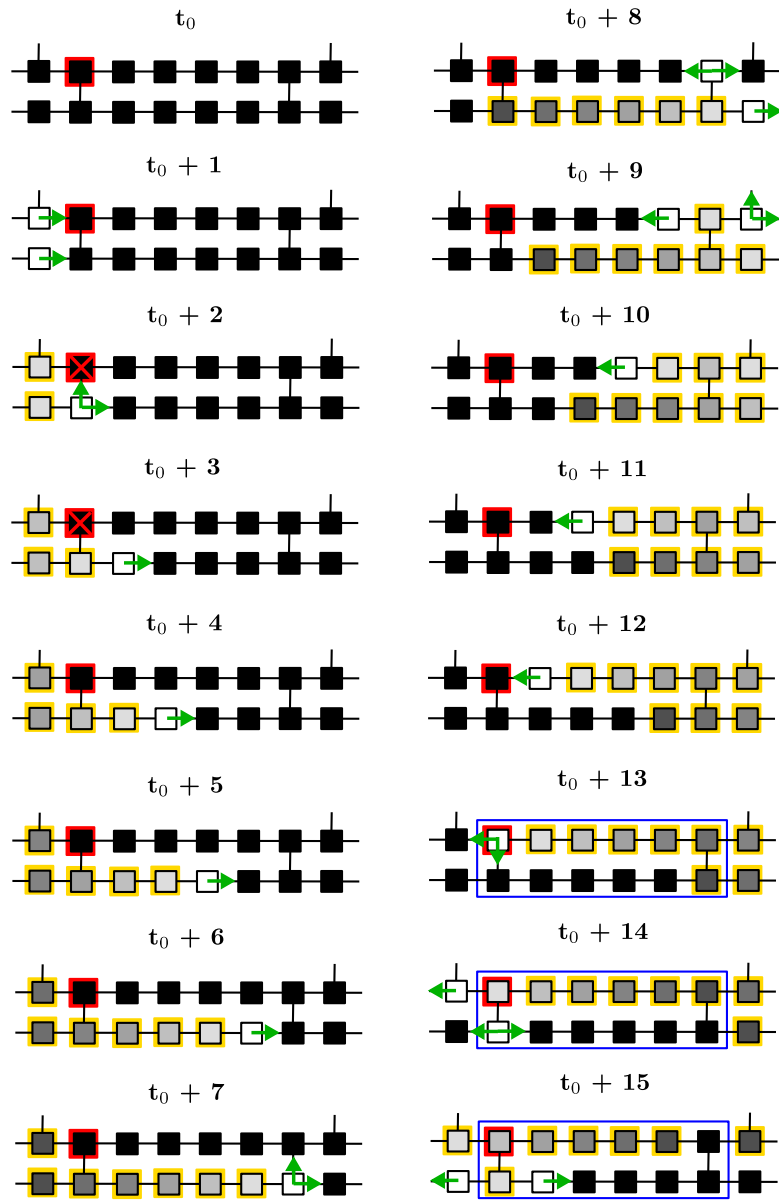


Figure D.3: **Successful activation of the critical structure presented in Fig. 3.14 (c).** Resting cells are shown in black. Excited cells are shown in white. Refractory cells are shown in grey-scale with a yellow border. Green arrows indicate the movement of the excitation wavefront. Red bordered cells are susceptible to conduction block. A red cross indicates that a cell susceptible to conduction block has failed to activate when prompted to do so by a neighbour. The blue box indicates the region corresponding to an active re-entrant circuit. This figure has been extracted from [20], see appendix B.1 for details about attributions and permissions.

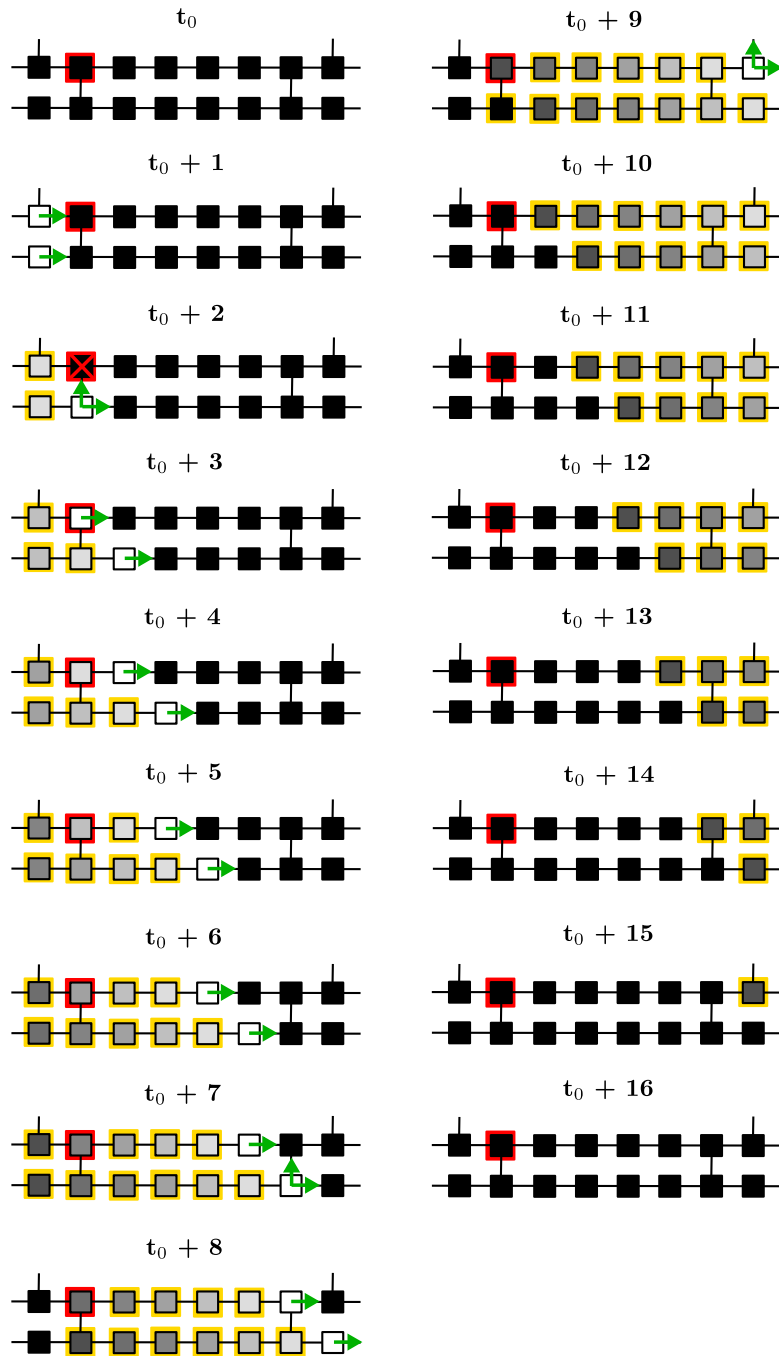


Figure D.4: **Failed activation of the critical structure presented in Fig. 3.14 (c).** Resting cells are shown in black. Excited cells are shown in white. Refractory cells are shown in grey-scale with a yellow border. Green arrows indicate the movement of the excitation wavefront. Red bordered cells are susceptible to conduction block. A red cross indicates that a cell susceptible to conduction block has failed to activate when prompted to do so by a neighbour. The blue box indicates the region corresponding to an active re-entrant circuit. This figure has been extracted from [20], see appendix B.1 for details about attributions and permissions.

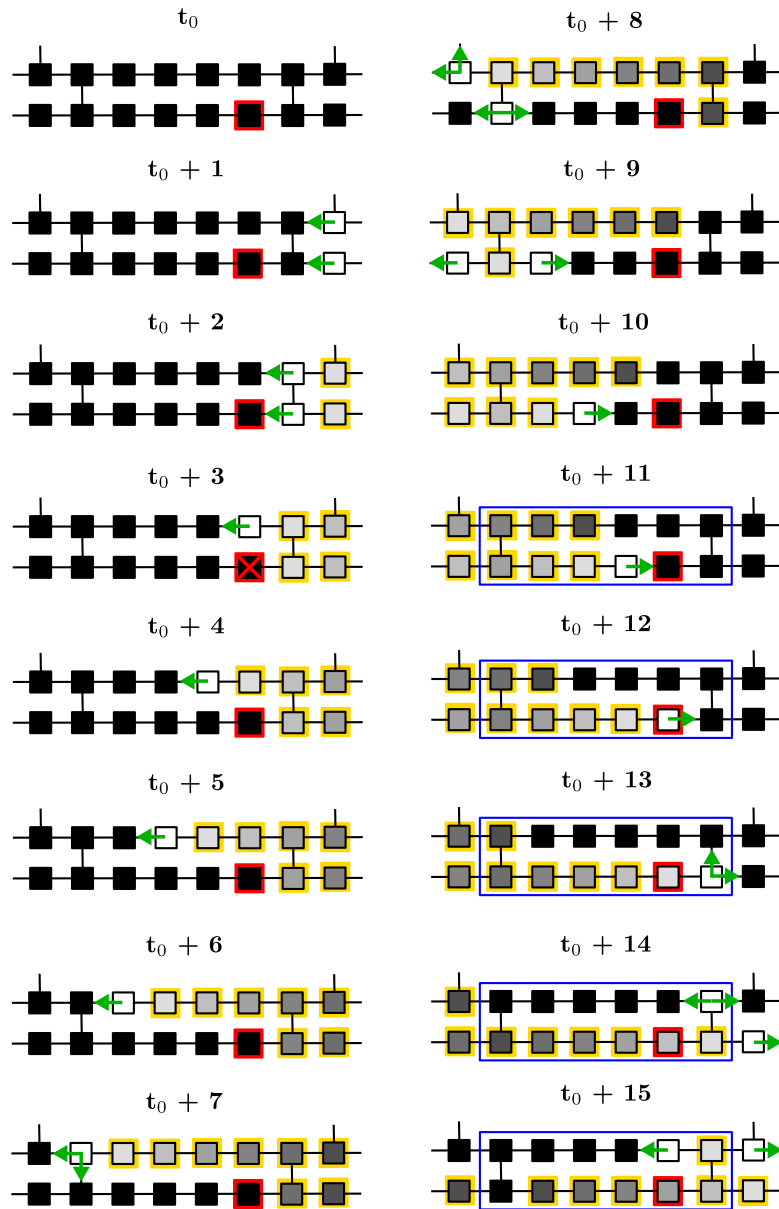


Figure D.5: **Successful activation of the critical structure presented in Fig. 3.14 (d).** Resting cells are shown in black. Excited cells are shown in white. Refractory cells are shown in grey-scale with a yellow border. Green arrows indicate the movement of the excitation wavefront. Red bordered cells are susceptible to conduction block. A red cross indicates that a cell susceptible to conduction block has failed to activate when prompted to do so by a neighbour. The blue box indicates the region corresponding to an active re-entrant circuit. This figure has been extracted from [20], see appendix B.1 for details about attributions and permissions.

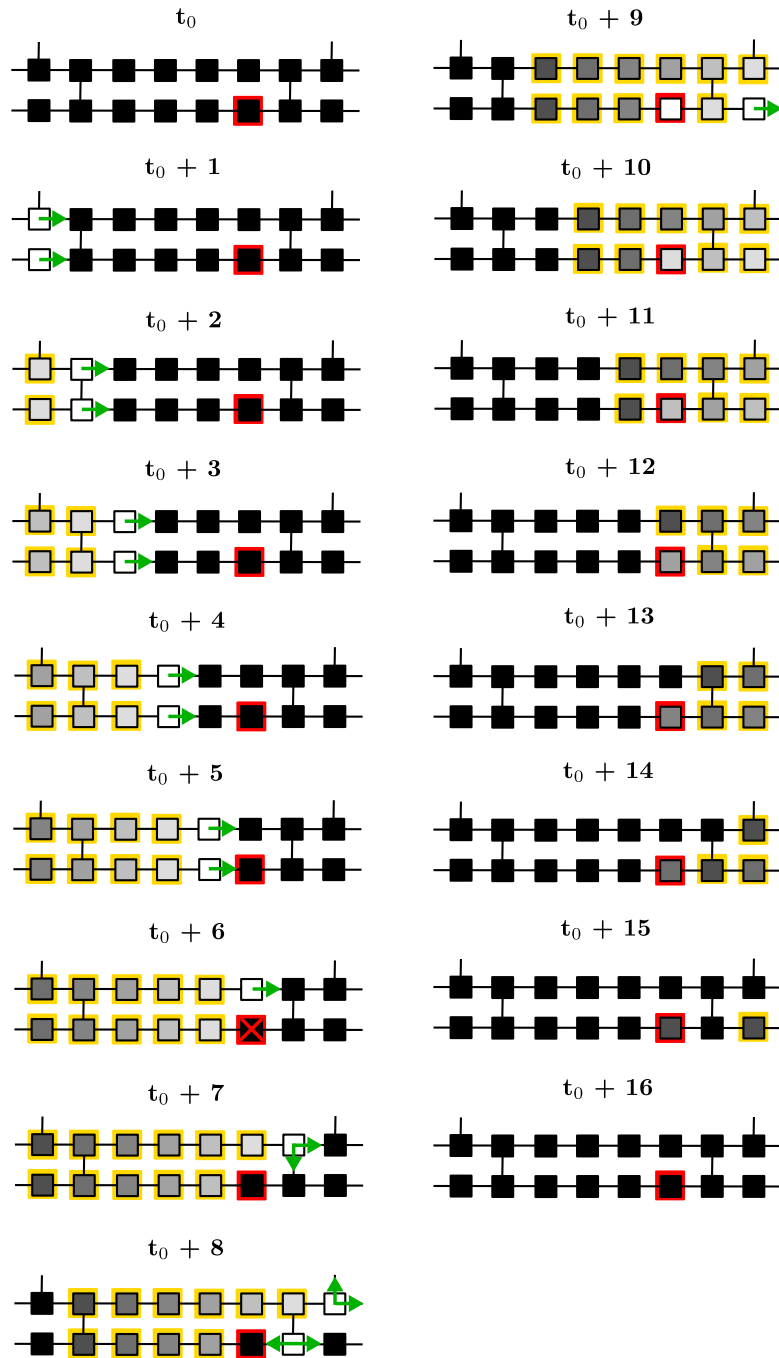


Figure D.6: **Failed activation of the critical structure presented in Fig. 3.14 (d).** Resting cells are shown in black. Excited cells are shown in white. Refractory cells are shown in grey-scale with a yellow border. Green arrows indicate the movement of the excitation wavefront. Red bordered cells are susceptible to conduction block. A red cross indicates that a cell susceptible to conduction block has failed to activate when prompted to do so by a neighbour. The blue box indicates the region corresponding to an active re-entrant circuit. This figure has been extracted from [20], see appendix B.1 for details about attributions and permissions.

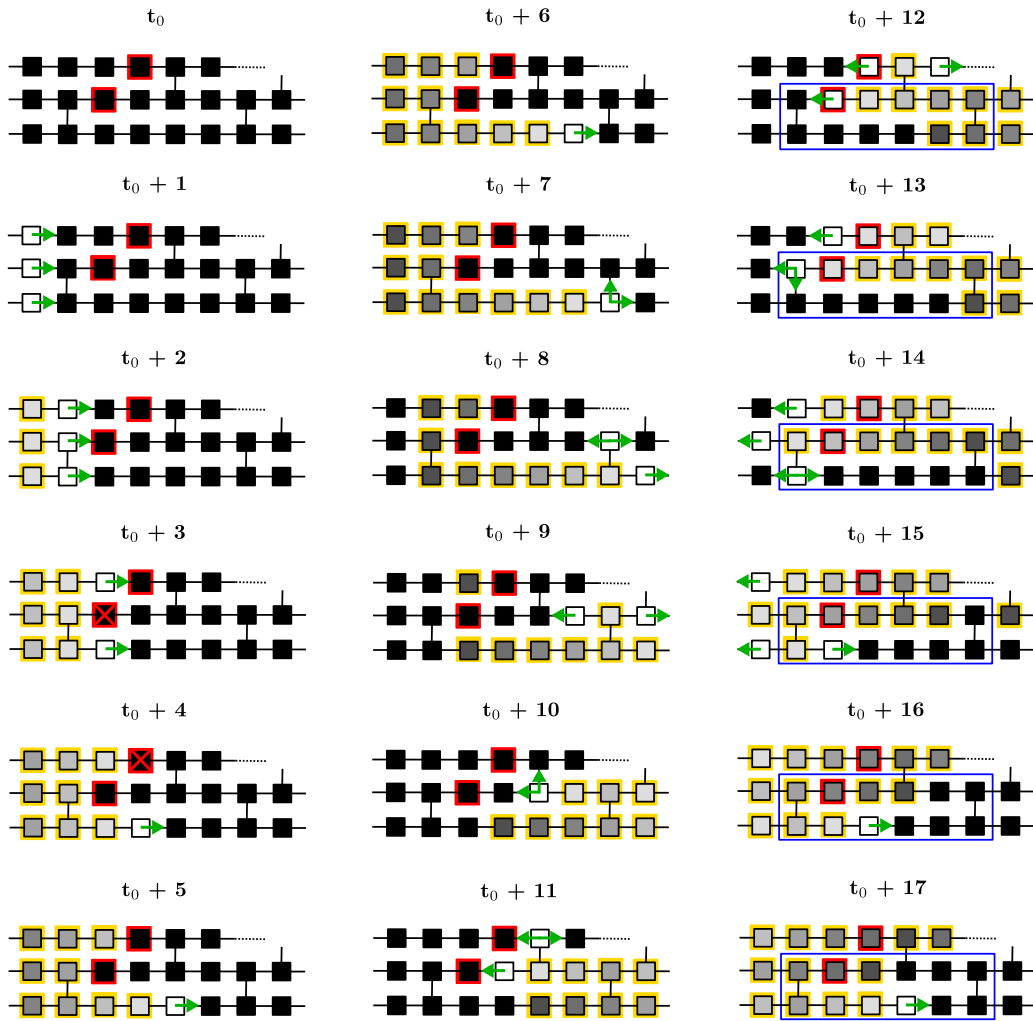


Figure D.7: **Successful activation of the critical structure presented in Fig. 3.14 (e).** Resting cells are shown in black. Excited cells are shown in white. Refractory cells are shown in grey-scale with a yellow border. Green arrows indicate the movement of the excitation wavefront. Red bordered cells are susceptible to conduction block. A red cross indicates that a cell susceptible to conduction block has failed to activate when prompted to do so by a neighbour. The blue box indicates the region corresponding to an active re-entrant circuit. This figure has been extracted from [20], see appendix B.1 for details about attributions and permissions.

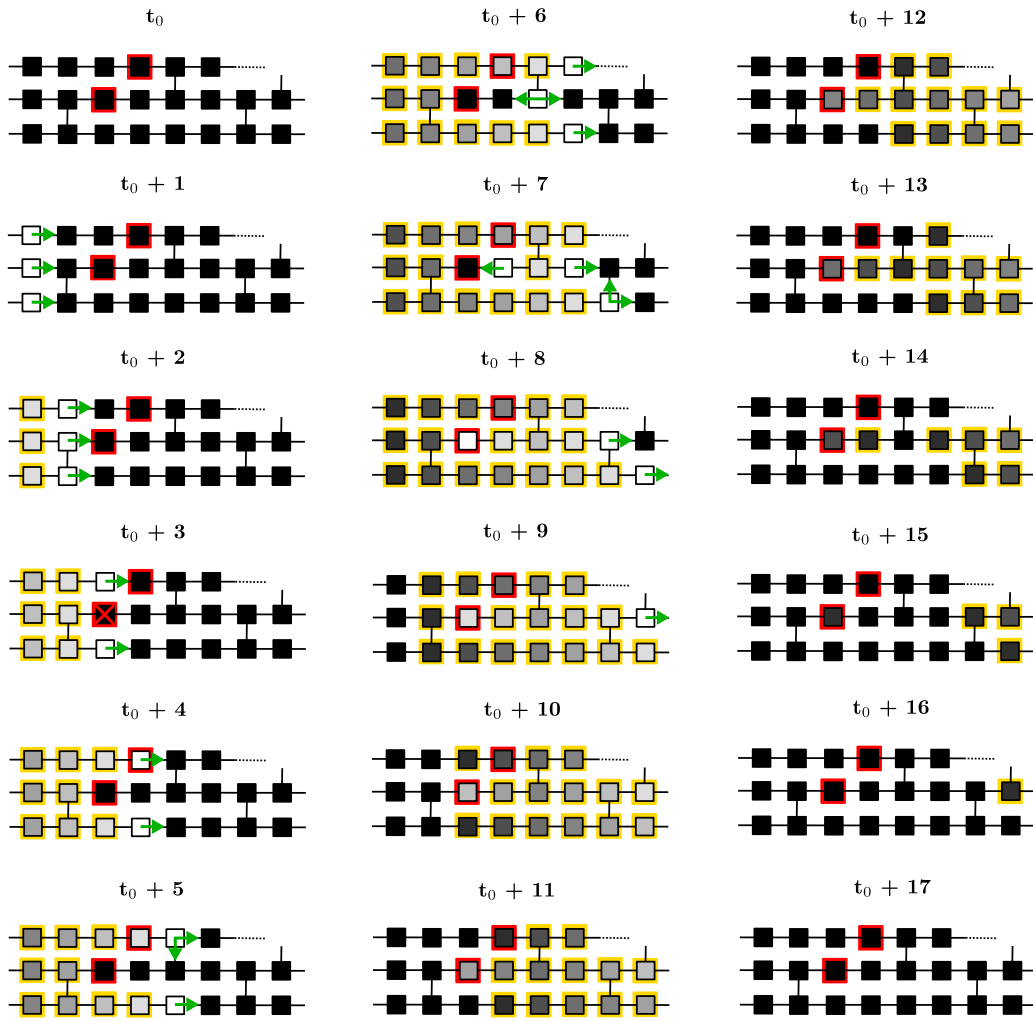


Figure D.8: **Failed activation of the critical structure presented in Fig. 3.14 (e).** Resting cells are shown in black. Excited cells are shown in white. Refractory cells are shown in grey-scale with a yellow border. Green arrows indicate the movement of the excitation wavefront. Red bordered cells are susceptible to conduction block. A red cross indicates that a cell susceptible to conduction block has failed to activate when prompted to do so by a neighbour. The blue box indicates the region corresponding to an active re-entrant circuit. This figure has been extracted from [20], see appendix B.1 for details about attributions and permissions.

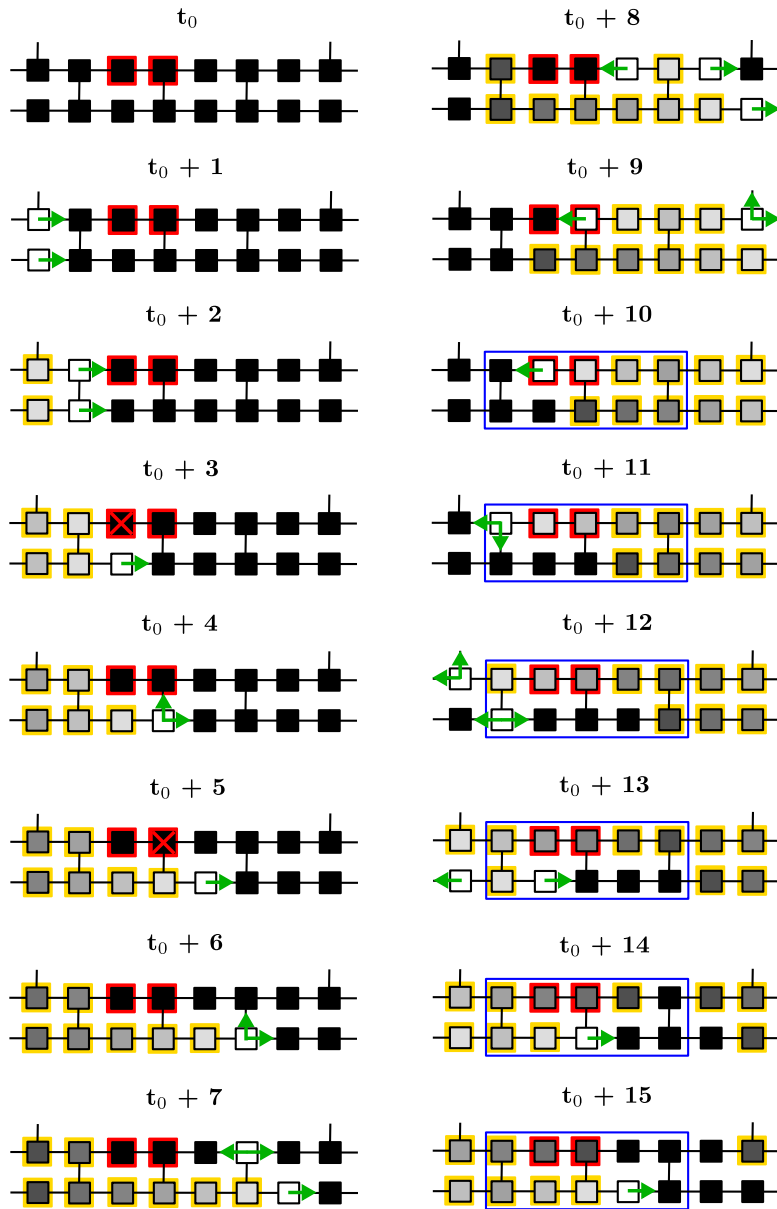


Figure D.9: **Successful activation of the critical structure presented in Fig. 3.14 (f).** Resting cells are shown in black. Excited cells are shown in white. Refractory cells are shown in grey-scale with a yellow border. Green arrows indicate the movement of the excitation wavefront. Red bordered cells are susceptible to conduction block. A red cross indicates that a cell susceptible to conduction block has failed to activate when prompted to do so by a neighbour. The blue box indicates the region corresponding to an active re-entrant circuit. This figure has been extracted from [20], see appendix B.1 for details about attributions and permissions.

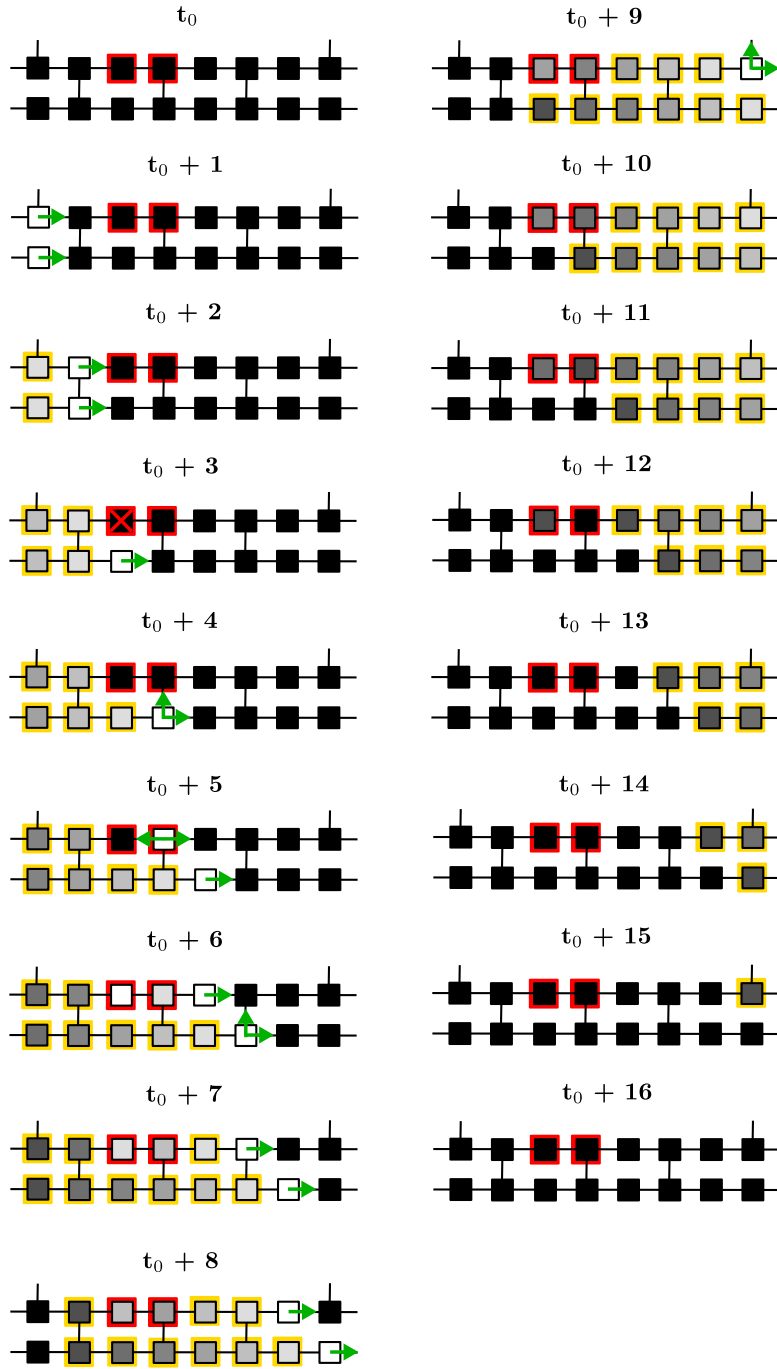


Figure D.10: **Failed activation of the critical structure presented in Fig. 3.14.** Resting cells are shown in black. Excited cells are shown in white. Refractory cells are shown in grey-scale with a yellow border. Green arrows indicate the movement of the excitation wavefront. Red bordered cells are susceptible to conduction block. A red cross indicates that a cell susceptible to conduction block has failed to activate when prompted to do so by a neighbour. The blue box indicates the region corresponding to an active re-entrant circuit. This figure has been extracted from [20], see appendix B.1 for details about attributions and permissions.

D.2 Activation maps for critical structures appearing in Figs. 3.23-3.24



Figure D.11: Activation and deactivation of the complex critical structure presented in Fig. 3.23. Resting cells are shown in black. Excited cells are shown in white. Refractory cells are shown in grey-scale with a yellow border. Green arrows indicate the movement of the excitation wavefront. Red bordered cells are susceptible to conduction block. A red cross indicates that a cell susceptible to conduction block has failed to activate when prompted to do so by a neighbour. The blue box indicates the region corresponding to an active re-entrant circuit. This figure has been extracted from [20], see appendix B.1 for details about attributions and permissions.



Figure D.12: Sequence of activations of the coupled re-entrant circuits presented in Fig. 3.24. Resting cells are shown in black. Excited cells are shown in white. Refractory cells are shown in grey-scale with a yellow border. Green arrows indicate the movement of the excitation wavefront. Red bordered cells are susceptible to conduction block. A red cross indicates that a cell susceptible to conduction block has failed to activate when prompted to do so by a neighbour. The blue box indicates the region corresponding to an active re-entrant circuit. This figure has been extracted from [20], see appendix B.1 for details about attributions and permissions.

D.3 Activation patterns in the CMP Model

The CMP model is a highly simplified, physics style model of AF, focusing on the initiation and maintenance of micro-anatomical re-entrant circuits. The CMP model does not consider the maintenance of AF from rotors (spiral waves). As a result, the macroscopic activation patterns in the CMP model do not directly reflect what might be observed clinically or in other reaction-diffusion models of fibrillation.

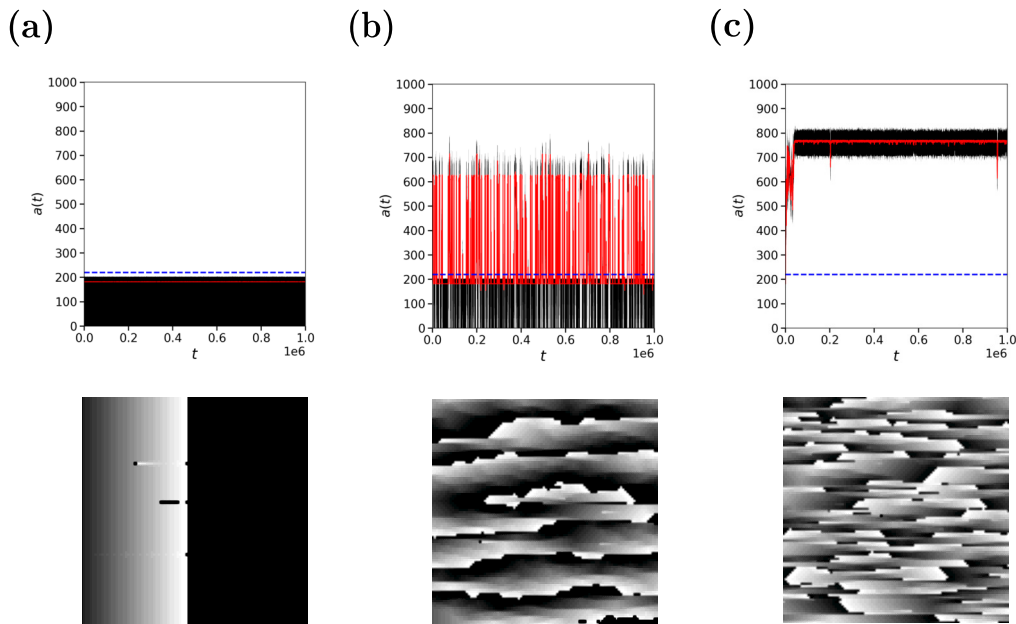


Figure D.13: **Activation patterns in SR, paroxysmal AF and persistent AF.** The number of active cells per time step, $a(t)$; top row, and the corresponding activation patterns observed in a 100×100 snapshot of the CMP model, bottom row, in (a) sinus rhythm, (b) paroxysmal AF, and (c) persistent AF. Active nodes are shown in white, refractory in greyscale, and resting in black. This figure has been extracted from [20], see appendix B.1 for details about attributions and permissions.

Fig. D.13 shows typical activation patterns observed in the CMP model and the corresponding trace of the number of active cells. As expected, in sinus rhythm, the number of active cells is constant and falls below the threshold for AF. When the number of active cells exceeds the AF threshold, we can observe a number of different AF phenotypes in the CMP model from paroxysmal to persistent AF. Qualitatively, the activation patterns in paroxysmal and persistent AF do not show major differences, although persistent AF is typically associated

with a higher dominant frequency of activation. Interestingly, there is some clinical evidence to suggest that increased dominant frequency predicts an increase in the persistence of AF [427]. In Fig. 3.17 (h), an episode of persistent AF is shown where the number of active cells is stable over time. The simulation was generated at $\nu_{\perp} = 0.11$, where the average number of simple structures in the CMP model is $N < 2$, see appendix D.4. This suggests that the example shown in Fig. 3.17(h) could plausibly be the result of one single stable re-entrant circuit (although not a simple one). As a result, this example may be better thought of as a persistent episode of AT rather than AF. However, many examples of persistent AF are also observed in the CMP model where the number of active cells shows frequent fluctuations, but where the activation remains above the AF threshold, see Fig. D.14.

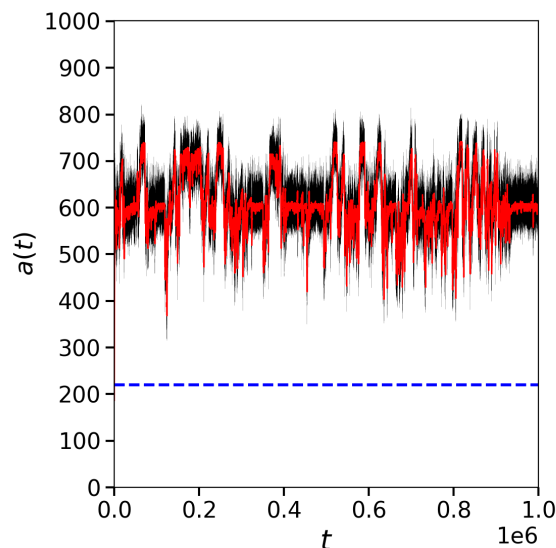


Figure D.14: **An example of persistent AF in the CMP model.** When $\nu_{\perp} = 0.05$ the number of active nodes per time step shows significant fluctuations over time. The black line indicates the raw data, with the red line indicating the moving average over a time window of $T = 220$. The blue dashed line indicates the threshold above which the CMP model is said to be in persistent AF. This figure has been extracted from [20], see appendix B.1 for details about attributions and permissions.

D.4 Correspondence between the number of simple re-entrant circuits and overall coupling

As discussed in section 3.5.4, it is possible to identify the number of simple critical structures, N , regions capable of forming a simple re-entrant circuit, in a given instance of the CMP model. Previously, we have presented the time in AF in the CMP model as a function of the overall coupling ν_{\perp} .

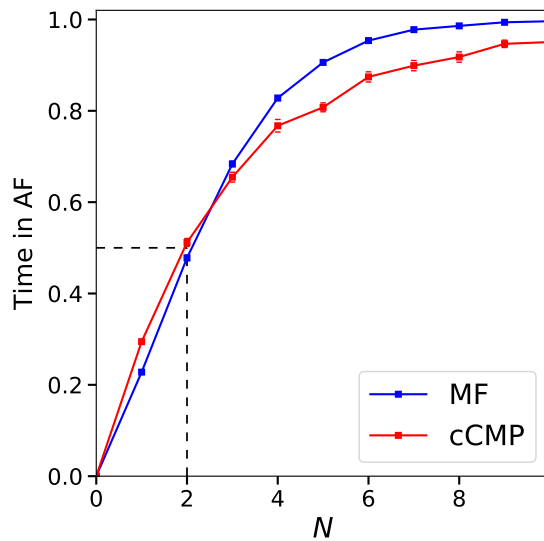


Figure D.15: **Critical structures and time in AF.** The average time in AF for the cCMP (red) and MF (blue) models as a function of (1) the number of tracked simple critical structures N in the cCMP model, or (2) the MF model with the corresponding number of particles. This figure has been extracted from [20], see appendix B.1 for details about attributions and permissions.

In Fig. D.15 we show the time in AF as a function of the number of critical structures, N , identified in the cCMP model where we control the placement of conduction blocking nodes. For each instance of the cCMP model, the corresponding value of N is used to generate a simulation of the MF model. Fig. D.15 demonstrates that at low N ($N < 2$), the time in AF in the cCMP model slightly exceeds the corresponding value of the MF model. In contrast, the converse is observed at large N ($N > 2$) where the time in AF in the MF model exceeds the corresponding value in the cCMP model. This is a consequence of the spatial elements

of the cCMP model which are absent in the MF model. At low N , AF episodes last a little longer in the cCMP model than in the MF model (due to slight differences in the activation and deactivation rates of the models). Conversely, at high N , the activation (or deactivation) of a particle in the MF model is independent of any other particle in the model, whereas in the cCMP model, an active re-entrant circuit can suppress the activation of other critical structures which are longer than the currently active re-entrant circuit. As a result, the time in AF in the cCMP model is above (below) the MF value for low (high) N .

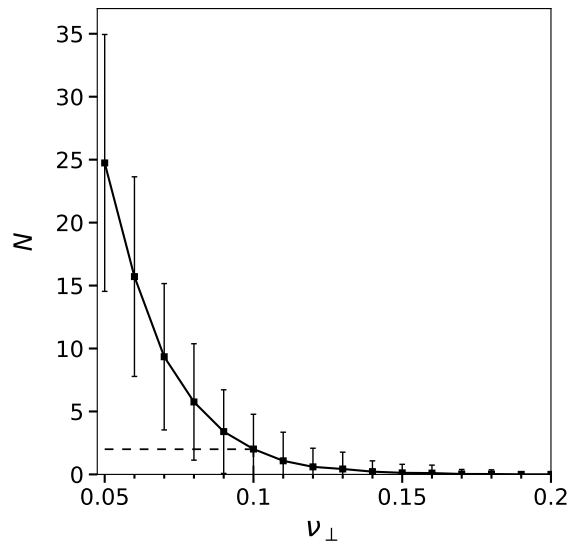


Figure D.16: **The average number of tracked simple critical structures N as a function of the overall coupling value ν_{\perp} in the cCMP model.** The errors bars indicate the 95% confidence interval calculated over 50 simulations. This figure has been extracted from [20], see appendix B.1 for details about attributions and permissions.

Fig. D.16 shows the average number of simple critical structures detected in an instance of the cCMP model as a function of the overall coupling, ν_{\perp} . For Fig. D.16, the error bars have been chosen to show the 95% confidence interval of possible N values at a given coupling value. Fig. D.15 shows that $N \approx 2$ is the crossover value above (below) which the time in AF is larger (smaller) in the MF model than in the cCMP model. Fig. D.16 indicates that $N = 2$ corresponds to a coupling value of $\nu_{\perp} \approx 0.1$. Hence, the small difference in the time in AF shown in Fig. 3.22 can be understood as being a consequence of the slightly different time in AF values at fixed N indicated in Fig. D.15.

Note, if $N = 1$, a single dominant re-entrant circuit drives fibrillation in the CMP model. Hence,

at a simplified level, this can be thought of as a form of atrial tachycardia (AT), however, this is very rare at low coupling. When multiple drivers are competing ($N > 1$), the activity in the CMP model is better associated with AF.

Appendix E

Supplementary materials for section

3.6 ***

Note

This appendix includes text and images that have been extracted, with any eventual alteration and extension, from an article I have co-authored [26]. This material appears in the following sections:

- E.1

Details on copyrights, permissions and personal contributions to [26] are reported in appendix B.2.

E.1 Parameters calibration

To induce fibrillation in the in-silico model, we must define a suitable action potential duration (APD henceforth) restitution curve and an appropriate activation function for the probability of a cell depolarising as a function of its received charge (in dimensionless units). These functions are outlined in Eqs. (3.24) and (3.23).

Calibrating the APD restitution curve and activation probability function is non-trivial given that suitable experimental data for these values during fibrillation and under the action of gap-junction modulation is limited. As a result, several different parameter choices have been tested to demonstrate the robustness of our results.

The first step of model calibration involves defining the time resolution of the model. The lattice defined for simulation purposes has dimensions 70×120 cells, corresponding to approximate tissue dimensions for the experimental rat hearts of $1.4\text{cm} \times 2.4\text{cm}$. Hence, the linear scale of a single cell in the insilico model corresponds to 0.2mm in real space. At baseline, before the infusion of Pinacidil or gap-junction modulation, the approximate macroscopic conduction velocity observed in experimental rat hearts is around $100\text{cm s}^{-1} = 1\text{mm ms}^{-1}$, such that one cell in the insilico model is crossed in approximately $\Delta t = 0.2\text{ms}$. This defines the microscopic timescale of the model. At baseline with a cycle length of around 200ms , the experimental rat hearts have an observed APD of approximately 80ms corresponding to 400 time steps in the insilico model.

With a microscopic conduction velocity in the model of one cell per time step, the observed APD at baseline corresponds to a refractory wavelength of approximately 8 cm , significantly larger than the experimental tissue dimensions. For this reason, fibrillation is only inducible in the model under significant APD restitution both as a result of burst pacing and through the simulated action of a drug such as Pinacidil. This is in line with the experimental protocol used to induce fibrillation in the rat hearts.

A consequence of using a discrete lattice based model of fibrillation dynamics is that APD restitution must be predefined using an appropriate restitution function, see Eq. (3.24) rather than emerging naturally as a result of ion channel dynamics which are simulated in continuous models of cardiac electrophysiology. However, it is not clear how to define a suitable restitution function which accounts for APD restitution due to the action of Pinacidil and due to short activation cycle lengths during burst pacing. As a result, we calibrate APD restitution in the model post infusion of Pinacidil such that, for simulation purposes, the baseline action potential duration already accounts for APD shortening from Pinacidil. Extensive data on the action of Pinacidil in rat hearts is not available, however, in explanted human hearts Pinacidil can shorten the baseline refractory wavelength by up to a factor of 3-4 [211]. The shortening of the refractory wavelength is dominated by APD restitution rather than CV restitution, although at high cycle lengths CV restitution is also observed. We reiterate here that in the discrete model the microscopic conduction velocity is fixed. Therefore, our chosen APD restitution curve must account for both APD and CV restitution such that the refractory wavelength at high cycle lengths is shortened appropriately. The parameters used to define the APD restitution curve include a maximum baseline APD, τ_{max} , a minimum APD value which limits the extent to which

the APD can shorten, τ_{\min} , and two arbitrary parameters which control the steepness of APD restitution, β and γ . This approach is consistent with APD restitution methods in previous discrete models of fibrillation [321]. Due to a lack of high quality data for APD restitution during fibrillation, an exact, experimentally verified restitution curve is hard to derive. As an alternative, we test a range of different plausible parameter combinations.

Firstly, we define two base restitution curves:

- Significant initial restitution from baseline with a gradual restitution slope at shorter diastolic intervals: $\tau_{\max}=160$, $\beta=0.85$ and $\gamma=250$, see red line in Fig. E.1. This restitution curve exhibits significant APD heterogeneity during fibrillation.
- Moderate initial restitution from baseline with gradual initial restitution and a very steep restitution curve at short diastolic intervals: $\tau_{\max}=250$, $\beta=1.5$ and $\gamma=100$, see blue line in Fig. E.1. This restitution curve exhibits significant APD heterogeneity at moderate diastolic intervals (lower frequency fibrillation), but minimal APD heterogeneity at very short diastolic intervals approaching 0.

These two restitution curves are tested at a minimum APD of $\tau_{\min}=30$ and $\tau_{\min}=50$, although we stress that re-entry does not necessarily organise to the minimum possible APD in practice. These minima have been chosen based on the approximate refractory wavelength observed experimentally using optical mapping. Observing stable reentry during fibrillation, the recorded activation maps from optical mapping show refractory wavelengths in the region of one third to a half of the vertical length of the rat ventricles. This corresponds to approximately 35 cells in the insilico model. Hence, the APD minima tested reasonably reflect plausible refractory wavelengths during fibrillation.

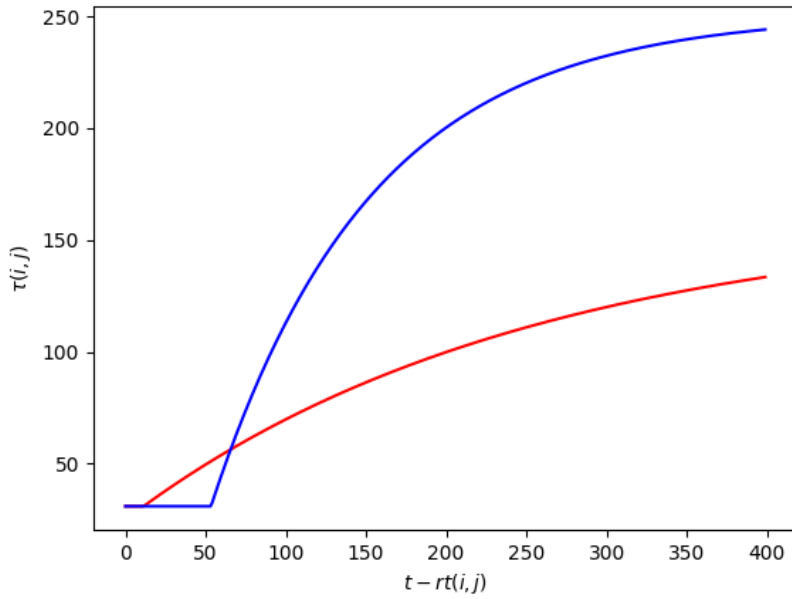


Figure E.1: **APD restitution curves in in the model.** The plot shows how the APD restitution curve presented in Eq. (3.24) varies with the distance (in time steps) between the current time t and the the last time step $rt(i, j)$ in which the (i, j) -th node entered a resting state. The colors of the two curves represent two distinct parameters set: $(\tau_{\min} = 30, \tau_{\max} = 160, \beta = 0.85, \gamma = 250)$ (red) and $(\tau_{\min} = 30, \tau_{\max} = 250, \beta = 1.5, \gamma = 100)$ (blue). This figure has been extracted from [26], see appendix B.2 for details about attributions and permissions.

Appendix F

Supplementary materials for section 3.7

Note

This appendix includes text and images that have been extracted, with any eventual alteration and extension, from an article I have co-authored [28]. This material appears in the following sections:

- F.1 and related subsections.
- F.2
- F.3

Details on copyrights, permissions and personal contributions to [28] are reported in appendix B.3.

F.1 Details on model definition and calibration of the model

F.1.1 Heart muscle structure

The area of the atrial muscle is $L'_x \times L'_y \approx 20\text{cm}^2$ [297, 298] while the thickness of the atrial muscle wall ranges from 1 mm to 7 mm [29]. A typical average is about $L'_z = 2.5\text{ mm}$ [299]. The atrial muscle tissue comprises tubular shaped heart muscle cells (myocytes) of length $\Delta x' \approx 100\mu\text{m}$ and diameter $\Delta y' = \Delta z' \approx 20\mu\text{m}$ [293, 294]. Cells are predominantly connected

longitudinally, forming fibres that connect transversally now and again. Hence a branching network of anisotropic cells provides an appropriate approximation of the atrial tissue.

F.1.2 Heart muscle physiology

The membrane potential of heart muscle cells shows that they can be in one of three states: excited, where the cell depolarizes, resting, where the cell can be depolarized by a neighbouring active cell, and refractory, where for some time τ' after excitation the cell cannot be re-excited. The shortest time scale is associated with a cell depolarizing, $\Delta t' \approx 0.6$ ms, whereas the refractory period lasts $\tau' \approx 150$ ms under rapid pacing. When a resting cell is induced to excite by a neighbouring excited cell, it contracts. The propagation speed of the activation wavefront is $\Delta x'/\Delta t' \approx 0.2$ ms⁻¹ and the heart's natural pacemaker (SAN) ensures the periodic propagation of a coordinated activation wavefront, causing atrial muscle contractions. The rate of excitations are controlled by the pacemaker cells that regularly self-excite with period $T' = 300$ -1000 ms. For example $T' = 660$ ms corresponds to approximately 90 beats per minute.

F.1.3 Dimensionless parameters of the model

We can translate real tissue values into dimensionless model parameters. We apply a similar conversion procedure to that presented in the original CMP model [25]. The dimension of the simplified 3d topology are $L_x = L'_x/\Delta x' = 1000$, $L_y = L'_y/\Delta x' = 1000$ and $L_z = L'_z/\Delta z' = 125$. We apply a coarse grain transformation $\Delta x' \rightarrow b\Delta x'$, $\Delta y' \rightarrow b\Delta y'$, $\Delta z' \rightarrow b\Delta z'$ such that we group b^3 cells within one node of the model. The propagation speed has to remain constant $\Delta x'/\Delta t' \approx 0.2$ ms⁻¹ so we must also coarse grain time $\Delta t' \rightarrow b\Delta t'$ [25]. By using $b = 5$, we find the dimensionless parameters of the model. For the 3d pipe structure, we have $L_x = L'_x/(b\Delta x') = 200$, $L_y = L'_y/(b\Delta y') = 200$ and $L_z = L'_z/(b\Delta z') = 25$. The renormalized excitation time $b\Delta t' = 3$ ms yields a dimensionless refractory period $\tau = \tau'/(b\Delta t') = 50$ and pacemaker activation period $T = T'/(b\Delta t') = 220$, assuming $T' = 660$ ms.

F.2 The spatial distribution of re-entrant circuits

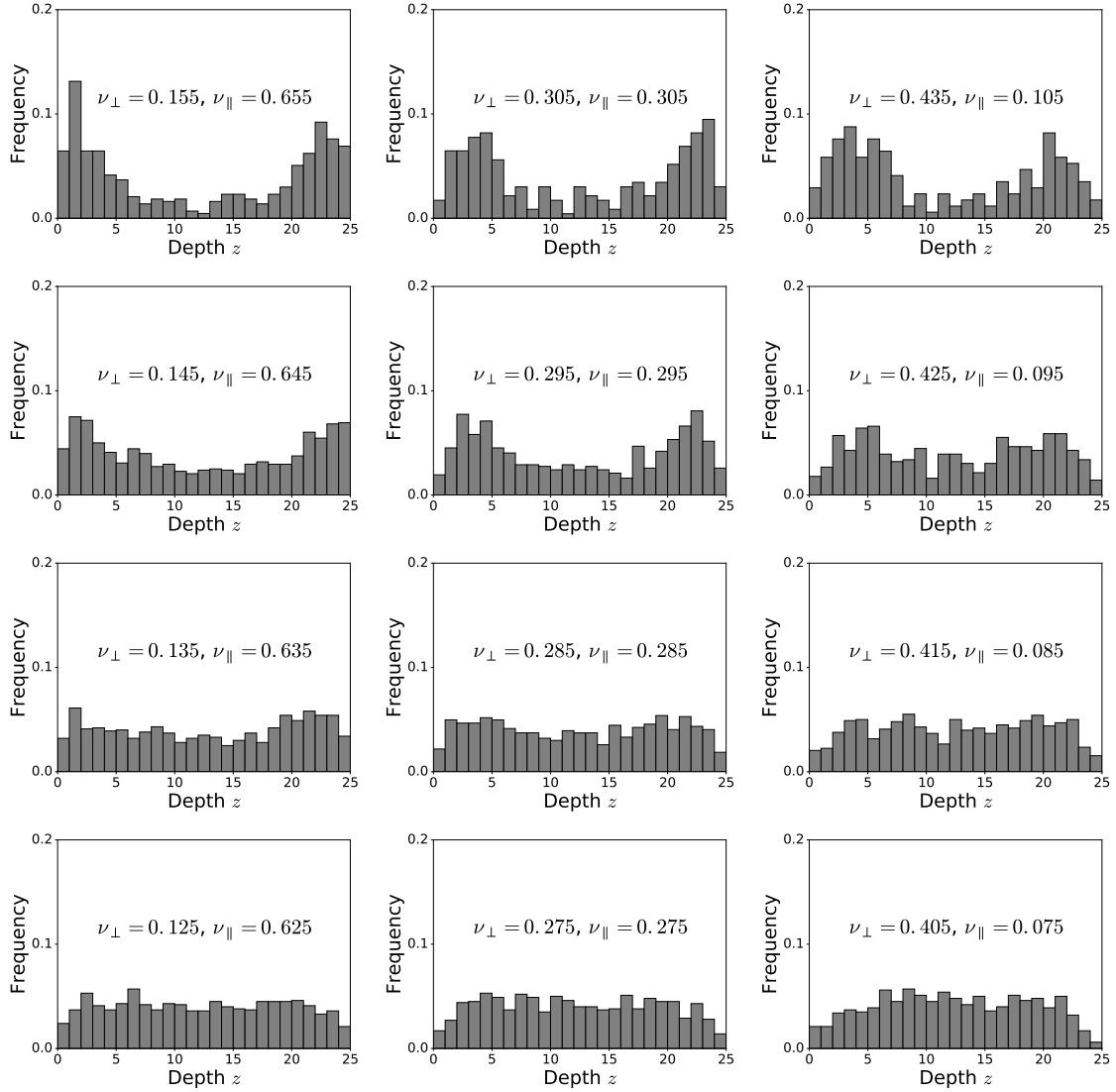


Figure F.1: **The distribution of re-entrant circuit depth z from the endocardium in the homogeneous model.** Fibre angle $\Delta\theta$ is constant across the tissue. AF progresses from paroxysmal AF (top row) to persistent AF (bottom row). The left column is for tissues with strong longitudinal coupling and weak transverse coupling. The central column is for tissues with equal longitudinal and transverse coupling. The right column is for tissues with weak longitudinal coupling and strong transverse coupling. Depth $z = 0$ ($z = 24$) corresponds to the endocardium (epicardium). In paroxysmal AF, re-entrant circuits are predominantly found near the atrial surfaces. When visualized from the atrial surface, these circuits will typically appear as re-entrant or rotational activity. In persistent AF, re-entrant circuits are uniformly distributed in the bulk of the atrial wall, away from the epicardium and endocardium. These circuits are more likely to result in breakthrough point (focal) activation patterns when visualized from the atrial surfaces. In the homogeneous model, the endocardium and epicardium are equivalent due to the symmetry. This figure has been extracted from [28], see appendix B.3 for details about attributions and permissions.

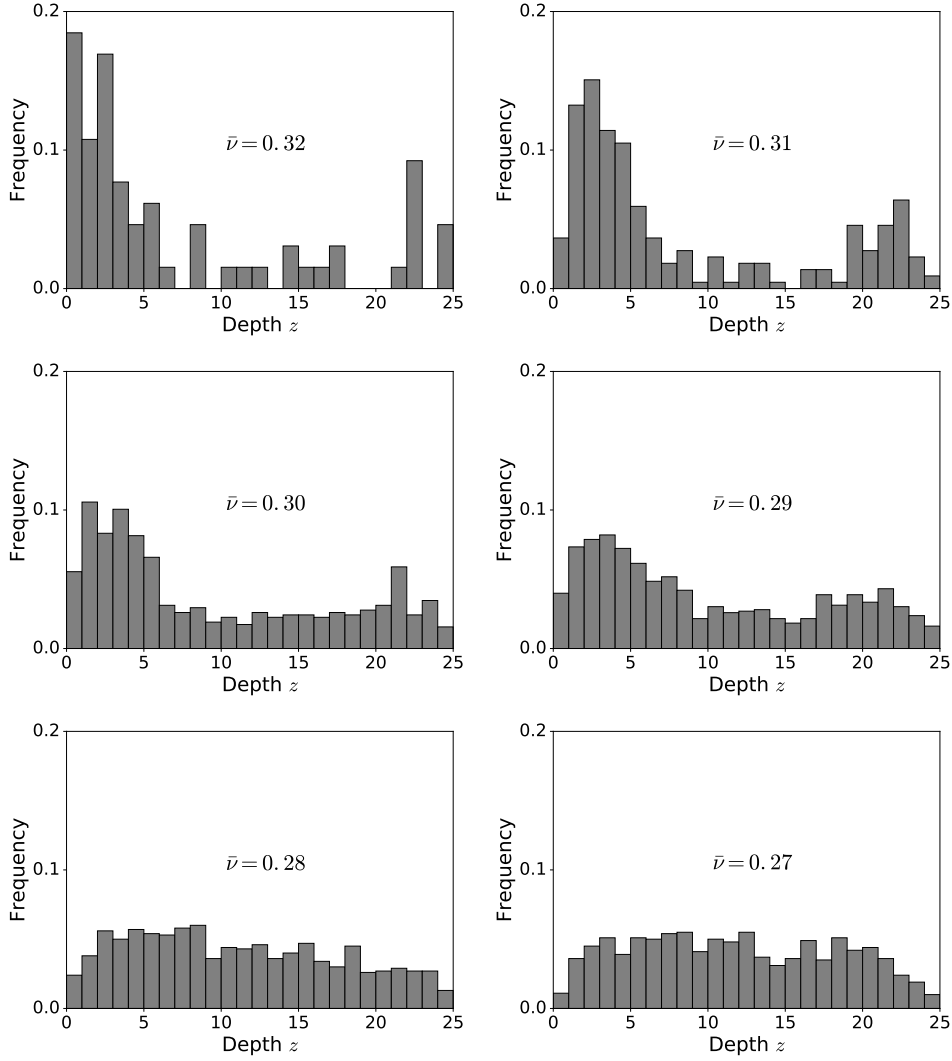


Figure F.2: **The distribution of re-entrant circuit depth z from the endocardium in the inhomogeneous model.** AF progresses from paroxysmal AF ($\bar{\nu} = 0.32$) to persistent AF ($\bar{\nu} = 0.27$). Fibre angle varies linearly across the tissue from $\Delta\theta_{\text{ENDO}} = 24^\circ$ on the endocardium to $\Delta\theta_{\text{EPI}} = 42^\circ$ on the epicardium. Depth $z = 0$ ($z = 24$) corresponds to the endocardium (epicardium). In the inhomogeneous model, the symmetry between the epicardium and endocardium is broken with the stronger longitudinal coupling on the endocardium than the epicardium. For paroxysmal AF, re-entrant circuits are predominantly found near the atrial surfaces, and significantly more circuits cluster near the endocardium than the epicardium. This is because fibres have much stronger longitudinal coupling on the endocardial surface than on the epicardial surface. When visualized from the endocardium, these circuits will typically appear as re-entrant or rotational activity. In persistent AF, re-entrant circuits are uniformly distributed in the bulk of the atrial wall, away from the epicardium and endocardium. These circuits are more likely to result in breakthrough point (focal) activation patterns when visualized from the endocardium. As AF has progressed from paroxysmal to persistent, the average depth of circuits from the endocardium at $z = 30$ has significantly increased – this hinders the effective use of catheter ablation for those circuits deep in the atrial bulk. This figure has been extracted from [28], see appendix B.3 for details about attributions and permissions.

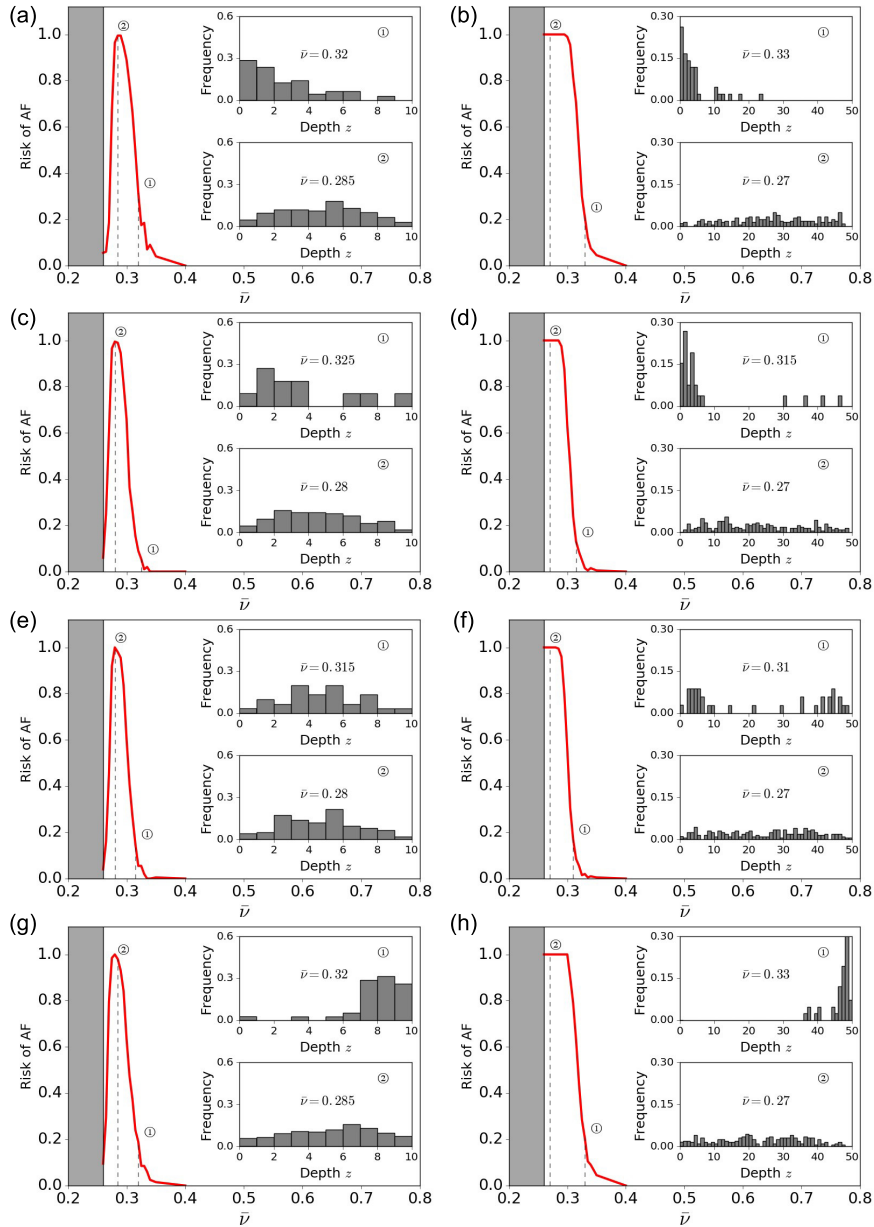


Figure F.3: **Risk of AF as a function of the topological features of the system.** Inhomogeneous coupling parameter risk curves (red graph) for various choices of fibre orientation and tissue thickness. Inset: Histograms showing the distribution of re-entrant circuits driving AF for paroxysmal AF (top) and persistent AF (bottom) as a function of depth z from the endocardium. Left column: Tissue thickness of 10 nodes (1.0 mm). Right column: Tissue thickness of 50 nodes (5.0 mm). (a) & (b) Strong longitudinal coupling on endocardium, $\Delta\theta_{\text{ENDO}} = 10^\circ$, and uniform coupling on the epicardium, $\Delta\theta_{\text{EPI}} = 45^\circ$. (c) & (d) Moderate longitudinal coupling on endocardium, $\Delta\theta_{\text{ENDO}} = 24^\circ$, and nearly uniform coupling on epicardium, $\Delta\theta_{\text{EPI}} = 42^\circ$. Parameters correspond to those used in Fig. 3.38(b) of main paper. (e) & (f) Very mild longitudinal coupling on endocardium, $\Delta\theta_{\text{ENDO}} = 40^\circ$, and very mild transverse coupling on epicardium, $\Delta\theta_{\text{EPI}} = 60^\circ$. (g) & (h) Uniform coupling on endocardium, $\Delta\theta_{\text{ENDO}} = 45^\circ$, and strong longitudinal coupling on epicardium, $\Delta\theta_{\text{EPI}} = 10^\circ$. (g) & (h) are identical to (a) & (b) with the endocardium and epicardium swapped. This figure has been extracted from [28], see appendix B.3 for details about attributions and permissions.

F.3 Details on ablation experiments

To simulate the effect of ablation in the model, see Fig. 3.40, we generate 500 independent tissues for each coupling value, $\bar{\nu}$. The random seeds used to generate these tissues are saved so that the tissues can be regenerated at a later stage. An additional seed is generated for each tissue which specifies the order in which nodes susceptible to conduction block fail to excite when prompted by an excited neighbour.

For the global success rate of ablation, see Fig. 3.40(a), a simulation is started in each tissue up to a maximum time of 10000 time steps. For simulations of length 10000 (~ 45 beats), with $\epsilon = 0.05$ and $T = 220$, if a structure exists capable of generating a re-entrant circuit is present, the probability it activates during the simulation is $> 90\%$. If a re-entrant circuit is detected during the evolution of the simulation, the simulation is stopped and the location of the circuit is recorded. Otherwise, we mark this structure as containing no re-entrant circuits and move on to the next. If a re-entrant circuit is detected, using the saved seeds, the exact same tissue is regenerated and we reset the order in which nodes susceptible to conduction block fail to fire. Before the simulation is restarted, a cuboid of side length 20 nodes and depth 25 nodes, centred on the x and y co-ordinate identified as the circuit location, is destroyed, mimicking a focal ablation. For a tissue of dimensions $200 \times 200 \times 25$ node³, this ablation lesion corresponds to 1% of the tissue. Destroyed nodes are permanently disabled and cannot be excited by neighbouring excited nodes. After the ablation lesion is applied, we restart the simulation for another 10000 time steps and observe whether another re-entrant circuit emerges at a different location in the tissue. If yes, this region can be ablated and the process can be repeated an arbitrary number of times – at this stage the focal ablation has been unsuccessful at terminating AF globally. If no, the ablation is considered successful and we move onto the next tissue.

The global ablation success curves shown in Fig. 3.40(a) of the main manuscript correspond to the percentage success that ablation prevents the emergence of AF anywhere in the tissue after a single ablation has been applied, and after up to ten individual lesions have been applied.

For the local success rate of ablation, see Fig. 3.40(b) in the main manuscript, we also generate 500 random tissues for each coupling value and save their seeds. Likewise, we save the seeds giving the sequence of failures for the nodes susceptible to conduction block. For each tissue, we run a simulation for up to 10000 time steps. If a re-entrant circuit is not identified we move onto the next tissue. If a circuit is identified, a cuboid of side length 20 nodes and depth z nodes,

centred on the x and y co-ordinate identified as the circuit location, is destroyed. Additionally, all nodes susceptible to conduction block with coordinates *outside* the x and y extent of the ablation lesion are prevented from exhibiting unidirectional conduction block. Hence, when the simulation is restarted, a re-entrant circuit can only form in the region directly below the ablation lesion, that is, a circuit can only form if it is at a co-ordinate corresponding to the x and y range ablated, but with depth greater than that of the ablation lesion. The simulation is now restarted for 10000 time steps and we observe whether or not a re-entrant circuit is detected. If yes, the local ablation has failed. If no, the local ablation has been successful. This process is repeated for a range of ablation depths z from a single node layer to the full tissue depth $z = 25$, using identical tissues such that different depth results can be compared like for like.

There are three reasons local ablation might fail: i) the ablation lesion is not deep enough to destroy a re-entrant circuit, ii) the targeted re-entrant circuit is destroyed but a different independent circuit is present below the ablation lesion, iii) the ablation lesion itself decouples nodes such that a circuit which was not present previously can now form by anchoring to the the ablation lesion itself.

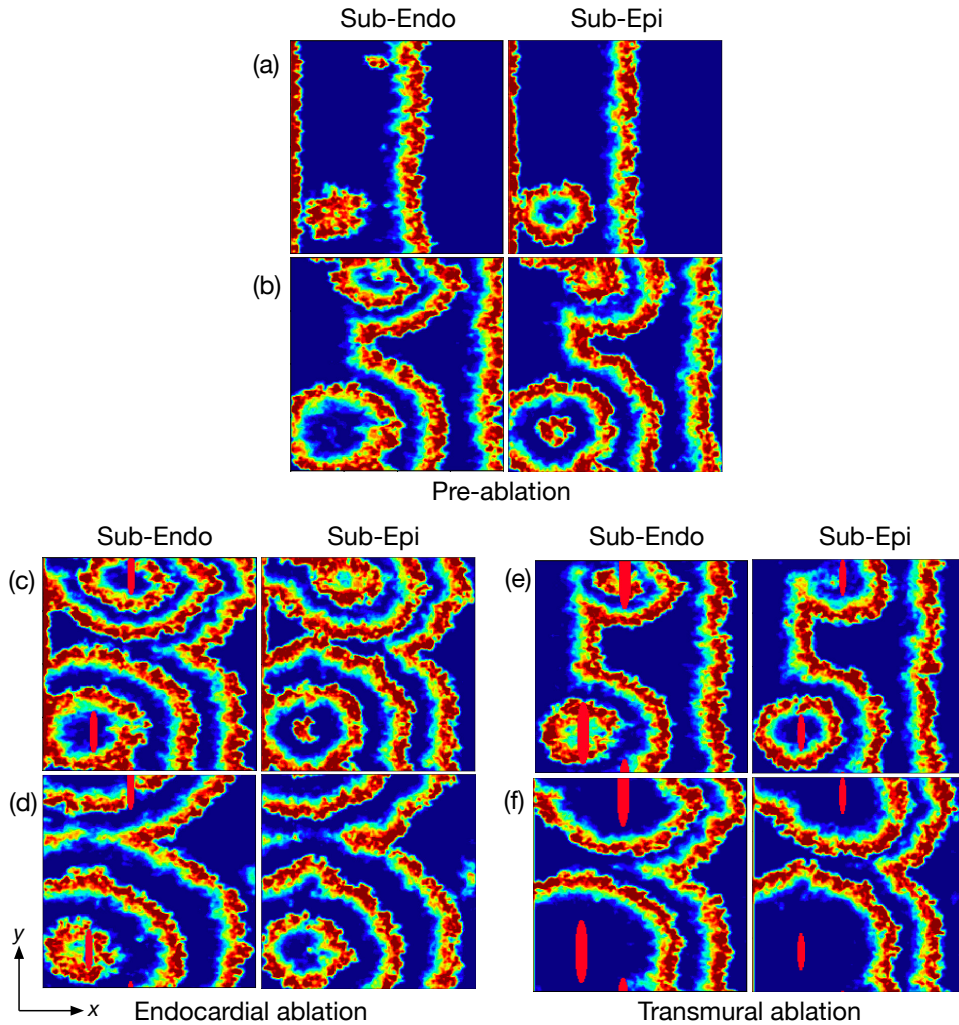


Figure F.4: **Simulated ablation in a tissue with multiple drivers.** This experiment demonstrates how the ability to terminate fibrillatory activity is closely related to driver depth. (a) AF emerges in the bottom left corner from a re-entrant circuit near the epicardium, and (b) at the top of the tissue from a separate re-entrant circuit near the endocardium. (c) Two shallow ablations (solid red in bottom left and top centre) are applied to the endocardial surface at the locations of the re-entrant circuits penetrating part of the way into the tissue. (d) The circuit near the epicardium has not been destroyed by the ablation since the ablation has not penetrated far enough into the tissue. The circuit near the endocardium has been destroyed successfully. However, since an active circuit remains in the tissue, AF has not been terminated. (e) & (f) show the same ablation process as demonstrated in (c) & (d), however, the ablation is now transmural, penetrating the full distance through the tissue. This is indicated by the solid red regions on the sub-epi view in (e) & (f). The ablations have successfully destroyed both re-entrant circuits. Hence, fibrillatory waves dissipate as shown in (f) and sinus rhythm will be restored. Note, transmural ablation is not always possible in clinical practice. Ablation lesions typically struggle to penetrate more than 2 mm [341] into the atrial wall which can be up to 7 mm thick in places [29]. Scale: 200×200 nodes (full tissue). This figure has been extracted from [28], see appendix B.3 for details about attributions and permissions.

Appendix G

Supplementary materials for section 4.5

Note

This appendix includes text and images that have been extracted, with any eventual alteration and extension, from an article I have co-authored [34]. This material appears in the following sections:

- G.1 and related subsections.
- G.2 and related subsections.

Details on copyrights, permissions and personal contributions to [34] are reported in appendix B.4.

G.1 Initialization and dynamic control of the Arbitrager Model

G.1.1 Introduction

Kanazawa *et al.* [386] have recently introduced a microscopic model of the interactions between high frequency traders (HFTs) and investigated its theoretical aspects by adapting Boltzmann and Langevin equations to this specific context. The results of this work have been further formalized in a parallel study from the same authors [428]. The dealing price updates in the

HFT model are driven by the following dynamics

$$\frac{dz_{i,\ell}(t)}{dt} = c_\ell^* \tanh\left(\frac{p_\ell(g_{t,\ell}) - p_\ell(g_{t,\ell} - 1)}{\Delta p_\ell^*}\right) + \sigma_\ell \epsilon_{i,\ell}(t), \quad i = 1, \dots, N_\ell \quad (\text{G.1})$$

where Δp_ℓ^* , c_ℓ^* are constants while the other variables and constants have the same meaning as in Eq. (4.19). It can be shown that setting $\Delta p_\ell^* \gg p_\ell(g_{t,\ell}) - p_\ell(g_{t,\ell} - 1)$ allows for a linear approximation of Eq. (G.1) that resembles the dynamics of the dealing price updates in the Arbitrager Model, see Eq. (4.19). This correspondence allows to exploit the theoretical results of [386, 428] to achieve a satisfactory control of the dynamics of the Arbitrager Model. For instance, Fig. G.3 shows that the average time between consecutive transactions in simulations of the Arbitrager Model is in strong agreement with its theoretical value estimated in the framework of Kanazawa *et al.* [386, 428]. The following sections provide details on how the parameters governing the evolution of the Arbitrager Model, see table 4.1, have been set in the simulations discussed in this study.

G.1.2 Initial state of the LOB

To initialize the ℓ -th LOB, the first step consists in fixing its initial center of mass $p_\ell(t_0)$ and the constant market making spread L_ℓ . The former is set arbitrarily to a value with the same magnitude of the mid-price patterns observed in real trading data, see Fig. C.1. Following the analysis of [386], the market making spread in the USD/JPY market is fixed to $L_{\text{USD/JPY}} = 0.05$. For simplicity, the market making spread in other markets is set such that it becomes proportional to the size of $p_\ell(t_0)$, that is $L_\ell = L_{\text{USD/JPY}} \times (p_\ell(t_0)/p_{\text{USD/JPY}}(t_0))$.

Exchange Rate	$p(t_0)$	L
EUR/USD	1.25	0.05
USD/JPY	110	$0.05 \times (110/1.25)$
EUR/JPY	137.5	$0.05 \times (137.5/1.25)$

Table G.1: **Initial center of mass and market making spread in each market.** Values of $p_\ell(t_0)$ and L_ℓ for EUR/USD, USD/JPY and EUR/JPY.

At this point the values in table G.1 are used to obtain the initial dealing prices for each trader

and market, thus revealing the initial profile of the LOBs

$$z_{i,\ell}(t_0) = \begin{cases} \frac{L_\ell}{2} (\sqrt{2u_{i,\ell}} - 1) + p_\ell(t_0), & \text{if } 0 < u_{i,\ell} \leq 0.5. \\ \frac{L_\ell}{2} (1 - \sqrt{2(1 - u_{i,\ell})}) + p_\ell(t_0), & \text{otherwise,} \end{cases} \quad (\text{G.2})$$

where $u_{i,\ell} \sim U(0, 1)$ is an uniformly distributed random variable. The expression in Eq. (G.2) is derived from the inverse function sampling procedure, see Fig. G.1. Let $r \equiv (z(t_0) - p(t_0))$ be the relative distance between an initial dealing price $z(t_0)$ and the initial center of mass price $p(t_0)$. The LOB profile is stable when the probability density function (PDF) of r is

$$\psi_\ell(r) = \begin{cases} \frac{2}{L_\ell} \left(1 - \left|\frac{2r}{L_\ell}\right|\right), & \text{if } |r| \leq \frac{L_\ell}{2}. \\ 0, & \text{otherwise.} \end{cases} \quad (\text{G.3})$$

It follows that the cumulative density function (CDF) of r is

$$\Psi_\ell(r) = \begin{cases} \frac{1}{2L_\ell^2} (L_\ell + 2r)^2, & \text{if } -\frac{L_\ell}{2} < r \leq 0. \\ -\frac{1}{2L_\ell^2} (L_\ell - 2r)^2 + 1, & \text{otherwise.} \end{cases} \quad (\text{G.4})$$

Then, the inverse function of Eq. (G.4) is computed

$$\Psi_\ell^{-1}(y) = \begin{cases} \frac{L_\ell}{2} (\sqrt{2y} - 1), & \text{if } 0 < y \leq 0.5. \\ \frac{L_\ell}{2} (1 - \sqrt{2(1 - y)}), & \text{if } 0.5 < y \leq 1. \end{cases} \quad (\text{G.5})$$

Finally, assuming that $y = u \sim U(0, 1)$, Eq. (G.5) is used to obtain the value of the initial dealing price $z_{i,\ell}(t_0)$, see Eq. (G.2).

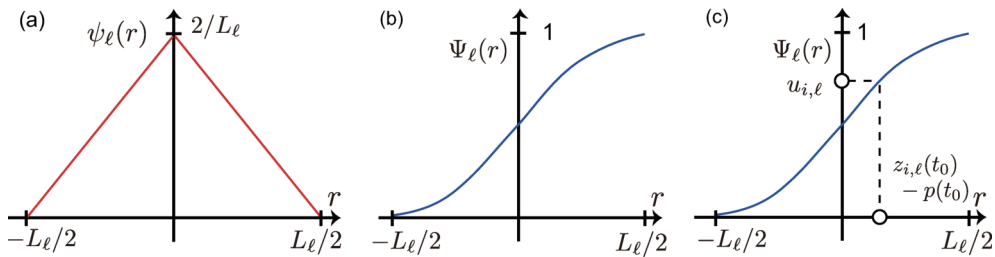


Figure G.1: **Inverse function sampling in the context of the Arbitrager Model.** (a) The LOB profile is stable if the PDF of r corresponds to the triangular function $\psi_\ell(r)$ [428]. (b) The CDF $\Psi_\ell(r)$. (c) Schematic of the inverse function sampling applied to $\Psi_\ell(r)$. This figure has been extracted from [34], see appendix B.4 for details about attributions and permissions.

G.1.3 Relationships between simulation time and real time

Kanazawa *et al.* [428] found that the average time between two consecutive transactions is

$$\Gamma = \frac{L_\ell^2}{2N_\ell\sigma_\ell^2}. \quad (\text{G.6})$$

For the sake of simplicity, the Arbitrager Model relies on the assumption that the three markets *moves at the same pace*, on average. This implies that Γ is the same in each market and constant in time. The parameter Γ is derived from real trading data. First, the average waiting times between consecutive transactions are calculated in each market and for each trading year. This leads to 12 averages (i.e., 4 years \times 3 FX rates). Finally, the median of these averages is computed to obtain a common value for Γ . In the dataset employed in this study it turns out that $\Gamma \approx 0.7$ sec, see Fig. G.2.

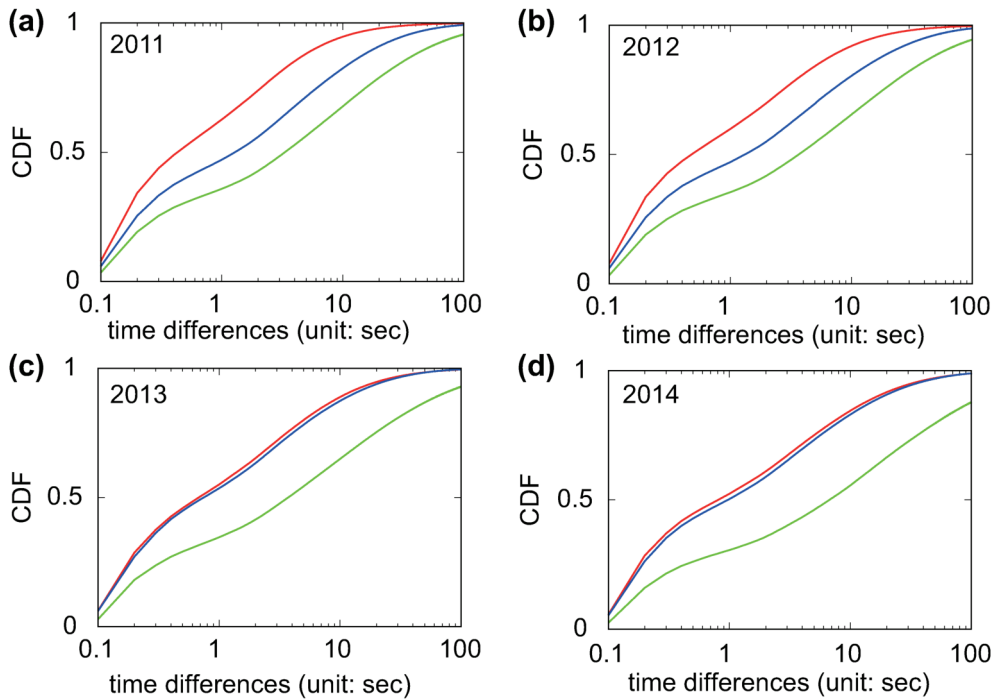


Figure G.2: **Waiting times statistics in real trading data.** Cumulative density functions (CDFs) of the waiting times between consecutive transactions for EUR/USD (red), USD/JPY (blue) and EUR/JPY (green) in (a) 2011, (b) 2012, (c) 2013 and (d) 2014. Data is provided by EBS, see section 4.5.2. This figure has been extracted from [34], see appendix B.4 for details about attributions and permissions.

To ensure that simulations of our model maintain $\Gamma \approx 0.7$ sec, the remaining free parameters N_ℓ and σ_ℓ must be fixed such that Eq. (G.6) is satisfied. The number of market makers participating

each market is set heuristically by considering several combinations ($N_{\text{EUR/USD}}, N_{\text{USD/JPY}}, N_{\text{EUR/JPY}}$) and examining how well the model-based cross-correlation function $\rho_{i,j}(\omega)$, see Fig. 4.12, replicates the same function built on real trading data. Having fixed N_ℓ , the volatility of the dealing price updates

$$\sigma_\ell = \frac{L_\ell}{\sqrt{2N_\ell\Gamma}} \quad (\text{G.7})$$

is found by rearranging Eq. (G.6). Finally, the amplitude of a discretized time step in the model simulation Δt should be set such that $\Delta t \ll \Gamma$. Therefore, this parameter is fixed to $\Delta t = 0.01$ sec and used in the discrete approximation of Eq. (4.19).

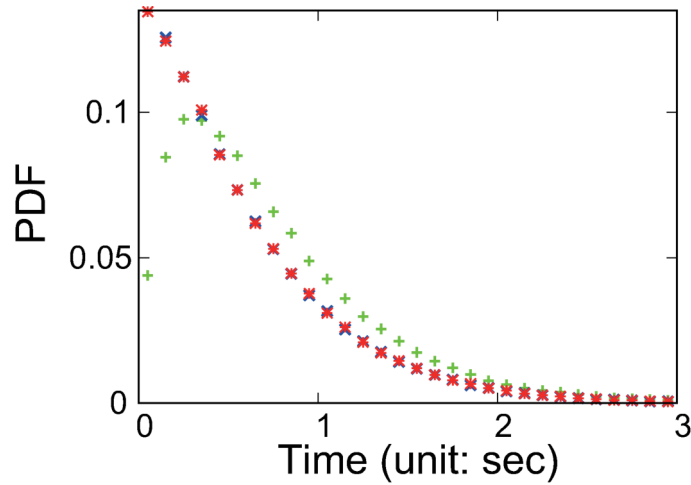


Figure G.3: **Waiting times statistics in the Arbitrager Model.** Probability density functions (PDFs) of the waiting times between consecutive transactions for EUR/USD (red), USD/JPY (blue) and EUR/JPY (green) in the Arbitrager Model. Simulations are performed under the same settings of the experiment presented in Fig. 4.12(b), bottom panel. For an adequate comparison against the theoretical predictions of the average time between consecutive transactions [428], the PDFs do not account for transactions triggered by the arbitrager. This figure has been extracted from [34], see appendix B.4 for details about attributions and permissions.

Fig. G.3 shows the distributions of the time between consecutive transactions in simulations of the Arbitrager Model. The average waiting time is $\tilde{\Gamma} \approx 0.65$ sec (65 time steps), which is very close to the theoretical value $\Gamma \approx 0.7$ sec. Acknowledging the simplifications that characterize the Arbitrager Model (e.g., Γ is the same in each market), the approximate equivalence $\Delta t = 0.01$ sec is used to convert simulation time steps in real time, see G.2 Table, and compare the

stabilization of the data-based and model-based cross-correlation functions $\rho_{i,j}(\omega)$, see Fig. 4.12 and Fig. G.6.

sec	time steps
1	100
10	1000
60	6000

Table G.2: **Approximate equivalences between real and model time.** The results of Kanazawa *et al.* [386, 428] are used to establish an approximate equivalence between real and model time. Assuming $\Delta t = 0.01$ sec, the table shows how many time steps roughly equate to 1 sec, 10 sec and 1 min.

G.1.4 Parameters involved in the calculation of the current price trend

The calculation of the price trend process $\phi_{n,\ell}(t)$, see Eq. (4.20), relies on two parameters: the number of accounted transaction price changes n and the scaling constant of the exponential weighting function ξ . In the simulations presented in Fig. 4.12 and Fig. G.6 these are arbitrarily set to $n = 15$ observations and $\xi = 5$. These choices allow to model a scenario in which trend-following market makers do not exclusively rely on the latest change in the transaction price to determine the current *direction* of the market. Instead, they compute a weighted average of the most recent price changes where weights are calculated according to an exponential function.

G.1.5 Trend-following strength parameter

The trend-following strength parameter c determines how the sign and value of the current price trend $\phi_{n,\ell}(t)$ affect the strategic decisions of the participating market makers. When $c > 0$, market makers are likely to update their dealing prices $z(t)$ upward when the price trend is positive and downward when the price trend is negative. Conversely, $c < 0$ indicates that market makers are more likely to update their dealing prices in the opposite direction of the price trend sign.

Recently, Sueshige *et al.* [429] have classified the strategic behavior of FX traders by examining EBS data covering the trading activity in the USD/JPY market during the week starting from

June 5th 2016. They found that a significant fraction of traders adopt trend-following strategies (i.e., $c > 0$). This observation is consistent with the model of Yura *et al.* [430].

Relying on these studies, the assumption that market makers populating the Arbitrager Model ecology adopt trend-following strategies (i.e., $c > 0$) is enforced. For simplicity, c is the same for every market maker and across markets. This parameter is fixed according to Eq. (91) in [428]

$$\Delta\tilde{p}^* = 1/(c\Gamma), \tag{G.8}$$

where $\Delta\tilde{p}^*$ is a non-dimensional parameter. Furthermore, $\Delta\tilde{p}^*$ shall take values that are not far from 2 for the model to produce the marginal trend-following behavior, which successfully replicated various statistical properties of real trading data in [428]. This allows to set $c = 0.8$, thus obtaining $\Delta\tilde{p}^* \approx 1.79$.

G.2 An extended version of the Arbitrager Model

G.2.1 Motivations

The Arbitrager Model qualitatively replicates the shape of the cross-correlation functions $\rho_{i,j}(\omega)$ and provides important insights on how the microscopic interactions between market makers and arbitragers entangles the dynamics of different FX rates. However, the cross-correlation functions $\rho_{i,j}(\omega)$ reproduced by this extremely simple model present two features that are not found in real trading data. First, on extremely short time-scales (i.e., $\omega \rightarrow 0$ sec) the model-based $\rho_{i,j}(\omega)$ does not approach zero as the same function built on real trading data. Second, the model-based $\rho_{i,j}(\omega)$ flattens when $\omega \gtrsim 30$ sec while the data-based $\rho_{i,j}(\omega)$ flattens when $\omega \gtrsim 10$ sec, see Fig. G.4. It is plausible that these differences stem from the extreme simplicity of the Arbitrager Model. To verify this assertion, a modified version of the model which mimics more features of real FX markets is introduced in this section. This extended, more realistic framework retains the same fundamental rules of the Arbitrager Model, that is, i) market makers continuously provide liquidity in a single market and ii) the arbitrager is the only agent allowed to operate across markets through the submission of predatory market orders. However, it also adds three distinct features inspired by real markets practices. First, agents' responses to triangular arbitrage opportunities emerge from a more rational decision making process in which they take into the account the risks associated to the implementation

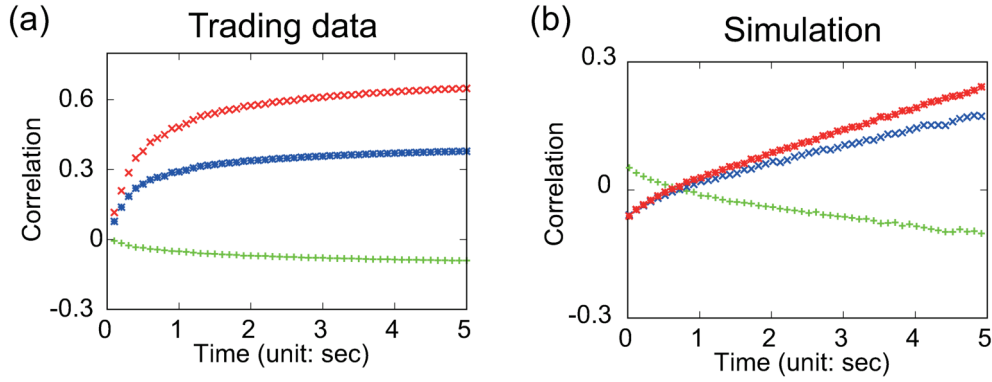


Figure G.4: **Trading data vs. model based cross-correlations functions.** Enlarged visualization of the cross-correlation functions $\rho_{i,j}(\omega)$ presented in Fig. 4.12. (a) Real market data (EBS) in 2013. (b) Arbitrager Model simulations. Contrarily to the cross-correlation functions displayed in (a), the model-based $\rho_{i,j}(\omega)$ takes non-zero values when $\omega \rightarrow 0$ sec and stabilizes on longer time-scales. Simulations are performed under the same settings of the experiment presented in Fig. 4.12(b), bottom panel. Details on the initialization of the model and the conversion between simulation time (i.e., time steps) and real time (i.e., sec) are provided in appendix G.1. This figure has been extracted from [34], see appendix B.4 for details about attributions and permissions.

of this strategy. Second, market makers foresee predatory market orders and re-adjust their quotes in advance, reducing the likelihood of being matched by arbitragers' orders. Third, market makers operating in the EUR/JPY market peg their quotes to the implied best bid and ask prices with probability γ . This introduces an additional toy (i.e., unrealistic) mechanism through which the dynamics of different FX rates become entangled.

G.2.2 The arbitrager

In the original model, see section 4.5.4, the arbitrager automatically submits predatory market orders as soon as Eqs. (4.18a) or (4.18b) exceeds the unit. In real FX markets this decision is far less trivial as these orders might not be executed at the prices used in the calculation of Eqs. (4.18a) and (4.18b). For instance, faster traders could have already exploited the existing opportunity, pushing back Eqs. (4.18a) or (4.18b) below the unit. As a result, the profitable misprice evaporates, exposing slower arbitragers to the risk of generating losses. To address this limitation, the extended Arbitrager Model introduces a more realistic decision making process

in which the arbitrageur takes into the account the risks associated with this trading strategy. In particular, the arbitrageur submits market orders if one of the following conditions is satisfied

$$\mu^I(t) \geq 1 + \zeta_A(t), \quad (\text{G.9a})$$

$$\mu^{II}(t) \geq 1 + \zeta_A(t), \quad (\text{G.9b})$$

where $\zeta_A(t) \sim \exp(\lambda_A)$. The parameter λ_A represents the risk profile of the arbitrageur. The higher the value of λ_A , the more profitable the gap between real and implied prices must be to *convince* the arbitrageur to exploit the current opportunity.

G.2.3 Market makers

The submission of predatory market orders ensures immediate execution, forcing the matched market makers to either sell *too low* or buy *too high*. In the original Arbitrageur Model, see section 4.5.4, market makers remain indifferent to triangular arbitrage opportunities, that is, they do not attempt to anticipate the arbitrageur to avoid predatory market orders. However, it is plausible that such a simplifying assumption does not adequately describe the behavior of liquidity providers acting in real FX markets. In this extension of the Arbitrageur Model the strategic behaviors of market makers are enhanced by allowing them to foresee the arbitrageur's moves and re-adjust their quotes accordingly. Their dealing price updates are driven by Eq. (4.19), however, they also track the likelihood of engaging in an unfavourable transaction with the arbitrageur. For instance, the i -th market maker operating in the EUR/JPY market monitors its exposure to predatory market orders by calculating the following ratios

$$\chi_{i,\text{EUR/JPY}}^I(t) = \frac{b_{\text{USD/JPY}}(t) \times b_{\text{EUR/USD}}(t)}{a_{i,\text{EUR/JPY}}(t)}, \quad (\text{G.10a})$$

$$\chi_{i,\text{EUR/JPY}}^{II}(t) = \frac{b_{i,\text{EUR/JPY}}(t)}{a_{\text{USD/JPY}}(t) \times a_{\text{EUR/USD}}(t)}, \quad (\text{G.10b})$$

where $b_{i,\ell}(t)$ and $a_{i,\ell}(t)$ are the current bid and ask limit prices of the i -th market maker and $b_\ell(t)$ and $a_\ell(t)$ are the current best quotes in the ℓ -th market. Clearly, Eqs. (G.10a) and (G.10b) can be straightforwardly rewritten for market makers operating in the USD/JPY or EUR/USD markets.

The more Eqs. (G.10a) or (G.10b) exceeds the unit, the larger the discrepancy between the current quote of the i -th market maker and the implied best cross FX rate. In the former case, the i -th market maker is underpricing EUR/JPY, facing the risk of selling *too low*. In the latter

case, the i -th market maker is overpricing EUR/JPY, facing the risk of buying *too high*. As the implied cross FX rate is the same for every agent, the market maker with the highest value of χ is always the one who is offering the best quote, hence the first to be matched by predatory market orders.

In the same spirit of Eqs. (G.9a) and (G.9b), the i -th market maker, perceiving a high risk of interacting with the arbitrageur, deletes and re-adjusts its current quotes if one of the following conditions is satisfied

$$\chi_{i,\text{EUR/JPY}}^I(t) \geq 1 + \zeta_{\text{MM, EUR/JPY}}(t), \quad (\text{G.11a})$$

$$\chi_{i,\text{EUR/JPY}}^{II}(t) \geq 1 + \zeta_{\text{MM, EUR/JPY}}(t), \quad (\text{G.11b})$$

where $\zeta_{\text{MM, EUR/JPY}}(t) \sim \exp(\lambda_{\text{MM, EUR/JPY}})$. The parameter $\lambda_{\text{MM, EUR/JPY}}$ represents the average risk profile (i.e., is the same for every market maker) in the EUR/JPY market. The lower the value of $\lambda_{\text{MM, EUR/JPY}}$, the less market makers tolerate their exposure to predatory market orders.

When Eqs. (G.11a) or (G.11b) is satisfied, the i -th market maker sets its dealing price to the current mid price $m_{\text{EUR/JPY}}(t) = (a_{\text{EUR/JPY}}(t) + b_{\text{EUR/JPY}}(t))/2$, rejecting the update imposed by Eq. (4.19) to reduce the risk of engaging in a transaction with the arbitrageur, see Fig. G.5. This mimics real traders deleting their limit orders queued in the very first levels of the LOB to replace them with new orders lying farther away from the current best quotes.

G.2.4 An additional price-entangling mechanism

The law of one price states that in frictionless markets the prices of two assets with the same cash flows must be identical [431]. The law of one price is maintained by two distinct mechanisms, triangular arbitrage and *shopping around*, which promptly correct temporary gaps between the prices of two identical assets [431]. The former has been extensively described in section 4.5.2 and it is the only way to enforce the law of one price in the standard version of the Arbitrageur Model, see section 4.5.4. The latter mechanism relates to the fact that rational traders, having detected two assets with identical cash flows but different prices, always buy the one with lower price and sell the one with higher price. This alters the demand and supply in the markets in which these assets are exchanged, thus closing the gap between their prices [431]. Reproducing the shopping around mechanism in the Arbitrageur Model requires market makers to operate in multiple LOBs. To avoid a complete overhaul of the fundamentals of

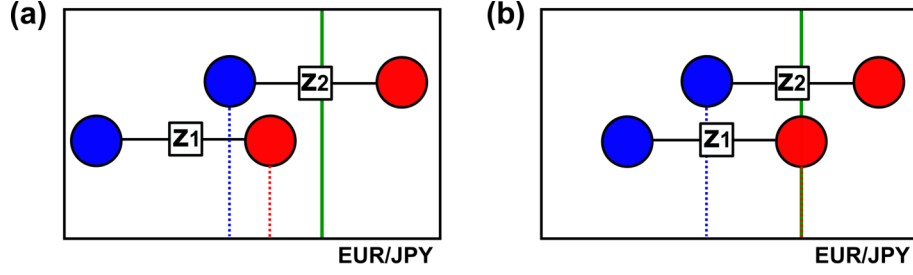


Figure G.5: **Foreseeing a triangular arbitrage opportunity in the Arbitrager Model.** The plot considers the EUR/JPY market. The best bid and ask quotes are marked by the blue and red dashed lines, respectively. The implied best bid price of EUR/JPY (i.e., $b_{\text{USD/JPY}} \times b_{\text{EUR/USD}}$) is denoted by the green solid line. (a) The current best ask quote $a_{\text{EUR/JPY}}$ (red dashed line) is smaller than the implied best bid quote $b_{\text{USD/JPY}} \times b_{\text{EUR/USD}}$ (green solid line). This misprice exposes Market Maker #1 to the risk of transacting with the arbitrager who wants to “buy low” $a_{\text{EUR/JPY}}$ and “sell high” $b_{\text{USD/JPY}} \times b_{\text{EUR/USD}}$. (b) When $\chi_{1,\text{EUR/JPY}}^I \geq 1 + \zeta_{\text{MM}, \text{EUR/JPY}}$, Market Maker #1 adjusts its dealing price $z_{1,\text{EUR/JPY}}$ to the mid price $m_{\text{EUR/JPY}}$ (i.e., the mid point between the best quotes in (a)). This action neutralizes the existing triangular arbitrage opportunity as the new best ask quote $a_{\text{EUR/JPY}}$ (red dashed line) matches or exceeds the implied best bid quote $b_{\text{USD/JPY}} \times b_{\text{EUR/USD}}$ (green solid line). This figure has been extracted from [34], see appendix B.4 for details about attributions and permissions.

the Arbitrager Model, its extension includes a simpler stylized mechanism which retains the basic feature that distinguishes shopping around from triangular arbitrage, that is, the absence of a *round trip* (e.g. $\text{JPY} \rightarrow \text{EUR} \rightarrow \text{USD} \rightarrow \text{JPY}$) [431]. Market makers operating in the EUR/JPY market peg their bid and ask quotes to the implied best bid and ask prices with constant probability γ , thus rejecting the dealing price update imposed by Eq. (4.19). For instance, the quotes of the i -th market maker that decides to peg its prices to the implied best quotes at time t are

$$b_{i,\text{EUR/JPY}}(t) = b_{\text{EUR/USD}}(t) \times b_{\text{USD/JPY}}(t), \quad (\text{G.12})$$

$$a_{i,\text{EUR/JPY}}(t) = a_{\text{EUR/USD}}(t) \times a_{\text{USD/JPY}}(t). \quad (\text{G.13})$$

This introduces an additional, simplistic mechanism through which the price of EUR/JPY is pushed towards its implied FX cross rate $\text{EUR/USD} \times \text{USD/JPY}$.

G.2.5 Cross-correlation diagrams and discussion

The inclusion of additional features of real FX markets improves the replication of the characteristic shape of $\rho_{i,j}(\omega)$. In particular, both the data-based and model-based cross-correlation functions $\rho_{i,j}(\omega)$ approach zero on extremely short time-scales (i.e., $\omega \rightarrow 0$ sec), see insets of Fig. G.6(b). Furthermore, the model-based $\rho_{i,j}(\omega)$ flattens on much shorter time-scales when compared to the standard Arbitrager Model, see Fig. 4.12(b) vs. Fig. G.6(b). This rapid stabilization is indeed observed in cross-correlation functions derived from real trading data, see Fig. G.6(a). These results suggest that the discrepancies between model-based and data-based

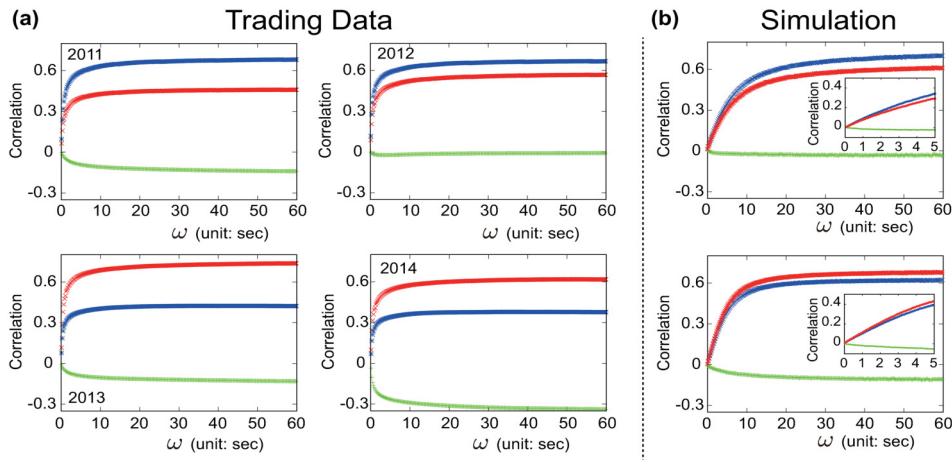


Figure G.6: **Trading data vs. model based cross-correlation functions.** Cross-correlation function $\rho_{i,j}(\omega)$ for $\Delta\text{USD}/\text{JPY}$ vs. $\Delta\text{EUR}/\text{USD}$ (green), $\Delta\text{EUR}/\text{USD}$ vs. $\Delta\text{EUR}/\text{JPY}$ (blue) and $\Delta\text{USD}/\text{JPY}$ vs. $\Delta\text{EUR}/\text{JPY}$ (red) as a function of the time-scale ω of the underlying time series. (a) Real market data (EBS) across four distinct years (2011-2014). (b) Extended Arbitrager Model simulations. The number of participating market makers $(N_{\text{EUR}/\text{USD}}, N_{\text{USD}/\text{JPY}}, N_{\text{EUR}/\text{JPY}})$ are $(30, 33, 20)$ in the first experiment, see (b) top panel, and $(30, 27, 20)$ in the second experiment, see (b) bottom panel. Details on the other settings of the simulations are provided in Fig. 4.12. The risk profile of the arbitrager is $\lambda_A = 0.01$ while the risk profiles of market makers are $\lambda_{\text{MM}, \text{USD}/\text{JPY}} = \lambda_{\text{MM}, \text{EUR}/\text{USD}} = \lambda_{\text{MM}, \text{EUR}/\text{JPY}} = 0.001$. The pegging probability in the EUR/JPY market is $\gamma = 0.01$. The insets in (b) provide an enlarged visualization of the cross-correlations functions $\rho_{i,j}(\omega)$ on very short time-scales (i.e. $\omega < 5$ sec). Details on the initialization of the model and the conversion between simulation time (i.e., time steps) and real time (i.e., sec) are provided in appendix G.1. This figure has been extracted from [34], see appendix B.4 for details about attributions and permissions.

cross-correlation functions stem from the extreme simplicity of the Arbitrager Model which neglects several features and practices of real FX markets. Nonetheless, the standard Arbitrager Model succeeds in providing a comprehensive and intriguing explanation on how the dynamics of different FX rates are entangled at a microscopic level. This result is remarkable, considering the limited number of input parameters and straightforward settings that characterize this model.

The effort of extending the Arbitrager Model provides few important insights. First, the inclusion of reacting market makers corrects the behavior of $\rho_{i,j}(\omega)$ when $\omega \rightarrow 0$ sec, that is, the model-based cross-correlation function collapses to zero as in real trading data. The key difference between arbitragers and market makers reactions to triangular arbitrage opportunities is that the former prompt simultaneous transactions, causing mid price changes in each market, while the latter cause a sequence of asynchronous mid price changes and eventually transactions. The characteristic shape of $\rho_{i,j}(\omega)$ presented in Fig. G.6(b) is based on a set of risk profile parameters that gives market makers a predominant role at the expense of the arbitrager. This means that a large fraction of triangular arbitrage opportunities are neutralized by market makers before the arbitrager can place predatory market orders. This result should not be interpreted as an estimate of the fraction of opportunities that are destroyed by market makers or exploited by arbitragers in real FX markets. However, it suggests that the entanglement of the dynamics of FX rates starts at different times in each market, depending on the current state of the LOB.

The second insight emerging from Fig. G.6 is that the interdependencies among currencies stem from the interplay of several agents' behaviors. While the interactions between triangular arbitrage and trend-following strategies retain a primary, necessary role in the entanglement of FX rates dynamics, the introduction of a second, complementary mechanism (i.e., *shopping around*) to close the gap between real and implied prices allows the model based $\rho_{i,j}(\omega)$ to stabilize on shorter time-scales ω , obtaining a characteristic shape that is strongly compatible with the same function derived from real trading data. This suggests that in real FX markets additional strategies are likely to interact with triangular arbitrage and trend-following behaviors to shape the features of cross-currency correlations.

Appendix H

Supplementary materials for section 4.6

Note

This appendix includes text and images that have been extracted, with any eventual alteration and extension, from an article I have co-authored [345]. This material appears in the following sections:

- H.1 and related subsections.
- H.2 and related subsections.
- H.3 and related subsections.
- H.4 and related subsections.
- H.5 and related subsections.

Details on copyrights, permissions and personal contributions to [345] are reported in appendix B.5.

Note that for copyrights reasons material appearing in this appendix is extracted from [345], which is the latest pre-print preceding [37], i.e., the published version.

H.1 Data processing

In each trading day we remove the first and the last 30 minutes of trading activity to filter out unusual events that are likely to occur around the opening and closing auctions. We split the day into 60s bins starting at 0930EST and finishing at 1600EST. Bins are semi-open, i.e., $[t_{\ell-1}, t_{\ell}[$, where t_{ℓ} is the ℓ -th bound. The last bin of the trading day is the only exception as a close interval is used to include any potential event that may take place at the exact closing time, i.e., 1600 EST.

To construct the OFI, we first detect the submissions of limit orders, executions of market orders, and cancellations/deletions of previously posted orders occurring within the considered time interval. Following [36], we compute the volumes that “reinforce” the demand with respect to the supply:

1. Buy limit orders placed during the considered time window.
2. Sell limit orders matched during the considered time window.
3. Sell limit orders cancelled during the considered time window.

and the volumes that “reinforce” the supply with respect to the demand:

1. Sell limit orders placed during the considered time window.
2. Buy limit orders matched during the considered time window.
3. Buy limit orders cancelled during the considered time window.

The OFI, being a measure of demand/supply imbalance, is obtained by subtracting the volumes in the second group from those in the first group.

We define a *mid price* as the mid point between the best bid and ask prices recorded in the LOBSTER dataset. In our analysis we sample the last mid price recorded before the upper bound of the considered bin. Finally, we calculate price changes ΔP_{ℓ} by taking the first order differences of the sampled time series.

In rare circumstances, e.g. slow trading or data issues, no LOB events may fall within a time bin. In this scenario, we set the OFI equal to zero and the current mid price is pegged to the

last available record.

To calculate the depth of the book we introduce some useful concepts.

Definition H.1 We define an \mathbb{R} -valued irregularly spaced time series Q as a sequence $(t_i, q_i)_{i \in I}$, where $I \subset \mathbb{N}$ is a set of indices, $t_i \in [0, T] \subset \mathbb{R}$, with $t_i \leq t_{i+1}$, and $q_i \in \mathbb{R}$, where t_i is the i -th timestamp and q_i is the i -th data point.

Definition H.2 Let Q be a time series over $[0, T]$, $\tau \in \mathbb{R}$ be the length of a time interval, $n = T/\tau$. We define the τ -time grid associated to Q to be the set $G = \{p_n\}_{n \in \mathbb{N}}$ where

$$p_n := \sup \{i \in I \mid t_i < n\tau\}.$$

Suppose we partition $[0, T]$ in N uniform intervals of length τ . We observe that p_n is the index of the last timestamp before the end of the n -th time interval.

Definition H.3 Given an irregularly spaced time series Q and an associated τ -time grid G , we define the averaged bin time series to be the series $\mathcal{Q} = (Q_n)_{n \leq N}$ as:

$$Q_1 = \frac{1}{\tau} \left(q_1 t_1 + \sum_{k=1}^{p_1-1} q_k (t_{k+1} - t_k) + q_{p_1} (\tau - t_{p_1}) \right)$$

$$Q_{n+1} = \frac{1}{\tau} \left(q_{p_n} (t_{(p_n+1)} - n\tau) + \sum_{k=p_n+1}^{p_{(n+1)}-1} q_k (t_{k+1} - t_k) + q_{p_{(n+1)}} ((n+1)\tau - t_{p_{(n+1)}}) \right) \quad n \geq 1$$

Given the time series (t_i, b_i) and (t_i, a_i) , where b_i and a_i are the bid and the ask size at time t_i respectively, we define the depth as

$$D_\ell = (B_\ell + A_\ell)/2 \quad \ell = 1, \dots, L \tag{H.1}$$

where B_ℓ and A_ℓ are the averaged bin time series of (t_i, b_i) and (t_i, a_i) . This implies that the depth over each the time interval $[t_{\ell-1}, t_\ell]$ is the weighted average of the size at the best quotes with weight proportional to the time a given size was available.

H.2 Technical details on the estimation procedure

The Kalman filter implementation is performed with the R package Fast Kalman Filter (FKF henceforth). The package is mainly written in C and relies on the FORTRAR LAPACK package

to perform fast computations of Kalman filtering and forecasting. Kalman smoothing was performed with an implementation of the forward-backward smoothing algorithm presented in Eq. (4.26). Before optimizing the log-likelihood presented in Eq. (4.28), we rescale the system in order to ease the optimization procedure. Let $\tilde{\phi}_{.,\ell} = \phi_{.,\ell}/\sigma_{.,\phi}$, where σ_{ϕ} is the sample standard deviation of the OFI and $\Delta\tilde{P}_{.,\ell} = \Delta P_{.,\ell}/(\sigma_{\Delta P})$, where $\sigma_{\Delta P}$ is the sample standard deviation of price changes. At this point, the system presented in Eq. (4.23) can be rewritten as

$$\Delta\tilde{P}_{.,\ell} = q_{.,\ell}\beta.\pi_{\ell}\tilde{\phi}_{.,\ell} + \epsilon_{.,\ell} \quad \epsilon_{.,\ell} \sim \text{NID}(0, \sigma_{.,\epsilon}^2) \quad (\text{H.2a})$$

$$q_{.,\ell+1} = (1 - \rho.) + \rho. q_{.,\ell} + \eta_{.,\ell} \quad \eta_{.,\ell} \sim \text{NID}(0, \sigma_{.,\eta}^2). \quad (\text{H.2b})$$

Following [392], we also re-parametrize the volatilities as $s_{.,\epsilon} = \log(\sigma_{.,\epsilon})$ and $s_{.,\eta} = \log(\sigma_{.,\eta})$ to attain an unconstrained optimization problem. The priors for the state space are set to $\mathbf{q}_{.,1} = 1$ and $\mathbf{P}_{.,1} = 2$.

H.3 Econometric and modeling issues

H.3.1 Exogeneity of the OFI

The OFI introduced in [36] provides a simple tool to account for both the price impact of trades, i.e., market orders, and orders, limit order placements and deletions. The authors proposed a simple linear regression model of the relationship between OFI and price fluctuations which successfully captures multiple empirical regularities of intraday market liquidity. However, the extreme simplicity of their model limits the study of this relationship to the contemporaneous effects between the two variables. It is worth whether the data at 60s time-scale requires the OFI to be endogenous. In that case, it would be necessary to model the joint dynamics of price changes and OFI. Following [390], we apply a vector auto-regressive model (VAR henceforth) as a validation of the exogeneity assumption. We introduce the following model¹:

$$\begin{bmatrix} 1 & b_0 \\ 0 & 1 \end{bmatrix} \begin{bmatrix} \Delta P_{\ell} \\ \text{OFI}_{\ell} \end{bmatrix} = \begin{bmatrix} a_1 & b_1 \\ c_1 & d_1 \end{bmatrix} \begin{bmatrix} \Delta P_{\ell-1} \\ \text{OFI}_{\ell-1} \end{bmatrix} + \begin{bmatrix} v_{1,\ell} \\ v_{2,\ell} \end{bmatrix}, \quad (\text{H.3})$$

where the immediate effect of the OFI on price fluctuations is measured by the b_0 coefficient. The goal is to test whether modelling the joint dynamics for OFI and price changes becomes necessary at 60s time-scale. In line with [390], v_1 and v_2 are jointly and serially uncorrelated

¹Note that for the sake of consistency the following VAR is fitted in calendar time

with zero mean. We assert that the settings of the model introduced in Eq. (H.3) capture the fact that the price fluctuations and OFI are, by construction, not determined simultaneously: the change in the mid-price follows the last update of the OFI whereas ΔP_ℓ cannot contemporaneously influence the OFI. In addition, we truncate the potentially infinite order of the VAR representation at one lag. The purpose of the present analysis is to assess whether some lagged effects exist even at a relatively low frequencies, i.e., 60s. We assert that the eventual presence of serial dependencies is likely to be caused by microstructural features, such as price discreteness and delays in the reception of newly released information.

Table H.1 displays the regression coefficients associated with contemporaneous and lagged effect along with the corresponding t -statistics. We report averages of the estimated parameters over the sampling period. Also, we check that the reported results are in line with day-by-day estimates. We observe that the contemporaneous effect of the OFI, i.e., $-b_0$, is positive and significant. On the other hand, the lagged effects are not significant with the notable exception of AAPL. This analysis supports the idea that there is a significant instantaneous dependence of price fluctuations on the OFI, but the latter does not display any significant auto-correlation and therefore it is reasonable to assume it as exogenous. These results validate the implementation of our model even at 60s time-scale.

H.3.2 Is Kalman the right filter?

From an estimation perspective, the appealing feature of the proposed model is that it can be estimated via Kalman filter. One main feature of this filter is its robustness. Moreover, it is well known [432] that it is the optimal filter, i.e., minimum mean-square error, if the innovations are normally distributed. In Eq. (4.24) the disturbances are *i.i.d.* normal. This assumption is not compatible with the discrete nature of price changes at a 60s time-scale. In particular, the disturbances have to be uncorrelated with the regressors, therefore normality seems to be an implausible assumption at first sight. We address this concern explicitly and we quantify the severity of this potential misspecification. We follow the literature [392] and we examine, at any generic day i , the time series of the standardized one-step ahead forecast errors: $\hat{\epsilon}_{\cdot,\ell} = \hat{v}_{\cdot,\ell} / \sqrt{\widehat{F}_{\cdot,\ell}}$, $\ell = 1, \dots, L$ obtained from the estimation procedure. In appendix H.4 we display sample autocorrelations of $\hat{\epsilon}_{\cdot,\ell}$ and $\hat{\epsilon}_{\cdot,\ell}^2$, as well as quantile-quantile plots for $\hat{\epsilon}_{\cdot,\ell}$. We note some very weak heteroskedasticity of $\widehat{\epsilon}_{\cdot,\ell}$ and a slight deviation from normality in the tails.

Ticker	Parameters values (t -stats)				
	b_0	a_1	b_1	c_1	d_1
CSCO	-2.59e-06 (-26.85***)	0.040 (0.17)	-5.61e-08 (0.005)	-27661.86 (-1.19)	0.02 (0.34)
INTC	-5.50e-07 (-28.81***)	-0.005 (-0.025)	1.75e-08 (0.14)	-124098.13 (-0.84)	0.04 (0.50)
MSFT	-1.23e-06 (-30.83***)	0.054 (0.27)	-9.18e-08 (-0.23)	-65617.70 (-1.02)	0.08 (1.00)
CMCSA	-1.03e-04 (-12.05***)	-0.012 (-0.15)	2.115e-08 (0.05)	-15320.32 (-0.86)	0.034 (0.48)
AAPL	-2.94e-06 (-22.98***)	0.135 (0.68)	-8.86e-07 (-0.90)	-38559.31 (-1.48*)	0.25 (2.23**)

Table H.1: **Estimates of the VAR parameters.** Statistically significant coefficients at 10%, 5% and 1% confidence levels are marked with one, two and three stars, respectively.

We argue that the model we are introducing is an optimal trade-off between achieving a perfect statistical fit of the data and retaining practical implementability.

H.3.3 Statistical issues in the two-step estimation procedure

In this subsection we discuss the statistical properties of the two-step estimator of the model introduced in section 4.6.5. In this two-steps estimation procedure errors emerging in the first stage might propagate through the second stage. To address this statistical concern, we perform a dedicated numerical experiment. We choose a simulation setting that resembles as close as possible the main features of our data. In particular, we assume that a trading day extends for 6.5hs and simulate $N = 100$ distinct time series comprising $L = 390$ observations, i.e., data points are sampled every 60s, from the model presented in Eq. (4.24). We use the following data generating process (DGP henceforth). First, we extract representative time series of the intraday pattern of price impact and the OFI from real data as well as the hyper-parameters vector $\Theta = (\beta, \rho, \sigma_\epsilon, \sigma_\eta)$. Then, we sample i) the daily level of market impact from a positive uniform random variable with support $(0, 1.5\beta)$, ii) the order flow imbalance $\phi_{\cdot,\ell}$, $\ell = 1, \dots, L$, from a zero-mean Gaussian random variable with standard deviation derived from empirical

data², and iii) the coefficient ρ from a positive uniform random variable with support $(0.2, 0.4)$. Finally, $\epsilon_{.,\ell}$ (resp. $\eta_{.,\ell}$), $\ell = 1, \dots, L$, are sampled from independent and identically distributed Gaussian random variables with a standard deviation equals to $\tilde{\sigma}_\epsilon$ (resp. $\tilde{\sigma}_\eta$), where $\tilde{\sigma}_\epsilon$ (resp. $\tilde{\sigma}_\eta$) are sampled from a positive uniform random variable with support $(0.8\sigma_\epsilon, 1.2\sigma_\epsilon)$ (resp. $(0.8\sigma_\eta, 1.2\sigma_\eta)$). We perform our simulation study with values of parameters, intraday pattern and OFI consistent with those found in empirical data for both large, e.g., MSFT, and small, e.g., AMZN, tick stocks. Fig. H.1 displays the true and estimated time-of-the-day pattern. In the large tick stocks setting the estimated intraday pattern is indistinguishable from the true one, whereas in the small tick stocks setting it presents some bias, especially in the final segment of the fictional trading day. In this case, the bias might be the symptomatic of the presence of a non-negligible fraction of simulated price change and OFI data points with opposite sign, i.e., the parameter ρ becomes negative. Table H.2 reports the outcomes of this experiment after excluding the aforementioned cases. Parameters estimated on simulated data are compatible with those obtained on real trading data. We observe that the auto-regressive coefficient ρ is overestimated if the intraday pattern is not taken into account in the large tick stocks setting. Accounting for the intraday pattern reduces the dispersion of parameter estimates in both settings.

H.4 Diagnostic testing for Kalman filter

Fig. H.2 displays examples of sample auto-correlations of the standardized one-step ahead forecast errors, sample auto-correlations of the squared standardized one-step ahead forecast errors, and the quantile-quantile plots of the standardized one-step ahead forecast errors.

H.5 The performance of the model for small tick stocks

In this appendix we investigate the performance of the model for small tick stocks. This group present features that are at odds with the hypotheses of the model. In this analysis we cover Amgen, Inc. (AMGN henceforth) Amazon.com Inc (AMZN henceforth) and Alphabet Inc Class

²We ignore the temporal correlation of ϕ . However, in first approximation, this is consistent with what is observed in real data.

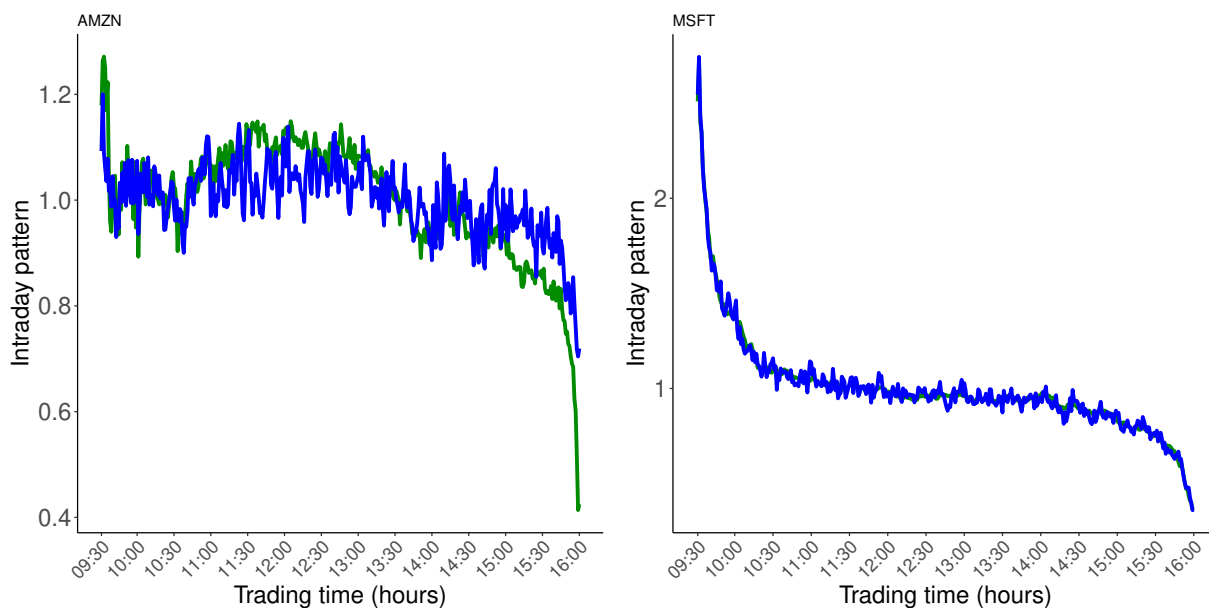


Figure H.1: **Simulated and real intraday price impact pattern.** We compare the price impact intraday pattern derived from real (green) and simulated (blue) data. The left panel displays a small tick stocks setting example, i.e., AMZN, while the right panel displays a large tick stocks setting example, e.g., MSFT. This figure has been extracted from [345], see appendix B.5 for details about attributions and permissions.

C (GOOG henceforth). Tables H.3 and H.4 present basic descriptive statistics for these stocks.

Fig. H.3 displays the analogous quantities of Fig. 4.20 for AMZN. The right panel shows that the goodness of fit of the model for small tick stocks is significantly lower than the one observed for small tick stocks. Next, we perform the VAR analysis presented in appendix H.3. Table H.5 reports the regression coefficients derived from Eq. (H.3) and the corresponding t -statistics. Contrary to the large tick stocks case, both the coefficient c_1 – which captures the effect of past mid-price changes on the current value of OFI – and d_1 – which captures the effect of past OFI on the current value of OFI – are highly significant for two out of three stocks.

The coefficients of lagged price change on the current level of OFI c_1 are negative and significant. Consider the following intuition. Suppose that a cancellation at the best ask depletes the queue prompting a positive price change. This leads to an increase in sell market orders, cancellations of buy limit orders, and an increase in sell limit orders, i.e. the OFI decreases. Moreover, even if the initial cancellation does not deplete the queue, the same reasoning applies since it is well known that the bid/ask queue imbalance retains significant predictive power for the direction of the next mid-price movement, see [433]. Finally, we note that if one neglects limit orders and

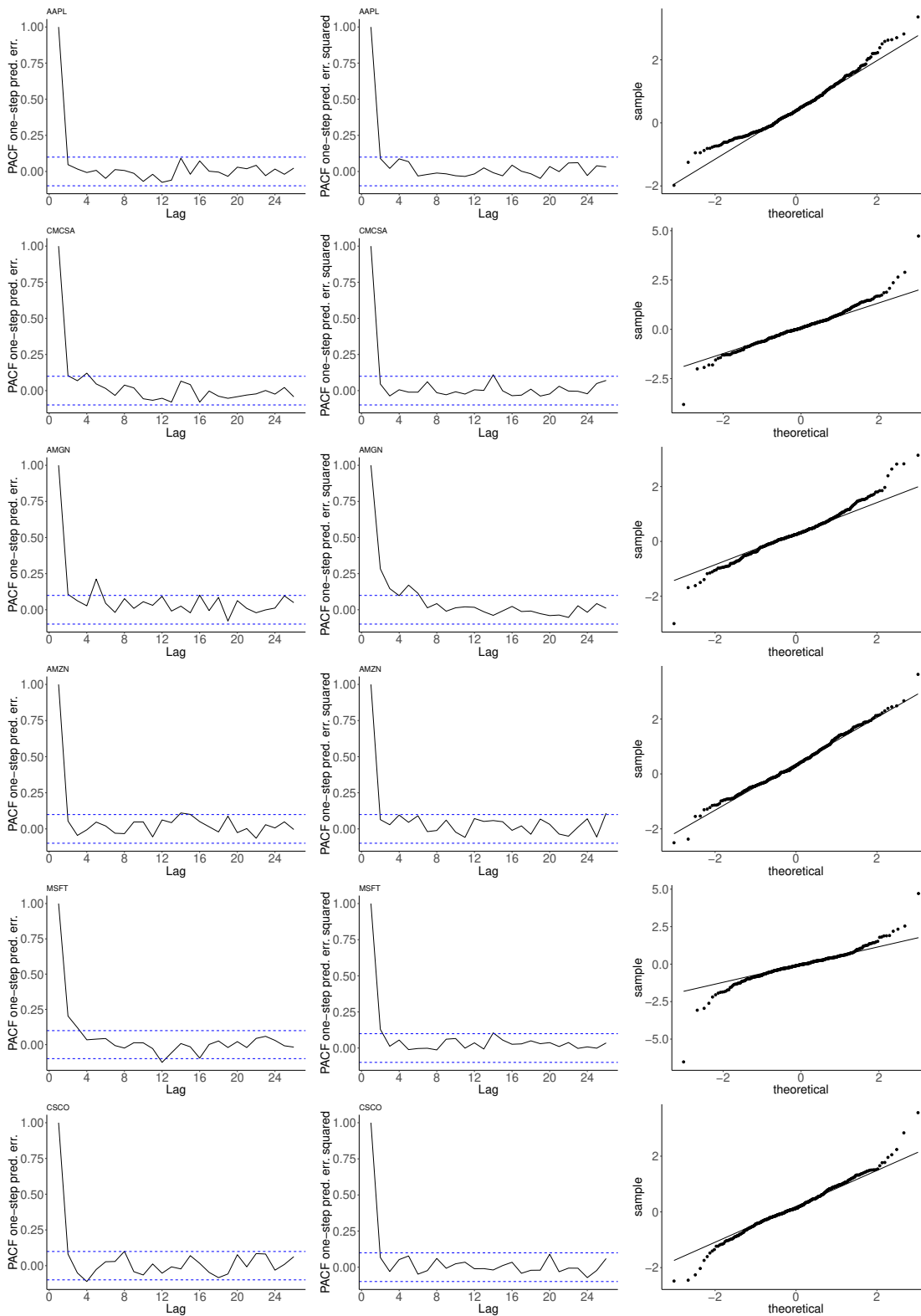


Figure H.2: **Some statistical properties of the standardized one-step ahead forecast errors.** Each row represents a stock: AAPL (first from top), CMCSA (second), AMGN (third), AMZN (fourth), MSFT (fifth), CSCO (sixth). The grid displays the sample auto-correlations of the standardized one-step ahead forecast errors (left column), the sample auto-correlations of the squared standardized one-step ahead forecast errors (central column), the quantile-quantile plot of the standardized one-step ahead forecast errors (right column). This figure has been extracted from [345], see appendix B.5 for details about attributions and permissions.

Parameter	True value	Estimated value I	Estimated value II
Large tick stocks setting			
β	$\overset{d}{\sim} U(0, 1.5\beta)$	1.140×10^{-6}	1.256×10^{-6}
	$\beta = 1.413 \times 10^{-6}$	(5.784×10^{-7})	(5.283×10^{-7})
σ_ϵ	$\overset{d}{\sim} U(0.8\sigma_\epsilon, 1.1\sigma_\epsilon)$	9.938×10^{-3}	9.224×10^{-3}
	$\sigma_\epsilon = 9.628 \times 10^{-3}$	(1.224×10^{-3})	(1.111×10^{-3})
ρ	$\overset{d}{\sim} U(0.2, 0.4)$	0.78	0.33
		(0.14)	(0.15)
σ_η	$\overset{d}{\sim} U(0.8\sigma_\eta, 1.2\sigma_\eta)$	0.198	0.248
	$\sigma_\eta = 0.275$	(0.115)	(0.05)
Small tick stocks setting			
β	$\overset{d}{\sim} U(0, 1.5\beta)$	7.83×10^{-5}	7.87×10^{-5}
	$\beta = 9.739 \times 10^{-5}$	(4.195×10^{-5})	(4.176×10^{-7})
σ_ϵ	$\overset{d}{\sim} U(0.8\sigma_\epsilon, 1.1\sigma_\epsilon)$	0.283	0.284
	$\sigma_\epsilon = 0.301$	(0.026)	(0.0262)
ρ	$\overset{d}{\sim} U(0.2, 0.4)$	0.36	0.33
		(0.24)	(0.12)
σ_η	$\overset{d}{\sim} U(0.8\sigma_\eta, 1.2\sigma_\eta)$	0.532	0.498
	$\sigma_\eta = 0.540$	(0.285)	(0.16)

Table H.2: **Parameter estimates obtained from simulated data.** Top panel: simulation setting for large tick stocks. Bottom panel: simulation setting for small tick stocks. Columns, from left to right: parameter, distributional value, i.e., True value, estimate after the first stage, estimate after the second stage.

cancellations, the negative lagged ΔP_ℓ coefficient in the ϕ_ℓ specification implies Granger-Sims causality running from quote revisions to trades, and it is consistent with the findings in [390]. The auto-correlation of the (aggregated) OFI is captured by the parameter d_1 . To better understand why this coefficient is statistically significant for AMGN and AMZN we first define the following variables: $\Delta M_\ell \equiv M_\ell^b - M_\ell^s$, $\Delta L_\ell \equiv L_\ell^b - L_\ell^s$, $\Delta C_\ell \equiv C_\ell^b - C_\ell^s$. Then, we perform the following regression

$$\phi_\ell = \beta_1 \Delta M_{\ell-1} + \beta_2 \Delta L_{\ell-1} + \beta_3 \Delta C_{\ell-1} + \eta_\ell, \quad (\text{H.4})$$

Stock	Ticker	Mid-price		Spread		Relative Spread	
		Avg.	Std	Avg.	Std	Avg.	Std
		Amgen, Inc.	AMGN	151.998	5.513	0.086	0.022
Amazon.com Inc	AMZN	622.819	69.093	0.416	0.107	6.84	2.22
Alphabet Inc Class C	GOOG	717.521	21.643	0.473	0.129	6.61	1.88

Table H.3: **Descriptive statistics for the investigated small tick stocks.** The sample period spans between January 4th 2016 and June 30th 2016. Mid-price and Spread are expressed in USD while the Relative Spread is expressed in basis points.

Symbol	Bid $Q_{1,\ell}$		Ask $Q_{1,\ell}$		Bid $Q_{1,c}$		Ask $Q_{1,c}$		Bid $Q_{1,m}$		Ask $Q_{1,m}$	
	#Ev.	Avg.Vol.	#Ev.	Avg.Vol.	# Ev.	Avg.Vol.	#Ev.	Avg.Vol.	#Ev.	Avg.Vol.	#Ev.	Avg.Vol.
AMGN	16412.88	234.23	16186.08	232.55	10223.09	137.75	9922.26	134.91	4375.17	48.93	7486.83	83.74
AMZN	17863.07	780.85	17629.69	793.85	11593.60	432.32	11186.28	436.26	5108.44	178.90	11444.78	392.32
GOOG	19005.85	914.45	24914.89	1011.14	12355.18	514.16	17500.40	565.43	3580.73	136.56	7653.50	291.92

Table H.4: **Sample statistics for the orderbooks of the covered small tick stocks.** The sample period spans between January 4th 2016 and June 30th 2016. We report the number of events (#Ev.) and average volume (Avg.Vol in units) of limit orders placed at the best bid (Bid $Q_{1,\ell}$) and best ask (Ask $Q_{1,\ell}$), cancellations at the best bid (Bid $Q_{1,c}$) and best ask (Ask $Q_{1,c}$) and executions at the best bid (Bid $Q_{1,m}$) and best ask (Ask $Q_{1,m}$).

where η_ℓ is a noise term. Table H.6 summarises the outcomes of this exercise. We observe that for small tick stocks the auto-correlation of the OFI is induced from the Granger-Sims causality running from market orders and cancellations to OFI.

In conclusion, extending the model to small tick stocks requires a proper accounting of these additional dependencies. Such exercise is beyond the scope of this project and is left for future work.

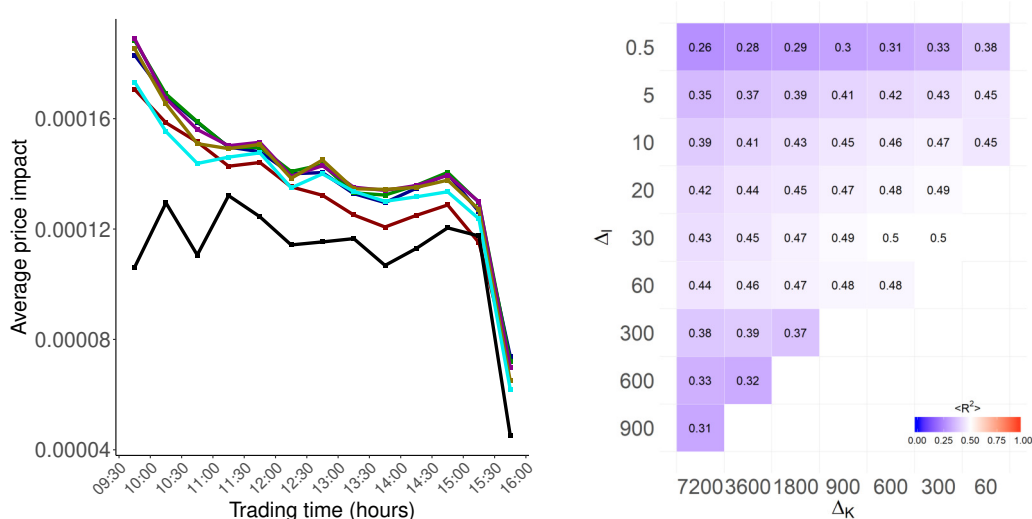


Figure H.3: **Fitting the Cont-Kukanov-Stoikov model to a small tick stock.** The left panel displays the shape of the average intraday pattern of the price impact coefficient estimates $\hat{\beta}_k$ derived from Eq. (4.14) fitted on AMZN trading data. We set $\Delta_K = 1800s$ and examined different values for Δ_ℓ : 0.5s (red), 5s (blue), 10s (green), 20s (magenta), 30s (gold), 60s (cyan) and 300s (black). The right panel displays the average R^2 coefficients across days as a function of the regression window Δ_K and sampling frequency Δ_ℓ . This figure has been extracted from [345], see appendix B.5 for details about attributions and permissions.

Ticker	Parameters values (t -stats)				
	b_0	a_1	b_1	c_1	d_1
AMGN	-2.87e-05	0.102	-8.97e-06	-5419.17	0.34
	(-19.74 ^{***})	(0.78)	(-1.24)	(-3.22 ^{***})	(5.09 ^{***})
AMZN	-1.04e-04	0.092	-4.06e-05	-1265.3	0.42
	(-15.20 ^{***})	(1.22)	(-2.86 ^{**})	(-3.44 ^{***})	(7.64 ^{***})
GOOG	-3.31e-07	-0.01	1.84e-08	-112226.99	0.01
	(-27.78 ^{***})	(-0.003)	(0.15)	(-0.46)	(0.14)

Table H.5: **Estimates of the VAR parameters.** Statistically significant coefficients at 10%, 5% and 1% confidence levels are marked with one, two and three stars, respectively.

Ticker	Parameters values (t -stats)		
	β_1	β_2	β_3
AMGN	0.212 (2.02**)	0.13 (0.06)	-0.05 (-0.05)
AMZN	0.406 (4.90***)	0.215 (0.06)	-0.171 (-2.02**)
GOOG	0.008 (0.03)	0.030 (0.06)	-0.060 (-0.63)

Table H.6: **Estimates of the regression in Eq. (H.4).** Statistically significant coefficients at 10%, 5% and 1% confidence levels are marked with one, two and three stars, respectively.